UNIVERSITY OF SOUTHAMPTON

FACULTY OF ENGINEERING, SCIENCE & MATHEMATICS

SCHOOL OF OCEAN AND EARTH SCIENCE

Methane in deep sea hydrothermal plumes.

Development of a new in-situ methane sensing technology.

by

Cédric Boulart

Thesis submitted for the degree of

Doctor of Philosophy

September 2008

Graduate School of the
National Oceanography Centre, Southampton

This PhD dissertation by

Cédric Boulart

has been produced under the supervision of the following persons

Supervisor/s
Prof. Christopher R. German
Dr. Douglas P. Connelly
Dr. Matthew C. Mowlem

Chair of Advisory Panel
Prof. Peter J. Statham

UNIVERSITY OF SOUTHAMPTON

ABSTRACT

FACULTY OF ENGINEERING, SCIENCE & MATHEMATICS

SCHOOL OF OCEAN AND EARTH SCIENCE

Doctor of Philosophy

METHANE IN DEEP-SEA HYDROTHERMAL PLUMES. DEVELOPMENT OF A NEW IN-SITU METHANE SENSING TECHNOLOGY.

by Cédric Boulart

Information on the concentration and distribution of dissolved methane (CH_4), together with other geochemical tracers, in real time is of great value in detecting, monitoring, and understanding the functioning of hydrothermal plumes.

Water column anomalies of light transmission, dissolved CH_4, manganese (Mn), and iron (Fe) were located over segments 15 and 16 of the Central Indian Ridge (CIR 20ºS), in December 2006. Along segment 15, a hydrothermal plume was present at 19°33'S/65°50'E. The source might be located north of that position and dispersed along the western flank by NW-SE currents. Methane to manganese ratios suggest that methane is produced by magmatic processes. On Segment 16, evidence for 1 or 2 hydrothermal plumes were detected over a lava plain (18°20'S/65°18'E). These data suffered from uncertainties due to sampling issues, which demonstrate the need for a reliable in-situ methane sensing technology.

Current in-situ methane sensing technology is based on gas partitioning across gas permeable membranes, which are poorly characterised and variable in terms of permeability and environmental pressures.

Two optical techniques were laboratory tested for the measurement of dissolved methane; Near Infrared Fibre-optic Evanescent Wave Spectroscopy (FEWS) and Surface Plasmon Resonance (SPR). No detection (at the μM level) was possible with FEWS, but the second technique using SPR sensors associated with a methane specific binding chemically showed great promise. A limit of detection of 0.2 nM and a linear concentration range from 1 to 300 nM was demonstrated, under a range of temperature and salinity.

In-situ deployments confirmed the suitability of the method for in-situ measurements. Values given by the sensor correlated well with the concentrations measured by traditional techniques. Future work is needed to decrease instrumental noise and to reduce the response time, and associated hysteresis effect.

Tables of Contents

List of Tables

List of Figures

Declaration of Authorship

I, Cedric Boulart, declare that the thesis entitled "METHANE IN DEEP-SEA HYDROTHERMAL PLUMES. DEVELOPMENT OF A NEW IN-SITU METHANE SENSING TECHNOLOGY" and the work presented in it are my own. I confirm that:

- this work was done wholly or mainly while in candidature for a research degree at this University;
- where any part of this work has been submitted for a degree or any other qualification at this University or any other institution, this has been clearly stated;
- where I have consulted the published work of others, this is always clearly attributed;
- where I have quoted from the work of others, the source is always given. With the exception of such quotations, this thesis is entirely my own work;
- I have acknowledged all main sources of help;
- where the thesis is based on work done by myself jointly with others, I have made clear exactly what was done by others and what I have contributed myself;
- parts of this work have been published as:

  Cédric Boulart, Matthew C. Mowlem, Douglas P. Connelly, Jean-Pierre Dutasta, Christopher R. German. 2008. A novel, low-cost, high performance dissolved methane sensor for aqueous environments. *Optics Express*, **16**, 12607-12617.

Signed:

Date:

Acknowledgements

First of all, I would like to thank my supervisors Prof. Chris German, Dr. Doug Connelly, and Dr. Matt Mowlem who gave me the chance to do this research at the frontier between deep-sea science and engineering. I have been lucky to work with them – they have always been supportive and of invaluable advice in every aspect of science (from details to general research). I do not want to forget Dr. Ralf Prien, who supervised the PhD at the very beginning. Thanks to them, I have been involved in a European network – MoMARnet – which has been such a great opportunity to work at an international level.

Chris has always been a source of motivation with a lot of ideas. Thanks a lot for the invaluable advice on the Central Indian Ridge data! Thanks to Doug who has been such a great and enthusiastic supervisor and for his precious help with the gas chromatograph, his availability to discuss the results and the sensor data, his 'English Language and Culture' lessons, and his sense of humour…; Thanks to Matt for his support, advice, ideas (I never left his office without a new idea to try or to test), enthusiasm, and… the Wednesday evening sailing… That was very useful for my sanity.

Thanks to Dr. Ed Austin, with whom I worked on the fibre-optic sensor and with whom I desperately tried to make it work! His advice and ideas were very useful, although we did not have time to test them.

Many thanks to Dr. Jean-Pierre Dutasta: without Jean-Pierre, all the cryptophane work would have not been possible. Although we have never met, our long conversations on the phone and our exchange of emails were always useful and precious.

Thanks also to Mairi Sanderson and Shahanara Banu who introduced me to the clean lab facilities at Highfield and the techniques of polymer coatings.

I also have to thank the crew and the scientific party of the KH-06-4 cruise. That was an amazing experience!
Many thanks to the people from 'downstairs' (Cedric F., Sarah, Steve, Matt B., Ed, Ian, Alan, David, Lee, Samir, Andy) for… the lunch at 12.25. Thanks especially to Steve,

Andy, and Lee for their help with the technical things, Cedric for his ideas, Sarah for her support, Matt B. for his humour, Ed for his help (and the tools I sometimes borrowed)…

As I said at the beginning of these acknowledgements, this PhD work was part of a European network, MoMARnet, which gathered 14 laboratories through Europe. That was an amazing and very rich experience to exchange with everyone within the network. Thanks to Mathilde who managed this project so brilliantly (and also for her support), and to all the MoMARnet 'Fellows'. That was always a pleasure and a good fun to get all together somewhere in Europe.

Two persons deserve special thanks: Alice and Nelia. Not only housemates but also very good friends! I really enjoyed these 3 years with you.

Thanks to everyone who has contributed to such a great few years at NOCS and for making life in Southampton easier: Teresa, Igor, Lev, Clara, Mimi, Jeroen, and all the others who I have unintentionally omitted.

And for the last persons on the list, I will do it in French:

Merci à ma famille qui a toujours été un soutien pour moi, surtout au tout début de la thèse, durant laquelle il a fallu s'adapter à un nouveau pays, une nouvelle culture… Cela n'a pas été facile tous les jours! Mais l'expérience vaut le coup d'être vécue.
Merci à Nico, Marie, Vincent, Aurélien, et tous ceux qui ont eu à me supporter pendant ces 3 années de thèse! Et maintenant, vous avez la preuve que je n'ai pas fait que prendre l'avion pendant tout ce temps.

This PhD thesis has been supported and funded by EU-FP6-MoMAR network (MRTN-CT-2004-505026).

List of Abbreviations

AUV	Autonomous Underwater Vehicle
CIR	Central Indian Ridge
CTD	Conductivity-Temperature-Depth
EPR	East Pacific Rise
ESONET	European Seafloor Observatory NETwork
FEWS	Fibre-optic Evanescent Wave Spectroscopy
FID	Flame Ionisation Detector
GC	Gas Chromatography
GC-MS	Gas Chromatography - Mass Spectrometry
HC	Hydrocarbons
HS-GC	Headspace Gas Chromatography
JFR	Juan de Fuca Rise
LOD	Limits of Detection
MAR	Mid-Atlantic Ridge
MIR	Mid Infrared
MS	Mass Spectrometry
NEPTUNE	North-East Pacific Time-series Undersea Networked Experiments
NIR	Near Infrared
PDMS	Poly-DiMethyl-Siloxane
RI	Refractive Index
ROV	Remote Operated Vehicle
RTJ	Rodriguez Triple Junction
SCANNER	Submersible Chemical Analyser
SERS	Surface Enhanced Raman Spectroscopy/Scattering
SPR	Surface Plasmon Resonance

CHAPTER 1: GENERAL INTRODUCTION

1.1 Methane on Earth

1.1.1 Methane

Methane (CH_4, Figure 1.1) is the main component of the natural gas (75 %) present in the environment, which reacts with oxygen (O_2) to form water (H_2O) and carbon dioxide (CO_2) and absorbs long wavelength radiation emitted from the Earth's surface (infrared) in the 4-100 μm wavelength (Graedel and Crutzen, 1993). CH_4, the most abundant hydrocarbon present in Earth's atmosphere (Reeburgh, 2003), is classified as a greenhouse gas, as are water vapour, nitrous oxide, ozone (O_3), CO_2, and chlorofluorocarbons (CFC) (Lacis et al., 1981; Hansen et al., 1988; Ramanathan, 1988). CH_4 has been studied for over 200 years (Reeburgh, 2003) but it was only in the early 1950s, with the development of gas chromatography and the flame ionization detector (Halász and Schneider, 1961) that the global cycle of methane began to be studied in detail.

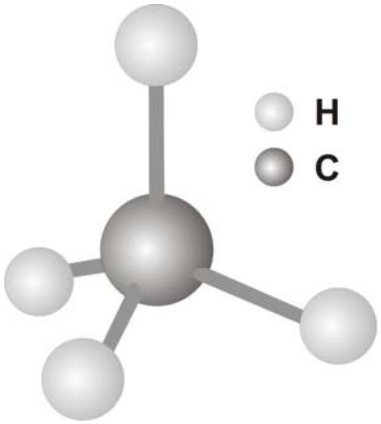

Figure 1.1: Methane molecule

Methane has a relatively short lifetime of 8-12 years in the atmosphere (Wahlen, 1993; Zellner et al., 1999) but its stronger absorption band at 7.66 μm (infrared), where water vapour (H_2O) and carbon dioxide (CO_2) absorb weakly, makes CH_4 an important contributor to the Earth's radiative balance. Although CH_4 is a trace gas, it

contributes up to 20% of the greenhouse effect due to its high global warming potential (25 times more powerful than CO_2 over a 100 year timescale) (IPCC, 2007). Since 1930, with the advance of the industrial revolution, atmospheric concentrations of methane have increased from 0.7 to 1.75 ppmV (Houghton et al., 1990 ; Zellner et al., 1999; Reeburgh, 2003; Artuso et al., 2007). Houghton et al. (1990) have suggested that a contribution of 1.7 $W.m^{-2}$ to the greenhouse effect results from the present atmospheric methane concentration.

In the atmosphere, methane contributes to the production of water vapour and to the build-up of CO_2 by reacting with the hydroxyl radical $OH^{\bullet}$, which is its main atmospheric sink (Zellner et al., 1999; Artuso et al., 2007). $OH^{\bullet}$ is formed when ozone (O_3) is photodissociated into O_1, which combines with H_2O to give two hydroxyl radicals. About 90 % of the atmospheric methane is oxidised through these reactions (Cicerone and Oremland, 1988; Reeburgh, 2003). In the stratosphere, methane reacts with atomic chlorine forming HCl, which is the terminal step of stratospheric ozone destruction (Cicerone and Oremland, 1988; Zellner et al., 1999; Reeburgh, 2003). About 5% of the atmospheric methane escapes to the stratosphere to undergo these reactions (Cicerone and Oremland, 1988).

Methane is produced and released to the atmosphere by a large variety of sources, both natural and anthropogenic, which are summarized in Table 1.1. The increase in concentration is partly related to anthropogenic sources since the industrial revolution (Houweling et al., 1999); if we distinguish anthropogenic from natural emissions, human activities could account for twice the natural emissions (Artuso et al., 2007). However, data from ice cores clearly show a natural variability of atmospheric methane due to fluctuations occurring between glacial and interglacial periods (Artuso et al., 2007). It is therefore essential to determine the variability of the natural sources and sinks of methane, and especially the global flux from natural sources, such as freshwater and marine ecosystems.

Most of the atmospheric methane is biologically produced by the microbial decay of fresh organic matter facilitated by anaerobic bacteria commonly known as methanogens (Lovley et al., 1982) that require strong anaerobic and reducing conditions (found in wetlands, swamps, rice paddies) (Hakemian and Rosenzweig, 2007). Recent studies have

shown that natural vegetation can also account for 10 to 30 % of the annual emissions of methane (Keppler et al., 2006). Termites, the oceans and gas hydrates also play significant roles in the global methane budget (Reeburgh, 2003).

The marine contribution to the global net atmospheric budget is relatively small and cannot be expected to have played a major role in the current-era atmospheric concentration increase (Artuso et al., 2007). The typical methane concentrations in the open ocean fall in the nanomolar range (Reeburgh, 2007), contrasting with the enormous input from continental shelves, where concentrations of hundreds of nM can be found (e.g. Berner et al., 2003; Collier and Lilley, 2005; Damm et al., 2005; Newman et al., 2008). Bange et al. (1994) estimated that the oceanic supply, including shelf and estuarine environments, lies in the range: 11-18 Tg CH_4/yr. Coastal environments account for 75% of the oceanic emissions to the atmosphere, which contribute to about 2% of the global atmospheric emission (Rehder et al., 2002). Various pathways allow methane to enter the water column: coastal runoff, diffusion from sediments, seeps, hydrothermal vents, and mud volcanoes. Sources of methane to the water column include microbially-mediated degradation of organic matter in sediments, abiotic production through different thermodynamic reactions, water/rock interactions occurring under high pressure and temperature conditions, and decomposition of methane hydrates along continental margins (Reeburgh, 2007). Biological production of methane in ocean waters is limited due to thermodynamic, kinetic, and physical constraints (Lovley et al., 1982; McCollom, 2000; Reeburgh, 2007). For example, methanogenesis (biological production of methane), which only happens in anoxic ecosystems (without O_2), is not expected to occur at as a large scale process in most open-ocean waters due to the presence of abundant dissolved oxygen (Reeburgh, 2007).

Despite the high concentrations of methane present in both fluids and sediments, the oceans remain under-saturated with respect to the atmosphere because of the effective consumption of any added methane by microbial oxidation (Reeburgh, 2007). Therefore, understanding the sources and sinks of methane to, from, and within the oceans represents an important step toward understanding the CH_4 balance between the oceans and the continents.

Table 1.1: Global net CH_4 emission, consumption, and gross production (Tg CH_4 yr^{-1}). From Reeburgh (2003, 2007).

E + C = P with E: Net emission, C: Consumption, and P: Gross production. The table uses the net CH_4 budget in Reeburgh (2003), adds oxidation estimated from oxidation rate measurements and mass balances, and produces an estimate of gross CH_4 production. Hence, the gross production takes into account the net emission (after microbial oxidation) and the amount of methane that would be released to the atmosphere without the microbial oxidation. From this table, more than half of the estimated CH_4 production is oxidized by microbes before emission to the atmosphere.

Sources/sinks term	*E* *Net emission*	*C* *Consumption*	*P* *Gross production*
Animals	80	0	80
Wetlands	115	27	142
Tundra (boreal)	35	15	50
Swamps/alluvial	80	12	92
Rice production	100	477	577
Biomass burning	55	0	55
Termites	20	24	44
Landfills	40	22	62
Oceans, freshwaters	10	75	85
Hydrates	5	5	10
Coal production	35	0	35
Gas production	40	18	58
Venting, flaring	10	0	10
Distribution leaks	30	18	48
Total sources	500		
Chemical destruction	-450		
Soil consumption	-10	40	
Total sinks	-460	688	40
		Total production	1,188

1.1.2 Methane in the Deep Ocean

Methane production in the water column and in the deep-ocean is essentially related to the presence of seep and vent systems along continental margins and mid-ocean ridges (Reeburgh, 2007). While the release of methane from the seafloor along active subduction zones has been reported in many locations along the continental margins (e.g. Aharon et al., 1997; Clark et al., 2000; Van Dover et al., 2003; Charlou et al., 2004; Collier and Lilley, 2005; Valentine et al., 2005; Mastalerz et al., 2007), a measurable impact on the upper water column and the atmosphere, as described by Mau et al. (2007) is not always observed (Rehder et al., 2002). Fluid and gas emissions are strictly controlled by tectonism and over-pressure in sediments leading to the formation of different structures like mud volcanoes, pockmarks, and gas hydrates (Figure 1.2). Methane clathrate hydrates are nonstoechiometric solid structures composed of cages of water molecules surrounding methane molecules (Buffett, 2000). Estimates of the size of the methane reservoir sequestered as hydrates along continental margins and subduction zones are on the order of ~10 Tt (1Tt = 10^{18}g) (Kvenvolden, 1988), which represents ~30% of the ocean dissolved inorganic carbon reservoir (Reeburgh, 2007).

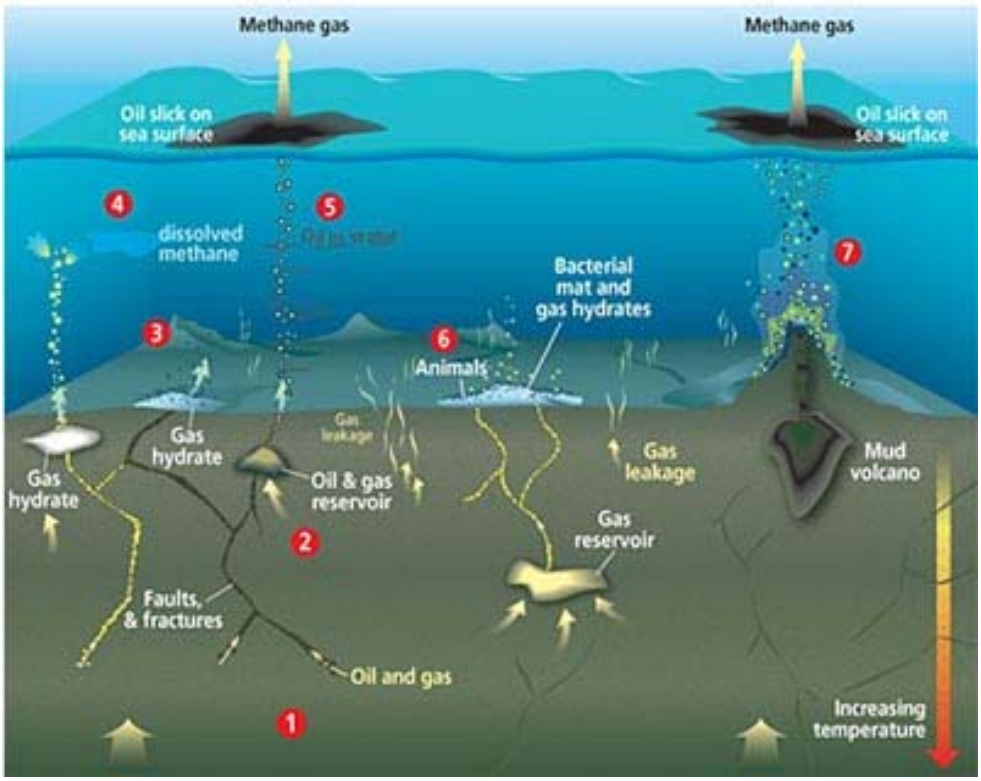

Figure 1. 2: Sources of methane along continental margins (from http://www.whoi.edu/oceanus, Jayne Doucette).

1: Circulation of oil and gas through faults and fractures; 2: Formation of oil and gas reservoirs; 3: Formation of gas hydrates on the seafloor; 4: Degassing and production of dissolved methane; 5: Direct degassing and bubbling from oil and gas reservoirs; 6: Microbial processing of the organic matter and methanogenesis; 7: Methane degassing from mud volcanoes

Hydrothermal vent systems along mid-ocean ridges are another significant source of methane for the deep ocean (Cowen et al., 2002). Methane concentrations in hydrothermal fluids range from 0.05 mM at most unsedimented ridges (e.g. Edmond et al., 1979, Welhan and Craig, 1979; Welhan and Craig, 1983) to 7 mM at sedimented ridges (e.g. Von Damm et al., 1985). On the basis of the ratio of basalt-derived methane to Helium (He) and the ^{3}He flux, the hydrothermal methane flux from the worldwide ridge system has been estimated to be 1.6 10^{8} m^{3} $year^{-1}$, which would be sufficient to replace all deep-sea methane on a timescale of ~30 years (Reeburgh, 2007). However, fluid flux measurements are notoriously difficult to make, so, inevitably, the amount of methane supplied by hydrothermal systems cannot be estimated accurately. The sources and sinks of methane in hydrothermal systems are multiple: methanogenesis or bacterial production, direct degassing from the magma, thermodynamic reactions, and water-rocks interactions. These sources will be detailed further in Chapter 3.

To summarize, significant uncertainties about the amount of methane emitted and absorbed by the oceans still exist, due to the high variability of methane emissions and also due to the unknown distribution and the patchiness of marine sources and sinks. Further the evaluation of the amount of methane produced by the oceans, and more generally by aquatic ecosystems, might simply be underestimated due to a lack of high resolution measurements of methane worldwide.

1.2 In-situ chemical sensing and development of new strategies for ocean studies

1.2.1 Chemical sensors

Measurements of concentrations of chemicals in seawater still rely, primarily, on water sampling from oceanographic ships and then bringing water samples on board, or even on shore, for analysis. Some sampling techniques currently used date back decades (Prien, 2007) although there is a continuous cycle of improvements in at-sea sampling techniques (e.g. SCOR, 2007). Sampling water at depths greater than 4000 m means that the ship remains on station for a long time (3-4 h), limiting the number of measurements and samples, and involving a strong risk of sample contamination and degradation. Ocean processes span a large range of spatial and temporal scales that cannot be assessed by the collection of discrete samples (Klinkhammer, 1994; Seyfried et al., 2000; Varney, 2000; Kroger and Law, 2005a). Besides, seawater chemistry is complex with a wide range of concentrations and comparable species, which requires both sensitivity and specificity from any method of analysis. All of these problems can potentially be addressed by in-situ chemical sensing to gain new insights to how biogeochemical cycles proceed (Varney, 2000; Kroger and Law, 2005a; Prien, 2007).

In-situ chemical sensors are defined as autonomous analytical systems for the estimation of the concentration of chemical species in real time (Figure 1.3 – Mizaikoff, 1999; Varney, 2000; Prien, 2007). Chemical sensors have to operate at the same time scale as the investigated process, under varying conditions of pressure, temperature, salinity, pH, and concentrations of possibly interfering compounds (Varney, 2000; Prien, 2007), and have to meet at least the same precision accuracy, and reliability as the well-established laboratory techniques. The development of chemical sensors is therefore a challenging

task and only a few in-situ sensors are actually used (e.g. O_2, Fe/Mn, nutrients). Many other sensors are currently being developed for several species (e.g. dissolved gases, PolyAromatics Hydrocarbons – PAHs, NH_4^+…) but only exist, to-date, as prototypes.

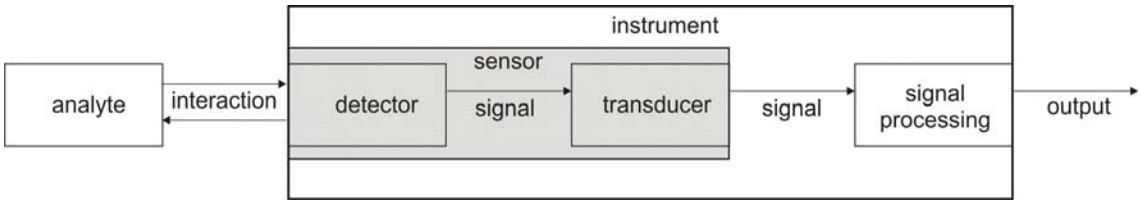

Figure 1.3: Generalised in-situ chemical instrument (from Prien, 2007).

Johnson et al. (1986) initiated the development of sensors for seawater studies by developing the SCANNER (Submersible Chemical Analyzer), an in-situ analyser for nutrients (N, P), manganese (Mn) and iron (Fe). Different techniques are actually used according to the target: optical absorption spectroscopy (nutrients, Fe, Mn – e.g. Gamo et al., 1994; Le Bris et al., 2000), microelectrodes (pH, H_2, H_2S, CO_2 and some metals – e.g. Le Bris et al., 2001; Luther III et al., 2008), optodes (O_2 – e.g. Glud et al., 2001; Tengberg, 2004; Sosna et al., 2007), Raman spectroscopy (PAHs, CO_2, hydrocarbons – e.g. Schmidt et al., 2004; Dunk et al., 2005; White et al., 2006; Bake and Walt, 2008), in-situ mass spectrometry (dissolved gases – e.g. Camilli and Hemond, 2004), biosensing (e.g. Kroger and Law, 2005b; Kroger et al., 2002), and microelectromechanical analysers (Merkel et al., 1999; McDonald et al., 2000; Bruhn et al., 2005).

Marine observation strategies are currently shifting towards the use of fixed or mobile platforms instrumented for acquiring data at remote locations. Figure 1.4 provides an overview of some of the common observational strategies used in oceanography. The different mobile platforms (ships, gliders, ROV, AUV, profilers, towed instruments, drifters) and the combination of the observational strategies offer the possibility to cover a wide range of spatial scales, while fixed platforms such moorings or bottom landers allows long-term temporal observations (Tengberg et al., 1995; Kroger and Law, 2005a; Tengberg et al., 2003).

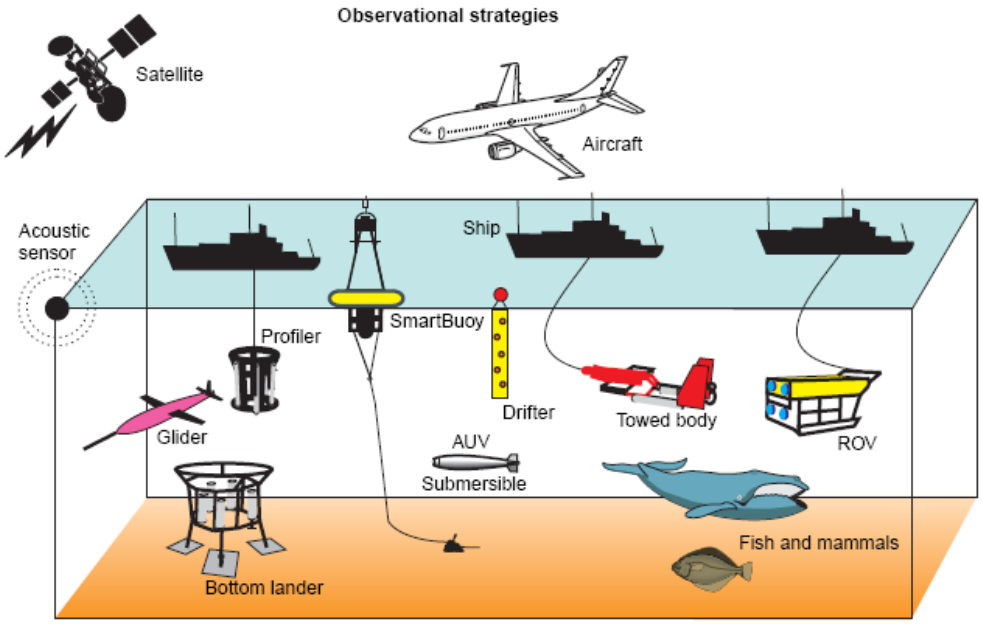

Figure 1.4: Marine observational strategies. From Kroger and Law (2005a)

1.2.2 Deep Sea exploration

In the case of deep-sea exploration, several complementary approaches help to discover venting systems, which are generally small sites, just hundreds of meters across. Surface-based cruises combining bathymetry, side-scan sonar, bottom photography, and coupled with detection for physical and chemical anomalies in the water column using sensors and water samples help to narrow the potential areas. Later, submersibles (manned or autonomous) and ROV are used to precisely locate the vents and to study them in detail (Baker et al., 1995; Bougault et al., 1998; Cave and German, 1998; German et al., 2008b).

Exploration is most often performed with a CTD-TO probe (Conductivity Temperature, Depth, Light Transmission, Optical sensor), associated with a "rosette multi-sampling system" (Figure 1.5). This rosette carries Niskin bottles and allows the water column to be sampled at several discrete depths (typically, 12 or 24 samples per cast). The main difficulty in venting-activity detection remains in the efficiency of progressing from plume detection to location, imaging, and sampling of a vent-site at the seafloor because plumes are subject to advection in response to near-bottom current flows that can alter and even reverse at tidal and other periods (Walker et al., 2004). Sampling strategies

include vertical casts or tow-yos establishing a vertical profile of the water column or dynamic hydrocasts giving a horizontal profile (Figure 1.5).

Once the vent-area has been precisely delimited, a detailed exploration is performed using different tools and platforms, such as manned submersibles, Remotely Operated Vehicles (ROV), Autonomous Underwater Vehicles (AUV) or towed bottom instruments carrying sensors and water sampling systems (Figure 1.5). These strategies have allowed the discovery and the study of many hot vent sites (e.g. Gamo et al., 1996a; German et al., 1998a; German et al., 2000; German et al., 2006) and cold seeps (e.g. Paull et al., 1995; Charlou et al., 2003; Charlou et al., 2004). During the last decade, there has been a strong interest in using in-situ chemical sensors as well as traditional optical sensors for the exploration of deep-sea.There are two key reasons for this. First, dissolved tracers can disperse much farther from a vent-site than suspended particulate matter (the cause of the backscatter signals in the mid-water column) that settles to the underlying seafloor. Second, optical backscatter signals provide relative measures of high or low particle loading but do not allow quantification of the strength of a chemical anomaly that can be related to analyses of source end-member vent-fluid that would allow processes within dispersing plumes to be investigated.

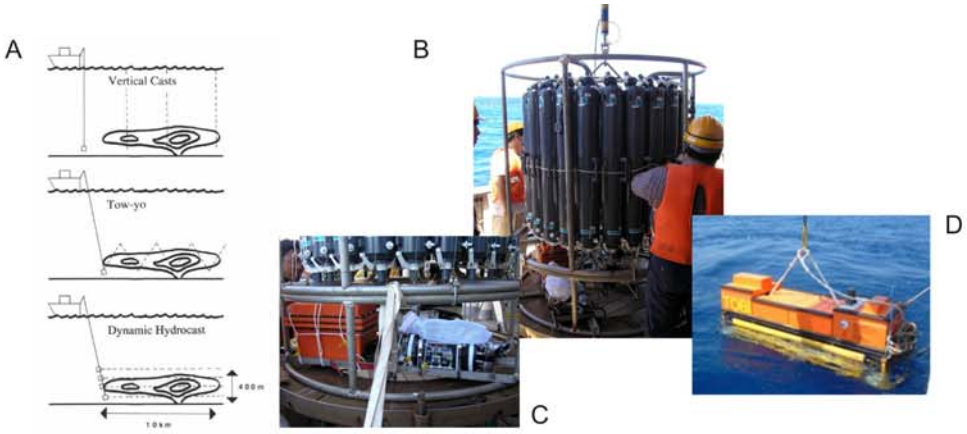

Techniques of exploration (A) performed by CTD-Rosette (B) hydrocasts equipped with in-situ sensors (C). D: Towed Ocean Bottom Instrument used as in-situ sensor platform.

Remotely Operated Vehicles (ROV). A: Victor 6000 (IFREMER - France) being launched; C: Isis (NERC-NOCS - UK)in Antarctica; C: Jason (WHOI - USA) being launched

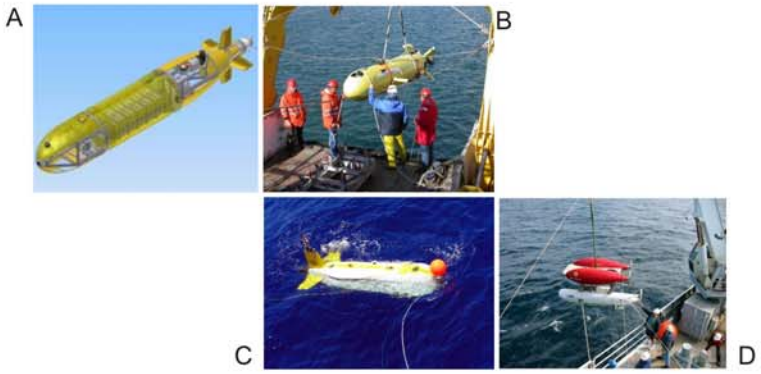

Autonomous Underwater Vehicles (AUV). A: Autosub 6000 (NERC-NOCS - UK); B: Aster-X (IFREMER - France); C: r2D4 (JAMSTEC - Japan); D: ABE (WHOI - USA)

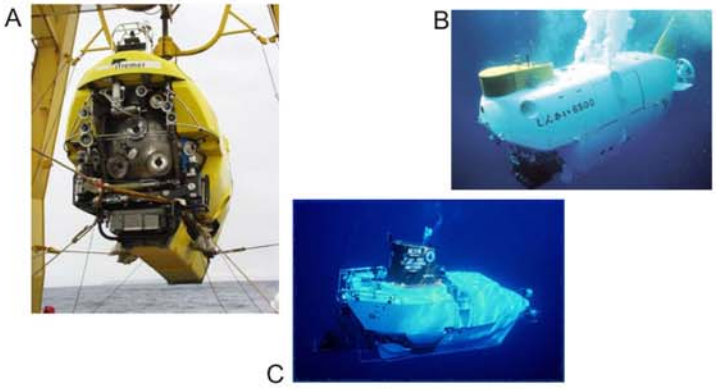

Manned submersibles. A: Nautile (IFREMER-France); B: Shinkai 6000 (JAMSTEC - Japan); C: Alvin (WHOI - USA)

Figure 1.5: Techniques of deep-sea exploration and examples of deep-sea platforms currently used.

Alongside the development of in-situ chemical sensors, there is a strong interest in the development of deep-sea long-term observatories through national and international programs, such as ESONET (European Sea Floor Observatory Network – http://www.abdn.ac.uk/ecosystem/esonet/), NEPTUNE (North-East Pacific Time-series Undersea Networked Experiments – www.neptunecanada.ca), or GEOSTAR (Beranzoli et al., 2003). A seafloor observatory, as defined in Favali and Beranzoli (2005), is an unmanned station, capable of operating in the long-term on the seafloor, supporting the operation of a number of instrumented packages related to various disciplines. Important requirements for the full realisation of the potential of seafloor observatories are the development of a new generation of scientifically useful, real-time, in situ, physical and chemical sensors, able to operate on a long-term basis. Although many sensors are currently available for underwater use, there remains a lack of new – particularly biogeochemical – sensors, especially for long-term deployment in the deep sea environment.

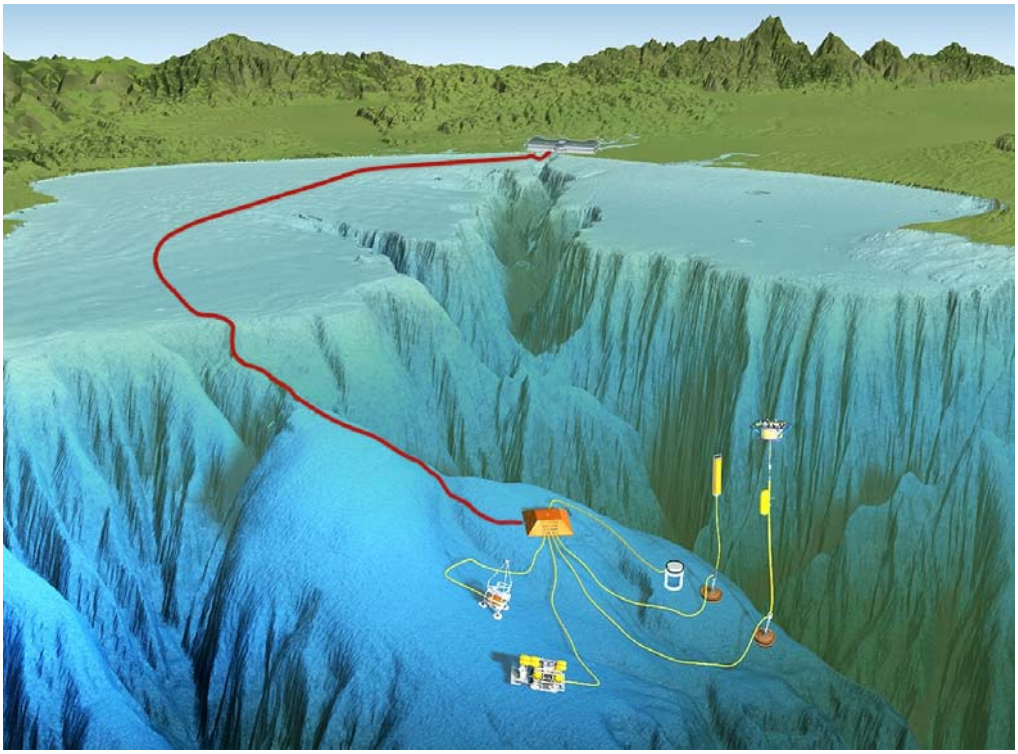

Figure 1.6: An illustration of the MBARI's MARS undersea observatory showing its cable links (credit: David Fierstein, MBARI)

1.3 Objectives and thesis structure

The initial aim of this Ph. D. Thesis was to provide a new methodology for the study of the geochemical cycle of methane in oceanic environments and a tool for the exploration of deep-ocean structures, where it is important to calculate more accurate geochemical budgets. The two objectives were, therefore, 1) to investigate the role of methane as a geochemical tracer of hydrothermal processes along the Central Indian Ridge; and 2) to develop a new methodology for the in situ measurements of dissolved methane in aquatic environments.

1.3.1 Objectives

1.3.1.1 Role of methane as a geochemical tracer for hydrothermal activity over the Central Indian Ridge

Hydrothermal activity strongly impacts the geochemical cycle of many elements in the deep seas. However, only 10% of the mid-ocean ridges have been explored systematically, to-date, for hydrothermal vent distributions (Baker and German, 2004). Consequently, modern values for hydrothermal inputs may remain largely underestimated. Optical and geochemical tracers are used to detect the presence of hydrothermal vents as well as to calculate the contribution of hydrothermal inputs to global geochemical cycles. Methane in deep sea environments is an important tracer for the detection of hydrothermal venting along spreading ridges (Charlou et al., 1988; Keir et al., 2008) as well as fluids seeping along continental margins (Collier and Lilley, 2005; Heeschen et al., 2005). Besides, methane is also a geochemical tool for the comprehension of geological, chemical, and biological processes occurring in deep sea environments and more especially in vent plumes. Plumes provide opportunities to study the effect and the influence of deep venting on the water column and possibly on the atmosphere. The objective, here, is therefore to assess the role of the geochemical tracers for the detection and the characterization of hydrothermal plumes over the Central Indian Ridge, and the assessment of the underlying processes generating the hydrothermal plumes.

I.3.1.2 Development of Methane sensor technology

The detection of deep ocean plumes and vents is based on the detection of anomalies of physical or optical tracers such as temperature, salinity or nephelometry. It has long been established that geochemical tracers such as methane or manganese concentrations are more sensitive than physical or optical tracers (e.g. Baker, 1990; Kadko, 1993; German et al., 2008b). But the lack of sensors allowing direct concentration measurements prevents us from using these tracers efficiently, hence the continuing reliance upon backscatter devices for much of our work (German et al., 2008a). The progress made in sensing technology and in the development of geochemical sensors is motivated by the permanent need of real time measurements. The second objective is hence to review the different technologies available for the in situ measurements of dissolved methane and to develop a new methodology for in situ methane sensing.

I.3.2 Thesis structure

After a presentation of the methodology used for the measurements of dissolved methane concentrations (Chapter 2), the role of methane as a tracer of hydrothermal venting is studied in Chapter 3 through the analysis of samples and the interpretation of data collected during an exploration of the Central Indian Ridge (18-20ºS) in December 2006. That Chapter highlights the role of optical and chemical sensors to detect hydrothermal activity and to guide the sampling, but also highlights the necessity of a reliable, compact, and high performance methane sensor.

Since the late 1990s, a strong interest in in situ methane sensing has lead to the development of techniques and instruments for dissolved methane measurements, which are reviewed in Chapter 4. Existing designs have been proven to be poorly adapted to their task and show some limitations in term of sensitivity, selectivity, reliability and cost. As described by Reeburgh (2007), the “ideal” dissolved methane sensor would be chemically reactive, reversible, fast, and highly sensitive (capable of detecting nM concentrations).

More and more, optical sensing schemes have gained importance. In particular, the introduction of novel optical fibres able to serve as waveguides for signal transportation

as well as representing the actual transducer permits the transformation of bench top optical techniques to portable and compact sensors (Mizaikoff, 1999). In the first part of Chapter 5, I describe a first design that has been tested, based on Fibre-optic Evanescent Wave Spectroscopy (FEWS) and using optical fibres as a sensing element. The results of this preliminary work have lead to the development of a second, more successful, technique, which uses surface plasmon resonance sensors and chemically reactive surfaces (second part of Chapter 5). Finally, some perspectives for further development of this technique, beyond the scope of the current project, are presented (Chapter 6).

CHAPTER 2: METHODOLOGY FOR DISSOLVED METHANE ANALYSIS

2.1. Overview of dissolved methane measurements

Measurements of dissolved methane are more difficult than atmospheric methane because of the necessity to separate the dissolved gas from the water phase. Before the introduction of gas chromatography (GC) and gas extraction methods, dissolved gas measurements were performed using manometric (Scholander, 1947) and microgasometric techniques (Peters and Van Slyke, 1932).

Since its development in the early 1950's (James and Martin, 1952), volatile compounds and atmospheric gases have been generally analysed by GC. Gas chromatography is an analytical technique using a column to physically separate and identify the components of a gaseous mixture (Kolb and Ettre, 1997). In GC, the gases are separated on the column by means of partitioning between a stationary phase (a non volatile liquid within a long thin column) and a mobile phase (an inert gas also called carrier gas, e.g. N_2). The compounds are detected at the end of the column and are differentiated by the retention time (time between the introduction of the sample and the detection), which is a characteristic of the compound. The concentration of the compound is determined by the area of the signal (peak area) (Kolb and Ettre, 1997).

Different detectors are used depending on the components to be detected. A flame ionisation detector (FID) measures concentrations of hydrocarbons by burning the sampled gas in an air-hydrogen flame. When burnt, hydrocarbons produce a high level of ionisation, proportional to the number of carbon atoms within the sample. More details on hydrocarbons detection using FID can be found in Halász and Schneider (1961).

Swinnerton and Linnenbom (1967) first developed a method to measure dissolved methane and other light hydrocarbons (C1 to C4) in water samples, based on gas extraction – or stripping – from the aqueous phase followed by GC analysis. In their method (the so called "strip-and-trap" method), dissolved hydrocarbons (HC) were first stripped from solution by purging with helium, and then concentrated in cold traps

containing appropriate adsorbents. The HC were subsequently released by increasing the temperature and swept into the chromatograph by a second stream of helium carrier gas. In this setup, two cold traps (-77ºC) were used in series. In the first, activated alumina was used to trap all hydrocarbons, except methane; in the second, activated charcoal was used to trap methane. Once the stripping was complete, the traps were isolated and their temperature was raised to 90 ºC. Helium carrier gas was then used to strip each adsorbent and to carry the gases to the GC for further separation and analysis. With this technique, sample size was not restricted and solutions with low HC concentrations could be analyzed.

The headspace extraction technique is a common method used for most of the oceanic measurements (Reeburgh, 2007). Different techniques of gas extraction can be differentiated: 1) purge-and-trap or dynamic headspace extraction (Kolb and Ettre, 1997), and 2) static headspace extraction (e.g. Jalbert and Gilbert, 1994; Kolb and Ettre, 1997; Demeestere et al., 2007). The purge-and-trap method, directly based on that of Swinnerton and Linnenbom (1967) has been used and optimized for the automated analysis of dissolved methane in the ocean water column (Charlou et al., 1991a; Charlou and Donval, 1993; Hashimoto et al., 2001), where concentrations are typically nanomolar (Reeburgh, 2007). Gaseous compounds are purged through an inert gas flow followed by collection of the analytes on an appropriate trap. Methane is usually collected and concentrated on a charcoal trap maintained at -80°C (Charlou and Donval, 1993). Then the gas sample is released into the capillary column by heating the trap rapidly up to 200-250°C. The 'purge-and-trap' technique is particularly well-adapted to the very low concentration of methane in open ocean waters (Charlou et al., 1998) but requires optimization of the purge-and-trap system, i.e. the flow-rate of the purging gas, the purging time, and the trap temperature (Hashimoto et al., 2001).

Static headspace gas chromatography analysis (HS-GC – Kolb and Ettre, 1997) refers to the analysis of the gas (vapour) phase of a binary heterogeneous system in equilibrium. It is a 'one-step' method of extraction, based on the principle that gases will undergo a partitioning between a vapour phase and a liquid phase that are in contact with each other. For water samples, bottles of known volume are filled without trapping bubbles and are capped with a crimp-seal stopper. A headspace of sufficient size (empirically derived) to contain >95% of the dissolved methane at equilibrium is introduced to the

inverted bottles using two syringes needles: one to slowly introduce the headspace to the top of the inverted bottle, and another near the stopper to remove the displaced water. Following equilibration, the methane concentration in the headspace is determined by gas chromatography (Reeburgh, 2007).

The static headspace extraction has been further modified to include ultrasonic vacuum degassing (Schmitt et al., 1991); in this system, methane (and other dissolved gases) is extracted in a vacuum system while the water sample is exposed to ultrasonic energy. Gases are released as fine bubbles and collected in a gas burette, then either sampled for GC analysis or transferred to an evacuated vial (Reeburgh, 2007). However, this method requires large volumes of sample (250-1000 mL) and materials resistant to vacuum conditions (Schmitt et al., 1991; Jalbert and Gilbert, 1994).

Due to its simplicity and rapidity, as well as access to sufficiently large sample volumes, static HS-GC analysis was used in this work i) to determine the methane concentration in samples collected along the Central Indian Ridge, as discussed in Chapter 3, and ii) to calibrate the response of the different sensing techniques presented in Chapters 5. The next section of this Chapter, therefore, will focus on the optimization of that methodology in terms of extraction efficiency, limits of detection, precision and accuracy.

2.2. Methodology used for dissolved methane analysis and its optimization

2.2.1. Gas Chromatography analysis

The GC system used for methane determination was an HP Agilent® 6850, fitted with a capillary 30.0m x 530 µm Agilent 115-3432-e GS-Q column and a FID (Figure 2.1). The GC setup used for the analysis of methane is presented in Table 2.1. The carrier gas was nitrogen of high purity grade with a flow rate of 3.1 mL/min through the column. An increase of the flow rate decreased the retention time but the peak resolution was degraded as a result. Hence, 3.1 mL/min was considered the optimum (Table 2.2). The column temperature was 40°C; higher temperatures increased the retention time for the

samples but degraded the peak resolution (Table 2.2). All peak processing, integration, and reporting were performed using the proprietary ChemStation® software (Agilent®).

Figure 2.1: Agilent® 6850 Gas Chromatograph (left) and details of the column, the injection and ports and the oven (right)

Table 2.1: GC setup for the analysis of methane

Method: METHANE.M		
Inlet	Mode	Split (N_2)
	Heater	200ºC
	Pressure	13.00 PSI
	Total flow	11.1 mL/min
	Split ratio	1.9:1
	Split flow	5.8 mL/min
	Gas saver	no
Column	Pressure	constant
	Source	Inlet
	Pressure	13.00 PSI
	Flow	3.1 mL/min
	Avg velocity	48 cm/sec
	Column	115-3432-e GS-Q
Oven	Set point	60ºC
	Time	2 min
Detector	Heater	250ºC
	H_2 flow	40 mL/min
	Air flow	450 mL/min
	Makeup flow (N_2)	5.0 mL/min

Table 2.2: Influence of oven temperature and flow rate through the column on retention time and peak area.

SD: Standard deviation on 10 ppm standard samples

Flow rate: 3.1 mL/min		
Temp Oven	Ret. Time (min)	Peak Area ± SD
40ºC	1.013	28.46 ± 0.12
60ºC	1.101	30.31 ± 0.13
100ºC	1.166	25.68 ± 0.61

Temp Oven: 60ºC		
Flow rate	Ret. Time (min)	Peak Area ± SD
2 mL/min	1.213	28.11 ± 0.03
10 mL/min	0.98	22.63 ± 0.88

Methane peak separation is observed in less than 2 minutes with this set-up (Figure 2.2 (a)). Calibration was performed daily by injecting different amounts of certified gas standard purchased from Air Products® UK (CH_4 10 ppm in N_2). Figure 2.2 (b) presents an example of a calibration curve. The detection limit (3 times the standard deviation on blank samples, n=20), the precision (given in % of the relative standard deviation) and the accuracy of the method are given in Table 2.3.

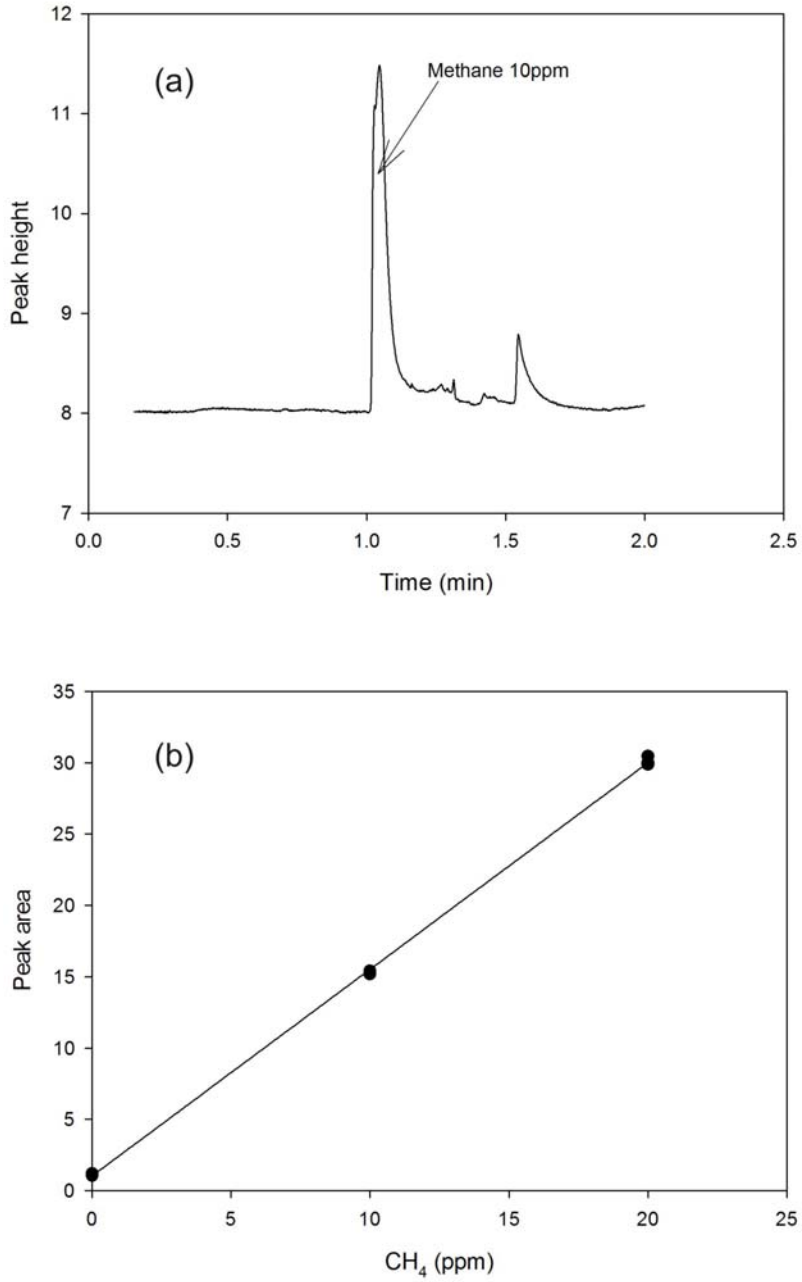

Figure 2.2: Chromatogram obtained for a 10ppm methane standard (a) and (b) example of daily GC calibration curve.

Table 2.3: Limits of Detection (3 times the standard deviation on blank samples, n=20), precision (reproducibility, %RSD) and accuracy (degree of conformity of a measured quantity to its certified value in %) of GC measurements (gas phase).
Precision is here 5% (RSD) and accuracy measurement comes out at 100.5% of the certified value.

LOD (ppm)	0.5
Precision (%RSD)	5
Accuracy	100.5

2.2.2. Gas extraction

In this Ph.D. thesis, three types of samples were taken for dissolved methane analysis: seawater samples from the Indian Ocean (Central Indian Ridge), synthetic seawater samples from the lab (calibration of the dissolved methane sensor), and NOCS dock seawater samples for inter-comparison between methane sensor output and traditional analysis during the first deployments of the methane sensor.

Three types of bottles were used to collect samples: 250 mL brown glass bottles (CIR samples), 60 and 100 mL clear glass bottles (sensor and dock samples respectively). The bottles were flushed and filled with water samples, poisoned when necessary (100 µL of saturated $HgCl_2$), crimp sealed, and stored until analysis.

The dissolved methane was extracted at room temperature by introducing a headspace of inert gas (N_2) into the bottle. The bottle was then shaked for a certain time (extraction) and after equilibration between the liquid phase and the gas phase, a sub-sample (500 µL) of the headspace was introduced into the injection port of the GC system using a gas-tight syringe.

The conversion of methane concentration in the headspace (given by the GC in ppm) to concentration in seawater (nM) is given in Eq. 2.1 (Kolb and Ettre, 1997):

$$C_{diss} = \left(\frac{C_{HS} \times P}{22.4 \times \left(\frac{273.15 + t}{273.15} \right)} \right) \times \left(\frac{V_{HS}}{V_{water}} \right) \times 1000 , \qquad (2.1)$$

where C_{diss} is the concentration of methane dissolved in water (nM), C_{HS} the concentration in the headspace given by the GC (ppm), P the pressure (mmHg), *t* the temperature (°C), V_{HS} the volume of the headspace (mL), and V_{water}, the volume of the water sample (mL), from which the methane has been extracted.

Eq. 2.1 has to be corrected with the extraction efficiency, which characterises the percentage of methane recovered by equilibration between the dissolved and gas phases (Kolb and Ettre, 1997). To calculate the extraction efficiency, it is necessary to 1) optimize the equilibration time and 2) determine the best headspace / sample volume (HS/VS) ratio, which allows a complete extraction of the gas from the dissolved phase.

The equilibration time was optimized by analysing seawater samples (taken from the NOCS dock) by headspace extraction followed by GC analysis. The HS/VS ratio was chosen according to the literature (1/10 – Kolb and Ettre, 1997). Figure 2.3 gives the variation of the methane concentration in the gas phase as a function of time for HS/VS of 1/10. Under these conditions at least 30 minutes are necessary to reach equilibrium. Hence, all following experiments were based on a minimum extraction time of 45 minutes.

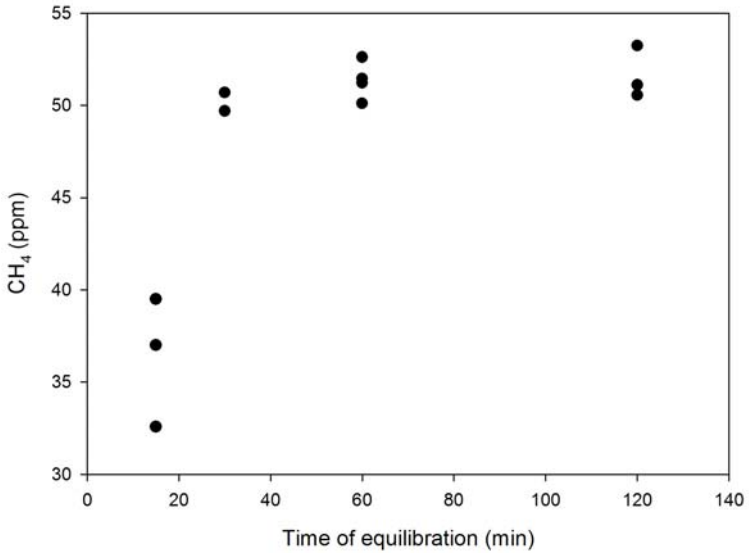

Figure 2.3: Headspace methane concentration vs. time of equilibration at room temperature (20ºC) and atmospheric pressure.

Figure 2.4 shows the variations of the dissolved methane concentration as a function of the HS/VS ratio for the different bottles and an equilibration time of 45 minutes. The highest dissolved methane concentration was reached for a ratio of 0.3 for the different types of bottles. Considering that the complete transfer of methane from the sample to the analyte occurs at HS/VS = 0.3, it is possible to determine the efficiency of the equilibration and therefore to correct the final concentration from it. Results are summarized in Table 2.4.

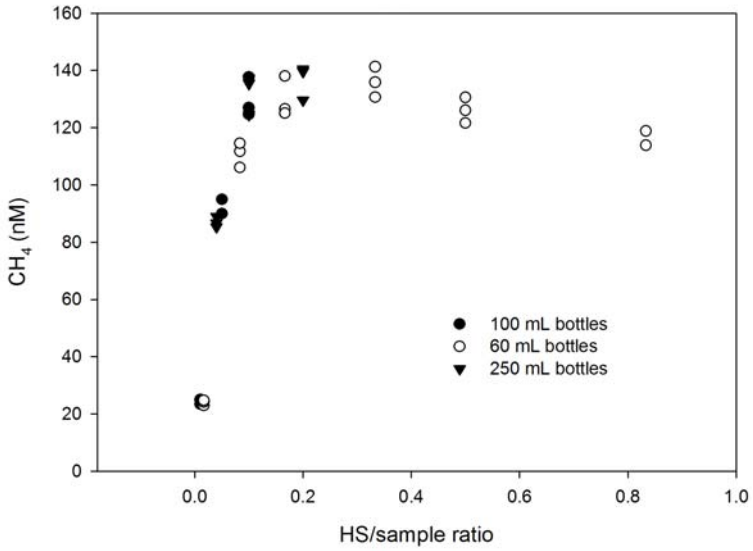

Figure 2.4: Dissolved methane concentration vs. HS/VS ratio

Table 2.4: Precision (reproducibility between measurements, RSD) and efficiency of the headspace extraction as a function of the ratio HS/Vsample. Efficiency takes into account both equilibration time and HS/VS ratio.

Ratio	Precision	Efficiency
0.1	0.02	0.96
0.2	0.02	0.99
0.3	0.005	1.000
0.5	0.07	0.96

According to Table 2.4, the efficiency, i.e. gas phase and dissolved phase are at equilibrium, is maximal at HS/VS = 0.3 and T = 45 minutes. For a HS/VS of 0.1, the extraction is considered as “less efficient”. However, a HS/VS of 0.1 is used in the next

Chapters for convenient reasons: for smaller bottles, the introduction of a bigger headspace would induce bigger analytical errors during the equilibration process.

2.2.3. Limits of detection, precision, accuracy

Blank samples prepared from artificial seawater and sodium chloride (40 $g.L^{-1}$) were analysed by static headspace extraction followed by gas chromatography. The limit of detection (3 times the standard deviation on dissolved methane concentration, n=20) was found to be 0.45 nM. Precision (relative standard deviation) and accuracy were 0.05 and 1.005 respectively.

2.3. Conclusions

Dissolved gas analysis by GC is a delicate procedure dependent on physical-chemical parameters (vapour pressure, water solubility, and temperature) and the sampling conditions (bottles, headspace volumes, extraction time, and temperature).

Within the entire analytical scheme, the headspace extraction is the most time consuming and challenging step. The main tasks to be fulfilled for an accurate extraction are 1) optimization of the equilibration time between the sample volume and the gas headspace that is introduced, based on the expected concentration level and 2) optimization of the HS volume. For optimal results, it is recommended that the extraction is performed as soon as possible after sample recovery (Kolb and Ettre, 1997). If not, storage is still possible (chilled room at 5-6ºC). The sample-containing material, however, has to be carefully chosen (gas- and water-tight glass bottles) with no plastic parts, which can be a source of contamination or leaks due to gas permeability. Results presented in this chapter showed that the volume of the sampling bottles did not interfere with the final result, so long as the corresponding headspace volume was chosen accordingly.

In the method used in this work, the gas extraction took 45 minutes and a headspace/sample volume of 1/10 was chosen. The final concentration was corrected from the extraction efficiency (0.96). Despite its limitations (Jalbert and Gilbert, 1994), the limit of detection measured with this method was 0.45 nM with good precision and accuracy (0.05 and 100.5 respectively).

The ‘purge-and-trap’ method is more generally used for dissolved methane measurements in open ocean waters due to its better sensitivity at low concentration (Charlou and Donval, 1993). However, the static headspace GC analysis is still suitable for oceanic measurements (Reeburgh, 2007). This technique was chosen here for its simplicity and rapidity.

CHAPTER 3: METHANE IN HYDROTHERMAL PLUMES

3.1. Mid-Ocean Ridge hydrothermal activity: a source of oceanic methane

3.1.1. Hydrothermal vent systems

Important exchanges of heat and matter from the oceanic crust to the hydrosphere occur at mid-ocean ridges, driven by a combination of conduction and convection (e.g. Von Damm, 1990; Lowell et al., 1995; Van Dover, 2000; German and Von Damm, 2003; Baker and German, 2004). Hydrothermal activity and associated venting fields are one of the manifestations of these transfers and represent 25 % of the total heat flux from the lithosphere and 33 % of heat transferred from the seafloor to the water column (Von Damm, 1990; Lowell et al., 1995; Van Dover, 2000; German et al., 2004; German and Lin, 2004).

The first evidence for hydrothermal venting on the seafloor was reported as an anomaly of temperature and salinity in the Red Sea water column (1948) with an increase in suspended particulate matter (Bruneau et al., 1953). Similar anomalies were observed later on the Mid-Atlantic Ridge (26°N) in 1972-1973 (Rona et al., 1975) and near the Galapagos Spreading Centre (Klitgord and Mugie, 1974), which guided the first observations of warm fluid seeping from the seafloor in February-March 1977 along the Galapagos Rift (Corliss et al., 1979; Edmond et al., 1979). After 30 years of seafloor exploration, hydrothermal venting is now known to discharge along mid-ocean ridges in every ocean (Figure 3.1), spanning the global range of spreading rates, and in a diversity of geological settings, although, to-date, only ~10 % of the global ridge crest has been explored systematically for hydrothermal venting (Baker and German, 2004; German et al., 2008b).

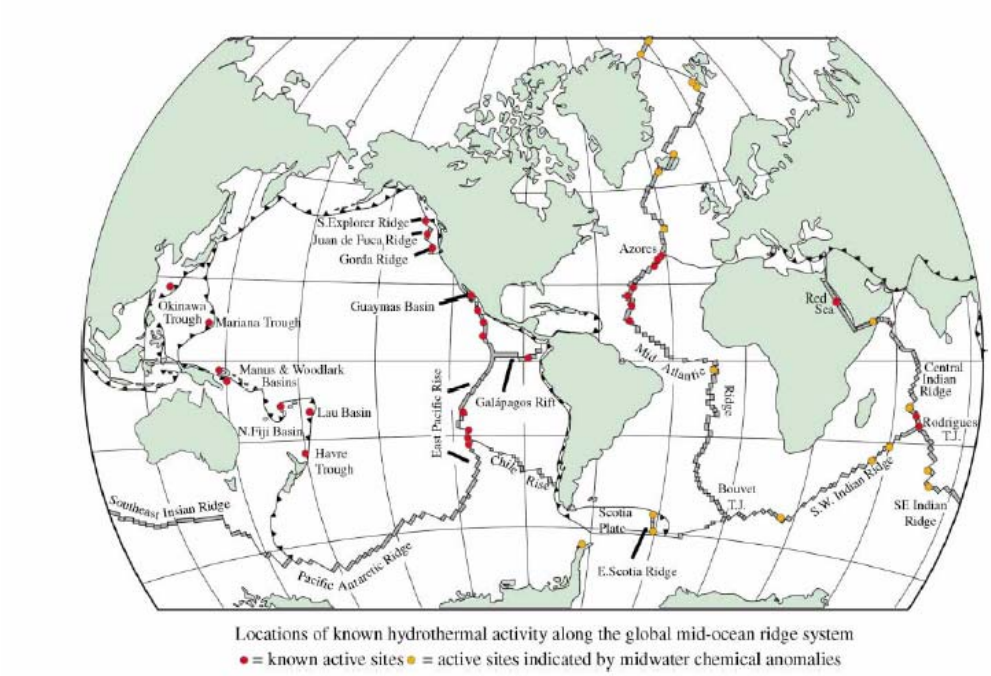

Figure 3.1: Distribution of known hydrothermal vents and water anomalies indicating the presence of active sites along mid-ocean ridges and subduction zones (from German and Von Damm, 2003).

Hydrothermal circulation (Figure 3.2) arises as the result of the penetration of cold (~1ºC), dense seawater through young and fractured oceanic crust that is created at the axes of spreading ridges. The seawater chemistry is strongly modified as seawater circulates through the oceanic crust close to a heat source (magma chamber or hot rock) where temperature exceeds thousands of degrees C, which leads to the formation of hydrothermal fluids. As the fluid penetrates the 'recharge zone' (Figure 3.2), the fluid undergoes water-rock reactions due to the increase of pressure and temperature. Deeper, close to the heat source, in the reaction zone, the fluid acquires its main chemical composition characteristics of end-member fluid (Welhan and Craig, 1983, German and Von Damm, 2003); this fluid becomes so buoyant that it rises rapidly to the surface and exits the seafloor at high temperature due to the convection and the increase of volume. The hot and anoxic fluids mix with ambient seawater, forming chimneys by precipitation of sulphides (Figure 3.3) and alter the composition of surrounding waters and potentially the oceanic crust (Lowell et al., 1995). Thus, hydrothermal circulation significantly impacts the global geochemical cycles of many elements (e.g. Fe, Mn, CH_4 – Wolery and Sleep, 1976; Charlou et al., 1991a; Lowell et al., 1995; Elderfield and Schultz, 1996; Van Dover, 2000). For some elements (e.g. Mn, Fe, Li) the contribution of hydrothermal venting to the total oceanic discharge is equal to or greater than riverine inputs (Edmond et al., 1979; Elderfield and Schultz, 1996; German and Von Damm, 2003).

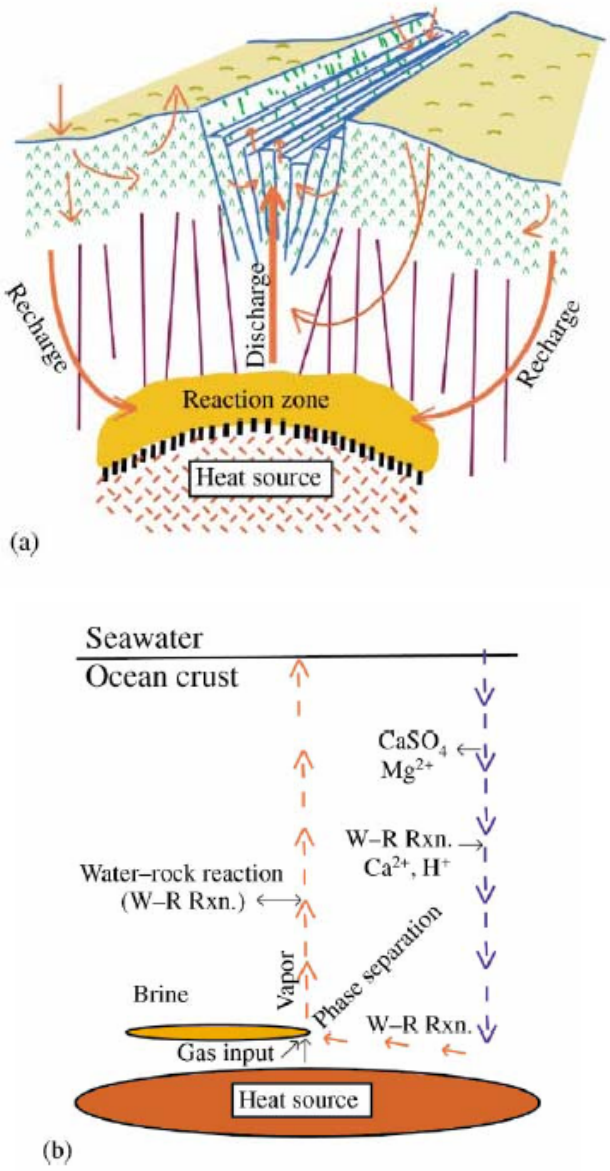

Figure 3.2: (a) General scheme of hydrothermal circulation. (b) Processes that control the composition and the characteristics of the fluid.

Seawater penetrates the oceanic crust through fractures, reaches the recharge zone, and reacts as it goes deeper under increasing conditions of temperature and pressure. The main characteristics of the fluid are acquired in the reaction zone, close to the heat source (i.e. magmatic chamber or hot rock) before the fluid rises back to the discharge zone. As the water penetrates the recharge zone, water-rock interactions occur with precipitation of anhydrite ($CaSO_4$) as well as Mg2+ with addition of H+. Close to the heat source, the fluid may undergo phase separation depending on the conditions of temperature and pressure, producing a gas phase and a brine phase. A direct gas input may also occur due to direct degassing from the magma. As the fluid rises back, new water-rock reactions can occur. From German and Von Damm, 2003.

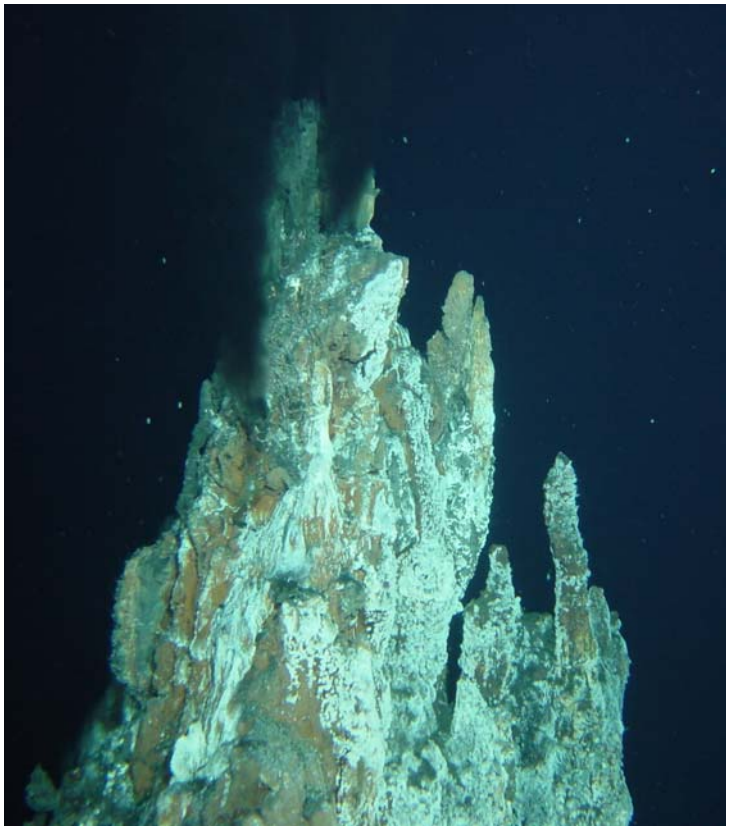

Figure 3.3: Hydrothermal vent and black smokers on the Mid-Atlantic Ridge (Y3 vent on the Lucky Strike vent field).
Picture taken during MOMAR '08 – leg I cruise by the ROV Victor on board N/O L'Atalante (August 2008). © IFREMER.

The composition of a vent fluid is highly variable from a site to another, i.e. every hydrothermal vent discovered is characterized by a different fluid composition (German and Von Damm, 2003). The interest in understanding the composition of hydrothermal fluids and the factors that control this composition is to determine how the fluids control the ocean chemistry. The composition of the end-member fluid exiting the seafloor is the final product of all the reactions that occurred in the crust and is the record of the conditions of temperature and pressure (German and Von Damm, 2003).

Hydrothermal fluids are generally anoxic, highly reducing (presence of H_2S), acidic (pH ~ 3.5, although some exceptions exist, e.g. Lost City (Mid-Atlantic Ridge) where pH is ~10 (Kelley et al., 2005) and enriched by up to a factor of 10^7 in several species relative to seawater (Table 3.1 – Von Damm, 1990). The chemical composition can be affected by several factors such as subsurface and seafloor temperature, pressure, rock composition and state of alteration, presence of sediments, chemical kinetics, phase

separation, subsurface mixing, and subsurface heat conduction (Von Damm, 1990; Lowell et al., 1995). However, four processes affecting the fluid composition are generally considered, i.e. i) phase separation, ii) water-rock interactions, iii) biological processes, and iv) magmatic degassing (German and Von Damm, 2003).

As seawater penetrates the oceanic crust through the hydrothermal system there are water-rock reactions with precipitation of anhydrite (i.e. $CaSO_4$, leading to the formation of anhydrite deposits) and magnesium (Mg^{2+}) and subsequent addition of proton (H^+), lowering the pH of the fluid. Studies on fluid composition showed in particular a strong enrichment in metals (Fe, Mn) and dissolved gases (He, H_2, H_2S, CO_2 and CH_4) with respect of seawater. This is mainly the result of the phase separation process (Bischoff and Rosenbauer, 1989; Lowell et al., 1995), which occurs deeper, close to the heat source, and depends on the pressure-temperature conditions (Bischoff and Rosenbauer, 1989; Lowell et al., 1995). During this process, gases will separate into the vapour phase while chloride and metal-chloride complexes will separate into the brine phase (e.g. Von Damm et al., 1997). Addition of gases (He, H_2, CO_2, CH_4) may also occur from direct mantle degassing, although it has been established only for a few vent systems (e.g. 9º50'N and 32ºS on the EPR – Lupton et al., 1999). ^3He for example is related to a direct degassing from the mantle; H_2, H_2S and CO_2 are derived from magmatic sources; methane is generated by abiogenic or biogenic processes. Biological processes can only occur at temperature <120ºC (the current known limit of life). Hence, the influence of these processes on the fluid composition is limited to the low-temperature vents (German and Von Damm, 2003).

Table 3.1: Example of chemical composition of a typical 350°C vent fluid compared to deep seawater. From Elderfield and Schultz (1996); Van Dover (2000).

	Hydrothermal Fluid	Deep Seawater
T (°C)	360-407	2-5
O_2 (μM)	0	1-5
H_2S (mM)	3-13	0
Na (mM)	537	464
K (mM)	12-33	10
Ca (nM)	11-55	10
Mg (mM)	0	53
Si (mM)	15-22	0.05
SO_4^{2-} (mM)	0	30
Mn (μM)	360-1100	<0.001
Fe (μM)	750-6500	0
Cu (μM)	10-40	0.01
Zn (μM)	40-100	0.01
CH_4 (μM)	25-100	0

The fluid exiting the seafloor is rapidly diluted and reaction with the cold seawater causes certain elements to be directly precipitated, forming mounds and chimneys on the seafloor (e.g. Von Damm, 1990; Fouquet, 1997 – Figure 3.2). The hot fluid rises entraining the ambient seawater, forming a buoyant plume, until neutral buoyancy is achieved and the plume is carried away by oceanic currents (Baker, 1990; Baker et al., 1995; German et al., 1998b). Plumes are not only an indicator of a nearby hydrothermal fluid discharge but they also integrate hydrothermal heat and mass flux (Baker et al., 1995), provide natural laboratories for measuring the reactions that control the dispersal of chemical species (German et al., 1998b), and may be a pathway for the vent-fauna dispersal (e.g. Mullineaux and France, 1995; Fusaro et al., 2008). More generally these chemically enriched plumes are considered as a tool for hydrothermal exploration and geological interpretation of hydrothermal processes (due to the enrichment of many chemical species relatively to the background seawater) (Baker et al., 1995), but also for the discovery of ore deposits formed by precipitation of the fluid, which could represent a valuable source for industries (e.g. German, 2004; de Wit, 2005)

Hydrothermal plumes are detectable at significant distances using physical (temperature, salinity, nephelometry, light scattering, and light attenuation) and chemical tracers (Baker et al., 1995). Optical tracers (light transmission, light scattering) are usually employed to detect the presence of particles in the water column, which are often a good indication for the presence of hydrothermal plumes. On the other hand, geochemical tracers like manganese (Mn), iron (Fe), methane (CH_4), or helium (He) are used to define plumes in more detail, calculate their dilution factors, and provide information about the nature of their venting-source.

3.1.2. Methane in hydrothermal fluids and plumes

Fluid discharge from hydrothermal systems is a significant source of methane to the deep ocean (Cowen et al., 2002; Keir et al., 2005). Welhan and Craig (1983) calculated that the ocean ridge crests inject $4\pm1x10^9$ mol $CH_4.yr^{-1}$ to the entire ocean. End-member concentrations for methane are variable but always 10^5 to 10^7 times enriched over background concentrations (Charlou and Donval, 1993; Charlou et al., 1998; Cowen et al., 2002). This variability depends on processes that generate methane and on the environmental context. Table 3.2 summarizes concentrations of methane measured in hydrothermal fluids collected at different locations along mid-ocean ridges.

Table 3. 2: Concentrations of methane in hydrothermal fluids (modified from Charlou et al., 2002).

	Ocean	Authors	Depth (m)	T (°C)	pH	CH_4 (mM)
LOGATCHEV	Atlantic	Charlou et al., 1998	3000	347/352	3.3	2.1
MARK - 1/2	Atlantic	Campbell et al., 1987	3460	335/350	3.9/3.7	0.023/0.062
TAG	Atlantic	Charlou et al., 1996	3670	321/390	3.1	0.124/0.147
BROKEN SPUR	Atlantic	Lein et al., 2000	3200/3300	356/364		0.065/0.13
RAINBOW	Atlantic	Douville et al., 2002	2300	365	2.8	2.5
LUCKY STRIKE	Atlantic	Von Damm et al., 1998	1700	170/364	3.5/3.7	0.5/0.97
MENEZ GWEN	Atlantic	Charlou et al., 2000	850	275/284	4.2/4.3	1.35/2.63
ENDEAVOUR	Pacific	Cowen et al., 2002				1.8/3.4
21N EPR	Pacific	Cowen et al., 2002				0.06/0.09
SJdF	Pacific	Cowen et al., 2002				0.08/0.12
GUAYMAS	Pacific	Cowen et al., 2002				2.0/6.8
IR RTJ	Indian	Gamo et al., 2001	2450	360	3.5	0.082

In all cases, CH_4 may be derived from multiple carbon sources, such as thermal breakdown of complex hydrocarbons at temperatures >100ºC, biological production, outgassing of juvenile methane, and abiotic synthesis at >300-400 ºC (Welhan and Craig, 1983; Charlou and Donval, 1993; Charlou et al., 1998; Cowen et al., 2002; Gharib et al., 2005). Thus, methane is one the most dynamic and informative hydrothermal geochemical tracers (Mottl et al., 1995; Gharib et al., 2005).

The biogenic production of methane is accomplished by methanogens (bacteria and archeobacteria) found in anoxic environments (Mottl et al., 1995). Methanogenesis is the terminal step in the carbon cycle playing an important role in the degradation of organic compounds such as formate, acetate, methanol, and methylamines (Mah et al., 1977; Kotelnikova, 2002). Biological production of methane generally occurs at low temperature vent sites (Kotelnikova, 2002) but it may also occur at high temperatures (Mottl et al., 1995) under certain conditions, depending on the content of any sediment and organic carbon present.

Thermogenic production of methane is a result of the breakdown of heavier hydrocarbons derived from organic matter in sediments catalysed at high temperatures (>100ºC) (Mottl et al., 1995; Gharib et al., 2005). CO_2 is thermally reduced by hydrogen

generated from the oxidation of ferrous to ferric iron in presence of metal-alloy such Fe-Ni (Gharib et al., 2005). The CO_2 can be reduced to methane either while trapped in fluid inclusions or directly within the hydrothermal fluid (Gharib et al., 2005). Carbonates (HCO_3^-) can also be reduced into CH_4 in upper crustal mafic or ultramafic rocks catalysed by Fe-Ni alloy (Horita and Berndt, 1999).

Significant amounts of methane can also be transferred from the mantle to the hydrosphere through a reaction called serpentinization (Charlou et al., 1998). In an ultramafic context, hydrothermal alteration of peridotite is dominated by hydration reactions of olivine and pyroxene that lead to the formation of serpentine minerals (serpentinization) (e.g., Bonatti et al., 1971; Melson and Thompson, 1971). As described by Eq. 3.1, CO_2 is reduced to a variety of hydrocarbon gases and carbonaceous compounds through Fischer-Tropsh reactions. The conversion of the Fe(II) in the olivine leads to the formation of Fe(III) in the magnetite and involves an important degassing of hydrogen (H_2) and methane.

$$olivine + H_2O + CO_2 \rightarrow magnetite + serpentine + brucite + H_2 + CH_4 \quad (3.1)$$

In fact the conversion of CO_2 into methane is only possible if there is generation of H_2 first (Charlou et al., 1998). H_2 produced by serpentinization represents a source of energy for lithotrophic bacteria, but may also be combined with CO_2, at high temperature (350ºC), for the formation of organic compounds such as hydrocarbons and fatty acids through Fischer-Tropsch reactions (Holm and Charlou, 2001; Proskurowski et al., 2008). Holm and Charlou (2001) detected the presence of long hydrocarbon chains (16 to 29 C atoms) in hydrothermal fluids collected on an ultramafic hydrothermal vent system at Rainbow. Hence, from these findings, it is suggested that hydrothermal vents may have been a pathway for the origin of life.

Serpentinization appears to occur along slow-spreading ridges and has been described along the MAR (Charlou et al., 1988; Charlou et al., 1991b; Charlou et al., 1998; Charlou et al., 2002); South-West Indian Ridge (Bach et al., 2002), and Gakkel Ridge (Baker et al., 2004).

CH_4 can also be degassed directly from axial magma chambers or trapped in fluid inclusions in solidifying rocks and then leached by later contact with hydrothermal fluid (Artuso et al., 2007). For example, in the south-west Pacific Ocean, Lupton et al., 2006 showed a direct degassing of gases (CO_2, H_2S, CH_4, H_2) from a hydrothermal system near a submarine volcano in the northern Mariana Arc. Methane-rich bubbles have also been observed over the Reykjanes Ridge (Arctic Ocean) with concentration in the water column up to 18 nM (German et al., 1994). Outgassing of CH_4 is however difficult to demonstrate directly, although methane is often associated with ^3He that is generated in the mantle (Mottl et al., 1995).

The hydrothermal methane is detectable only some hundreds of meters above and only a few kilometres around from any given vent source.Vertically, high concentrations of methane are restricted to the water of the buoyant plume that rises some hundreds of meters due to its high temperature. Hydrothermal methane can by carried away by deep ocean currents. Contrary to other chemicals (e.g. He), methane is non-conservative (scavenging time of few days to few weeks – de Angelis et al., 1993) due to its mixing with water and the intensive oxidation by bacteria, limiting its detection to the seep area (Faber et al., 1994). Compared with more conservative tracers in the near-vent plume (e.g. Mn, He – residence time of few months to many years – Cowen et al., 1990), methane can provide information on the nature of the vent/hydrothermal processes, e.g. a high CH_4/Mn ratio is a strong evidence for serpentinization (Charlou et al., 1991b), and constitutes a diagnostic tool for the underlying source fluids.

In this Chapter the results of the analyses for the concentration of methane, iron, and manganese in plumes over the Central Indian Ridge (20ºS) are presented. The objective is to assess the role of the geochemical tracers for the detection and the characterization of hydrothermal plumes, and the assessment of the underlying processes generating the hydrothermal plumes.

3.2. Hydrothermal plumes over the Central Indian Ridge (KH-06-4 cruise)

3.2.1. Introduction

At the end of the 1980s, a particular interest developed for the Indian Ocean system characterized by three different spreading rate ridges, which meet at the Rodriguez Triple Junction (RTJ, Figure 3.4). Evidence for hydrothermal activity in the Indian Ocean was subsequently found at numerous locations: the Gulf of Aden (Jean-Baptiste et al., 1990), the Central Indian Ridge (CIR – Herzig and Pluger, 1988; Pluger et al., 1990; Gamo et al., 1996b; Gamo et al., 2001), the South-East Ridge (SEIR – Scheirer et al., 1998), and the South-West Ridge (SWIR – German et al., 1998a; Bach et al., 2002; Baker et al., 2004), and most recently, in the north along the slow-spreading Carlsberg Ridge (Murton et al., 2006).

Hydrothermal plumes were first discovered along the CIR between 21.5°S and 24.0°S in 1986 (Herzig and Pluger, 1988). The southernmost evidence for hydrothermal activity on the CIR was discovered immediately north of the RTJ at 25°20'S in 1993 (Gamo et al., 1996b). In 2000, high-temperature fluids were sampled by the Japanese ROV Kaiko (Gamo et al., 2001) on the Kairei vent field. The same site was revisited later by the American ROV Jason, which also discovered and sampled the Edmond vent-site at ~23 ºS (Van Dover et al., 2001). Further north, hydrothermal activity was suggested by the presence of a hydrothermal ^{3}He anomaly at 19°29'S (Jean-Baptiste et al., 1992). In 2001, during RRS Charles Darwin cruise CD127, evidence of hydrothermal activity (strong light scattering and geochemical anomalies) was found at 4 locations between 18° and 21ºS (German et al., 2001). In December 2006 (5^{th} – 23^{rd}), detailed tow-yos and CTD hydrocasts as well as AUV (r2D4, ORI) surveys were conducted over segments 15 and 16 (18-20ºS) during the KH-06-4-3 cruise of R/V Hakuho Maru (PI: K. Tamaki, ORI,[1]), in order to confirm and locate hydrothermally active vent areas.

[1] Ocean Research Institute, Tokyo, Japan

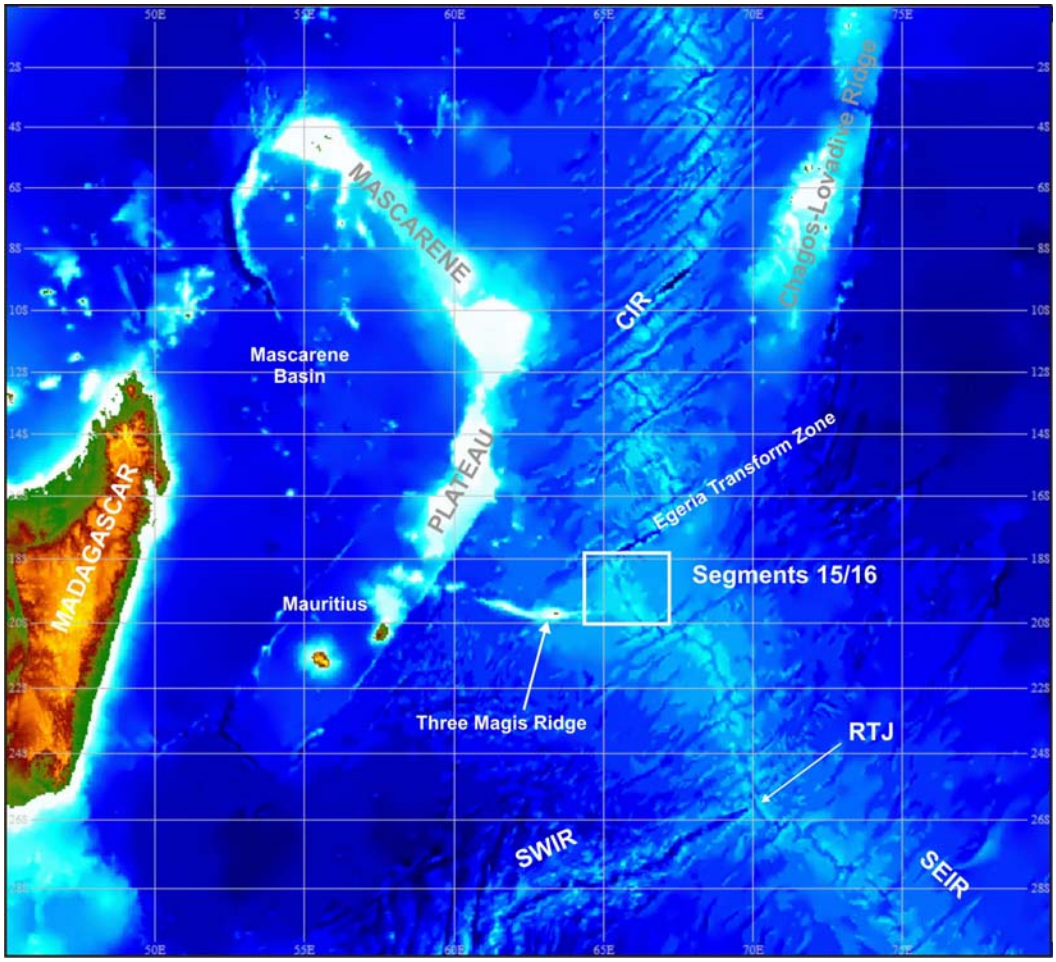

Figure 3.4: Map (GEBCO) of the Central Indian Ridge (CIR).
SWIR: South-Western Indian Ridge; SEIR: South-Eastern Indian Ridge; RTJ: Rodriguez Triple Junction.

3.2.2. Geological settings

The CIR (Figure 3.4) was initiated by the separation of the Mascarene Plateau and the Chagos-Lacadives Ridge (McKenzie and Sclater, 1971), and forms the southernward extension of the Carlsberg Ridge, ending at the RTJ (Munch et al., 1999). The spreading rate is 50-60 mm/yr (DeMets et al., 1990), i.e. slow to intermediate spreading rate. The ridge consists of a series of segments separated by NE-SW fracture zones (Langseth and Taylor, 1967; Fisher et al., 1967; Banghar and Sykes, 1969), with a 500 to 1000 m deep axial valley, 50 to 100 km long segments terminated by transform faults (<30 km long) and non-transform discontinuities (10 km long) (Tyler et al., 2007). Above the central valley (10-25 km wide), the water depth varies between 3200 m and 4000 m and increases southward from the Marie Celeste Fracture at 15-16 ºS (Briais, 1995).

Magmatic activity along the CIR is indicated by the presence of several seamounts and volcanic ridges, which have been delineated in a number of ridge segments. Segments 15 and 16, east of the Three Magis Ridge, are located immediately north of the Egeria Transform Zone (Tyler et al., 2007). The rock composition is dominated by lavas erupted along the rift axis, showing a trend from normal MORB (Mid-Ocean Ridge Basalt) to enriched basalts; the ridge itself is poorly sedimented (Munch et al., 1999; Murton et al., 2005).

3.2.3. Methodology

CTD-T (Conductivity, Temperature, Depth and light Transmission) hydrocasts and tow-yos were conducted along segments 15 and 16 based on AUV r2D4 observations and multi-beam seafloor mapping (SeaBeam) (Figure 3.5). The CTD-T package consisted of a Seabird® model 911+ and a SeaTech® 25 cm beam transmissometer coupled with an in-situ manganese sensor (GAMOS – Okamura et al., 2001). The system included a rosette (12 20L-Niskin bottles) for water sampling (trace metals and methane). Water samples were only taken when hydrothermal activity was suspected with the exception of the first CTD hydrocast, which was used as a background cast. Methane samples were collected in brown glass bottles (250 ml), poisoned (100 μL of saturated $HgCl_2$), sealed, and stored for onshore analysis. At NOCS, total dissolvable Iron (TDFe) and total dissolvable Manganese (TDMn) were analysed in the clean laboratory using standard methods (Connelly et al., 2007) and methane was analysed using the method described in Chapter 2.

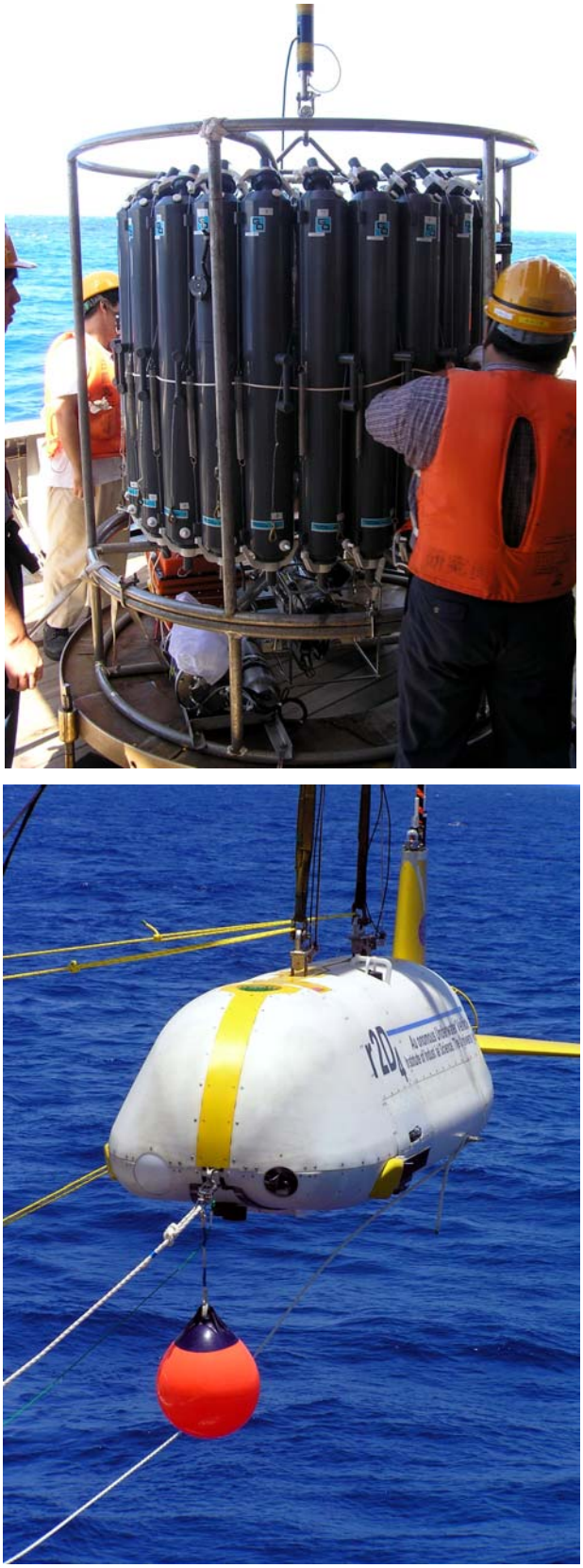

Figure 3.5: CTD-rosette showing the GAMOS sensor mounted on the bottom of the frame (top) and the AUV r2D4, equipped with both the CTD and GAMOS systems (bottom).

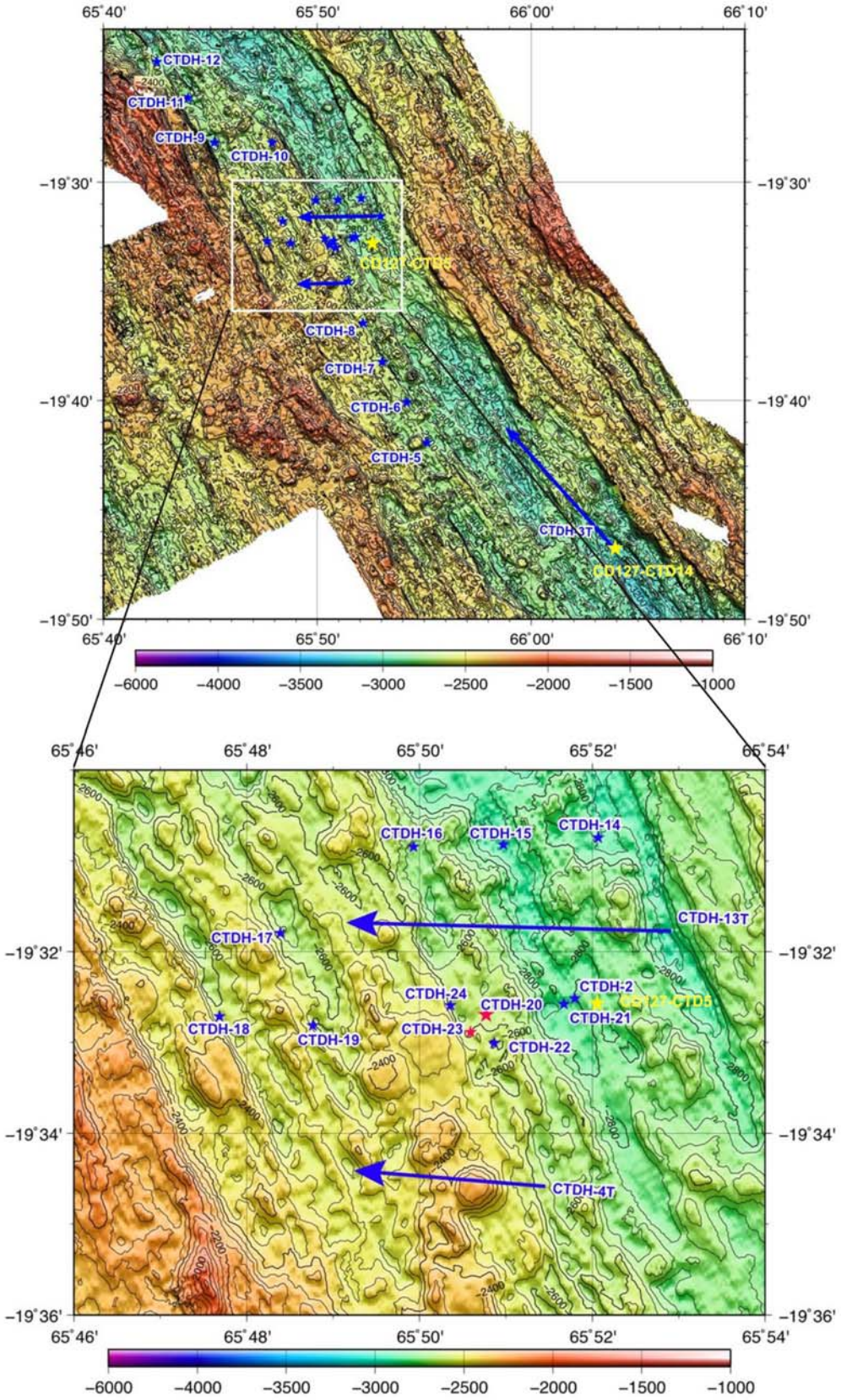

Figure 3.6: Bathymetric map of the Roger Plateau (Segment 15) and locations of CTD casts/tow-yos (blue stars and blue arrows).

Yellow stars are the location of the CTD stations occupied during CTD 127. Red stars are the stations where hydrothermal signals were found. Courtesy of K. Okino.

3.2.4. Characteristics of hydrothermal plumes[2]

3.2.4.1. Hydrothermal plumes along segment 15

Plume data

21 CTD hydrocasts at fixed locations and 2 tow-yos were conducted along the Roger Plateau (segment 15), based on locations (noted CD127-CTD5 and CD127-CTD14) at which hydrothermal signals were detected during the CD 127 cruise (Figure 3.6). One station (CTD2) was occupied in an off-axis area as a control.

A tow-yo (CTD3) was conducted northward from the CD127-CTD14 location. However, despite a slight light attenuation anomaly at 2100 to 2550 m close to the CD127-CTD14 location comparable with anomalies found by TOBI in 2001 as it was towed through the CD127-CTD14 location (German et al., 2001), no samples were taken as the anomaly was thought to be due to the presence of suspended matter, not correlated to the GAMOS signal. In 2001, TOBI showed light scattering anomalies at 2600-2720 m around the CTD14 location correlated with TDMn anomalies at 2700-2825 m (German et al., 2001). A second tow-yo (CTD4) was conducted westward, south of the CD127-CTD5, where a strong hydrothermal plume signal was also detected in 2001, in both light-scattering and TDMn profiles, but no signal was found along this transect in 2006.

A third westward tow-yo (CTD13) was performed, north of the CD127-CTD5 and gave significant light transmission and GAMOS signals at 2400 m that were related to hydrothermal activity. This anomaly was confirmed by hydrocasts CTD 20 to CTD 24. Figure 3.7 shows the vertical profile of light transmission, together with that of GAMOS response (Mn) at CTD 20 where significant light transmission and Mn anomalies were recognized at a depth of 2380 to 2480 m (0.2% and 4 nM respectively). The size of these physical and chemical anomalies are defined as the variation of each parameter relative to its value recorded in mid-water (Gamo et al., 1996b). The good correlation between both signals indicates that this plume is of hydrothermal origin (e.g. Mottl et al., 1995; Ishibashi et al., 1997).

[2] Chemical data are presented in Appendix I

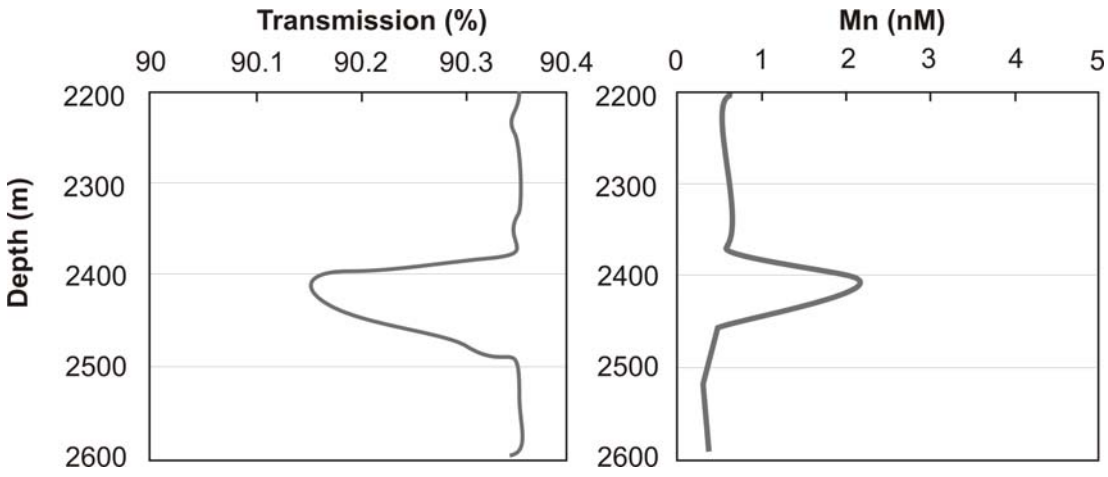

Figure 3.7: Light transmission (%) anomaly and GAMOS signal (Mn) during CTD 20 related to hydrothermal activity.

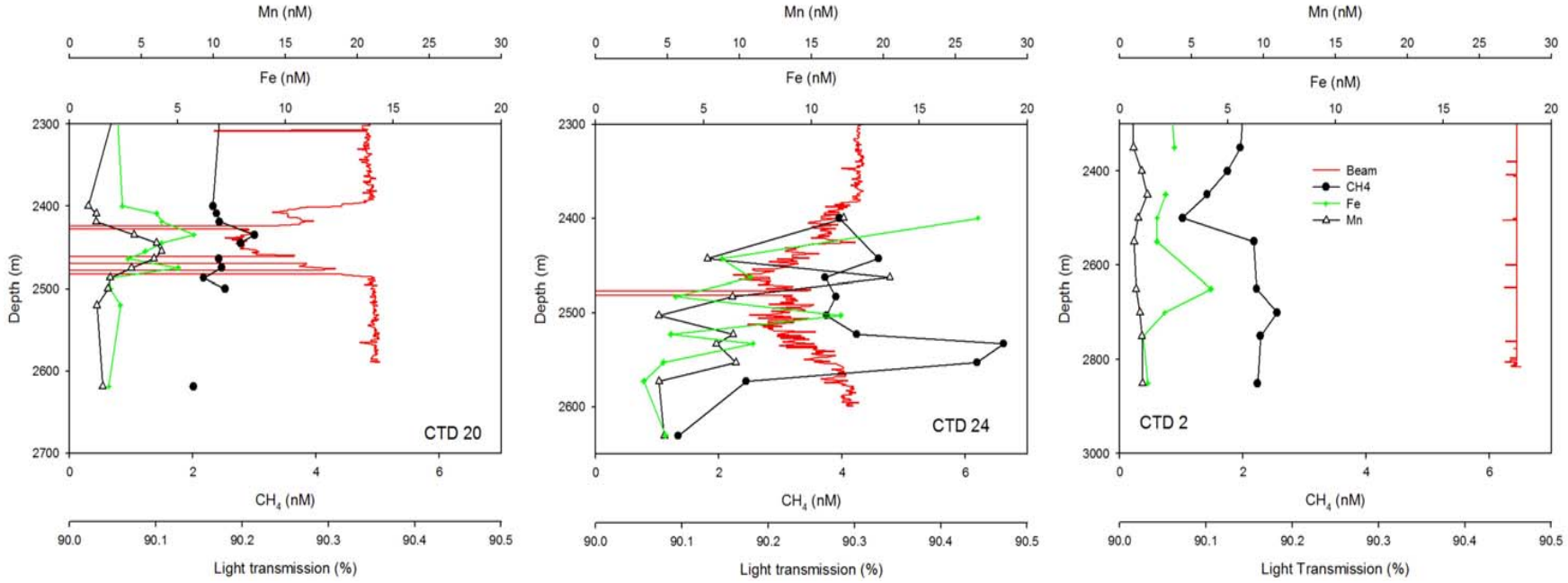

Figure 3.8: Light transmission (red solid line), CH_4 (black solid line/solid dots), TDMn (black solid line/open triangles) and TDFe (green solid line/green crosses) profiles at CTD 20, and CTD 24 compared with data from station CTD 2 (background station).

Figure 3.8 depicts vertical profiles of CH_4, Mn and light transmission at CTD 20 and CTD 24 stations, and at the control station (CTD 2). Concentrations of Mn, and CH_4 measured in the discrete samples correlated well with the light transmission profile anomalies and the GAMOS signal, not shown, which define a neutrally buoyant hydrothermal plume layer at 2400-2500 m depth, 200 m above the local seafloor. The correlation of CH_4 concentrations with the other parameters confirms, here, that it is unambiguously tracing input for hydrothermal activity at the seafloor (Gamo et al., 2001).

Table 3.3 summarizes the plume data (centre of the plume) for CTD 20 and CTD 24 together with background concentrations measured in the same area (CTD 2). At CTD 2, the average CH_4, Mn, and Fe concentrations below 1500 m were 1.99 nM, 1.11 nM, and 1.92 nM respectively, higher than the background values measured by Gamo et al. (1996) at 25ºS. This suggests that the background station located in the rift valley (19º32.527S/65º51.66E) might be under the influence of hydrothermal activity. The maximum CH_4, Mn, and Fe concentrations were 2.67 to 3.96 nM, 5.42 to 7.82 nM, and 4.26 to 6.19 nM respectively, which represent a significant enrichment over background concentrations measured at CTD 2 and typical deep ocean background concentrations (Charlou et al., 1991b; Charlou and Donval, 1993; Gamo et al., 1996a).

Table 3.3: Plume data (averaged concentrations measured in the centre of the plume).
The depth indicates the centre of the plume; LT%: Light Transmission anomaly relatively to adjacent deep water (CTD2); TDMn: Total Dissolvable Manganese; TDFe: Total Dissolvable Iron; MR: mixing ratio. NB: the whole data set is presented in Appendix 1.

Stations	Depth	CH_4 (nM)	TDMn (nM)	TDFe (nM)
CTD20	2430	2.67	5.42	4.26
CTD24	2500	3.96	7.82	6.19
CTD 2	2500	1.99	1.11	1.92

Stations	CH_4/Mn	CH_4/Fe	Fe/Mn	LT%
CTD20	0.49	0.63	0.79	0.20
CTD24	0.51	0.64	0.79	0.15

CH_4/Mn, CH_4/Fe, and Fe/Mn remained constant at CTD 20 and CTD 24, which would indicate that the plume sampled at both stations was the same (Charlou et al., 1991b), and hence originated from the same source. However, at CTD 20, the light transmission anomaly has a maximum at 0.15% and the plume has a sharp shape at the top and the bottom, overlying almost completely particle-free open ocean water. At CTD 24, the maximum of light transmission anomaly is less pronounced with a smoother and more coalesced profile. This pattern has already been shown for hydrothermal plumes above the Rainbow vent field on the MAR (German et al., 1996) and has been explained by the increasing distance to the source. At increasing distance from a common source, particle settling leads to a hydrothermal plume characterized by fine, suspended particles (i.e. more homogeneised), while at a close distance to the source, the particle settling has yet to be done (German et al., 1996). Hence, we can interprate the CTD 24 data from more distal portions of the same hydrothermal plume as CTD 20, which is closer to the vent source. Although the maximum concentration of the geochemical tracers is higher at CTD 24, the CH_4, Mn, and light transmission anomalies at station 20 coincide with the upper peaks in CH_4 and Mn at CTD 24 while there are larger chemical anomalies at CTD 24, where background concentrations are seen at CTD 20.

On a relevant time-scale for the Indian Ocean, the calculated ratios would help to determine the proximity of the source. Methane has a residence time of a few days to a few weeks in the plume (de Angelis et al., 1993). Most of the methane is oxidized by methanotrophs at an oxidation rate comprised between 0.1 and 28.9 nM day^{-1} (de Angelis et al., 1993). If the hydrothermal plume observed on segment 15 was derived from one single source, the chemical characteristics of the plume would vary with age. Hence, the CH_4/Mn ratio (a non conservative tracer vs. a conservative tracer) should increase closer to the source (Gamo et al., 1996a). Here, the ratio calculated for the plume remained identical within error from CTD 20 to CTD 24 (Table 3.3), indicating that the travel between the two stations is fast compared with any available reaction and/or removal kinetics. This interpretation is confirmed by the current data measured by the AUV, where speeds up to 16 cm/sec were measured. Hence the fact that the stations are not geochemically differentiated is not surprising, and can be compared with the data from the Rainbow vent site where CH_4/Mn ratios remained constant for several miles because of currents of 10 to 20 cm/sec (German et al., 1996).

3.2.4.2. Hydrothermal plumes along segment 16

The survey of the Segment 16 was based on AUV observations made during its deployment above the Great Dodo Lava Plain (Figure 3.9). Significant light attenuation (~0.2%) and GAMOS anomalies were detected at 18°20'S/65°18'E at a depth of 2700 m (Figure 3.10).

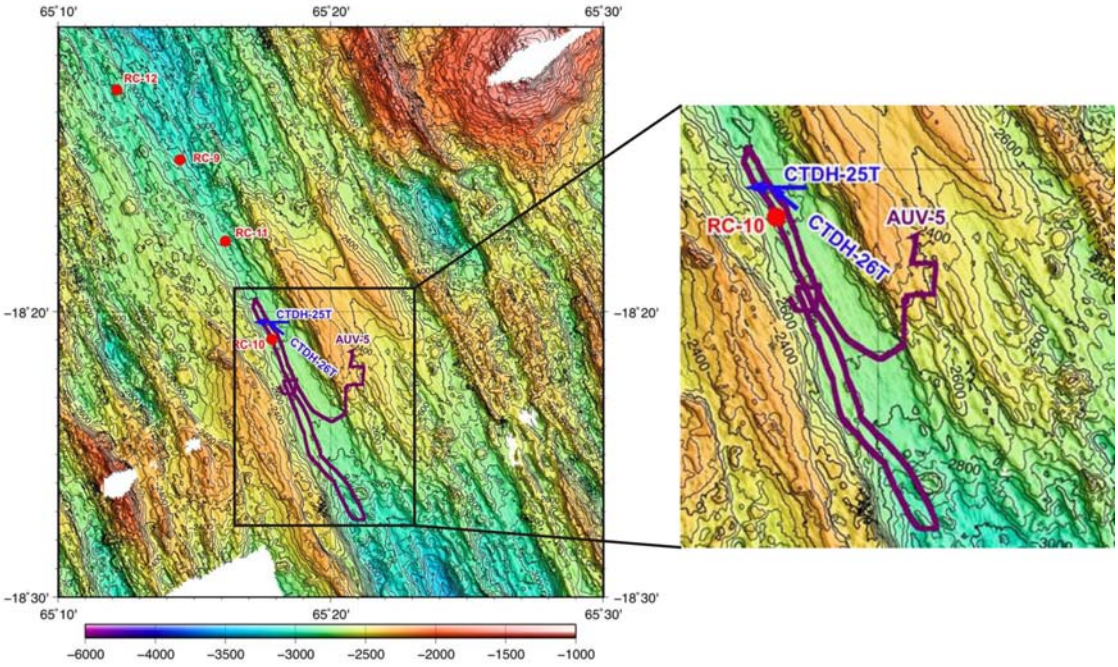

Figure 3.9: Bathymetric map, CTD/tow-yos locations, rock-coring (RC) and AUV track (AUV-5) along the segment 16 (Great Dodo Lava Plain).

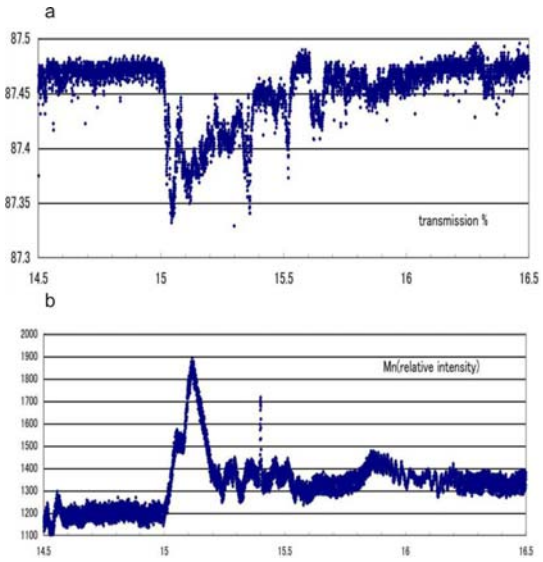

Figure 3.10: Light transmission and GAMOS signal measured during the AUV survey along segment 16.

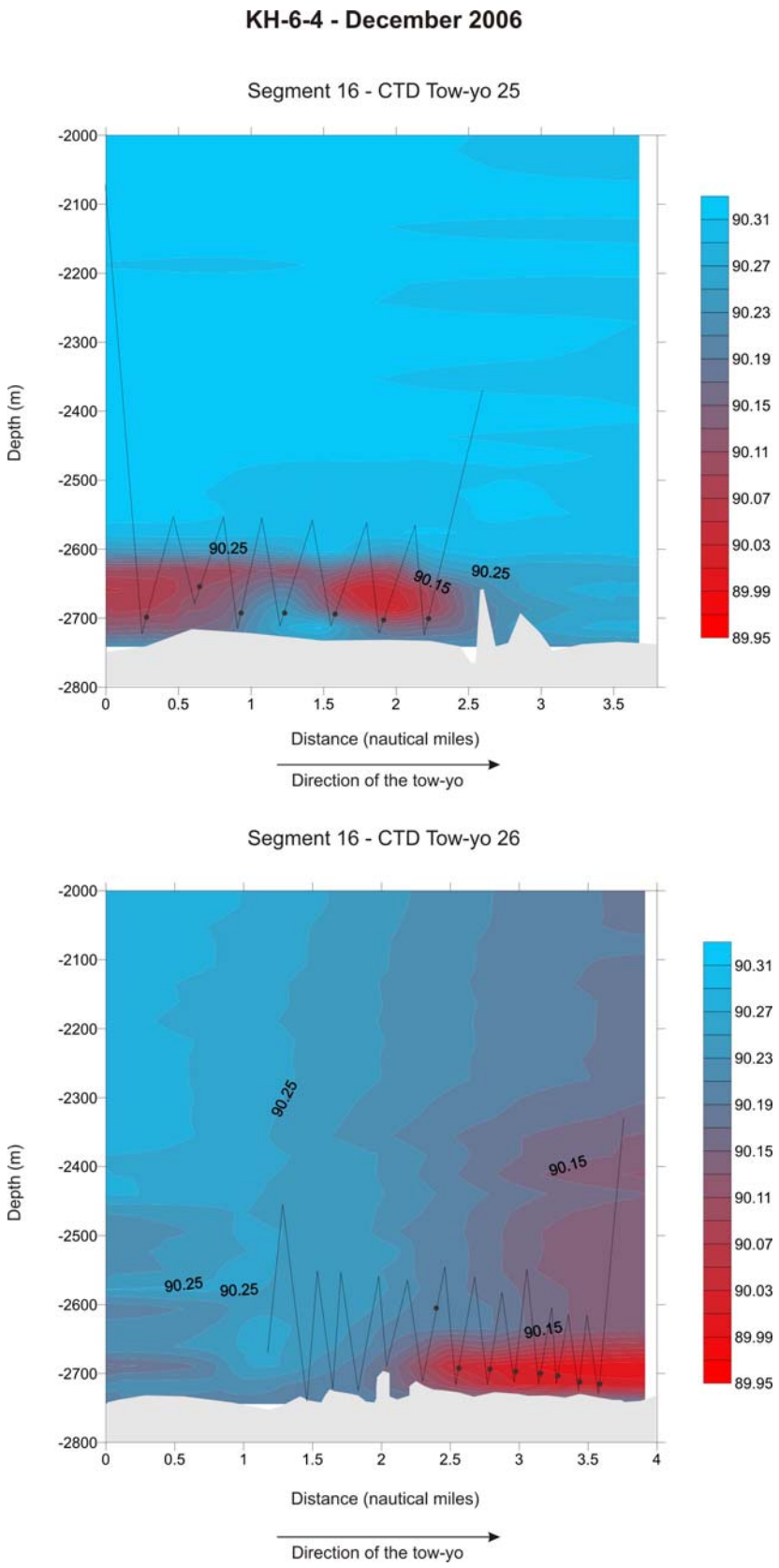

Figure 3.11: Contoured cross-sections of light transmission (%) signals obtained by CTD tow-yos through the hydrothermal plume along segment 16.

Tow-yo 25 was oriented East to West; tow-yo 26 was oriented South-East to North-West. Solid dots indicate where the bottles were fired.

Two tow-yos were therefore conducted (CTD 25 and CTD 26), to and from the position of the strongest anomaly. Figure 3.11 shows the vertical sections of light transmission anomalies along tow-yos CTD 25 and CTD 26, together with the zig-zag patterns of the CTD-rosette and the rough bottom topography.

CTD 25 tow-yo started westward from the position of the strongest anomaly detected during the AUV survey. A significant neutrally buoyant hydrothermal plume was observed at depths of 2600-2700 m, centred at 50 to 100 m above the local seafloor, which is very shallow probably due to the bathymetry (Figure 3.11) although that does not necessarily reflect height above bottom at the point of source. Although the light transmission anomaly remained around 0.2% in the centre of the plume, CH_4, Mn, and Fe concentrations were much higher than those measured in segment 15 (Table 3.4). A second plume was found as the CTD 25 tow-yo progressed westward (Figure 3.11). It is difficult to make chemical comparison between both the first and the second plumes as the bottles were fired consistently outside the core of the plume, missing important information of the chemistry of the plume. Hence, it is likely that the second plume originates from the same source.

Table 3.4: Results of chemical measurements for the water samples collected during the tow-yo observations.

TDMn: total dissolvable manganese; TDFe: total dissolvable iron.

CTD 25			
Depth (m)	CH_4 (nM)	TDMn (nM)	TDFe (nM)
2700	10.6	49.2	47.6
2674	8.9	27.2	76.2
2702	9.2	66.5	67.0
2700	6.4	68.2	81.6
2700	6.2	58.6	67.8
2710	6.2	68.6	44.6
2730	5.8	35.6	35.3
CTD 26			
Depth (m)	CH_4 (nM)	TDMn (nM)	TDFe (nM)
2600	3.9	70.7	34.3
2677	4.2	75.8	43.1
2687	3.9	71.1	47.8
2697	5.5	99.6	50.7
2707	7.5	137.2	57.5
2717	7.4	135.5	57.9
2737	7.2	131.8	59.3
2747	7.9	144.8	60.6

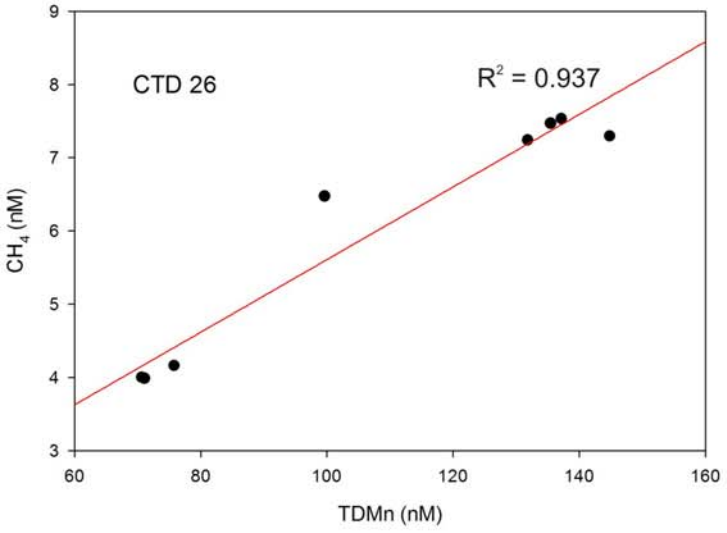

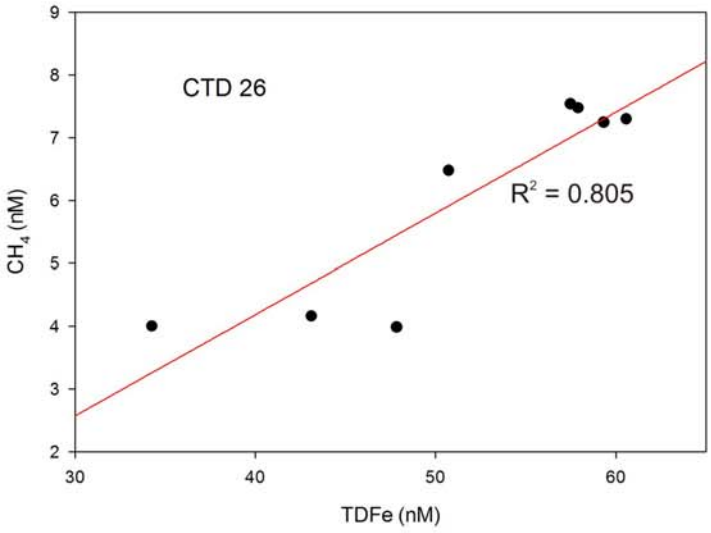

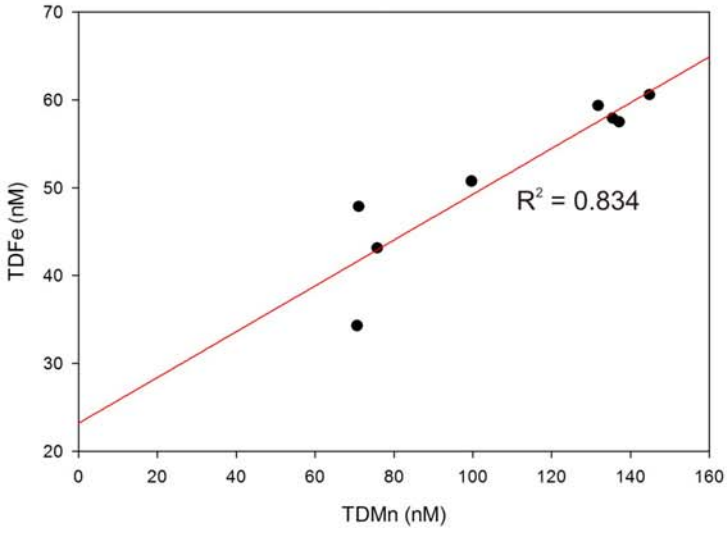

Figure 3. 12: Correlation between TDMn and CH_4, and TDFe and CH_4 in samples along CTD 26 tow-yo.

Immediately after the end of the tow-yo CTD 25, the tow-yo CTD 26 started along a SE-NW track to intersect the first track at the strongest anomaly position. At the beginning of this observation, no hydrothermal signals were found; however the light anomaly (~0.4%) became stronger as, apparently, we approached closer to the source. The anomaly at the end of tow-yo CTD 26 was greater than that observed at the beginning of tow-yo 25. CH_4, Mn, and Fe concentrations were also much higher (Table 3.4) but did not peak at the end of the cast. This would suggest that the plume was carried away by NW-SE currents along the axis of the ridge and the source was located further north from the last sampling location. The plume sampled along the CTD 26 tow-yo here originated from a single vent-source; it is shown clearly by the close correlations observed between TDMn and CH_4 (R^2=0.937), TDFe and CH_4 (R^2=0.805), and TDFe and TDMn (R^2=0.834) concentrations throughout this plume (Figure 3.12). Given the direction of the valley, the current at the time of sampling, and the bathymetry the vent source would be located NW from the last sampling point of tow-yo CTD 26, down-hill from the immediately underlying seafloor, probably at depth >2700 m. Hence, the rise of the plume would be >100 m, which is consistent with the plume data previously recorded on the CIR (Gamo et al., 1996b; German et al., 2001). Data provided by the AUV tend to confirm this result: at ~2.2 km NW from the CTD 26 location, the AUV recorded a temperature anomaly (an increase of the temperature over the background – T. Ura, *pers. comm.*), which provides strong evidence for the proximity of the source (German et al., 2008a).

The geological context is probably very different from segment 15 and from Kairei/Edmonds vent fields. While the $\Delta Mn/\Delta LT(\%)$ at CTD 24 is ~100, in a similar trend as that observed at Kairei (Gamo et al., 1996b), the ratio at CTD 26 is only 10, an order of magnitude lower, which suggest a significant difference in hydrothermal fluid chemistry at these two locations (Gamo, *pers. comm.*). At these latitudes (18-20ºS), the presence of the Reunion hot spot was thought to have an influence on the chemistry of the basalts collected on the CIR (Murton et al., 2005), and hence there could be a direct magmatic-hydrothermal interaction. In fact, two chemically and isotopically different provinces were actually described, the first under the influence of the hot spot (off-axis, Gasiteo Ridge between Three Magis Ridge and the CIR), and the second one with no influence of the hot spot (on-axis) (Nauret et al., 2006). Hence, although one could argue that the composition of the hydrothermal fluid is the result of the interaction between the

Reunion hot spot and the mantle underneath the CIR, no evidence has been collected so far.

3.2.5. Suggestions for the origin of methane along segments 15 and 16

Concentrations of methane measured in the neutrally buoyant plume in segment 15 were significantly lower than those measured over segment 16 (~3 nM and ~10 nM respectively). The low concentrations of methane show that the samples have been taken in a dilute plume, not in near-field plume. Although CH_4:Mn ratios are higher in Segment 15 than in Segment 16 (Appendix 1), these values are not very different from a range of basalt-hosted systems, such as TAG on the MAR (Charlou et al., 1991b) or Steinaholl (German et al., 1994). The segment was characterized by fresh lava flows and a poor sediment level (Magnani, *pers. comm.*), which suggests a magmatic origin for methane and a possible influence of the Reunion hotspot. In the case of a hotspot influence, the axial magma chamber is closer to the surface (Detrick et al., 2002), which could account for higher volatile content compared to segment 16, farther from the hotspot. The poor level of sediments also suggests that the biological production of methane, as well as the thermogenic production, is low in this area.

In segment 16, the concentrations of all three tracers are much higher, but this is especially the case for manganese and iron, associated with a stronger light transmission anomaly. It is clear that the water column is enriched in particles due to the presence of hydrothermal activity. Rock dredging showed the presence of fresh lava flows and a higher sediment cover in this segment at the time of sampling (Magnani, *pers. comm.*), which is entirely consistent with prior studies imaging the seafloor using the TOBI sidescan sonar instrument (Tyler et al., 2007). The process that generates methane on this part of the Central Indian Ridge is more likely a biological/thermogenic production, associated with a magmatic origin (due to a possible interaction with the hotspot, although the latter is farther). The CH_4:TDMn ratio measured in the plume over segment 16 (0.05) is typical of host-basalted, sedimented, and non serpentinized ridges (Charlou et al., 1991b).

3.3. Conclusions

On segment 15 of the Central Indian Ridge, a hydrothermal plume, probably originated from one single hydrothermal vent, is present at 19°33'S/65°50'E centred at 2400-2500 m on the western flank of the rift valley. The source of the hydrothermal plume might be located north of the CTD 24 position and dispersed along the western flank by NW-SE currents. Concentrations of methane are similar to those measured in the Kairei vent field where fresh lavas were found. Hence, it is suggested that methane is produced by magmatic processes on this part of the Central Indian Ridge. On Segment 16, 1 or 2 hydrothermal plumes were detected within a lava plain (18°20'S/65°18'E), characterized by fresh lava flows and the presence of a thin sediment layer. Higher methane concentrations were measured as the source was thought to be closer, but could be also due to biological production and/or thermal breakdown of organic matter.

Further exploration of these segments is required to 1) locate the sources and identify the vents, based on the data collected during the KH-06-4 cruise, 2) sample the fluids to confirm the assumptions made in this Chapter and 3) to determine whether there is a magmatic-hydrothermal interaction due to the presence of the Reunion hot spot.

This Chapter highlights the role of methane as a geochemical tracer for hydrothermal activity along mid-ocean ridges. Associated with other tracers (Mn, Fe, Light Transmission), methane can provide useful information on both the dynamics of hydrothermal processes and the nature of the vent-source. The data showed, clearly, the manner in which these parameters can be used to locate and characterise neutrally buoyant hydrothermal plumes. Light attenuation and geochemical anomalies correlated well in both plume-areas investigated and this has provided interesting first-order information about the likely physical and chemical characteristics of the underlying hydrothermal systems. Due to the differences of behaviour of the geochemical tracers, assumptions can be made about the potential differences in the source vent-fluids, yet to be located at the seafloor.

Tow-yos are an efficient way to intercept plumes, provided that there is a real time feedback from sensors mounted on the CTD-rosette frame. Hence, only physical/optical tracers allowed a detailed mapping of the plumes.

During the CIR cruise, a number of methane samples were degraded due to sampling and shipping issues, and therefore not usable for the geochemical interpretation of the plumes. Although some interpretations could have been made from the remaining samples, there is the kind of loss of information that only real-time in situ sensors can prevent. During the CIR cruise, the Mn sensor GAMOS provided very useful information on a real time basis, which guided the sampling. However, the current in-situ sensing techniques for dissolved methane are not comparably well adapted to the actual conditions in the deep sea environment. Given the value of, for example, hydrothermal plume CH_4:Mn ratios as diagnostic tracers of source and plume evolution, this needs to be remieded.

In the following Chapters, these limitations to pre-existing methane sensing techniques are reviewed and some experiments are described, which had the aim to adapt these techniques to aqueous environments, and hence to mid-ocean ridge exploration.

CHAPTER 4: IN SITU METHANE SENSING TECHNOLOGIES

4.1. Introduction

Accurate determination of dissolved methane concentrations is vital for the study of methane dynamics in a variety of aqueous environments, especially the deep sea. Contrary to free gas, which can be detected directly by acoustic methods (Merewether et al., 1985), dissolved methane measurements are currently performed by collecting discrete water samples from research vessels or from the shore into glass bottles for subsequent gas extraction followed by gas chromatography (GC) analysis (Reeburgh, 2007). Although methane determination by GC is a well established technique (see Chapter 2), with a good limit of detection, precision, and accuracy (Halász and Schneider, 1961; Swinnerton and Linnenbom, 1967), this sampling strategy can never provide more than a restricted dataset limiting comprehension of temporally and / or spatially variable biogeochemical processes (e.g. Varney, 2000; Kroger et al., 2002; Prien, 2007). There is also a strong risk of sample contamination and degradation during the recovery, transfer and subsequent analysis steps. Any of which might render the samples useless.

Since the late 1990s, several studies have focused on the development of instruments and technologies to detect and measure dissolved methane in real time in aquatic environments, from the water-sediment to the air-water interfaces. Such a sensor would provide invaluable data on geological, chemical, or biological processes (Reeburgh, 2007). The performances of chemical sensors are defined by the limits of detection (LOD) of the whole system, the response time to changes in concentrations of the analyte (often noted t_{90} as the time required for 90% change in the sensor signal), the drift of the signal, the resolution (i.e. the smallest change in analyte concentration detectable by the system), the accuracy (i.e. the agreement between the measurement and true value of the concentration), and the precision (i.e. reproducibility between measurements). Hence, the 'ideal' dissolved methane sensor would detect methane with a limit of detection of <5 nM (Reeburgh, 2007), show a fast response (seconds), and have a resolution of below 1 nM.

Only a few techniques have been developed for aqueous environments, adapting existing technologies for air measurements (e.g. metal-oxide semiconductors, infrared spectroscopy, mass spectrometry). These systems have been possible through the use of semi-permeable membranes that are permeable to gas but not to water (De Gregorio et al., 2005; Rego et al., 2005). However, these systems are currently limited in terms of response time, variable membrane permeability, flow sensitivity, poor limits of detection, and hysteresis (memory effect of the membrane). Current research is focusing on optical technologies (e.g. surface enhanced Raman spectroscopy – Schmidt et al., 1998) that negate the use of gas extraction systems and can perform direct measurements instead.

The different analytical methods for the detection and measurement of methane have been reviewed previously (Lawrence, 2006). The aim of this Chapter is to give an overview of the current systems (Table 4.1), which are used for the detection of methane in aqueous environments. In Table 4.1, the readiness of each system is assessed using the Technology Readiness Levels (TRL, Prien, 2007), presented in Table 4.2. In the first part of the Chapter, systems measuring methane in the gas phase are reviewed as well as techniques for gas extraction. In the second part, technologies usable for direct measurements of methane in the dissolved phase are presented.

Sensor	Measurement	Technology	Membrane / Sensitive layer	Concentration range	Limit of detection	T90	T°C	Depth range	Power supply	Manufacturer / Research Institute / Reference	TRL
METS	Gas phase	SnO_2 semi-conductors	Silicon rubber - 5 to 100 µm thick	10 nM - 150 mM	10 nM	1-30 min	2-40°C	0-3500m	35 to 100 mA at 12V	Capsum GmbH / Franatech GmbH Bussell et al., 1999	TRL 8
HydroC/CH4	Gas phase	Direct IR absorption spectroscopy (3.4 µm)	Modified silicon rubber - 2 to 10 µm thick	30 nM - 500 µM	< 10 ppm (3 nM)	17-30 sec	0-50°C	0-6000m	250 mA at 12V	Contros GmbH http://www.contros.eu	TRL 7
Deep-Sea Gas Analyzer	Gas phase	NIR - off-axis integrated-cavity output spectroscopy	Silicon rubber			less than 1 min	0-45°C	0-2000m	Internal battery	lginc (USA) Maddaloni et al., 2006	TRL 7
Deep-sea Methane sensor	Gas phase	Laser absorption spectroscopy (3.3 µm)	Silicon membrane tubes	40-320 ppm	40 ppm (10 nM)			0-2000m		Hokkaido University (Japan) Tsunogai et al., 2007	TRL 6
TETHYS	Gas phase	In situ mass spectrometer	Semi-permeable membrane inlet	no data	sub-ppm (<1 nM)			0-30m (200m possible)	20 W	WHOI (USA) Hemond and Camilli, 2002 Camilli and Hemond, 2004	TRL 7
MIMS systems	Gas phase	In situ mass spectrometer	PDMS membrane inlet	no data	1-5 ppb (1 nM)			0-30m (200m possible)	20 W	University of South Florida (USA) Short et al., 1999	TRL 7
Equilibrator	Gas phase	Photoacoustic spectroscopy	Glass marbles in tube	up to 400 µM	20 µM					Abril et al., 2006	TRL 6
Micro-sensor	Gas phase	Gas Chromatography / Photoacoustic spectroscopy	Silicon membrane	2-500 µM	2 µM			surface		Bussmann and Schink, 2006	TRL 5
Biosensor	Dissolved phase	Amperometry	Silicon membrane	up to 350 µM	5 µM			surface		University of Aarhus (Denmark) Damgaard et al., 1998	TRL 5
FEWS	Dissolved phase	Evanescent Wave spectroscopy	Optical fibre/sensitive layer								TRL 2/3
SERS	Dissolved phase	Surface Enhanced Raman Scattering	Silver-colloid SERS substrate		nM to µM					Technical University Berlin (Germany) Schmidt et al., 1998	TRL 4/5
SPR	Dissolved phase	Surface Plasmon Resonance	PDMS/cryptophane-A	0-400 nM	0.2 nM	2-5 min	45°C	Surface	1 mW	Boulart et al., 2008 (appendix 2)	TRL 4/5

Table 4.1: Current in-situ methane sensing technologies and technologies under development. TRL: Technology Readiness Levels.

Table 4.2: Technology Readiness Levels (TRL) framework, from Prien (2007).

Level	Description
TRL 1	Basic principles of technology observed and reported
TRL 2	Technology concept and/or application formulated
TRL 3	Analytical and laboratory studies to validate analytical predictions
TRL 4	Component and/or basic sub-system technology valid in lab environment
TRL 5	Component and/or basic sub-system technology valid in relevant environment
TRL 6	System/sub-system technology model or prototype demo in relevant environment
TRL 7	System technology prototype demo in an operational environment
TRL 8	System technology qualified through test and demonstration
TRL 9	System technology qualified through successful mission operations

4.2. Detection in the gas phase

4.2.1. Gas extraction systems

Methane sensing technology was initially developed for industrial and environmental monitoring in the atmosphere. Thus, the techniques were directly adapted to measurements in the gas phase. In the case of dissolved gases, those systems cannot be applied directly and require a gas extraction step in the whole analysis process. Semi permeable materials have been developed, therefore, that allow the extraction of the gas phase. The most commonly used system is a gas-permeable silicone membrane (Pandey and Chauhan, 2001; De Gregorio et al., 2005) with hydrophobic properties and characterised by a high permeability to many gases of interest. Other systems made of the same material (silicone) are used under different configurations, e.g. the membrane inlets used for in-situ mass spectrometers (Tortell, 2005). Gas equilibrators (Johnson, 1999) are another technique employed for the extraction of the dissolved gases.

4.2.1.1. Membrane extraction systems

Membranes are used in many applications, especially in gas sensing devices operating in aqueous environments, e.g. the METS sensor or HydroC^{TM} sensor, described later in this

section. The same principles are applicable to gas permeable membrane inlets used for in-situ mass spectrometers (e.g. Hemond and Camilli, 2002).

The gas-permeable membrane generally consists of a reinforcing substrate, made of a solid material with open porosity, and a continuous layer of a silicone rubber based polymer (Pandey and Chauhan, 2001; Carbonaro et al., 2004; Zhang et al., 2005). Diffusion of gas through the membrane is a spontaneous but not instantaneous process that occurs as a complex result of a variety of driving forces including pressure, gas concentration, and electrical potential across the membranes (Pandey and Chauhan, 2001). In an isobaric system, the diffusion is concentration gradient driven according to Henry's law, which states that at a constant temperature, the amount of a gas dissolved in a volume of liquid is directly proportional to the partial pressure of that gas in equilibrium with the liquid.

The diffusion process through the membrane can be described as the following:

$$p_p(t) = p_F\left[1 - \exp\left(-t\left(\frac{RT}{V}\right)\left(\frac{A}{L}\right)P_T\right)\right] \tag{4.1}$$

where $P_p(t)$ is the gas partial pressure in the detector room (Pa), p_F, the partial pressure of the gas in water (Pa), R the gas constant (8.314 J/mol K), T the water temperature (K), V the volume of the detector room (m^3), A the membrane permeation area (m^2), L the membrane thickness (m), t the elapsed time (sec), and P_T the permeability coefficient of the membrane for the dissolved gas. Eq 4.1, highlights clearly the influence of the permeation area (A) and the thickness (L) of the membrane on the transfer of the gas through the membrane. Thick and small membranes result in a slower diffusion of the gas (Pandey and Chauhan, 2001).

Factors that affect the membrane's permeability coefficient are the gas type (the diffusivity of the gas through the membrane depends on the size of the gas molecule – see Table 4.3), the type of silicone (different silicones can be used with varying permeability), the pressure, and the temperature. Permeability can be reduced when diffusion occurs at low temperature (Pandey and Chauhan, 2001) due to the modification of the free volume of the polymer. Temperature also influences the mobility of gas

molecules and the solubility of the gas molecules in the silicone membrane (Robb, 1968). The pressure has a role on the amount of gas that diffuses out through the membrane. The increase in the partial pressure differential of the gas at the interface results in the increase of permeability of the membrane (Robb, 1968).

In addition to these effects in non steady state conditions, or when a sensor consumes the analyte, sample flow past the membrane has an effect (Johnson et al., 2000). In high flow, convective transport ensures that the concentration of the analyte is very close to that of the bulk at the membrane interface despite removal of analyte through diffusion across the membrane. In low flow or stagnant conditions the concentration at the membrane interface drops due to the finite diffusion coefficient of seawater and the lack of convective transport.

To date a complete characterisation of membrane permeability and hydrodynamic flow effects has not been completed. Bell et al. (2007) have completed a characterisation of a membrane inlet system (with Mass Spectroscopy detection) in seawater from 0-2000m depth but at constant temperature and hydrodynamic conditions. Therefore there is considerable uncertainty in measurements made with sensors using gas extraction membranes as variation in membrane permeability remains not fully quantified. These effects will be particularly noticeable for sensors that consume analyte, though non consumptive sensors will also see variations in their response time due to varying permeability and flow.

Table 4.3: Permeability of polydimethylsiloxane (PDMS) to different gases (from Robb, 1968). STP: standard temperature and pressure.

Gas	Permeability 10^9 cm^3.cm/(s.cm^2.cmHg)	Diffusivity 10^6 cm^2/s	Solubility cm^3STP/cm^3.atm
CH_4	95	13	0.57
CO_2	323	11	2.2
O_2	62	16	0.31
H_2	65	43	0.12
He	35	60	0.045

4.2.1.2. Equilibrators

Equilibrators consist of tubes filled with gas partitioning material with water flowing in the opposite direction to gas pumped in a air circuit (Johnson, 1999; Katayama et al., 1999; Frankignoulle et al., 2001). The equilibrators improve the transfer of gasses across the gas-liquid interface by increasing the contact area and enhancing mixing of both the gas and the liquid. Hence, the concentration gradient is maximised at the interface.

This technique is equivalent to the gas headspace extraction presented in Chapter 2 as a headspace is maintained in the circuit while the water in the column is continuously replaced by the water samples. It is assumed that the headspace is at instantaneous equilibrium so that the partial pressure of the gas analyte in the headspace (p_g) equals the partial pressure of the dissolved gas in the water stream (p_d) (Johnson, 1999). Hence, the following relationships can be written:

$$p_d = p_g \tag{4.2}$$

$$C_d = \alpha \cdot C_g \tag{4.3}$$

where C_d and C_g are the concentrations of the dissolved gas in the water stream and in the headspace respectively (in µM) and α is the Ostwald solubility coefficient (defining the volume of water necessary to dissolve a known amount of gas at standard pressure and temperature) (Bieri, 1974). The latter is temperature and salinity dependent (Johnson, 1999); it is therefore necessary to control or measure both parameters to calculate the concentration of the gas in the dissolved phase. Thus, sensors using equilibrators are difficult to deploy in highly variable temperature and salinity conditions. In addition in highly variable concentration environments, traces of gas may remain bound on the extraction system and cause a hysteresis effect (Abril et al., 2006).

Most equilibrators have been developed for air-sea exchange studies with an open air circuit, which make those systems unsuitable for underwater studies (an open air source is necessary for air-sea exchange studies). An equilibrator was developed by Frankignoulle et al. (2001) to be completely immersed in the water (Figure 4.1). In this sytem, the water reaches the equilibrator from the top of the tube and air is pumped through a closed circuit, which allows circulation of the gas through the system and

equilibration with the dissolved phase. Due to the differences in pressure and the pressure dependence of the gas extraction process (the pressure controls the equilibration process), closed air circuits are also limited to a few meters depth (Johnson, 1999).

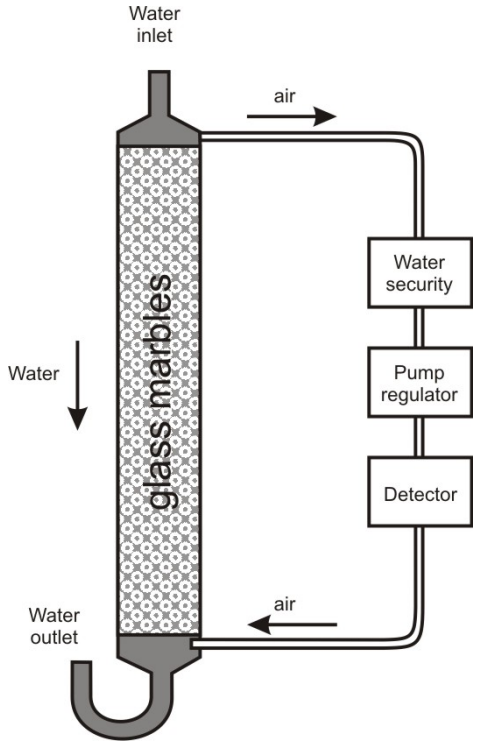

Figure 4.1: Equilibrator system (from Frankignoulle et al., 2001).
The water enters the equilibrator by the water inlet on the top of the tube and circulates through the glass marbles (gas extraction system) while air is pumped through a closed circuit.

4.2.2. Gas detection systems

4.2.2.1. Metal-oxide semiconductors

Metal-oxide semiconductors have been developed for the in-situ detection and monitoring of atmospheric gases (e.g. Yamazoe and Miura, 1994) and have been used since the early 1960s (Nicollian and Brews, 1982; Albert et al., 2000). Among these gases, light hydrocarbons (volatile alkanes, e.g. methane, ethane, propane) can be detected by using metal-oxide semiconductors (Debeda et al., 1997; Lawrence, 2006; Carotta et al., 2008). Semiconductors work on the principle of gas adsorption on a metallic active layer (Figure 4.2), which leads to electron exchange with oxygen present on the metal-oxide layer to form carbon dioxide and hydrogen (Nicollian and Brews, 1982). The consumption of oxygen during the reaction modifies the resistance of the

system, which results in a measurable and detectable change in the voltage. A basic tin-oxide (SnO_2) semiconductor sensor can detect concentrations of methane from 0 to 400 ppm with response times varying from 5 to 35 seconds and recovery times from 15 to 70 seconds (Albert et al., 2000). At high concentrations (~100 ppm), the response time decreases significantly but the sensor suffers from a hysteresis effect as the recovery time increases (Albert et al., 2000).

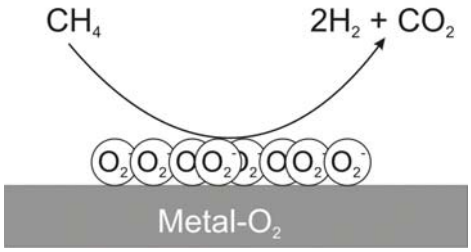

Figure 4.2: semi-conduction principle (modified from Lawrence, 2006).
Methane (CH_4) is adsorbed on the metal-oxyde layer and exchanges electrons with the oxygen (O_2) present on the surface of the metallic layer to form hydrogen (H_2) and carbon dioxide (CO_2).

This technique has been widely used in in situ gas sensing schemes due to its low-cost and robustness (e.g. Yamazoe and Miura, 1994; Barsan et al., 1999; Carotta et al., 2008); however these sensors suffer from a low selectivity or even non-selectivity in some cases (e.g. Schierbaum et al., 1992; Yamazoe and Miura, 1994; Skala et al., 2004; Mann et al., 2005). Metal-oxide semiconductors can respond to any kind of gas that can be oxidized. Usually, semiconductors are based on tin oxides (Nicollian and Brews, 1982; Williams and Coles, 1999; Lawrence, 2006), doped with transition metals such as Pd (Paladium) or Pt (Platinum) (Skala et al., 2004) or using catalytic layers (e.g. Al_2O_3 – Gutiérrez et al., 1998 or zeolites – Mann et al., 2005) to improve the sensing properties of the systems. Mann et al. (2005) improved the selectivity of a SnO_2 semiconductor by adding zeolites (aluminosilicate structures) to the sensing layer, of suitable size to trap methane but not bigger alkanes (especially ethane). Both zeolites and doping metals can be used to act as a filter for the investigated molecule.

Another important factor that controls the selectivity of the sensor is the temperature of the sensing layer (Nicollian and Brews, 1982), because this, too, influences the oxidation of gases. Fleischer and Meixner, 1995) showed that there is an optimal working temperature for the selective detection of methane at ~ 780ºC by a Ga_2O_3 (Gallium oxide) layer, with no effect from H_2 or CO. For a SnO_2 semiconductor, the oxidation of

methane has to occur at 400ºC to obtain the required selectivity of the sensor (Schierbaum et al., 1992). The temperature at which the sensor has to be operated creates condensation due to the formation of water vapour, which influences the response of the semiconductor (Sohn et al., 2008).

A further limitation of metal-oxide semiconductors in the detection of methane is the necessity of operation in aerobic conditions, as oxygen is required for the chemical reactions (Lawrence, 2006). Hence, these systems in environmental monitoring are limited as methane is often produced in anaerobic conditions (oxygen free environments) (van Rij et al., 2001).

- *METS sensor: the first in-situ methane sensor for aqueous environments based on a metal-oxide semiconductor*

The METS methane sensor (Masson et al., 1997) was introduced in 1999 as the first sensor for methane monitoring and detection underwater (Figure 4.3).

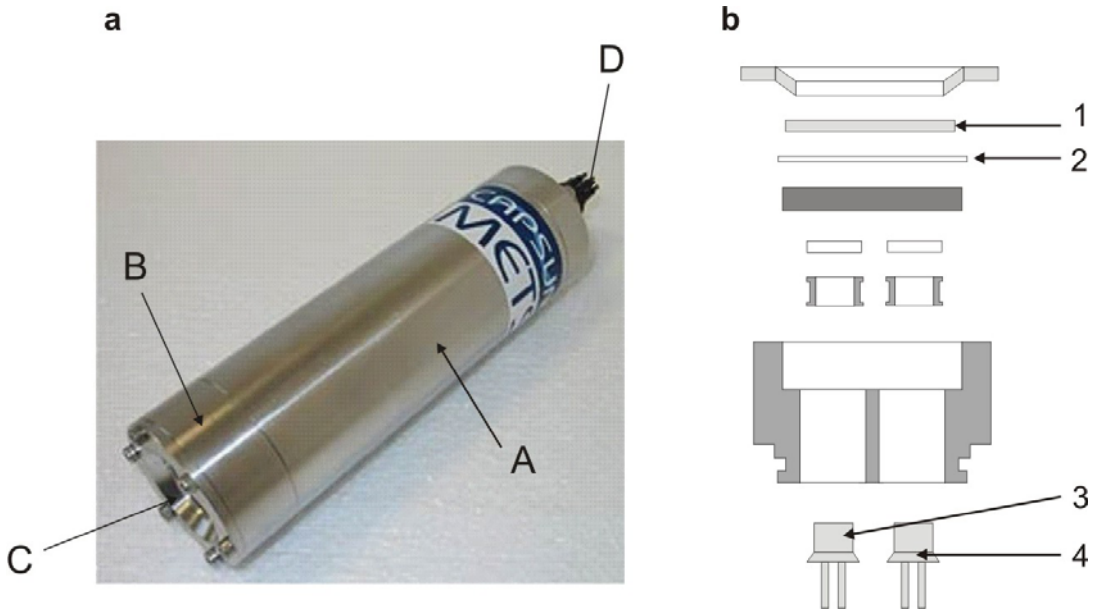

Figure 4.3: a) METS-CAPSUM-FRANATECH methane sensor. A: main body; B: sensor head; C: silicon membrane; D: connection. b) Internal structure of the sensor head. 1: silicone membrane; 2: sintered metal; 3: semiconductor detector; 4: temperature detector.

The detection chamber is separated from the surrounding seawater by a 5 to 100 μm thick silicone membrane. Support for this membrane is provided by a porous metal frit and a perforated metal plate, allowing diffusion of gases from seawater into the detection chamber (Fukasawa et al., 2006). The tin-oxide semiconductor based detector is placed on the backside of the sintered metal plate (Figure 4.3 (b)). Dissolved gases including water vapour permeate the silicone membrane until the gas partial pressures in both the liquid phase and the vapour phase become equal.

The METS-sensor can detect concentrations ranging from 50 nM to 10 μM in its standard version, up to 2 mM for some applications and can operate at 3500 m water depth at temperatures between 2 and 40°C (Lamontagne et al., 2001). However, operating in this range of temperature necessitates a good correction from the temperature effect. For example, significant differences of measurements between the temperature sensor mounted on METS and a SeaBird T-sensor were noted during a deployment in the Lau Basin, which limited the resolution of the METS output (Connelly, *pers. comm.*). The response time (t_{90}), given by the manufacturer, varies from 1 to 30 minutes depending on the configuration of the sensor. The device is 200 mm long with a diameter of 49 mm and a weight of 1.5 kg. The power consumption varies between 35 mA and 100 mA at 12V depending on the instrument version.

The METS-sensor has been widely used for oceanographic studies since its commercialization. It has been used in detecting methane-rich plume signals in the water column overlying cold-seep environments (Bussell et al., 1999; Collier and Klinkhammer, 2000; Lamontagne et al., 2001; Christodoulou et al., 2003; Newman et al., 2008) or for long-term monitoring (Marinaro et al., 2004). The system can easily detect changes of +10nM (Collier and Klinkhammer, 2000). However, because of the long diffusive path, the response is characterized by a significant time lag to changes in dissolved methane concentration, i.e. hysteresis (Collier and Klinkhammer, 2000; Newman et al., 2008). Once high concentrations of methane diffuse into the sensor cell, it takes a long time to return to low values, which limits quantitative applications (e.g. from CTDs).

Factors that affect METS sensor response include variable gas permeability of the silicon membrane, selectivity of the semiconductor, and volume of the detector chamber (closed

system) (Fukasawa et al., 2006). The latter has an influence on the response time: Fukasawa et al. (2006) have shortened the t_{90} from 9 minutes to 2 minutes by reducing the volume of the detector chamber to about 22% of the standard sensor. Though it has not been reported it is likely that there is flow sensitivity as the sensing principle consumes analyte and a membrane inlet system is used. The combined effects of these performance characteristics will probably limit the widespread acceptance of this device for at least some scientific applications.

4.2.2.2. Infrared absorption spectroscopy

Direct absorption spectroscopy

Infrared absorption spectroscopy is one of the most important technologies for gas sensing in environmental, safety, and industrial monitoring (Rogalski and Chrzanowski, 2002). The infrared absorption spectroscopy principle is based on absorption line detection: the frequency and shape of the line are intrinsic for the compound investigated (Nadezhdinskii et al., 1999; Rogalski and Chrzanowski, 2002) and can be recorded with great accuracy and resolution. Each compound has a unique "finger print" consisting of many lines (corresponding to multiple vibration modes, harmonics and combinations). Even in complex mixtures it is often possible to determine the presence and concentration of constituents through pattern recognition and chemometrics (e.g. Chung et al., 1999).

As partly depicted in Figure 4.4, methane absorption bands are found in four regions, 1300 nm, 1600 nm, 2300 nm, and 3300 nm (Ellis, 1927; Moorhead, 1932; Nielsen and Nielsen, 1935). Absorption bands exist also in the 7-8 μm region. The strongest (or fundamental) absorption lines are located in the mid-infrared (MIR, 3.3 μm region). This significant line strength (100-1000 stronger than the NIR) (Stewart et al., 1997) indicates that detection in the MIR region should be much more efficient than detection in the near infrared (NIR) (Culshaw et al., 1998).

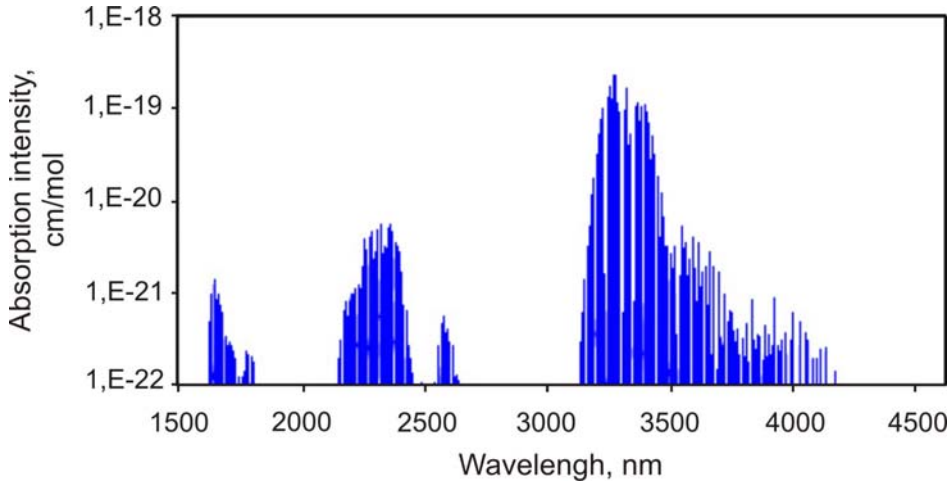

Figure 4.4: Absorption lines for methane in the infrared.
Absorption lines at 1300 nm are not depicted here for scaling reasons (modified from http://webbook.nist.gov/)

MIR spectroscopy of methane corresponds to the excitation of fundamental transitions between the ground state of vibrational mode (υ_0) and its first excited state (υ_1), as described in Figure 4.5, while NIR spectroscopy corresponds to the excitation of overtone vibrations (υ_2, υ_3) and combinations in vibrations ($\upsilon'_1 + \upsilon_1$). Sensors developed for environmental applications using IR spectroscopy are designed as a compromise between the sensitivity (MIR is more sensitive), the selectivity (NIR bands for methane are more selective – Silveira et al., 1998), and the operational mode of the system (NIR is easier to operate) (Werle et al., 2002; Lawrence, 2006).

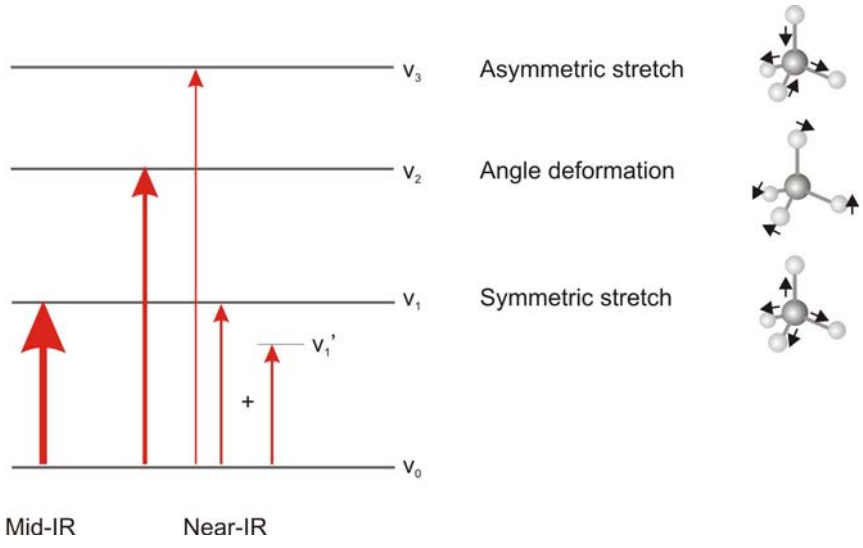

Figure 4.5: IR transitions (from Kraft, 2004) and modes of vibrations.

IR sensor set-ups include a radiation source (e.g. light emitting diode, semiconductor lasers, incandescent light), a detector, which converts electromagnetic radiation into electrical signals (e.g. photodiodes), and a closed absorption cell where the concentration of the gas is determined using the Beer Lambert's law (Werle et al., 2002), which describes the absorption of the infrared light by the hydrocarbon bond C-H (Eq 4.4 and 4.5):

$$A = \log_{10}\left(\frac{P_0}{P}\right) \tag{4.4}$$

$$A = \varepsilon \cdot b \cdot c \tag{4.5}$$

where A is the absorbance (no units), P_0 the initial power of the light beam, P the power after absorption, ε the molar absorptivity (L. mol^{-1} cm^{-1}), b the path length (cm), and c the concentration of the compound ($mol.L^{-1}$)

Sudden variations of temperature have a strong influence on the IR detection of methane, as IR detectors require 10 to 20 minutes to reach thermal equilibrium (Silveira et al., 1998). IR analyzers are also very sensitive to humidity in the detection chamber as water vapour absorbs IR in the same region as hydrocarbons (Silveira et al., 1998). Hence, most IR sensors are operated at temperatures above ambient to avoid condensation.

The sensitivity of the technique depends on the presence of other hydrocarbons. When alone, methane can be detected at a level of 1% in air but IR detectors saturate rapidly in the presence of a few percent ethane, propane or butane (Silveira et al., 1998). Usually IR detectors are calibrated for each of the compounds and chemometrics (statistical method) are used to discriminate the presence of different hydrocarbons (e.g. Chung et al., 1999).

- *Examples of in-situ methane sensors employing IR absorption spectroscopy*

HydroC™ (Contros GmbH – Figure 4.6) is an optically based methane sensor that measures the gas molecules diffusing through a special silicon membrane into a detector chamber. The detection principle is based on direct infrared absorption spectroscopy in the 3.4 μm region. The thickness of the membrane, given by the manufacturer, ranges

from 2 µm (for water up to 1000 meters) to 10 µm (for deep waters up to 6000 meters). The detection chamber contains an infrared source, an absorption cell and a detector.

Figure 4.6: Contros GmbH HydroC™/CH_4 sensor

The system can measure concentrations of methane ranging from 30 nM to 500 µM with a resolution between 3 and 30 nM. The t_{90} of the detector, given by the manufacturer, is ~30 seconds. However, no data are available for the whole system, including diffusion of the gas through the membrane, which is likely to slow the response considerably (minutes). The noise level is given to be 3 nM. The power supply is typically 250 mA at 12 V (3.5 W).

The HydroC™/CH_4 was deployed in 2007 during the RV Sonne cruise 190 (27/02 – 22/03) and was able to measure methane plumes (10 to 50 nM) over the New Zealand continental margin (Contros GmBH, *pers. comm.*). To date there are no published papers involving data collected by a HydroC™/CH4, as the system is still under development.

Tsunogai et al. (2007) have developed an in-situ methane analyzer, which uses gas-permeable membrane tubes. The methane concentration is measured by infrared spectroscopy in the 3.3 µm region, using a laser as a light source. The system is calibrated up to 320 ppm in the gas phase with a limit of detection of 40 ppm. No details on the sensor set-up or information on aquatic in-situ deployments are available for this system.

Cavity Spectroscopy

Absorption spectroscopic techniques based on high-finesse optical cavities have significantly advanced the monitoring of atmospheric gases (e.g. Nakagawa et al., 1994; O'Keefe, 1998; Baer et al., 2002; Maddaloni et al., 2006). Different techniques exist, i.e. cavity ringdown spectroscopy (CRS), cavity-enhanced absorption spectroscopy (CEAS), and integrated cavity output spectroscopy (ICOS) (Paul et al., 2001; Maddaloni et al., 2006). With the latter, quantitative detection of methane in the atmosphere reaching a minimum detectable concentration of 850 parts per trillion at atmospheric pressure has been possible (Malara et al., 2006)

In Integrated Cavity Output Spectroscopy, the absorption signal is obtained through the temporal integration of a laser intensity transmitted across a high-finesse cavity containing two mirrors (Baer et al., 2002). In the same way as in conventional absorption measurements, the absorption inside the cavity is measured from the light transmission (the cavity output), function of the mirror reflectivity inside the cavity and the losses between the mirror (O'Keefe, 1998). The difference with the conventional absorption spectroscopy is in the gain of sensitivity resulting from the temporal analysis of the signal rather than the amplitude analysis (O'Keefe, 1998).

In the off-axis ICOS, the laser beam is directed off axis with respect to the cavity (Figure 4.7), which allows a spatial separation of the multiple beam reflections until the beam retraces its path through the cavity (Paul et al., 2001). The sensitivity is thus enhanced by increasing the number of reflections (i.e. light pathlength) within the cavity (Maddaloni et al., 2006; Malara et al., 2006). Hence, the analyte concentration can be determined from the measured spectra integrated over the entire absorption pathlength (Baer et al., 2002).

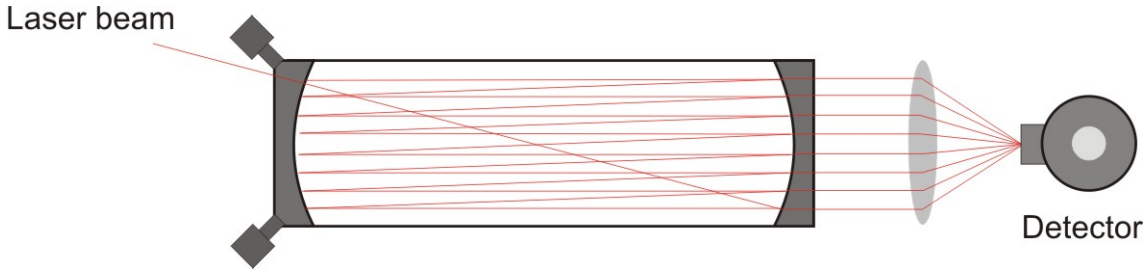

Figure 4.7: Schematic of the off-axis alignment evidencing the multiple-reflection beam path through the cavity (from Maddaloni et al., 2006)

The transmitted laser intensity (I) through an empty cavity may be expressed by:

$$I = \frac{I_L C_P T}{2(1-R)}\left(1-\exp\left(-\frac{t}{\tau}\right)\right), \tau = \frac{\frac{L}{c}}{1-R}, \tag{4.6}$$

where I_L is the incident laser intensity, C_P the cavity coupling parameter (value comprised between 0 and 1), R and T the mirror intensity reflection and transmission coefficients, τ the characteristic cavity decay time, L the distance between the mirrors, and c the speed of light. With an absorbing gas between the mirrors, R is replaced by $R' = R \cdot \exp(-\alpha_\nu)$, where α_ν is the optical depth of the gas over the cavity length, comparable with the Beer Lambert's law (Paul et al., 2001; Baer et al., 2002). The output intensity contains therefore all the absorption information (Baer et al., 2002).

- *Deep Sea Gas Analyzer*

The Deep-Sea Gas Analyzer (http://www.lgrinc.com) employs a gas permeable membrane and a transduction method based on off-axis integrated-cavity output spectroscopy.

The Deep Sea Gas Analyzer, as described by the manufacturer, can detect most dissolved gases, including methane and carbon dioxide. As a result of the detection process, according to the manufacturer, the instrument is self calibrated and provides an absolute, accurate gas concentration without gas standards. The response time given by the manufacturer is less than 1 minute. No data are available on the characteristics of this system in real conditions. However, due to the use of a gas permeable membrane, a

longer response time can be expected for the whole system. Thus, the response time given by the manufacturer would be the response time of the detector in the detection chamber and not for the whole instrument. The operational temperature range is between 0 and 45°C and the operational depth is up to 2000 m.

4.2.2.3. Photoacoustic spectroscopy

Photoacoustic spectroscopy is performed by sending modulated radiation into a sample gas cell containing a microphone (Zeninari et al., 2003). In this technique, a pulsating light is emitted and absorbed by the gas present in the cell. The absorption causes increase and decrease in the temperature of the gas and subsequent variations in the pressure within the cell. Two ultrasensitive microphones mounted in the cell are used to measure this pressure wave, which is directly proportional to the concentration of the gas (Middelburg et al., 1996; Zeninari et al., 2003). Zeninari et al. (2003) achieved detection of methane concentration at a sub-ppm level (0.3 ppm detection limits) with a photoacoustic system, employing a 1.65 μm diode laser.

- *Example of in-situ methane sensor based on photoacoustic spectroscopy*

Equilibrators connected to an infrared analyser were developed, initially, for the in situ study of CO_2 fluxes from oceanic systems to the atmosphere (Frankignoulle et al., 2001). The system was subsequently modified by Abril et al. (2006) for the measurement of methane concentrations in seawater. The system comprises a plexiglas cylinder, 8 cm diameter, 60 cm long in which water flows at 1.5 $L.min^{-1}$. The air volume in the equilibrator is 0.5 L, whereas the gas exchange surface is maximized to ~1.2 m^2. The gas analyzer is a Bruel and Kjaer type 1312, based on the photoacoustic infrared detection method, which allows CH_4 measurements every 2 minutes.

Calibration of the field system ranges up to 10,000 μatm for methane (up to 400 μM). However, at low concentrations (<0.5 μM), the equilibror is affected by a hysteresis effect from high concentrations to low concentrations (Abril et al., 2006), which is representing a significant limitation for sensors to be used in highly variable environments. In addition equilibrators are difficult to construct, operate and calibrate in-situ (see 4.2.1).

4.2.2.4. Mass spectrometry

Mass spectrometry (MS) is mainly used to describe the composition of a physical sample by generating a spectrum representing the masses of the sample components (Dass, 2007). All mass spectrometers consist of three distinct regions 1) the ionizer (or ion source), 2) the ion analyzer, 3) the detector (Figure 4.8).

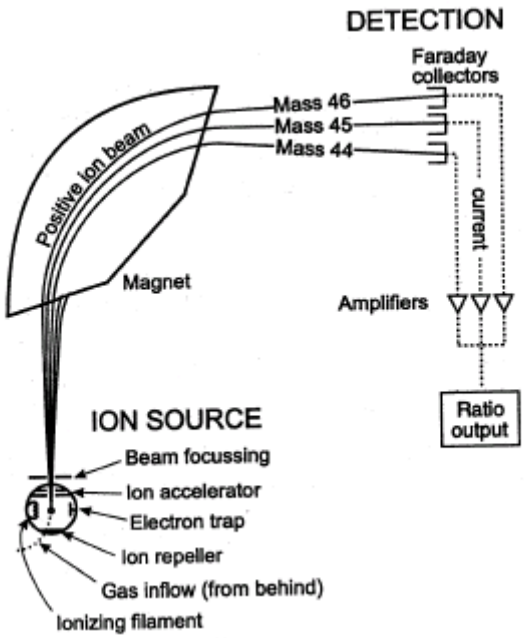

Figure 4.8: Schematic of a simple mass spectrometer (from Dass, 2007)

Details on mass spectrometry theory can be found in Dass (2007). In the case of mass spectrometers, molecules are ionized by a high energy electron beam (ionizer or ionizing filament) in a vacuum. The principle is to remove an electron from the initial molecule to produce a molecular ion, which breaks into smaller ions due to its instability (Dass, 2007). The products of this reaction are then accelerated (in the ion accelerator) and distributed in the mass analyzer (by an electro-magnetic field) as a function of their mass-to-charge ratio (Dass, 2007). The detection occurs in the mass detector where mass spectra are generated. The mass analyzer can be configured in different ways (e.g. quadrupole ion trap, sector, time-of-flight) according to the sensitivity and selectivity required.

- *In-situ Mass Spectrometers*

Mass spectrometers (MS) are usually large laboratory instruments. However, since the development of small mass analyzers (quadrupole mass filters and ion-trap mass spectrometers - March, 1997), portable instruments are now available (Syage et al., 2001) and this has led to the idea of adapting MS to aqueous environments (Short et al., 1999; Hemond and Camilli, 2002; Camilli and Hemond, 2004; Kibelka et al., 2004) (Figure 4.9).

Current In-situ MS systems use a semi-permeable membrane inlet to separate the sample from the high-vacuum of the MS. However, the membrane inlet must be designed to allow the adequate introduction of gases into the vacuum chamber while maintaining an internal pressure of 10^{-5} to 10^{-6} Torr (Short et al., 1999). Hence, membrane geometry and material are a compromise between performance (response time, selectivity) and resistance to the pressure differential between the environment (atmospheric to deep sea pressure) and the internal cavity (vacuum). Very small membranes are the best compromise, offering an effective interface between the water column and the vacuum system and very low detection limits. Short et al. (2001) used a common PDMS capillary (0.01m long, 0.001 m in diameter), connected to stainless-steel tubes. Hemond and Camilli (2002) developed a flat-plate configuration inlet, using a sheet supported by a porous support plate. The porous plate is 0.08 cm in thickness and 0.63 cm in radius with a porosity of 12%.

In-situ mass spectrometry is capable of measuring dissolved methane at the sub-ppb level (Short et al., 2001). Analysis cycle times are typically 5 to 15 minutes (Short et al., 1999).

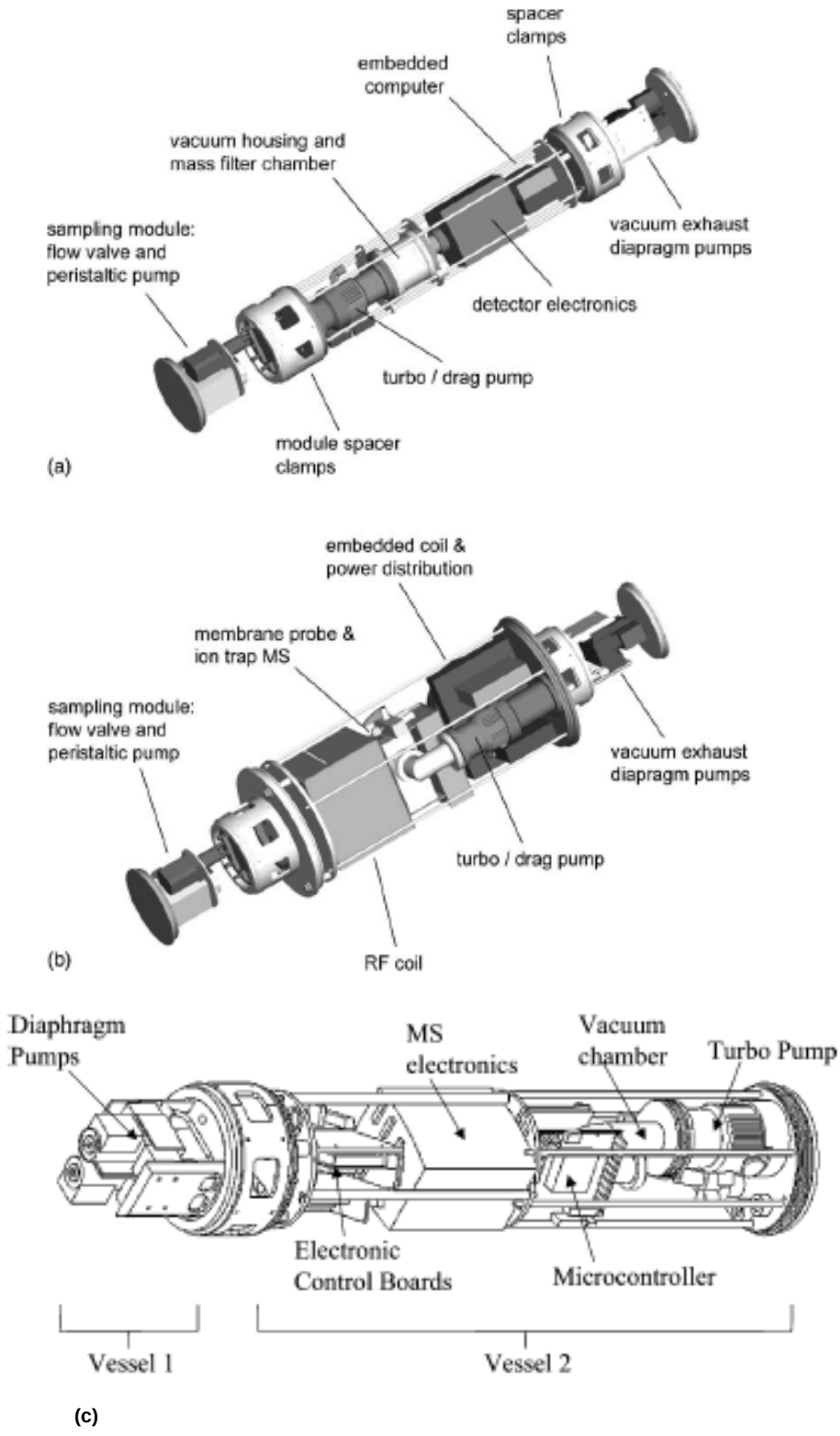

Figure 4.9: (a) underwater linear quadrupole mass spectrometer system and (b) underwater ion trap mass spectrometer system developed by Short et al (1999; 2001) and Kibelka (2004). (c) Linear quadrupole underwater MS system developed by Camilli and Hemond (2002)

Despite the high-quality data that in-situ MS systems are able to supply (e.g. Tortell, 2005), their development is limited by the pressure differential between the environment and the ionization system, which has to be at high vacuum. Current systems cannot be deployed deeper than 200 m (Camilli and Hemond, 2004). To increase the resistance to the pressure differential across the system, the membrane has to be thick, which influences the sensitivity and the response time, as detailed earlier. In addition, due to the maintenance of internal vacuum and ionisation of the analyte, MS systems are consumptive, and therefore membrane permeability variations and flow affect the measurement. Technical improvements are therefore needed in depth capabilities and membrane characterisation to allow full ocean depth deployment. In-situ MS are also characterised by a high power consumption, which limits their autonomous deployments considerably. A high power supply is necessary to maintain a vacuum in the system and for the functioning of the pumps. The ionization system also requires a hot filament that consumes a large amount of power (at least 20W – 100W during sampling periods), dictated by heat-transfer physics (Camilli and Hemond, 2004).

4.3. Measurements in the dissolved phase

4.3.1. Surface Enhanced Raman Spectroscopy (SERS)

Spectroscopy based on the Raman Effect has been used for gas, solid, and liquid identification and analysis for several decades. It is a non invasive, non destructive form of vibrational spectroscopy yielding fingerprinting spectra of analytes suitable for substance identification and for quantitative analysis (Long, 1977; Schmidt et al., 1998; Brewer et al., 2004; White et al., 2006).

Raman spectroscopy measures the scattered light from a molecule when the molecule is excited by a specific light source. The scattered radiation (approximately 1 in 10^8 photons are Raman scattered) has frequencies different from the incident beam, due to the exchange of energy between the incident photons and the molecule. The Raman Effect is defined as the shift in light frequency (Long, 1977). The resultant spectrum (intensity vs. frequency shift) provides a unique fingerprint to the analyte.

One main disadvantage of Raman spectroscopy is its low sensitivity due to the weak Raman Effect and the extremely small cross section of the Raman process (10^{-31} to 10^{-29} cm^2 per molecule). Hence, highly concentrated samples and / or expensive laser sources are required to improve the sensitivity and obtain detection limits in the ppm range (Brewer et al., 2004; White et al., 2006). Raman also suffers from fluorescence interferences, which are abundant in natural waters (presence of chlorophyll and related pigments), and can completely mask the Raman spectrum (Brewer et al., 2004).

Despite these disadvantages, there are many important targets in aqueous environments that can be accessible by Raman spectroscopy: in-situ identification of rocks and minerals and the determination of the chemical composition of pore waters, gas seeps, and even seafloor hydrothermal vents (Brewer et al., 2004; Dunk et al., 2005). However, most Raman active dissolved chemical species are only present at very low concentrations (nM) in seawater, limiting the Raman Effect (Brewer et al., 2004).

The surface enhanced Raman scattering (SERS) effect, discovered in 1974 (Fleischmann et al., 1974), and using specific roughened metal surfaces, allows a significant improvement of the Raman Effect (e.g. Weissenbacher et al., 1997; Murphy et al., 2000; Schmidt et al., 2004; Sackmann and Materny, 2006). The SERS effect is based on the resonance of surface plasmons (theory described in the next section), which enhance the Raman signal by producing an electromagnetic field around the analyte (Sackmann and Materny, 2006).

The enhancement of the Raman scattering of molecules at metal surfaces is due to an electromagnetic effect (enhancement of the optical fields due to the excitation of electronic resonances on metallic surfaces), and a chemical interaction between the adsorbed molecule and the metal surface (resulting from a resonance Raman Effect via a charge-transfer intermediate state) (Sackmann and Materny, 2006). To maximize the SERS enhancement, the size and shape of the surface roughness features are designed to couple the electromagnetic energy of the exciting light into the metal substrate (Mullen et al., 1992).

Silver and gold are the most widely used materials for SERS substrates and are most commonly used in the form of spherical particles on the nanometre scale (Stiles et al.,

2008). The enhancement factor of the Raman Effect provided by the SERS substrate ($10^{14} – 10^{15}$) allows single molecule detection (Schmidt et al., 1998; Young et al., 2004). Fluorescence interferences are greatly reduced due to the absorption of the analyte to the metal surface (Young et al., 2004).

The development of a continuously operating in situ SERS system for the marine environment is difficult due to the difficulties with reproducing and stabilizing SERS substrates (Schmidt et al., 1998). SERS surface are sensitive to photodegradation, which occurs with high intensity laser sources (Murphy et al., 2000). It is therefore necessary to find a compromise between the intensity of the source and the long-term stability of the reactive surface. In addition, adsorption of molecules on SERS substrates is highly unpredictable and depends on the concentration of the analyte. At low concentrations (nM), SERS enhancement may be significantly reduced because a critical concentration is required to start the aggregation of molecules on the substrate. Sackmann and Materny (2006) showed that slight variations in the preparation of the SERS substrates may result in changes of the adsorption geometry and, hence, high variations in the enhancement factor. Quantitative measurements are, therefore, extremely difficult and limited, instead, to a broad concentration range (10^{-7} M).

Sol-gel techniques are applied to improve the mechanical and chemical stability of encapsulated silver colloid surfaces (Schmidt et al., 1998). Recent work (e.g. Schmidt et al., 2004) has improved the long-term stability of SERS substrates in seawater and, consequently, the sensitivity of such sensors for different species. Schmidt et al. (2004) have shown that sol-gel derived SERS substrates with colloidal silver are suitable for the detection of low molecular weight aromatic hydrocarbons in seawater down to the μM level. Hence, these systems are adapted to the detection of dissolved methane (Pironon et al., 2003) provided that the SERS substrate has been especially designed for methane. Several instruments have been or are currently being developed for in-situ applications in aqueous environments, with different targets, e.g. Volatile Organic Compounds (Mossier-Boss and Lieber, 2003); pesticides (Weissenbacher et al., 1997; Yea et al., 2005); Polycyclic Aromatic Hydrocarbons (Schmidt et al., 1998 ; Murphy et al., 2000; Ha and Kronfeldt, 2004; Costa et al., 2006); CO_2 (Dunk et al., 2005).

4.3.2. Fibre-optic Evanescent Wave Spectroscopy (FEWS)

4.3.2.1. Principle

Methane cannot be measured by direct IR absorption due to the strong water O-H absorption (Buerck et al., 2001). Thus, to allow the use of infrared absorption spectroscopy for the in-situ detection of dissolved methane, systems were developed based on gas extracting membranes (e.g. HydroC^{TM}).

An alternative strategy is to allow dissolved gas to diffuse into a hydrophobic medium that has low optical absorption in the infrared (or spectral region of interest) and perform spectroscopy in this material. To enable short response times, high permeability and short diffusion paths are required. The latter can be achieved by using a thin membrane. Sensitivity may be enhanced by using a material with a high partition coefficient (i.e. the concentration in the hydrophobic material is enhanced compared to the concentration in the dissolved phase). Coupling light into such thin layers is difficult. One solution is to employ evanescent wave spectroscopy using a waveguide such as an optical fibre (Tai et al., 1987; Culshaw et al., 1992; Stewart et al., 1997; Raichlin et al., 2004). The principle of evanescent waves was discovered by Goos and Hanchen (1947) and uses the attenuated total reflection (ATR) pattern (Harrick, 1979): if a light beam is directed through a transparent material to an interface with a material of lower refractive index (RI), a part of the beam will be reflected by total internal reflection at the interface; a standing wave results that penetrates a small distance into the lower RI medium where it can interact with molecules (Figure 4.10). The resulting standing wave is called an evanescent wave (EW). In an optical fibre a high RI core is encased in a cladding material that has a relatively low RI. Total internal reflection guides light down the core of the fibre and the EW is present in the cladding. Thus if a hydrophobic cladding permeable to the analyte of interest and optically transparent in the spectral region of absorption lines is chosen, IR spectroscopy is possible in an aqueous environment (Mizaikoff, 1999; Kumar Suresh et al., 2002).

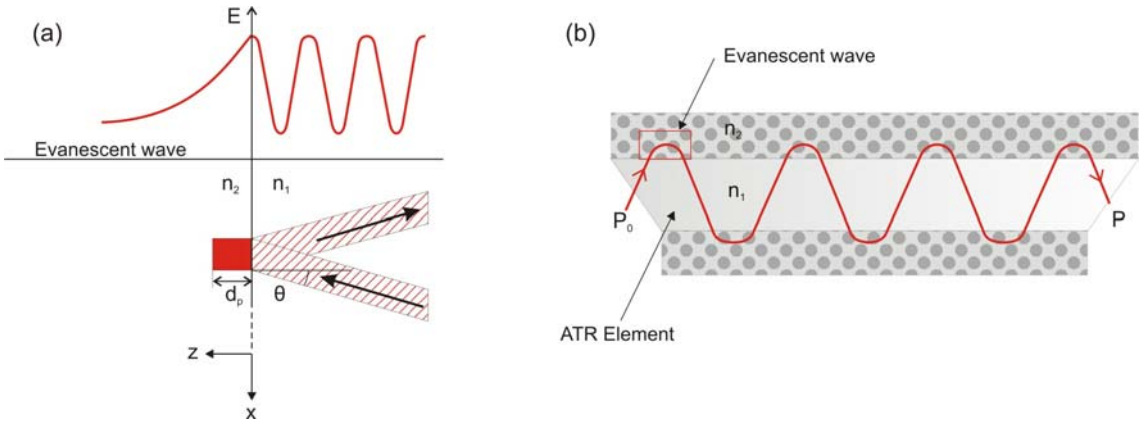

Figure 4.10: (a) Evanescent wave behaviour at the interface between two medias and (b) evanescent waves in a waveguide (ATR element), in contact with the surrounding medium.
E: evanescent field; n1: refractive index of the core; n2: refractive index of the surrounding medium; dp: penetration depth; θ: angle of incidence (modified from Schwotzer et al., 1997)

According to Snell's Law, the critical angle depends only on the refractive index of the two media:

$$\sin\theta_c = \frac{n_2}{n_1}, \tag{4.7}$$

The RI of the cladding (n_2) has to be smaller than the RI of the fibre core (n_1), and if the difference of RI increases, the critical angle decreases and more light is transported. All along the waveguide, at every point of reflection, there is an evanescent wave, which penetrates over a short distance into the surrounding medium (Figure 4.10 (b)). The evanescent field is described by the following equation:

$$E_z = E_0 \exp^{\frac{-z}{dp}}, \tag{4.8}$$

where z is the distance normal to the interface, E_0 the wave amplitude at $z = 0$, and d_p the penetration depth, which is the perpendicular distance from the interface at which the electric field magnitude, E, has fallen to $\frac{1}{e}$ of its value (Xu et al., 2006). The penetration depth is given by:

$$d_p = \frac{\lambda}{2\pi \cdot n_1 \sqrt{\sin^2 \theta - \left(\frac{n_2}{n_1}\right)^2}}, \tag{4.9}$$

where λ is the vacuum wavelength, θ is the angle of incidence to the normal at the interface, and n_1, n_2 are the refractive index values of the core and the cladding, respectively. For small differences between n_1 and n_2, the penetration depth is increased and more light energy is available for interaction with the external medium (Stewart et al., 1997). At the same time, less light is transported through the waveguide core due to the increase of the critical angle, i.e. if $\frac{n_2}{n_1} \approx 1$, d_p becomes infinite and no reflection occurs (Messica et al., 1994).

Evanescent wave absorption measurements are performed by comparing the light intensity in the presence of the analyte to the light intensity at the initial state. Thus, if the polymer is a solvent for the analyte, then the analyte penetrates into the cladding and can interact with the evanescent field (Raichlin et al., 2004). The enrichment of the cladding in the analyte causes both absorption at wavelengths corresponding to the analyte's spectral signature, *and* a change in the RI of the cladding (n_2), hence, a change in the critical angle. This change in critical angle changes the losses in the waveguide and the numerical aperture (NA), defined by

$$NA = \sqrt{\left(n_1^2 - n_2^2\right)}, \tag{4.10}$$

is modified. At a non-absorbing wavelength, the absorption due to refractive index modification is given by

$$-\log\left(\frac{P}{P_0}\right) = \log\left(\frac{NA_0}{NA}\right), \tag{4.11}$$

where P is the transmitted light power when the analyte is present and P_0 is the transmitted light power at the initial state. At an absorbing wavelength, a modified Beer-

Lambert law is applied (Buerck et al., 1996; Messica et al., 1996; Schwotzer et al., 1997):

$$-\log\left(\frac{P}{P_0}\right) = \varepsilon \cdot \eta \cdot C \cdot l + \log\left(\frac{NA_0}{NA}\right), \tag{4.12}$$

with P_0, P the power, NA, NA_0 the numerical aperture of the fibre, ε the molar absorption coefficient, C the concentration of the analyte in the polymeric cladding, l the length of the effective evanescent wave interaction of the fibre and η the refractive index of the polymeric cladding. Hence, according to this Equation, both terms are dependent on the quantity of the analyte present in the cladding, as the first term describes the normal Beer-Lambert law (with $\eta.l$ as the interaction length) while the second describes the variation in the light transmission due to the changes in the numerical aperture.

4.3.2.2. FEWS sensors for methane

FEWS has been investigated for the detection of methane in both the gas and the dissolved phase (e.g. Tai et al., 1987), and both in the MIR and in the NIR range (e.g. Culshaw et al., 1992; Taga et al., 1994). As described earlier, the main absorption bands for methane lie in the MIR range between 3 and 10 μm (Culshaw et al., 1998). Table 4.4, modified from Culshaw et al. (1998) presents the expected sensitivity for the detection of methane by direct absorption spectroscopy in the NIR and in the MIR.

Table 4.4: Estimated sensitivity at room temperature for the detection of methane by direct absorption at different wavelengths.
From [1] Culshaw et al. (1998) and [2] Okajima et al. (2006).

Absorption line wavelength (nm)	Line strength ($cm^{-2}atm^{-1}$)	Estimated sensitivity (ppm)
1330[1]	0.3 x 10^{-2}	0.1
1667[1]	1.5 x 10^{-2}	0.02
3260[2]	5.27	<0.001

Sensors operating in the MIR require specific components, i.e. optical fibres transparent in the MIR (silver, chalcogenide or tellurium fibres – Heise et al., 1997; Mizaikoff, 1999), light sources emitting in the MIR (incandescent lamps, MIR-LEDS, laser diodes –

Werle et al., 2002), and specific spectrometers (Deng et al., 2007). In order to achieve reasonable signal to noise ratios, detectors operating at long optical wavelengths (3000 nm) where the photon energy is of the order of 0.3 eV must be cooled (Culshaw et al., 1998). The cost and mass of these systems is, therefore, relatively high (Mizaikoff, 1999).

On the other hand, methane possesses overtone and combination lines in the near infrared, which can be addressed by common silica fibres from the telecommunication industry (e.g. Culshaw et al., 1992). Silica waveguides are robust, chemically inert, and allow transmission of light over distances of several hundred meters between sensing elements and spectrometers (Buerck et al., 2001). Due to the expansion of the telecommunications industry, optical fibres, spectrometers, and a large range of inexpensive components (light sources, connectors) are now readily available for the NIR and can be used in relatively small and cheap sensor schemes. An example of the realisation of an NIR FEWS sensor is described in Chapter 5 (section 5.2). Unfortunately, the results from that work showed insufficient sensitivity, most likely attributable to a low methane partitioning coefficient when using a PDMS cladding in seawater. Despite these disappointing initial results the FEWS technique merits further investigation in the future, using enhanced affinity polymers.

4.3.3. Surface Plasmon Resonance

4.3.3.1. Principle

The Surface Plasmon Resonance (SPR) phenomenon is widely used in the field of optical sensors to monitor refractive index variations of chemical or biological material near a metal film (e.g. Nylander et al., 1982; Zhang and Uttamchandani, 1988; Miwa and Arakawa, 1996; Nitkin et al., 1997; Homola, 2003; Smith and Corn, 2003; Mauriz et al., 2006; Le Person et al., 2008). In particular, SPR was used for the detection of gas molecules (Nylander et al., 1982; Miwa and Arakawa, 1996) and more recently for the measurement of a gaseous methane concentration at 1800 ppm level (Urashi and Arakawa, 2001).

SPR arises from the interaction of the incident light with plasmonic waves: a wave observed in free electrons at the interface between two materials of different dielectric constant (also called surface plasmons – SP) propagating at a metal / dielectric (non-conducting) interface (Figure 4.11). The excitation of a SP by optical waves (p-or TM-polarized light beam, i.e. parallel to the SP wave) results in the transfer of energy into the SP and a resonant absorption of the optical wave's energy. The surface plasmon propagation constant is very sensitive to variations in the refractive index (n_s) of the sample medium adjacent to the metal layer (Smith and Corn, 2003).

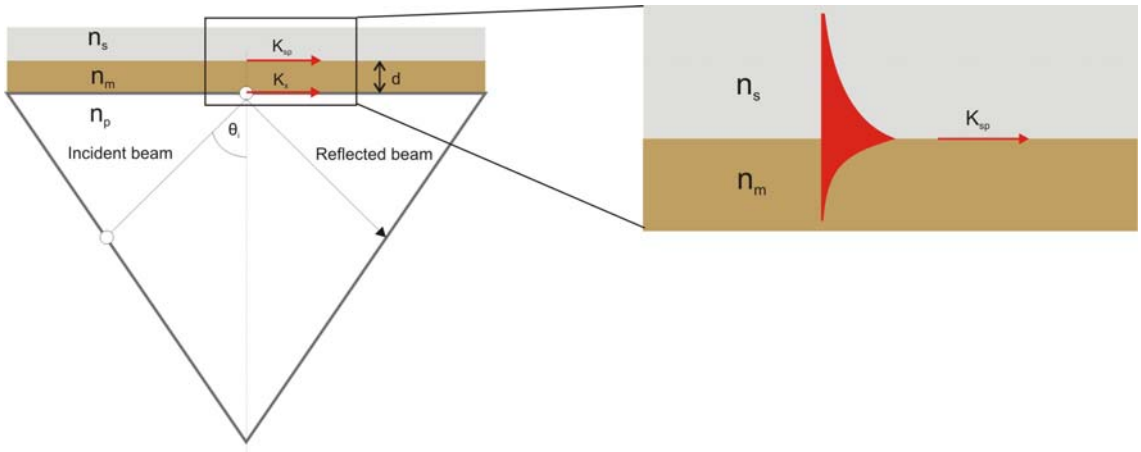

Figure 4.11: Excitation of the SPR via the evanescent wave and propagation of the plasmon field along the interface between the metal layer and dielectric media (modified from Homola et al., 1999).

In the configuration presented in Figure 4.11 (Krestchmann configuration, Kretschmann and Raether, 1963), visible light is directed through the prism and then reflected from the gold film. At resonance (i.e. excitation of the plasmons), the propagating vectors of both the surface plasmons and the electromagnetic waves are equal. The plasmons are represented by the dispersion relation for two homogeneous media (Smith and Corn, 2003; Nuster et al., 2006; Pitarke et al., 2007)

$$k_{sp} = \frac{\omega}{c}\sqrt{\frac{\varepsilon_m \cdot \varepsilon_s}{\varepsilon_m + \varepsilon_s}} \quad , \tag{4.13}$$

where k_{sp} is a wave vector of surface plasmons, ε_m and ε_s are the permittivity of the metal and dielectric sample media, ω the wave frequency, and c the velocity of light. The conversion of the incident wave to the SP wave is achieved by matching the projection of the wave number of the incident beam on the surface k_x to the surface plasmon wave

number k_{sp} at a specific combination of the incident frequency ω and the angle of incidence (or angle of resonance) θ:

$$n_p \frac{\omega}{c} \sin\theta = k_{sp} \tag{4.14}$$

When resonance occurs, energy from evanescent waves associated with the incident light is coupled into the surface plasmons causing a strong attenuation of the internally reflected light. The minimum in the intensity of the reflected light is observed at the angle of resonance. The resonant angle is extremely sensitive to changes in the dielectric constant of the adjacent sample medium, i.e. the refractive index, within the sensing distance of the plasmon field. Any change in the refractive index is therefore detected through the shift of the angular position of the plasmon resonance angle (Smith and Corn, 2003).

Surface plasmons have a maximum intensity in the metal film, and they decay exponentially in a perpendicular direction from the surface in both the metal and the dielectric layer (Ince and Narayanaswamy, 2006). The decay length of the SPs is dependent on the wavelength of the incident light and on the dielectric constants of both layers (Table 4.5).

Table 4.5: Major characteristics of surface plasmon waves at the gold-water interface (modified from Homola et al., 1999).
Any species that is farther from the metal film than the SP decay length will not effect the generation of surface plasmons (Smith and Corn, 2003). The use of longer wavelength light provides higher sensitivity, but lower lateral resolution.

Wavelength of the excitation light	630 nm	850 nm
Propagation length (μm)	3	24
Penetration depth into metal (nm)	29	25
Penetration depth into dielectric (nm)	162	400
Concentration of field in dielectric (%)	85	94

4.3.3.2. Sensitivity and selectivity of SPR measurements

The sensitivity of SPR measurements lies in the ability to detect very small changes in the refractive index of the medium close to the metallic layer and is described as the derivative of the angle of resonance with respect to the refractive index (Ince and Narayanaswamy, 2006). As shown in Table 4.4, better sensitivity of SPR measurements can be obtained at longer wavelengths. But the sensitivity also depends on the dielectric constant of the SP active layer, i.e. better sensitivity is obtained with a higher dielectric constant (e.g. silver) (Homola, 1997), and on the refractive index difference between the metallic layer and the adjacent medium. A greater difference between the refractive indices results in better sensitivity (Homola, 1997). SPR sensors are able to detect variations of refractive index down to 10^{-6} refractive index units (RIU) (Chinowsky et al., 2003). Hence, detection of very low concentrations of analyte is possible depending on the characteristics of the layer adjacent to the metal surface.

The selectivity of SPR measurements depends on the characteristics of the material deposited on the SP layer, i.e. the material has to be designed according to the analyte. In the case of methane, several studies (e.g. Benounis et al., 2005; Benounis et al., 2008) have shown variations in the refractive index of polymers (e.g. PDMS) in the presence of methane. However, these polymers are not necessarily selective and need to be chemically modified to increase the affinity for the analyte under investigation. In Chapter 5 (section 5.3) I will present a highly sensitive technique for methane (detection limits <0.2 nM) achieved by using a sensitive SPR sensor and an enhanced partition coefficient PDMS (attained by including an indicator in the polymer).

4.3.4. Methane biosensors

An electrochemical biosensor was developed in late 1990s based on immobilized methane-oxidizing bacteria for methane measurement in rice paddies (Figure 4.12 – Damgaard et al., 1995; Damgaard et al., 1998). Methane diffuses through the sensor tip membrane, made of silicon, and is oxidised by bacteria (Methylosinus trichosporium) with a concomitant decrease of oxygen inside the detection chamber (Damgaard et al., 2001). The variations in oxygen concentrations are measured by an internal oxygen

microsensor, and translated into a methane concentration by calibration (Damgaard et al., 2001).

This technique is insensitive to hydrogen, ammonia, and carbon dioxide. By contrast, hydrogen sulphide and oxygen do interfere with signals, although the oxygen interference can be overcome using of an oxygen guard electrode (Damgaard et al., 2001). These sensors are only designed for high methane concentration levels: however, the resolution is equivalent to aqueous concentration of 5 µM (Damgaard et al., 2001).

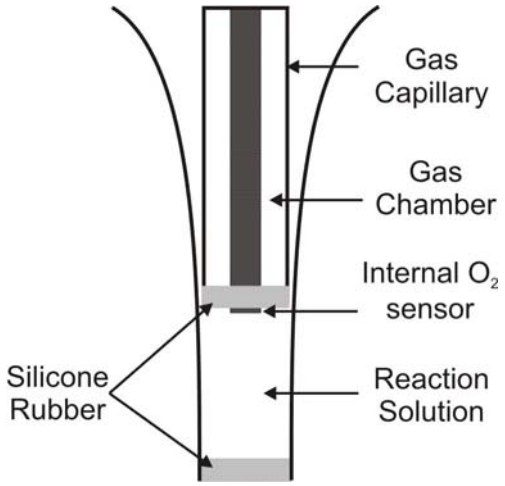

Figure 4.12: Methane biosensor (from Daamgard *et al.*, 2001)

4.4. Perspectives

Despite the high degree of interest in the scientific community for in situ methane sensing, only a few sensors have been developed, – with variable detection limits and performances – for aqueous environments, using different technologies, generally adapted from laboratory systems. With the exception of biosensors, all commercially available devices rely on measurement in the gas phase requiring the use of gas-permeable membranes to separate the aqueous phase from the measuring cell of the sensor. Although detection technologies (IR spectroscopy, MS) are well-established and competitive in terms of limits of detection and quality of data, the main limitation of these devices arises from reliance upon membranes, which remain poorly characterised and variable. In addition they have to be designed as a compromise between resistance to

high in-situ pressures and timely response; thick membranes will resist pressure but their permeability will decrease, ultimately increasing response time for any given sensor.

The recent advances in optical technologies, associated with the development of new, sensitive, and specific reactive layers represent a further step in the development of in-situ methane sensing. The main characteristic of these techniques is an ability to detect methane directly, in the aqueous phase without any gas extraction systems, using a sensitive interface whose optical properties are modified in the presence of methane. Surface enhanced Raman spectroscopy is one technique currently under investigation that offers promising applications but still suffers from limitations that could be more easily overcome by other optical techniques such as FEWS and SPR. It is these latter two techniques, therefore, that are tested in the next Chapter for the detection of dissolved methane in seawater.

CHAPTER 5: INVESTIGATION OF OPTICAL TECHNIQUES FOR THE IN-SITU MEASUREMENT OF DISSOLVED METHANE

5.1. Introduction

In Chapter 4, a review of current technologies for in-situ methane sensing was presented, highlighting the current interest in the development and use of optical techniques. In this Chapter, two of the optical techniques described earlier – Near Infrared Fibre-optic Evanescent Wave Spectroscopy (NIR-FEWS) and (indicator enhanced) Surface Plasmon Resonance (SPR) – are experimentally tested and the results presented.

For the first technique, the strategy was to allow dissolved methane to diffuse into a thin hydrophobic medium (PolyDiMethylSiloxane – PDMS) that had low optical absorption in the near-infrared and perform spectroscopic measurements on this material. The technique combined the extraction and enrichment of methane in the hydrophobic polymer coating of the optical waveguide with the direct IR absorption of methane in the polymer using the evanescent wave of the light transmitted in the waveguide (Burck and Sensfelder, 1999). The first part of the Chapter investigates the response of a FEWS sensor operating in the NIR to changes in dissolved methane concentrations, using silica waveguides, and low-cost optical components readily available from telecommunication industries.

The second scheme presented in this Chapter was developed based on the preliminary results obtained with the NIR-FEWS technique. Due to the selective inclusion of CH_4 into appropriate host molecules, a cryptophane-coated SPR sensor can be used as a compact methane sensor. The second part of this Chapter presents the concept of the methane sensor and the first results obtained in the laboratory: calibration for dissolved methane up to 300 nM; and detection limits <0.2 nM; and data from first in-situ deployments.

5.2. Fibre-optic Evanescent Wave Spectroscopy (FEWS)

This experiment was based on Buerck et al. (1996; 1998; 2001), in which a NIR-FEWS sensor had been developed for dissolved hydrocarbons in water (C6 to C8) at a low level of concentration (mg.L^{-1}). With this technique, Buerck et al. (2001) demonstrated that no frequent re-calibration was necessary as the sensor showed no drift of the absorbance values with time. However, the sensor had a long response time to changes in concentrations of hydrocarbons (~20 minutes) due to the long diffusion time of heavy HCs through the polymer, which should be reduced for lighter hydrocarbons, such as methane. Hence, the technique has the potential to be applicable to our needs.

5.2.1. Theoretical investigation

Based on the theory described in Chapter 4 (section 4.3.2), attenuation of light in the fibre can be calculated from the equation:

$$A_{fibre} = \log\left(\frac{P_{out}}{P_{in}}\right) \tag{5.1}$$

where A_{fibre} is the attenuation (no unit), P_{out} the power measured at the end of the fibre and P_{in} the power of light launched in the fibre.

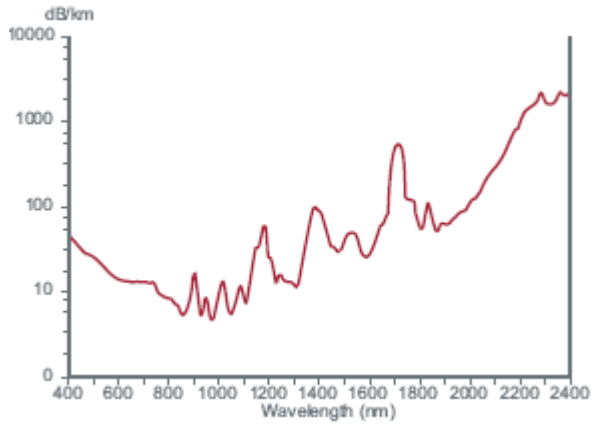

Figure 5. 1: Theoretical spectral attenuation in the Anhydroguide PCS low OH VIS-IR Fibre (from Fiberguide Industries)

Using Figure 5.1, $\log\left(\frac{P}{P_0}\right)$ can be determined and is equal to -0.008 for a wavelength λ = 1.6 μm. For low analyte concentrations, the absorbance can be approximated by a modified Beer-Lambert law (Buerck et al., 2001):

$$-\log\left(\frac{P}{P_0}\right) = \varepsilon_{CH4} \cdot \eta \cdot C_{CH4} \cdot l \tag{5.2}$$

with ε_{CH4} the molar absorption coefficient for methane, C_{CH4} the concentration of methane in the polymeric cladding, l the length of the effective evanescent wave interaction with the fibre (60 m) and η the refractive index of the polymeric cladding (1.41). ε_{CH4} was estimated from Buerck *et al.* (2001), by scaling the coefficient measured for larger hydrocarbons by the number of C-H bonds, as approximately 0.0023 m^{-1} mM^{-1}. Hence, substituting values into Eq. 5.2, the lowest concentration C_{CH4} detectable by this method would be $C_{CH4} = \frac{0.008}{\varepsilon_{CH4} \cdot \eta \cdot l} = 0.041\,\text{mM}$, i.e. 41 μM. In theory, even if one ignores anticipated losses due to termination and connection, this technique could never allow measurements of dissolved methane concentrations below a detection limit of 41 μM.

Considering our needs (detection at the nM level), this technique did not have the required resolution. However, the length of the sensitive part of the fibre plays an important role in the sensitivity of the technique. The aim of the following experiment, therefore, has been to validate the methodology for the detection of methane at the sub-μM level using a 60 m optical fibre, and to propose ideas to improve the method's resolution.

5.2.2. Materials and methods

5.2.2.1. Experimental NIR-FEWS sensor

The experimental sensor was built by coiling a multimode waveguide on a glass-fibre board modified to have a comb-like structure. The fibre was threaded through the teeth of

the board and the whole system was inserted inside a Teflon^{TM} cylinder, connected to the light source at one end and to the spectrometer at the other end (Figure 5.2).

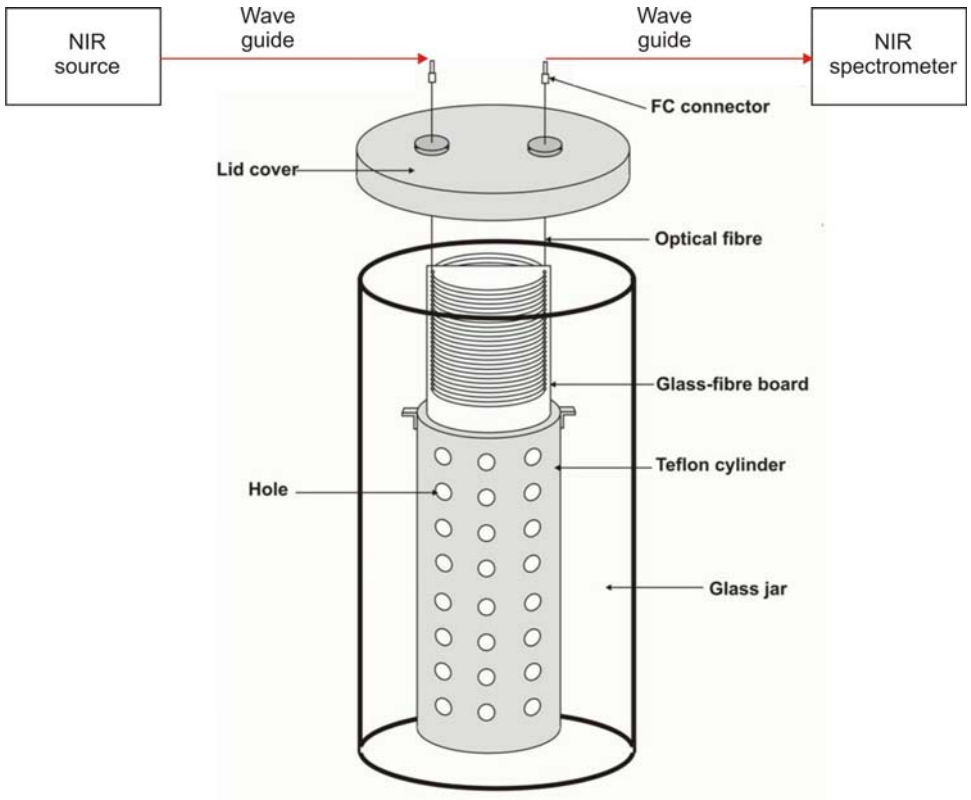

Figure 5. 2: Experimental NIR-FEWS sensor.
The fibre is coiled around a comb-like glass fibre plate and inserted inside a Teflon cylinder. The fibre is connected at one end to the light source and at the other to the IR spectrometer.

The optical fibre used here was a commercially available (FiberGuide Industries, USA) multimode polymer-clad silica (PCS) fibre with a low hydroxide quartz core of 210 µm diameter, surrounded by the nylon cladding, and operating in the visible-IR range of light (Figure 5.3). When the nylon jacket (20 µm thick) is removed (see below), the PDMS (PolyDiMethylSiloxane) cladding (10 µm thick) acts as a hydrophobic layer, which reversibly extracts methane from water (Toepke and Beebe, 2006). Hence, interactions between the light propagating in the evanescent wave and any methane penetrating into the cladding can be measured. Table 5.1 summarizes the characteristics of the waveguide.

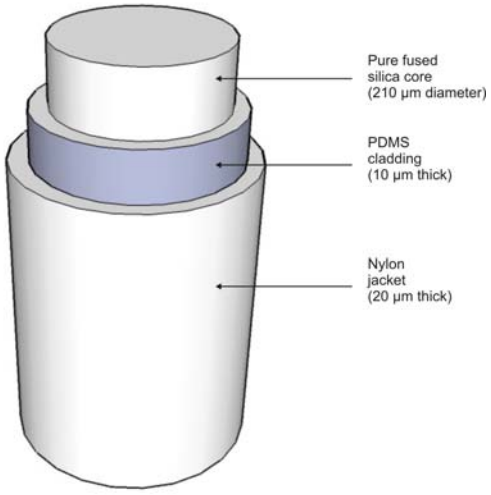

Figure 5. 3: Anhydroguide PCS low-OH vis-IR optical fibre

Table 5.1: Characteristics of the Anhydroguide PCS low-OH vis-IR optical fibre.
The attenuation represents the loss of light power through the fibre as a function of the wavelength.

APC210N	
Diameter core (µm)	210±2%
Diameter cladding (µm)	230±2%
Diameter jacket (µm)	270±5%
Temperature range	-40 – 100ºC
Attenuation at 1.6 µm	-8 dB/km

To turn the waveguide into a sensing element, it is necessary to remove the nylon protective jacket while avoiding the degradation of the PDMS layer (Buerck et al., 2001). To achieve this, the nylon jacket in the sensing region (i.e. the coil) was first dissolved in 1,2-propanediol at 160°C for 2 h. After cooling, the fibre was then rinsed with acetone and pure water. Approximately 1.5m at each end of the fibre remained unstripped. These unstripped ends were then attached to the lid and terminated with FC connectors (Ocean Optics®).

The light source is a Light Emitting Diode (LED 16 – Lambda Photonics®), designed to emit at a spectral range centred on 1650 nm, where a band of methane absorption lines exists (see Chapter 4, Fig. 4.4).

The NIR absorption measurements were performed with a commercially available grating spectrometer Ando aq6135A (resolution 0.05 nm). Light was launched into the waveguide by butt-coupling the LED to the fibre-optic cable terminated end of the waveguide. The position of the LED was adjusted whilst observing the power at the terminal end to maximise the launch efficiency. The sensing part (the coil) was then immersed in synthetic seawater of varying CH_4 concentration and variations in the output light were measured with the spectrometer (Figure 5.2).

5.2.2.2. Experimental set-up

Experiments for detection were performed at room temperature and atmospheric pressure by dissolving pure gaseous methane (Air Products® – UK) until a high concentration was reached (~300 μM verified by headspace extraction and gas chromatography), in artificial seawater (35 mg/L) prepared from degassed Q-water (18.2 MΩ cm) and NaCl (analytical grade).

Two systems were built, one, a reference fibre, with a long (60 m) unstripped and terminated optical fibre and one with a long (60 m) stripped and terminated optical fibre. Light spectra were acquired for both systems in methane saturated seawater and degassed seawater. A very short unstripped fibre (5 cm) was also prepared to measure, experimentally, the magnitude of light losses that might arise, both due to coupling and along the length of the fibre, at 1650 nm.

5.2.3. Results and discussion

An initial comparison between spectra recorded with the short unstripped fibre and the long unstripped fibre shows a difference of 10.89 dB (Figure 5.4). Compared with the data given by the manufacturer at 1.6 μm (-80 dB/km or -0.08 dB/m, Figure 5.4), this represents a loss of light of -0.198 dB/m, i.e. 2.5 times higher than the value expected. The actual attenuation A_{fibre} was therefore -0.02 dB.

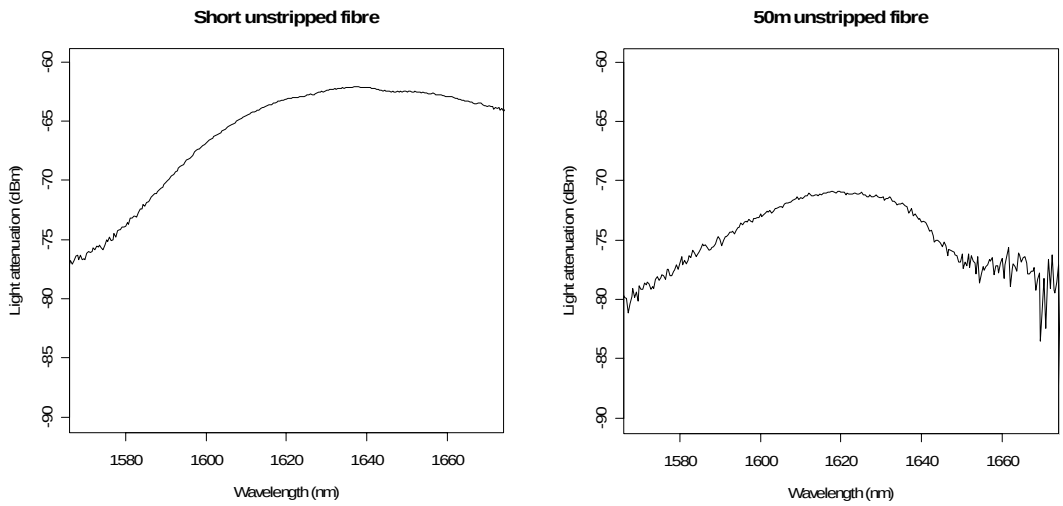

Figure 5.4: Light losses in the optical fibre

By replacing theoretical attenuation with the actual measured value in Eq 5.2 the lowest concentration detectable was in fact increased to

$$C_{CH4} = \frac{0.02}{\varepsilon_{CH4} \cdot \eta \cdot l} = 0.102 \text{ mM, i.e. } 102 \text{ µM.}$$

Despite the high losses observed from this first experiment, tests of dissolved methane detection were still performed, because the CH_4 concentration in our system was above 300 µM. Comparison of the stripped and unstripped long-fibre spectra (Figure 5.5) does not show any absorption of light in the 1.6 µm area, where a methane absorption band occurs.

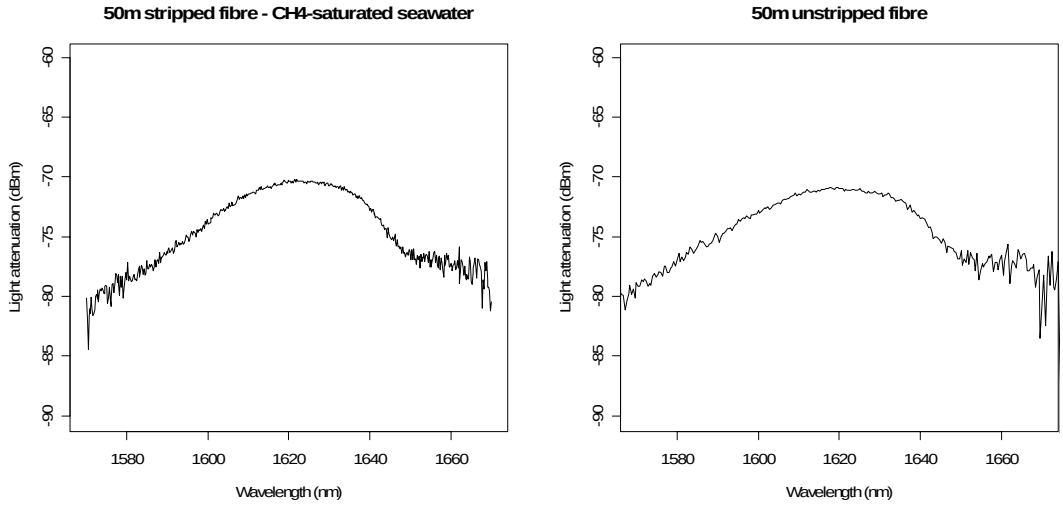

Figure 5.5: Results of methane detection tests

Our calculations, above, show that losses of light at the termination and connection cannot fully account for the absence of any signal in the stripped 60m fibre, when compared to the unstripped fibre, while the actual concentration of methane in the laboratory system was ~300 µM. The non detection of methane in this set up could be explained by the partition coefficient of PDMS for methane. The partition coefficient *K* is calculated as follows:

$$K = \frac{C_p}{C_w} \tag{5.3}$$

where C_p and C_w are the concentrations of methane in the PDMS and in the water respectively (Hylton and Mitra, 2007).

PDMS has a low partition coefficient for methane (1.30), which is a characteristic of dissolved hydrocarbons gases (Abraham and Matteoli, 1988). On the other hand, the partition coefficient for higher hydrocarbons is >4 (Hylton and Mitra, 2007), which means that better extraction into the PDMS is achieved for heavy hydrocarbons. In fact the enrichment factor for low-solubility compounds (e.g. heavy hydrocarbons) is higher than for high-solubility analytes (e.g. methane) (Hylton and Mitra, 2007). The enrichment of the PDMS is driven by the gradient of concentration between the aqueous phase and the PDMS, which is limited by the partition coefficient.

Hence, according to Eq. 5.3, for a given concentration in the aqueous phase, enrichment into the PDMS will be more efficient for compounds with high partition coefficient than for those with low partition coefficient. For a concentration in the aqueous phase of 300 µM and a K = 1.3, the expected concentration in the polymer is 390 µM. On the other hand, for the same concentration but with K = 4, the concentration in the polymer would be 1200 µM, which would create a much steeper gradient between the different phases and absorption into the PDMS would, therefore, be better.

5.2.4. Conclusions

The sensor developed by Buerck et al. (2001) was well adapted for the detection of heavy hydrocarbons in water but is limited for dissolved HC gases, essentially due to the low

partition coefficient of methane into PDMS. Compared with the typical concentrations found in deep-sea environments (1 nM to 10 μM in hydrothermal plumes), this technique, both theoretically and experimentally, does not currently have either sufficient resolution or a low enough limit of detection for practical applications.

Nevertheless, in-situ methane evanescent wave sensors using enhanced reactive (indicator) layers have shown promising results elsewhere (Culshaw et al., 1992; Culshaw et al., 1998; Benounis et al., 2005; 2008) in terms of both sensitivity and optical properties of the layer. In the work of Benounis et al. (2005; 2008), enhancement of the reactive layer has allowed for better partitioning of methane into the PDMS. This results in a large change in RI, which, in turn, enhances sensitivity. The optical properties of this reactive layer are described in the next section and are used in a quite different sensor scheme.

5.3. Cryptophane enhanced indicator with Surface Plasmon Resonance detection

The development of supramolecular chemistry (i.e. chemistry of "van der Waals" molecules) together with polymeric materials has provided new opportunities for advanced sensing of dissolved gases in aqueous environments (Collet et al., 1993; Bartik et al., 1998; Benounis et al., 2008). Among synthetic supramolecules, cryptophane-A can be considered as a molecular receptor for methane, showing interesting optical properties when included in an optically transparent polymer. Benounis et al. (2005) have shown that the specific absorption of gaseous methane in cryptophane-A, incorporated in an organic transparent cladding, led to an increase in the refractive index of the polymer that is proportional to the amount of encapsulated methane. This property was used, previously, to enhance the performance of evanescent wave optical fibre sensors for the detection of methane in air (Benounis et al., 2005) and the detection of gases in oil-filled transformers (Benounis et al., 2008). Thus, the refractive index of the polymer may be considered as a proxy for methane concentration.

The change in the refractive index measured by Benounis et al. (2005) was large enough to suggest that detection by surface plasmon resonance (which is more sensitive than the optical fibre technique) could provide a resolution better than 1μM. The recent development of low-cost, portable, and sensitive SPR sensors (i.e. Spreeta®, Chinowsky

et al., 2003) has allowed the implementation of SPR sensing directly in the field. The technique is promising, therefore, for in-situ sensor implementation.

5.3.1. Background

Cryptophanes are synthetic organic compounds with a cage-like structure resulting in a lipophilic cavity that is able to completely encapsulate substrates of specific molecular size (Gabard and Collet, 1981; Collet et al., 1993). Holman, 2004) described these molecules as the first molecular 'container'. The presence of the cavity makes cryptophanes particularly suitable for complexation of neutral molecular species (Garel et al., 1993; Souteyrand et al., 1996; Holman, 2004).

The general structure of cryptophanes is given in Figure 5.6. A molecule of cryptophane is made of two cyclotriveratrylene (CTV) units, i.e. cup-shaped, C_3-symmetric, orthocyclophane units, assembled by three bridges (Z) (Collet, 1996). The cavity volume is determined by Z functionalities, the external properties are dependent on the X and Y groups.

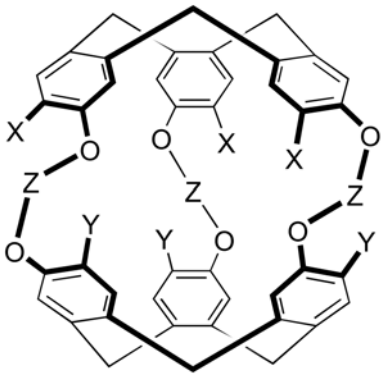

Figure 5.6: General structure of cryptophanes (from J-P. Dutasta, *pers. comm.*)

The construction of a cryptophane molecule was reported by Canceill et al. (1987), Collet (1987), Canceill and Collet (1988), Cram et al. (1991), Collet et al. (1993), and Holman (2004), and can be accomplished via three methods: i) the 'template method', ii) the "two-step method', and iii) the 'capping method'. The three methods, based on aromatic substitution reaction and depicted in Figure 5.7, use vanillyl alcohol (3,4-disubstituted benzyl alcohol) as a starting material (Canceill et al., 1987). The apertures of the cavity are determined by the nature of the substituents X (Holman, 2004).

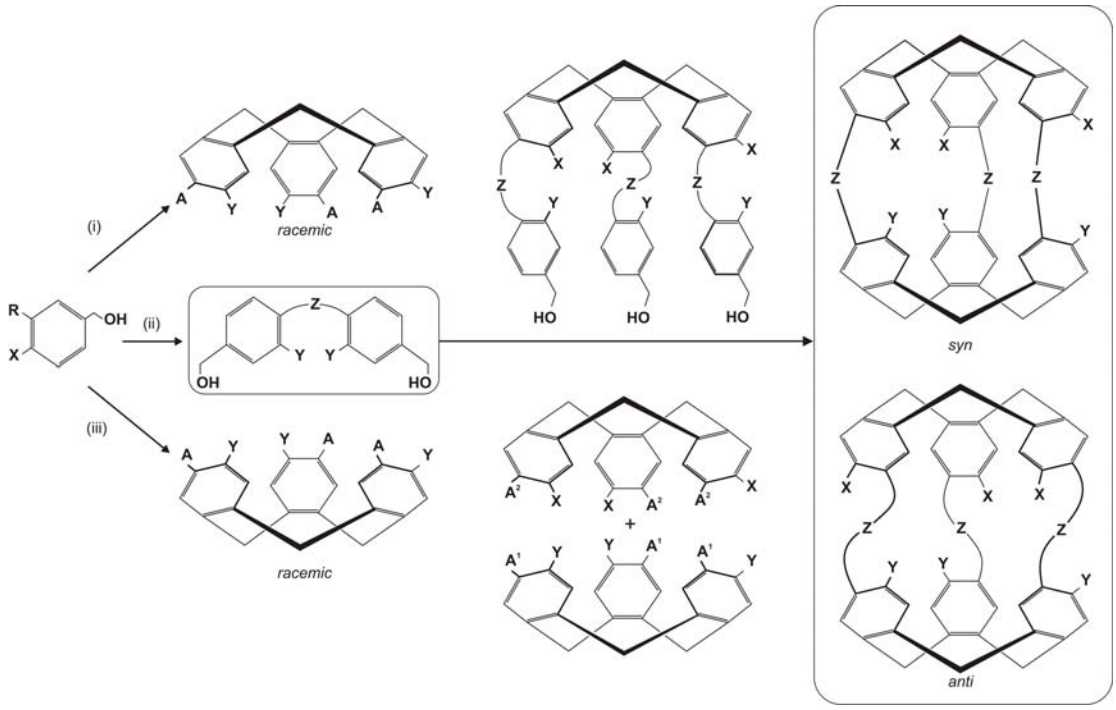

Figure 5.7: Synthesis of cryptophanes.
(i) Template method. (ii) Two-step method. iii) Capping method. From Holman (2004).

Following these methods, several species of cryptophanes have been synthesized (Holman, 2004) with different molecular structures (number of bridges, substituents, stereochemistry,…) and properties. The nomenclature of the cryptophanes is based principally on the chronology of their description, e.g. the first member of the family was named cryptophane-A (Collet, 1987). Table 5.2 summarizes the first described cryptophanes, possessing complex-forming abilities and shows the principle of nomenclature.

Table 5.2: First described cryptophanes possessing demonstrated complex-forming abilities (modified from Holman, 2004)

Structure			Name	
Bridges (Z)	**X**	**Y**	***anti***	***syn***
3 x $O(CX_2)_2O$, X=H/D	OCX_3	OCX_3	A	
	OCH_2CO_2H	OCH_2CO_2H	A3	
	OCH_3	H	C	D
3 x $O(CH_2)3O$	OCH_3	OCH_3	E	F
	OCH_2CO_2H	OCH_2CO_2H	E3	

One of the smallest of the series, cryptophane-A (Figure 5.8) (Gabard and Collet, 1981), has an internal cavity suitable for accommodating small volatile compounds such as methane, chlorofluorocarbons (Garel et al., 1993) or xenon (Bartik et al., 1998) (Figure 5.9). Guests smaller or larger than the optimal volume are bound less effectively, and those that are too large to occupy the cavity are not complexed (Collet, 1996). The cryptophanes can effectively differentiate guests on the basis of volume differences of <5%.

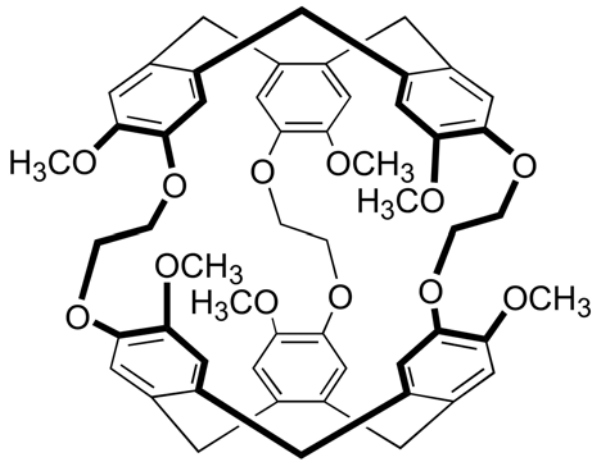

Figure 5.8: Cryptophane-A (from J.-P. Dutasta, *pers. comm.)*

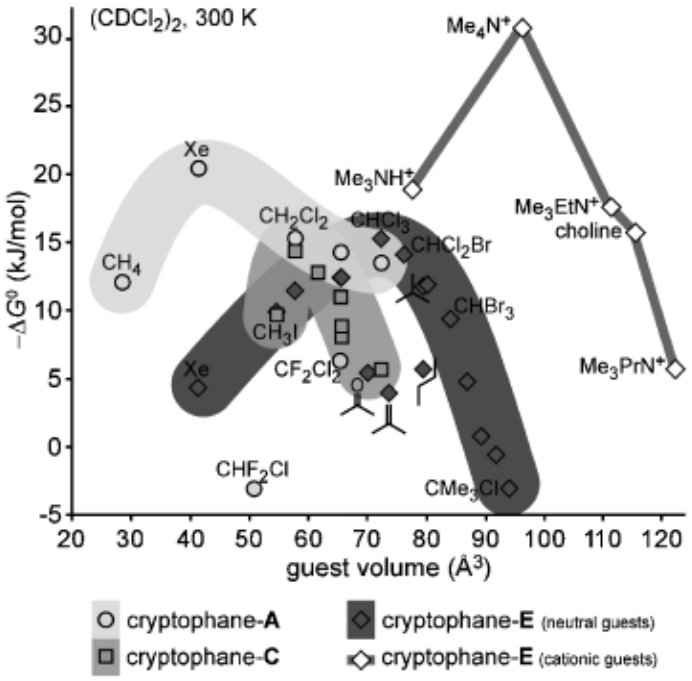

Figure 5.9: Gibb's molar free energies of complexation for various cryptophane-guest complexes at 300K, from Holman, 2004

In solution, cryptophane-A exhibits a strong affinity towards methane characterized by a constant association of 130 M^{-1} at 295 K, in $(CDCl_2)_2$ (Garel et al., 1993). Only one methane molecule is reversely bound to a cryptophane-A host, which has a spherical cavity of 81.5 Å (Garel et al., 1993). The occupancy factor in that case is 0.348. The complex cryptophane-A – CH_4 has a half-time ($t_{1/2}$) of 6 10^{-6} s at 298K and 9 10^{-3} s at 199K (Garel et al., 1993).

Once included in the cavity of a cryptophane-A molecule, methane behaves as an integral part of the host, being bound by weak van der Waals interactions (Figure 5.10 – Garel et al., 1993; Tosner et al., 2004). The interior of the complex can be compared to a supercritical fluid, in which the methane molecule behaves like a small sphere colliding with the walls of the cavity for a few microseconds before escaping (Garel et al., 1993).

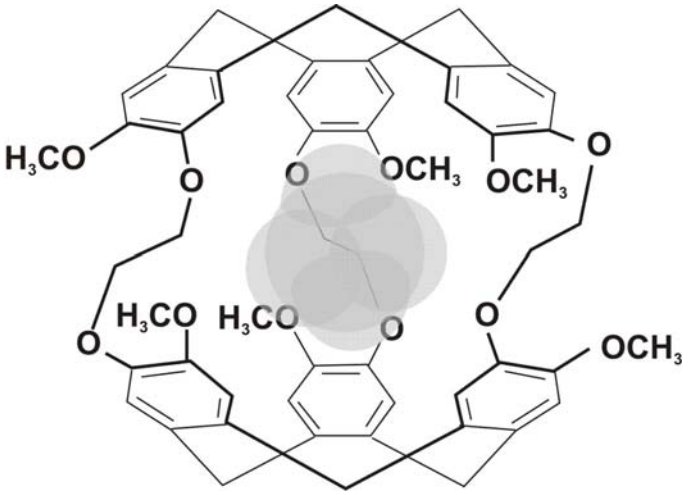

Figure 5.10: Structure of the cryptophane-A – CH_4 complex. Spheres indicate the van der Waals radii of the guest.

Since the early 1990s, the development of supramolecular compounds has opened a large field for sensor applications, especially due to their ability to encapsulate guest molecules, based on a 'key-lock' system (Souteyrand et al., 1996). Souteyrand et al. (1996) studied the behaviour of cryptophane-A in a gas medium to determine the feasibility of using cryptophanes as new chemical receptors in gas sensor schemes. It appeared that the use of specific sensing layers including cryptophane-A led to a specific and sensitive response to the presence of gas, and, further, that the strength of that response was a function of the quantity of gas present in the environment.

In parallel, the progress in the elaboration of gas-permeable silicon polymers, such as PDMS has opened new perspectives in the design of gas sensors. Benounis et al. (2005; 2008) showed that the specific absorption of gaseous methane in cryptophane-A, incorporated in an organic transparent polymer, led to an increase of the refractive index of the polymer proportional to the amount of encapsulated methane. The change in the refractive index can be explained, readily, by the formation of the host-guest complex, which is optically less transparent than the host alone.

5.3.2. Experimental methane sensor

5.3.2.1. Instrumentation

The SPR methane sensor is based on the association of a polymer sensing film and a SPR Spreeta® chip, a low-cost, low-weight, and low-power electronic system, developed by Texas Instruments® for environmental applications (Chinowsky et al., 2003). The SPR kit used in this work included the SPR sensors, a 12-bit analog to digital sensor control box, sensor cable, AC adapter, PC serial communications cable, and software.

The Spreeta® contains all of the optical components necessary for SPR sensing and is designed to be manufacturable in very large quantities (Chinowsky et al., 2003). The device measures 30 x 15 x 40 mm, weighs ~7g and provides electrical connections using a 16-pin DIP connector (Figure 5.11). Current input is < 500 mA when the LED is on, < 5 mA when off and the operating voltage is 6V. Table 5.3 lists the different steps involved in the construction of the SPR sensor.

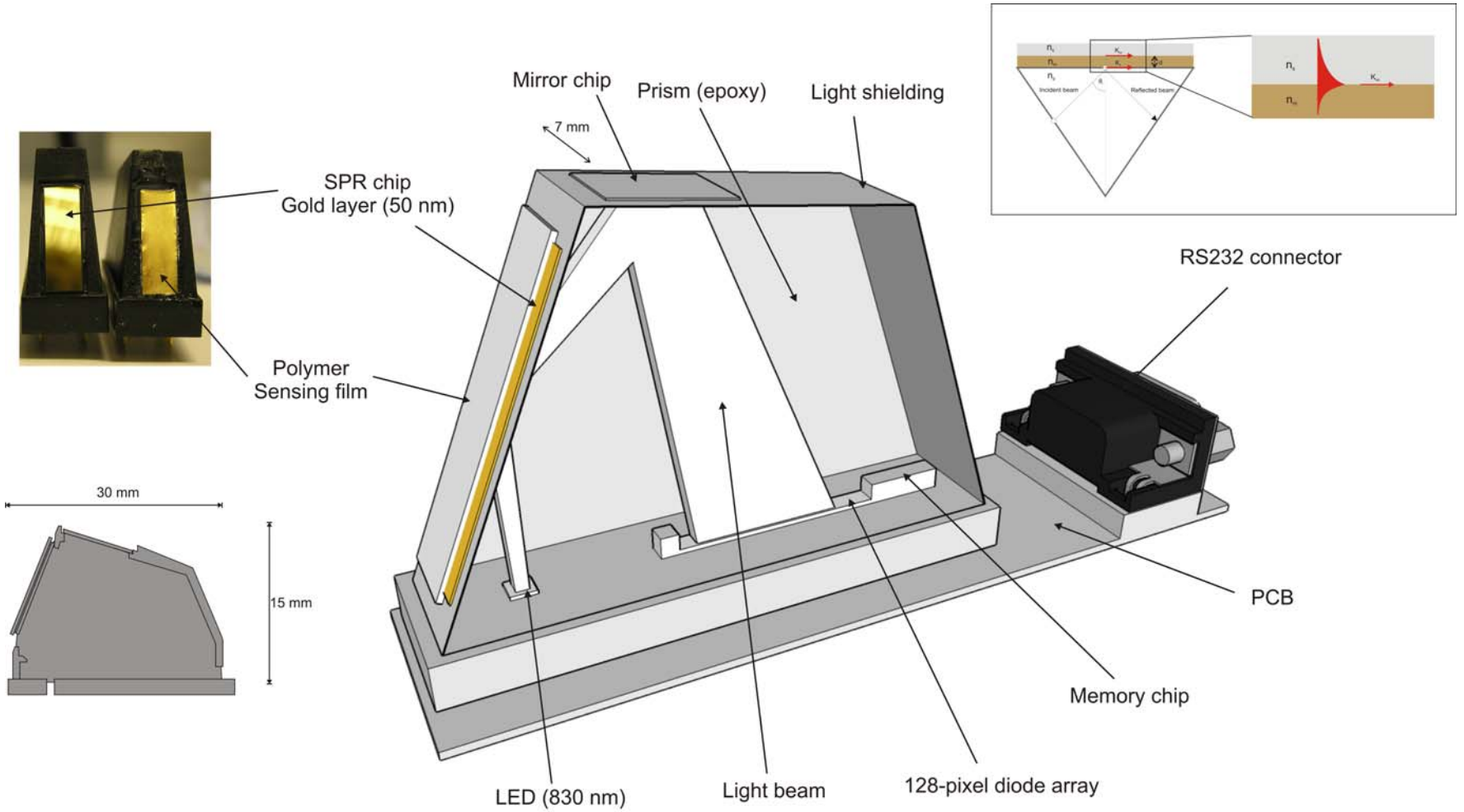

Figure 5. 11: Methane sensor incorporating a Spreeta chip and the sensing layer.

The Spreeta chip is shaped in a Kretschmann configuration recalled in the top-right box.

Table 5. 3: Manufacturing steps for production of Spreeta (from Chinowsky et al., 2003)

1	Wire bond LED, photodiode array, memory chip to sensor PCB
2	Test LED, photodiode array, memory for functionality
3	Injection-mold clear polycarbonate sensor prism
4	Inject black polycarbonate to form light shielding surrounding prism
5	Attach polarizer to sail using epoxy
6	Attach sail to PCB, using pins on sail and clear epoxy
7	Add black epoxy to complete light shielding
8	Attach mirror to upper prism surface using epoxy
9	Attach SPR chip to sensor surface using epoxy
10	Test LED, photodiode array, memory for functionality
11	Measure sensor spectra in air and water

The Spreeta® sensor contains an 830 nm AlGaAs Light-Emitting Diode (standard LED), a polarizer, a thermistor, a 128-pixel photodiode detector, and a non- volatile memory chip for data recording (Figure 5.11). All components are placed on a small printed circuit board (PCB) and encapsulated in a clear, optical epoxy prism (RI = 1.52), molded to have optically flat surfaces and shaped in a Kretschmann configuration (Kukanskis et al., 1999). A description of this configuration as well as the theory of SPR was given earlier in Figure 4.11 (Chapter 4). A mirrored surface is thermally evaporated onto the upper surface of the sensor. The surface plasmon layer (SPR chip) is a gold-coated glass slide modified with a 10-20 Å chrome adhesion layer evaporated onto the surface, followed by the evaporation of 50 nm of gold onto the chrome. The SPR chip is placed on the sensing side of the Spreeta® (over a thin layer of refractive index matching epoxy).

Light is passed through an aperture in the light source housing and is polarized. The beam is then directed through the epoxy prism onto the gold surface, with a limited range of incident angles. The light is reflected off the gold film and mirror and then projected onto the linear silicon photodiode detector array (Figure 5.11). The active area on the sensor surface is defined by the portion of light cone which projects on to the detector, and is a strip 0.2 mm wide by 4.5 mm long (Spreeta® datasheet).

The software (MultiSPR V10.78, Windows compatible), provided by Texas Instruments™, determines the refractive index measurement versus time from the angle

of resonance. Here, the SPR curve refers to as a plot of signal magnitude vs. pixel position on the array. Figure 5.12 shows an example of an SPR curve for water obtained with Spreeta®.

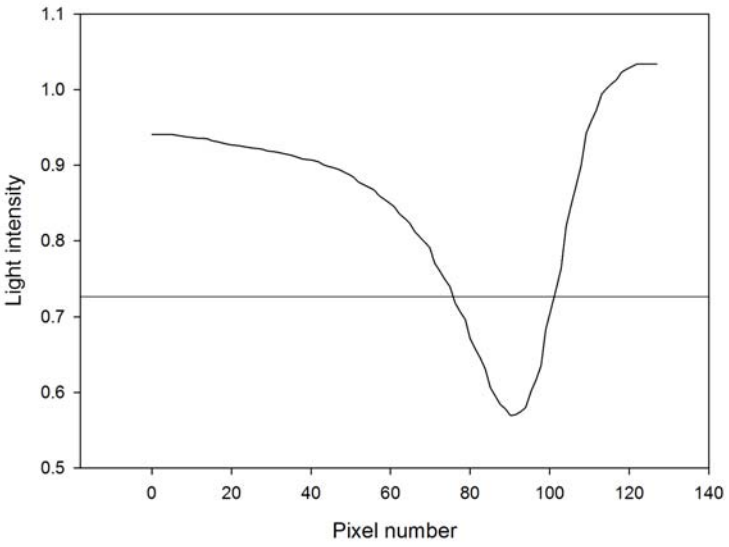

Figure 5.12: SPR curve for water obtained with Spreeta.
The minimum in light intensity is localized on pixel #92.

All the reflectance intensities are recorded by the pixels in the photodiode array. Each pixel is read individually and the pixel at which the reflectance is a minimum is then converted to an angle via a quadratic equation.

The Spreeta® sensor can sense very small changes in the refractive index of the material above the gold layer depending on the operating conditions, i.e. number of averages, stray light level, and analysis method (Chinowsky et al., 2003). The noise given by the manufacturer is 3 10^{-7} RIU (refractive index units) while monitoring a stable liquid over time, under conditions using 16 averages, no smoothing, the sensor enclosed in an opaque container, and utilizing the first-moment analyzing method. Three dominant factors intrinsic to the SPR sensor contribute to the noise observed: detector noise, shot noise and LED fluctuations (Chinowsky et al., 2003). Although the manufactured components have intrinsically low noise (Chinowsky et al., 2003), it is necessary to optimize the sensor performance by choosing an appropriate integration of signals as well as the RI measurement-time.

In fact several software parameters have to be set to ensure low system noise in the final data points (Kukanskis et al., 1999). To obtain one data point, the usual set-up is to average several SPR curves (integration). In our setup, one data point was taken from each by SPR curve. The second step is to set up the frequency of measurement, i.e. the minimum monitoring interval (the time to operate the sensor and to analyze the result). The frequency of measurement was adapted to be the same as the integration time, i.e. 30 to 50 ms. Then, the method to calculate the refractive index from the SPR curve was chosen. Five possible analysis methods are available to analyze the SPR curves: 1) first-moment of resonance (i.e. the first moment that the SPR curve is above or below a threshold); 2) the pixel number at which the SPR curve reaches a specific value; 3) the polynomial fitting to find the minimum position of the resonance; 4) determining where the first derivative of the SPR curve passes through zero as the position of the resonance minimum; 5) dot product of the SPR curve with its derivative. The first method was used as it requires only a single variable (i.e. light intensity) and provides the lowest noise. The threshold of light intensity was fixed at 0.72, i.e. there is resonance when the light intensity is below 72%. The First Moment was calculated by the software from the SPR dataset in the array as follows:

$$FirstMoment = \frac{\Sigma_{i=1}^{128}\left(i \times \left(threshold - DATA(i)\right)\right)}{\Sigma_{i=1}^{128}\left(threshold - DATA(i)\right)}, \tag{5.4}$$

5.3.2.2. Sensing layer

The sensing film (SF) was made of modified PolyDimethylSiloxane (PDMS), a transparent polymer with a refractive index of 1.412, loaded with a solution of cryptophane-A. The polymer was prepared from 1 mL of Siloprene K1000 mixed with 0.15 mL of cross-linking agent K11 (both supplied by SigmaAldrich). A solution of cryptophane-A, prepared from 20 mg of cryptophane-A (which comes as a powder) dissolved in TetraHydroFuran (THF, SigmaAldrich), was then mixed with the polymer. The molecules of the solvent are too large to be encapsulated by cryptophane-A. With this mixture, it was possible to coat 3 to 5 Spreeta® chips. Proportions of chemicals were adapted according to the number of sensors to be prepared.

Cryptophane-A powder was provided by the Laboratoire de Chimie de l'Ecole Normale Supérieure de Lyon. The synthesis of cryptophane-A followed the two-steps method, as described earlier (Canceill and Collet, 1988).

The mixture polymer-cryptophane, referred to as the sensing layer, was deposited on the gold chip of the SPR sensor by drop-coating and dispersed following the method described in Urashi and Arakawa (2001). After 10 to 15 minutes, the solvent was completely evaporated, leaving a homogeneous and thin polymeric layer. Figure 5.13 depicts a coated and a non-coated sensor. Layer thickness was measured by digital microscopic photography. Thicknesses obtained with this technique were usually between 50 and 100 μm. The sensing layer thickness does not influence the intrinsic response of the sensor (i.e. the formation of the complexes) but affects the diffusion of the dissolved gas through the polymer, hence influences the response time. The thicker the film, the greater the time required for methane to diffuse to the active gold surface.

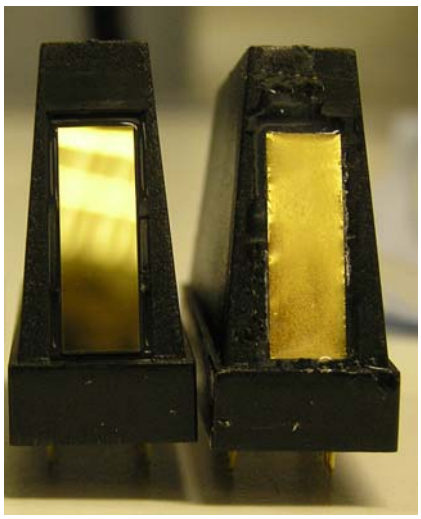

Figure 5.13: Non-coated (left) and coated (right) Spreeta chips.

5.3.2.3. Data treatment. Summary

Table 5.4 summarizes the general procedure for SPR measurements. Details on specific methodologies are given in the following sections. The sensor output was treated as a time-series and decomposed by a 30s moving window average method (Brockwell and Davis, 1986).

Table 5.4: Steps for SPR measurements

	Steps	Comments
1	Initialization of the Spreeta in air	SPR Curve = Sample signal / air reference
2	Calibration in water	SPR curve of water (must be 1.333)
3	Polymer coating	RI ~1.41
4	Calibration of the methane sensor	Use the calibration system and control by GC measurements
5	Monitoring (lab or in-situ)	Control of the response by water sample uptake
6	Post calibration or baseline in Q-water	

5.3.3. Experimental set-up

The first experiments (detection, reversibility, and first calibration of the sensor) were performed at room temperature and atmospheric pressure by dissolving 20 ppm methane gas in artificial seawater (35 mg/L) prepared from degassed Q-water (18.2 MΩ cm) and NaCl (analytical grade), as illustrated in Figure 5.14. The system was enclosed in a glove bag to control the environment around the experimental set-up and to prevent from possible outside contamination. The glove bag was filled with regular air. Seawater samples were taken at regularly timed intervals and analysed by headspace gas extraction followed by gas chromatography (see Chapter 2). The highest concentration obtained with this set-up was 50 nM after 2h of bubbling. To test the reversibility of the response, the sensor was dipped in N_2-purged seawater maintained at an equal temperature ([CH_4] = 5 nM).

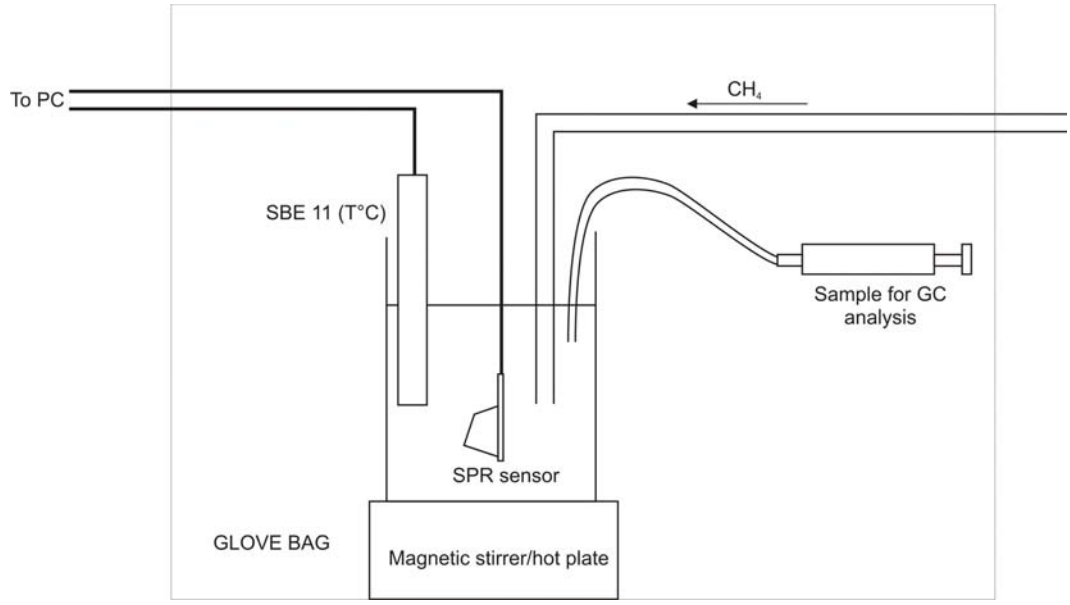

Figure 5.14: Experimental set-up for the initial experiments. Temperature was monitored using a Seabird SBE 11 temperature probe.

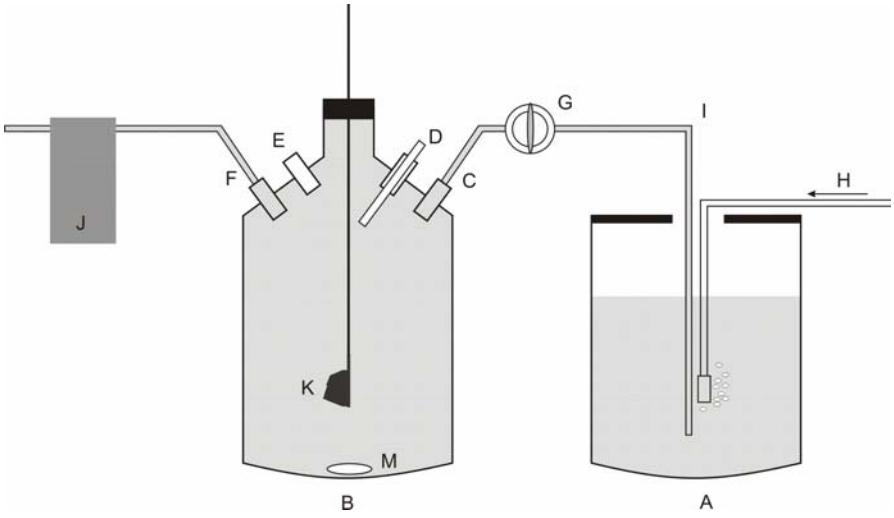

Figure 5.15: Schematic representation of the gas calibration system.
A: saturated solution reservoir, B: measurement cell, C: outlet connector, D: temperature probe, E: sampling port, F: outlet pump connector, G: valve, H: pure methane gas, I: glass tubing, J: pump, K: SPR sensor, M: magnetic stirrer adapted from [Sosna et al.].

The second set of experiments were carried out in a dissolved gas calibration system, adapted from Sosna et al. (2007) and illustrated in Figure 5.15. The principle consists of sequential replacement of an initially low methane-concentration solution (in closed vessel B) with volumes from a higher concentration solution drawn from reservoir (A), followed by homogenization (via stirring) after each addition. Following each incremental step of fluid addition and homogenization, sensor output values were recorded and averaged for 2 minutes. The calculated concentration in the cell was dependent on the number of replacements (i), the concentration of methane in the reservoir (C_{sat}), the volume exchanged (V_{ex}) and the volume of the measuring cell (V_{tot}), which remained constant throughout. After the *i*th addition, the methane concentration was:

$$c_i = c_{i-1} + \frac{c_{sat} V_{ex}}{V_{tot}} - \frac{c_{i-1} V_{ex}}{V_{tot}} \tag{5.5}$$

Eq. 5.5 was used to construct calibration plots that included a very large number of points due to the small volume displaced by the pump (50 µl). The system was post-calibrated at the end of the experiment by analysing water samples using headspace gas extraction followed by gas chromatography. For all experiments, temperature was recorded independently by accurate temperature probes (0.01ºC).

Several sensors were tested using both experimental setups in order to compare their responses to changes in dissolved methane concentration. The first sensor made was used for the preliminary experiments, whose aim was to validate the concept. Subsequent sensors were prepared in the same way but with a thinner reactive layer (~50 µm) to optimize the response time.

5.3.4. Results

5.3.4.1. Temporal response

The first sensor was dipped alternately in a degassed (5 nM) and in a more concentrated, 50 nM,dissolved CH_4 solution. The responses to changes in dissolved methane concentration are presented in Figure 5.16. Also shown, for comparison, are the

equivalent responses of a Spreeta® chip coated with a non-sensitive polymeric layer. A significant response can be observed for the methane sensor, whereas the RI of the non-sensitive polymeric layer did not change despibeing exposed to the same variations of dissolved methane concentration.

The response time (t_{90}) between low concentration (5 nM) and high concentration (50 nM) was 1.8 minutes, i.e. 2.4 sec.nM^{-1}. Although the response time to decreasing concentrations was longer (~6.6 sec.nM^{-1}), this hysteresis effect was shown to be reduced by stirring as shown by the step-like change at the C:D boundary in Figure 5.16. Stirring increases the concentration gradient between the sensing layer and the water which readily explains the observed response.

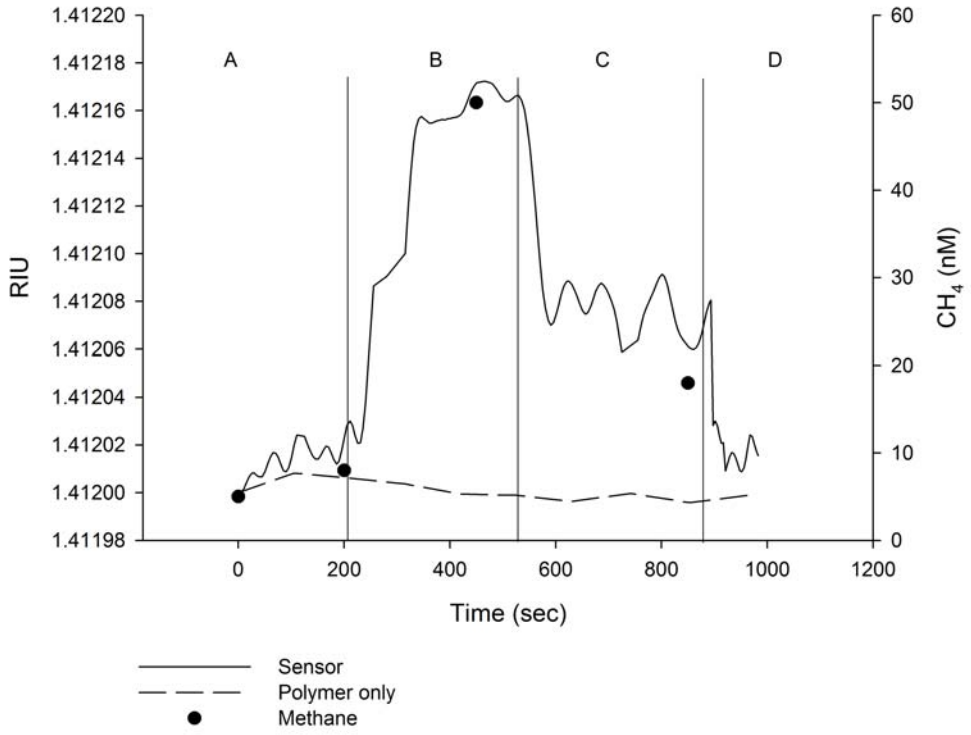

Figure 5.16: Response of the sensor due to changes in dissolved methane concentration compared with the response of the Spreeta chip coating with a non-sensing layer.
A: in degassed solution, B: in 50 nM CH_4-solution, C: in degassed solution, D: in degassed solution with mixing.

The response of the sensor is not controlled by the absorption-desorption of methane by cryptophane-A, which only takes only a few milliseconds to form the complex methane-cryptophane-A (Garel et al., 1993), but by the diffusion of the dissolved gas through the

polymer to the gold surface. This diffusion occurs following Fick's law (Schaetzel et al., 2001):

$$J = -D\frac{\partial C}{\partial x} \tag{5.5}$$

where J is the diffusion flux, D the diffusion coefficient, C the concentration of the diffusive molecule, and x the diffusion length.

5.3.4.2. Water absorption

The sensing layer exhibits strong water absorption, as shown in Figure 5.17, which is a common characteristic of PDMS-like polymers (Schirrer et al., 1992; Shioda et al., 2003). The sensing layer required immersion for ~10 minutes to stabilize the signal before methane measurements could be made.

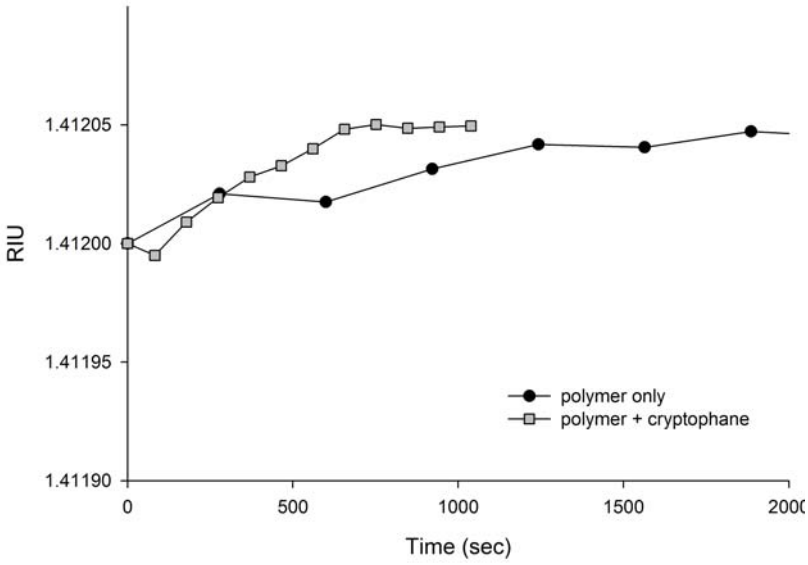

Figure 5.17: Water absorption effect.

5.3.4.3. Sensitivity

Figure 5.18 (a) shows the results of sensor calibration using the gas calibration system. The system was soaked for 15 minutes in the water before the first measurement was performed to eliminate the effects of water absorption on the sensor output and, hence,

the calibration. A good relationship was observed between methane concentration and the RI of the sensing layer (R^2=0.9885). Previously Benounis et al. (2005) reported that variations of the RI were dependent on the quantity of methane present in the media. The sensitivity calculated from our calibration curve is 5.5 10^{-6} RIU/nM. Several calibration curves (Figure 5.18 (b) and Figure 5.19) were obtained under varying experimental conditions (direct bubbling or dissolved calibration systems), with an averaged R^2 of 0.95, highlighting the reproducibility of the sensor output.

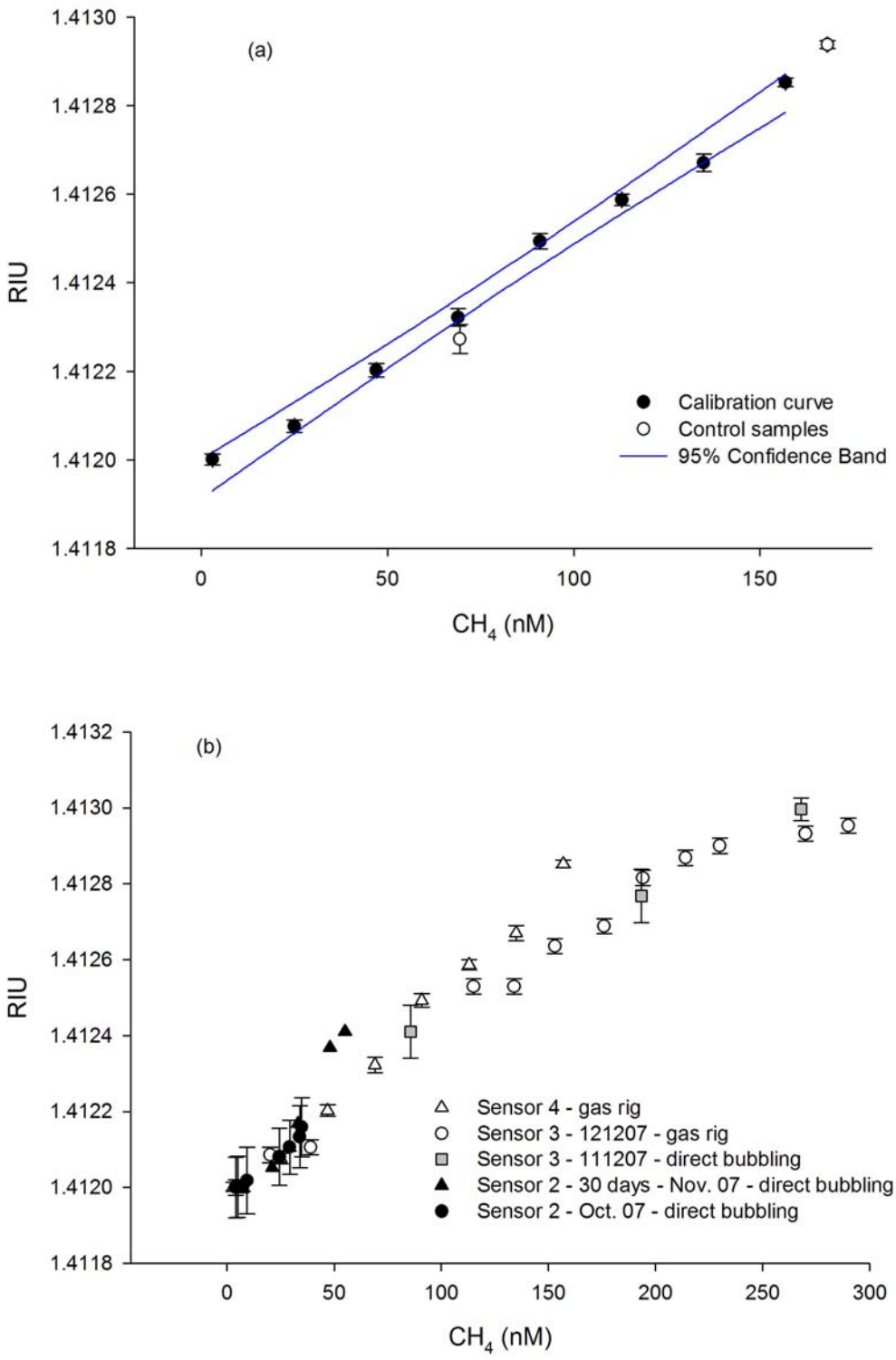

Figure 5.18: (a) Calibration curve obtained with "sensor 4" using the gas calibration rig (filled circles). Data were linearly fitted (R^2=0.9885). (b) Calibration curves obtained in different experimental conditions (direct bubbling and gas calibration rig).

Filled circles: sensor 2 (direct bubbling); filled triangles: sensor 2 – 30 days (direct bubbling); grey squares: sensor 3 (direct bubbling); opened circles: sensor 3 (gas rig); opened triangles: sensor 4 (gas rig). Errors bars are 2 times the standard deviation on RI measurement. Samples (opened circles) were taken for control.

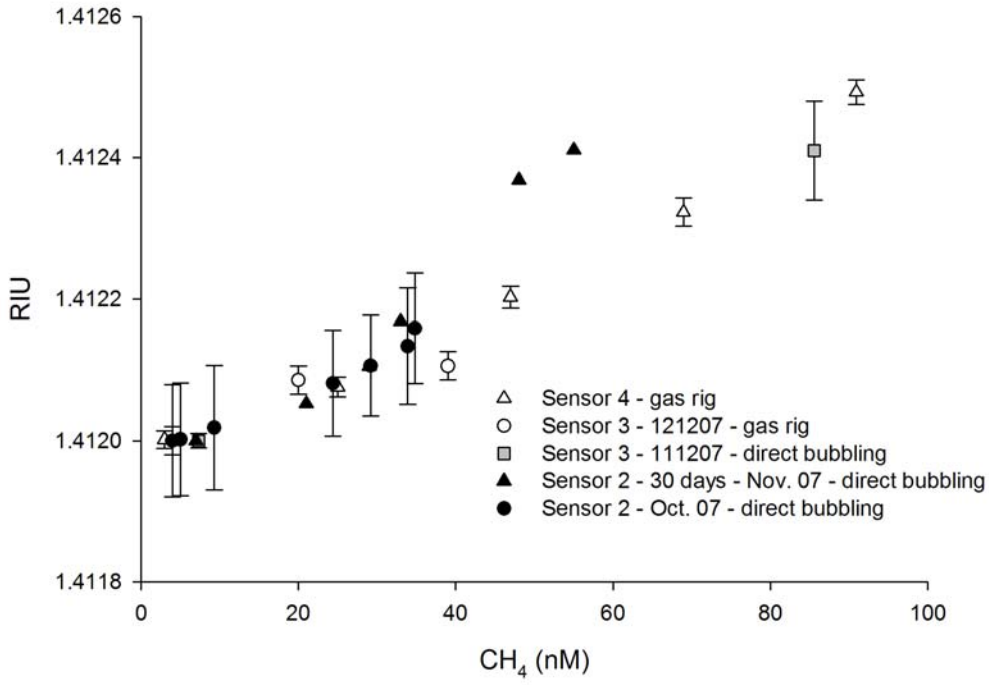

Figure 5.19: Calibration curves obtained in different experimental conditions (direct bubbling and gas calibration rig).
Filled circles: sensor 2 (direct bubbling); filled triangles: sensor 2 – 30 days (direct bubbling); grey squares: sensor 3 (direct bubbling); opened circles: sensor 3 (gas rig); opened triangles: sensor 4 (gas rig) (zoom on the 0-100 nM range).

Table 5.5 gives a comparison of the sensitivities obtained for a number of different sensors of the same design but with subtly varying sensing layer properties (due to manufacturing tolerances). With the exception of "sensor 2 – 30days", calculated sensitivities were all in the same range (3.2 to 5.5 10^{-6} RIU/nM), emphasizing the reproducibility of the coating process. Reduced sensitivity could be the result of a lower quality of the sensing film due to either the process of coating or the degradation of the layer over time. Contrary to Benounis et al. (2005), where the sensing film was stable for several months, it was noted that the sensing film detaches from the Au surface in our instruments overtime when used in seawater. To counter this effect, the sensing layer was replaced every two weeks.

Table 5.5: Sensitivity, noise and detection limits

	Calibration system	Sensitivity (10^{-6} RIU/nM)	Calibration curve R^2	Noise (10^{-6} RIU)	Detection limits (nM)
Sensor 1	Direct bubbling	7.8	0.906	10	1.28
Sensor 2	Direct bubbling	4.7	0.979	8	1.70
Sensor 2 – 30days	Direct bubbling	9.4	0.945	10	1.06
Sensor 3	Direct bubbling	3.7	0.985	7	1.89
Sensor 3 - 48h	Direct bubbling	4.5	0.921	7	1.56
Sensor 3 - 72h	Gas rig	3.2	0.949	0.9	0.28
Sensor 4	Gas rig	5.5	0.988	0.9	0.16
Manufacturer				0.1	

5.3.4.4. Noise, detection limits, and operation range

Sensor noise places a limit on the concentration of dissolved methane detectable by the sensor (Chinowsky et al., 2003). To correct for this, the noise for each sensor was calculated from the standard deviation of the measurement (3σ) during stable conditions (lowest concentration of methane and temperature). Results are given in Table 5.5. In our experiments, the integration time of SPR measurements was automatically chosen by the software during the initialization of the sensor and the RI measurement frequency was adapted to be the same as the integration time. The lowest noise level measured with our sensor was found to be 9 10^{-7} RIU (3σ – sensors 3 and 4). The noise level also depends on the experimental conditions as highlighted in Table 5.5. The highest noise levels were obtained using the direct bubbling calibration system, which produced strong concentration gradients and agitation of the sensing layer, hence, a high noise level.

Although detection limits should be calculated from blank measurements (i.e. in the presence of no methane – Currie, 1997), for these experiments they were obtained from the noise levels measured in the sample with the lowest methane concentrations

achievable in our laboratory, i.e. stable conditions. An estimate of these detection limits is given in Table 5.5 for each sensor. When using the calibration apparatus, which reduced the experimental noise level, the detection limit was 0.16 nM (3σ). This is the first time that such low detection limits have been achieved for any dissolved methane sensor.

Calibrations show a good linear relationship with dissolved methane concentration up to 180 nM. The response of the sensor to concentrations between 180 and 300 nM is still reproducible despite a lower sensitivity. At methane concentrations greater than 300 nM, the calibration curve plateaus revealing a possible saturation of the sensor. The encapsulation of methane into cryptophane is a reversible process that depends on the equilibrium between the aqueous phase and the polymer. Saturation of the cryptophanes will therefore be related to the quantity of methane present in the aqueous solution and the association constant (K_a). Variations in the thickness and roughness of the polymer sensing layer would not affect this saturation but would affect the temporal response of the sensor by modifying the rates of diffusion through the polymer.

5.3.4.5. Influence of temperature and salinity

Figure 5.20 displays the effect of temperature on RI measurements for the polymeric layer (i.e not loaded with Cryptophane-A) and the sensitive layer: the RI is inversely proportional to temperature. From these results it is evident that a high variation of temperature strongly influences the signal (2.35 10^{-5} RIU/°C) but it is unclear whether temperature influences the density of the polymer or the sensor performance itself. Changes in temperature modify the density of the polymer (i.e., number of C-H bonds per volume unit) and therefore the RI (Klunder et al., 1994). Spreeta® chips are also dependent on temperature variations as they have no active temperature control and need to be calibrated for the temperature effect (Chinowsky et al., 2003). Future developments will require a detailed characterization of the temperature effect on the operating device. Once these effects have been characterized measurement of water temperature will enable compensation and hence improved sensor accuracy. For the majority of applications in the environment one could argue that temperature changes are not expected to be rapid, and/or widely varying. However, further experiments are required

to study the sensor output when operated in different temperature ranges, as it might affect the K_a of the complex cryptophane-methane formation.

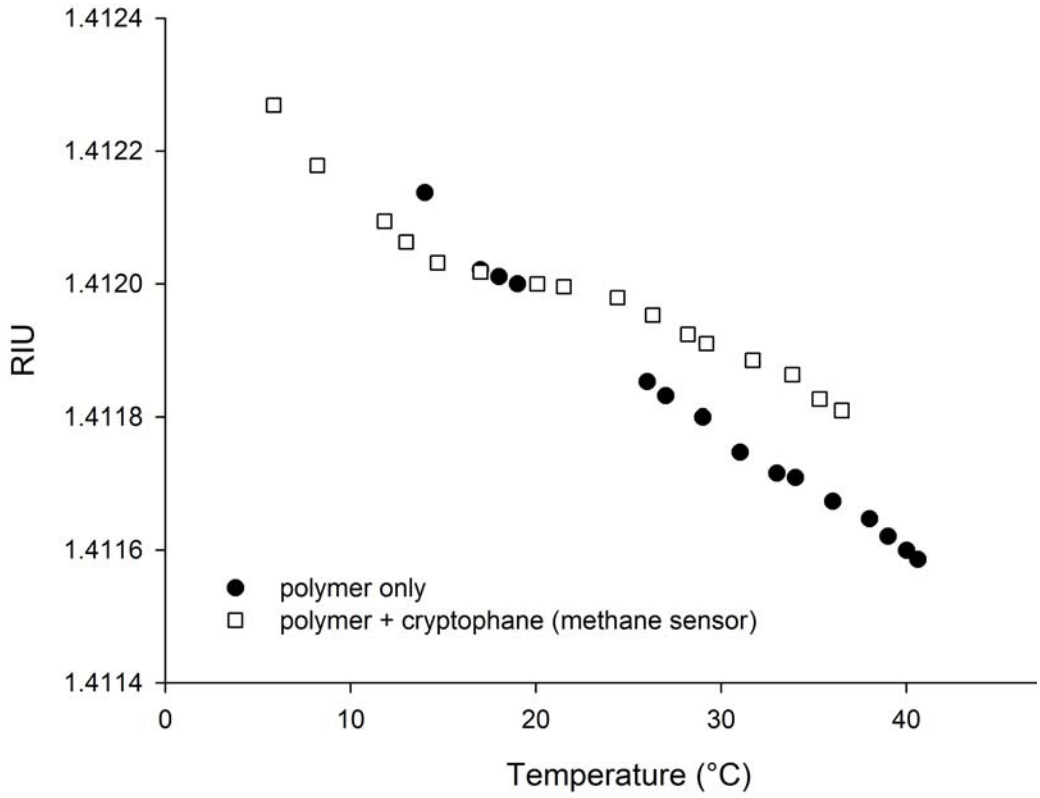

Figure 5.20: Temperature effect on the sensor response compared with the response of a non-sensing layer

As the future sensor will operate in various conditions (from fresh water to marine environments) the effect of salinity on the sensor operability and response was tested. This was done by adding increasing concentrations of NaCl to the test apparatus to obtain varying salinities (0, 5, 10, 20, 25, 30, 35 and 40 PSU) whilst measuring the RI of the polymer. The salinity does not influence the RI of the coating (Figure 5.21) as no significant RI changes were recorded.

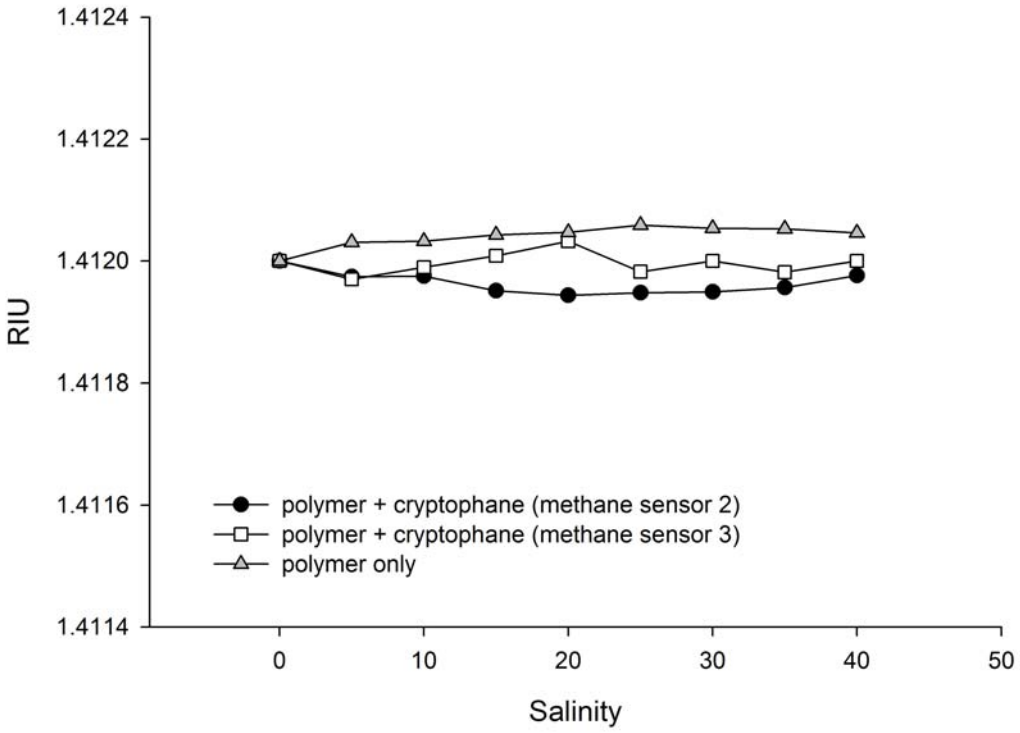

Figure 5.21: Salinity effect on the sensor response compared with the response of a non-sensing layer

5.3.5. First in-situ deployments

5.3.5.1. Methodology

To allow in-situ deployment of the sensor developed for laboratory-based experiments, the system was encapsulated in an epoxy potting, as depicted in Figure 5.22. All the electronic components were protected against water infiltration. Only the sensing layer was in contact with water.

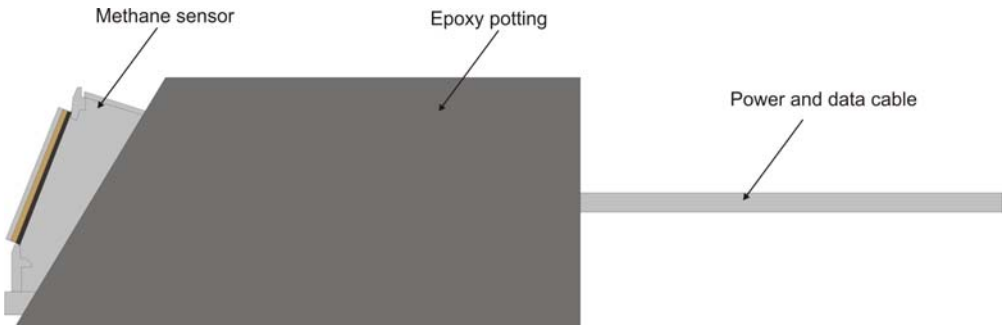

Figure 5.22: Scheme of the methane sensor for in-situ deployments

Before deployment, standard calibration curves were generated in the laboratory, as described earlier, and a baseline was acquired in artificial seawater. The sensor was left in water until deployment to counter the water absorption effect and allow stabilisation of the signal.

The sensor was deployed at ~1m depth from the dedicated pontoon for sensor development at NOCS, and data acquisition was continuous over a tidal cycle. At 1h intervals, samples (3 replicates) were taken for gas chromatography analysis to check the sensor output. The temperature of the water was recorded using a Seabird SBE-11 to correct the signal for any temperature effect. Data were acquired for at least 6 hours (tidal cycle) and analysed as a time-series. After recovery, the sensor head was rinsed thoroughly and dipped in pure seawater in order to get a baseline and check the instrumental drift.

The methane sensor was deployed 4 times (13/02, 14/02, 25/04, and 08/05/2008) in a tidal, estuarine environment, highly influenced by human activities (Figure 5.23).

Figure 5.23: Location of the sensor station (GoogleMap)

5.3.5.2. Field measurements

Figure 5.24 shows the response in nM of CH_4 of the sensor based on laboratory calibrations, corrected for the temperature effects, and compared with point-sample concentrations measured by HS/GC (solid dots). The sensor output, filtered and corrected for temperature effects is shown in red. The temperature record is depicted in grey. Note the change in the concentration scale for the measurements of the 08/05/08.

From these results, it is clear that the methane sensor responded to variations in methane concentrations over time. The concentration range measured by the sensor and confirmed by the samples (15-420 nM) is typical of estuarine, tidal environments where values from 5 to 600 nM can be found (Bange et al., 1994; Middelburg et al., 2002; Upstill-Goddard et al., 2000). Highest concentrations were measured during periods of high turbulence (due to strong winds, currents, and activity around the sensor station), creating a strong mixing of the water column (4-8 m deep). Upstill-Goddard et al. (2000) noted previously that turbidity of the water column and methane concentrations can be related in estuarine environments. For example, CH_4 may be released from anoxic underlying sediments during active particle resuspension and it is important to note that turbulence was strong on the 8th of May (highest concentrations of methane) due to high winds (25-30 knots) and high tidal currents. An alternative possibility, however, is that high measured methane concentrations might arise as a result of in situ CH_4 production in the water column, i.e. bacterial attachment to tidally trapped suspended particles could provide a vehicle for enhanced methanogenesis (Scranton, 1977; Upstill-Goddard et al., 2000). In Spring, the accumulation of organic materials in estuarine sediments is enhanced by phytoplanktonic blooms and the biological activity in general (Bange et al., 1994), which can enhance the sedimentary CH_4 production (Bange et al., 1998).

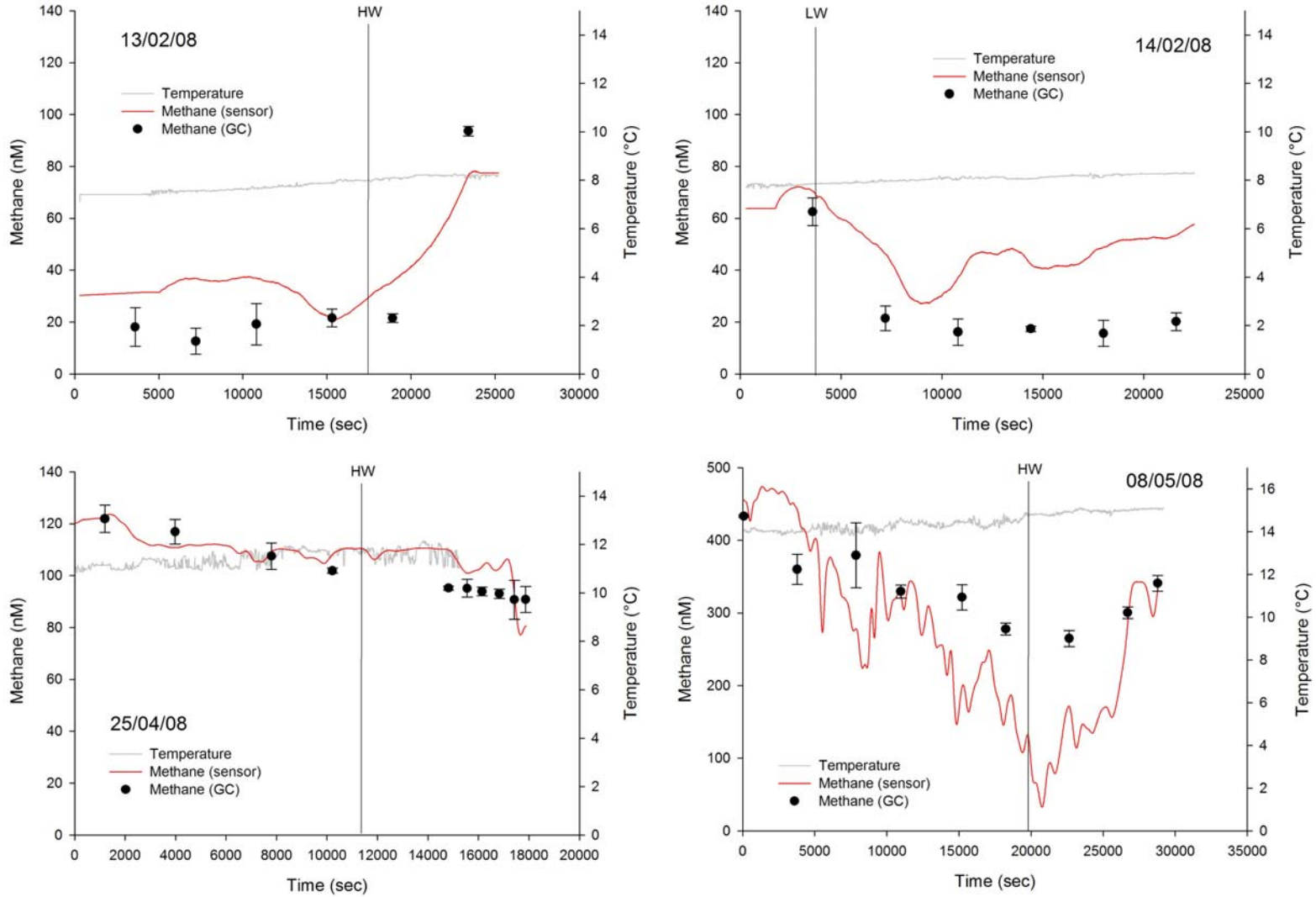

Figure 5.24: Responses of the methane sensor (converted to nM) during in-situ deployments in a dock environment.

Red plain line: calibrated sensor output corrected from temperature; black dots: methane concentrations (GC); grey line: temperature data; HW: high Waters; LW: Low Waters. Error bars: 3 times the standard deviation on methane measurements. Note the change in scale for methane concentrations.

The response of the sensor, corrected for any temperature effect using the temperature calibration performed in the laboratory, was coherent with the concentrations measured in the samples and the trend observed over time (Figure 5.24), although some differences were noted on the 14/02/08 and the 8/05/08 . Temperature variations were <1°C over the deployment, which are equivalent to a variation of 3 10^{-5} RIU, or 0.3 nM. These results show that the technique developed in the laboratory is suitable for monitoring dissolved methane in aqueous environments.

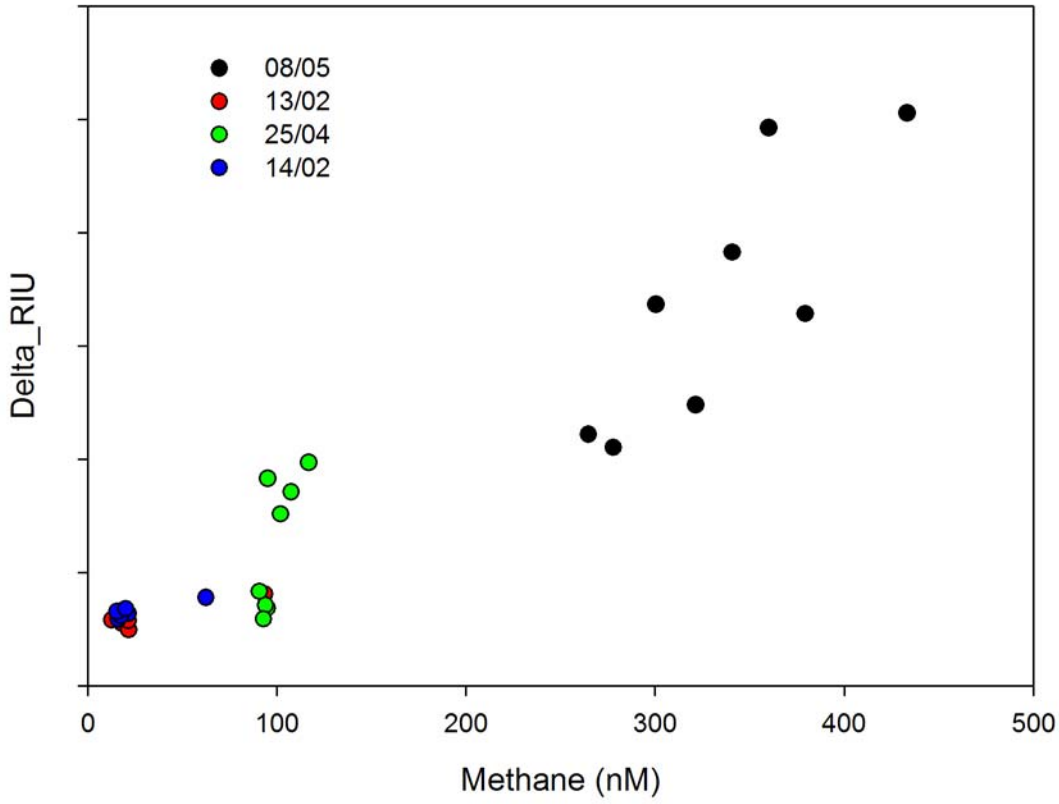

Figure 5.25: Methane data (GC) vs. sensor output for each deployment. R^2(13/02) = 0.864; R^2(14/02) = 0.807; R^2(25/04) = 0.584; R^2(08/05) = 0.677.

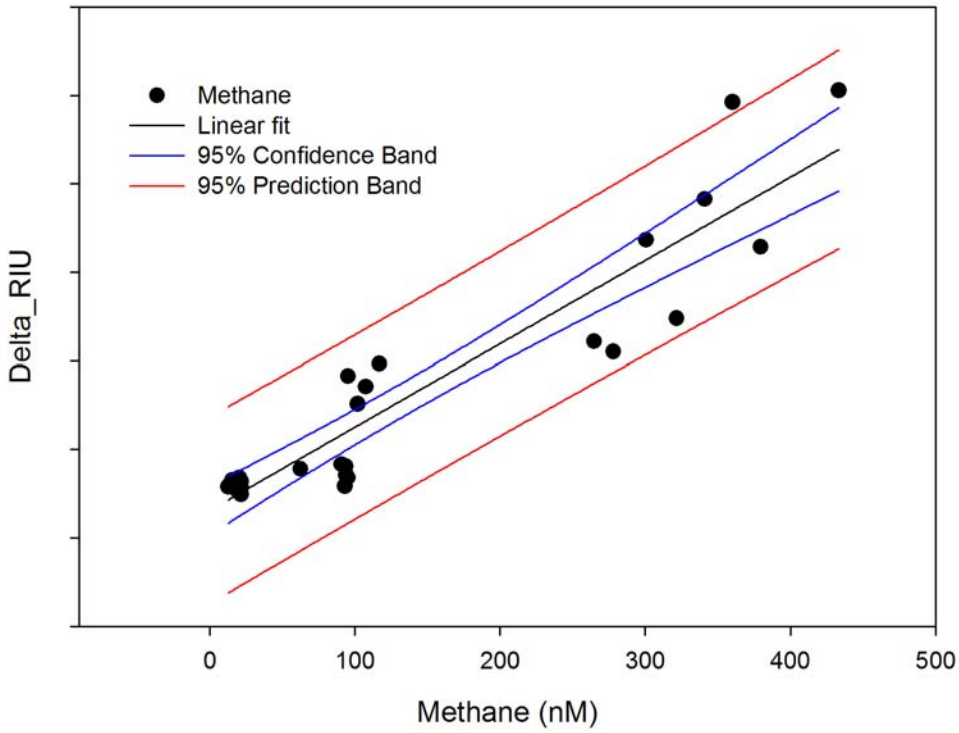

Figure 5.26: Methane data (GC) vs. sensor output for all deployments. The linear fitting is given with a R^2 of 0.872.

However, as depicted in Figures 5.25 and 5.26, correlations between sensor output and sample concentrations are not as good as measured in the laboratory (R^2=0.584 to 0.864). Several factors can explain this result and need to be tested and taken into account for further deployments:

- *Calibration:* the calibration of the sensor was performed in the laboratory at room temperature (20°C). Water temperature during the deployments varied from 7°C (13-14 Feb 2008) to 14 °C (25 Apr. and 8 May), which influenced the baseline level. Calibration was corrected for temperature but it might be necessary to calibrate the sensor at the operational temperature.

- *Noise level:* experiments in the laboratory showed that the sensor was sensitive to the environmental noise. Using the gas calibration system without direct bubbling allowed a dramatic reduction of the noise. During deployments in real conditions, the noise level was very high. The sensor output was disturbed by the waves and the movements of boats around the sensor platform in the NOCS dock (Figure 5.27), which influenced the sensitivity of the sensor. For further experiments, it

will be necessary to design a housing that will protect the sensitive layer from such noise (e.g. with a stop flow flow-head) and, hence, enhance the performance of the sensor.

- *Cross-sensitivity:* some studies have shown an affinity of cryptophane-A for NH_3 (Schramm et al., 1999; Rathgeb et al., 2000) which could influence the response of the sensor. Cross-sensitivity experiments need to be performed to evaluate the response of the sensor, not just to ammonia/ammonium, but also to other species with affinity for cryptophane-A that might be present in the environment.

- *Behaviour of cryptophane-A in the polymer/degradation of the sensitive layer:* no studies have been performed yet on the behaviour of cryptophane-A while in seawater for several hours. Hence, a specific characterization of the time-series stability of cryptophane-A as well as the sensing layer needs to be conducted.

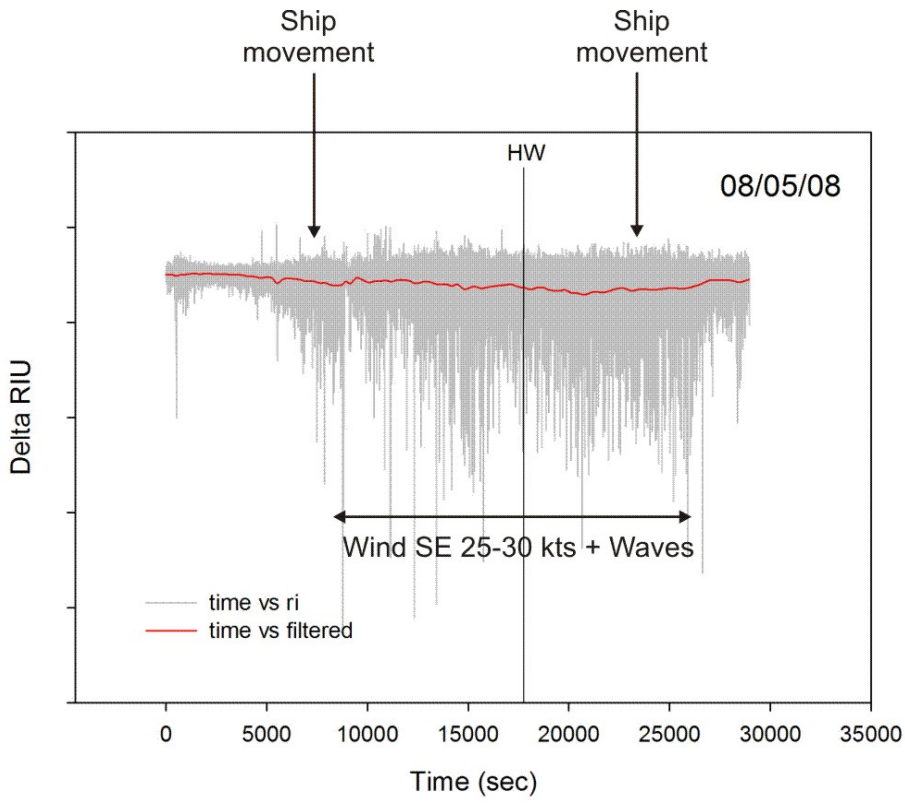

Figure 5.27: Raw sensor output and filtered output in relation with possible noise sources. #

5.3.6. Conclusions

A novel high sensitivity method for the determination of dissolved methane concentrations has been presented. Results obtained in the laboratory show that the method is suitable for miniaturisation and incorporation into in-situ sensor technology. The method is based on refractive index modulation of a PDMS layer loaded with cryptophane-A molecules that exhibit reversible but strong affinity for methane. The refractive index is accurately determined using surface plasmon resonance. With this sensitive sensor, it is possible to detect concentrations of dissolved methane in the low nM range (1-300 nM), typical of open ocean environments. Detection limits, based on the sensor noise, were found to be lower than 0.2 nM when in a low-noise environment.

In-situ deployments confirmed the suitability of the method for in-situ measurements. Values given by the sensor correlate with the concentrations measured by traditional techniques. However the data highlighted the extreme sensitivity of the technique to environmental noise, degrading the limits of detection, and also a possible gradual degradation over time.

CHAPTER 6: SUMMARY AND PERSPECTIVES

6.1. Conclusions

The main objective of this work was to investigate the different technologies available for the in-situ measurement of dissolved methane in aqueous environments. These technologies were reviewed and two schemes, based on optical methodologies, were selected for further investigation.

The importance of an in-situ instrument for the measurement of dissolved methane was illustrated through the example of exploration of the Central Indian Ridge for hydrothermal activity. Methane is an important geochemical tracer present in hydrothermal plumes that can provide, in concert with other tracers, important information on the processes underlying individual sites of hydrothermal activity and the nature of the hydrothermal vent-sources.

6.1.1. Hydrothermal plumes along the Central Indian Ridge (20°S)

CTD hydrocasts and tow-yos were conducted along the Central Indian Ridge, over the Roger Plateau (segment 15 – 19S) and the Great Dodo Lava Plain (segment 16 – 18S) in December 2006 (KH-06-4 cruise, JAMSTEC) to look for hydrothermal activity. Seawater samples were collected to determine the concentrations of iron, manganese, and methane in the hydrothermal plumes.

On segment 15, a hydrothermal plume, probably originated from one single hydrothermal vent, is present at 19°33'S/65°50'E centred at 2400-2500 m. The source of the hydrothermal plume might be located north of the CTD 24 position and dispersed along the western flank by NW-SE currents. Concentrations of methane are similar to those measured in the Kairei vent field where fresh lavas were found. Hence, it is suggested that methane is produced by magmatic processes on this part of the Central Indian Ridge. On Segment 16, 1 or 2 hydrothermal plumes were detected directly overlying an extensive a lava plain (18°20'S/65°18'E), characterized by fresh lava flows

and the presence of a thin sediment layer, if any. Higher methane concentrations were measured at this site suggesting that the source of venting was approached more closely at this site.

These data highlight the role of methane as a geochemical tracer for hydrothermal activity along mid-ocean ridges. Associated with other tracers (Mn, Fe, Light Transmission), methane can provide useful information on both the dynamics of biogeochemical reactions within the dispersing plumes and on the origin of the source. CIR data showed clearly how the use of these parameters can be employed to locate the source or sources of neutrally buoyant hydrothermal plumes. Light attenuation and geochemical anomalies correlated well and provided interesting first-order information about the physical and chemical characteristics of the underlying hydrothermal systems. Difference in behaviour of various geochemical tracers can even, under ideal circumstances, be exploited to deduce the age of a hydrothermal plume and its distance to the source.

Tow-yos are an efficient way to intercept plumes, provided that there is a real time feedback from sensors mounted on the CTD-rosette frame. Currently, only physical/optical sensors have been used routinely to conduct detailed mapping of neutrally-buoyant plumes.

During the CIR cruise, a number of methane samples were degraded due to sampling and shipping issues and, consequently, could not be used for any detailed geochemical interpretations. Although some interpretations could have been made from the remaining samples, there is a loss of information that only in-situ sensors can prevent. During the CIR cruise, the Mn sensor GAMOS provided very useful information on a real time basis, which guided the sampling. However, the current in-situ sensing techniques for dissolved methane are not well adapted to the actual conditions in the deep sea environment.

6.1.2. Technologies available for dissolved methane measurements and first steps towards a new in-situ methane sensor

Measurements of dissolved gases such as dissolved methane require a specific procedure to separate the dissolved gas from the aqueous phase before analysis by gas chromatography. Various methods of extraction have been developed: static headspace extraction, dynamic headspace extraction, and purge-and-trap extraction. In all cases, dissolved gas analysis is a delicate procedure dependent on both physical and chemical parameters (vapour pressure, water solubility, and temperature) and sampling conditions (bottles, headspace volumes, extraction time, and temperature).

Within the entire analytical scheme, the extraction phase is the most time consuming and challenging step. In this Thesis, the static headspace extraction technique was chosen for its simplicity and rapidity. The main tasks to be fulfilled for an accurate extraction are 1) optimization of the equilibration time based on the expected concentration level and 2) optimization of the HS volume. Assuming sampling has been performed without any contamination, it is also necessary to eliminate interferences during the equilibration stage. For optimal results, it is recommended that extraction is performed as soon as possible after sample recovery. The material used for the sampling apparatus also has to be carefully chosen (gas- and water-tight glass bottles) with no plastic parts because the latter can be a source of contamination or leaks due to gas permeability.

In the method used in this work, the gas extraction took at least 30 minutes and a headspace/sample volume ratio of 1/10 was chosen. The final concentration was corrected from the extraction efficiency (0.96). Despite its limitations, the limit of detection measured with this method was 0.45 nM with good precision and accuracy.

Despite the high degree of interest in the scientific community for in-situ methane sensing, only a few sensors have been developed, – with variable detection limits and performance – for aqueous environments. These methods have used a variety of using different technologies, generally adapted from laboratory systems. With the exception of biosensors all commercially available devices rely on measurement in the gas phase requiring the use of gas-permeable membranes to separate the aqueous phase from the measuring cell of the sensor. Although detection technologies (IR spectroscopy, MS) are

well-established and competitive in terms of limits of detection and quality of data, the main limitation of these devices arises from the use of membranes, which remain poorly characterised and highly variable. In addition they have to be designed as a compromise, especially for deep-sea applications, between resistance to high in-situ pressures and time response; thick membranes will resist high pressures but their permeability will decrease, ultimately increasing the response time of the sensor.

Recent advances in optical technologies, associated with the development of new, sensitive, and specific reactive layers offer the potential for a further step forward in-situ methane sensing. The main characteristic of these techniques is an ability to detect methane directly in the aqueous phase without any need for gas extraction systems. Instead, such techniques make use of a sensitive interface whose optical properties are modified in the presence of methane. Surface enhanced Raman spectroscopy is currently being investigated because it offers promising applications but, currently, still suffers from limitations that could more readily be countered by other optical techniques.

The first optical technique tested in this Thesis was based on Near Infrared Fibre-optic Evanescent Wave Spectroscopy (NIR-FEWS). The strategy for this approach is to allow dissolved methane to diffuse into a thin PolyDiMethylSiloxane (PDMS) layer that exhibits low optical absorption in the near infrared and then perform spectroscopic measurements on that material. Experiments carried out as part of this Thesis were based on a FEWS sensor developed and adapted for the detection of heavy hydrocarbons in aqueous environments. However, the results presented here in this Thesis show that the technique is only of limited potential for dissolved HC gases, primarily due to the low partition coefficient of methane into PDMS. Compared with the typical concentrations found in deep-sea environments (1 nM to 10 μM in vent plumes), this technique (both theoretically and experimentally), in its current state, offers neither sufficient resolution (41 μM in theory) nor an acceptably low limit of detection for practical in situ sensor applications.

Nevertheless, in-situ methane evanescent wave sensors using enhanced reactive (indicator) layers have shown promising results in terms of sensitivity and optical properties of the sensing layer. In the work of Benounis et al. (2005; 2008), enhancement of the reactive layer allowed a better partition of methane into the PDMS resulting in a

large change in RI, which was used to enhance sensitivity for measurements in air and oil transformers.

The development of supramolecular chemistry together with polymeric materials has provided new opportunities for advanced sensing of dissolved gases in aqueous environments. Hence, a novel high sensitivity method for the determination of dissolved methane concentrations was tested based on preliminary results obtained from Benounis et al. (2005, 2008). Results obtained in the laboratory show that the method is suitable for miniaturisation and incorporation to in-situ sensor technology. The method is based on refractive index modulation of a PDMS layer loaded with cryptophane-A molecules that exhibit reversible but strong affinity for methane. The refractive index is accurately determined using surface plasmon resonance. With this sensitive sensor, it is possible to detect concentrations of dissolved methane in the low nM range (1-300 nM), typical of open ocean environments. Detection limits, based on sensor noise, were found to be lower than 0.2 nM in suitably low-noise environments.

In-situ deployments confirmed the suitability of the method for in-situ measurements. Values given by the sensor correlate well with concentrations measured by traditional techniques. However, the data obtained also served to highlight the extreme sensitivity of the technique to environmental noise, degrading the limits of detection.

6.2. Future works

6.2.1. Development of the methane sensor and possible applications

The framework of Technology Readiness Levels, presented in Table 4.2 (Chapter 4), allows an assessment of the readiness of the current in-situ methane sensor. In this Thesis, two techniques were described, the first – NIR FEWS – failed at level TRL 3, while the second technique based on SPR is currently between TRL 4 and TRL 5, although improvements of the sub-system (i.e. the sensor used for lab experiments) will be required to progress the sensor to the next levels.

First, the sensitivity revealed during field deployments will be reduced by adapting a flow head, which will protect the sensing layer from pressure variations due to movements of the sensor in the water. Future work will also focus on the optimization of the sensing film to lower the response time when methane concentrations decrease. This can be done by developing a specific and reproducible technique of layer coating, i.e. spin-coating, which would require the SPR sensor to be modified by producing removable gold layers. The current gold surface is currently part of the SPR sensor and cannot be removed. Hence, to produce methane sensing layer, it will be necessary to modify the SPR sensor in order to change the sensing layer on a regular basis.

The sensing film is currently deposited on the SPR layer by the drop-and-spread coating technique allowing thicknesses of 50 to 100 µm. As the surface plasmon effect is measured within the first hundred nanometers above the gold surface, it is necessary to reduce the layer thickness to optimize the transfer of the analytes to the sensing region. That would optimize the response time and the sensitivity of the instrument.

Response of the sensor could be also optimized by mixing cryptophane-A to different polymers (e.g. Teflon AF®), which are characterized by a better gas permeability. Thus, the partition of the gas would be enhanced.

Once the sensor has been fully tested and validated in the laboratory, as well as in relevant environments, engineering work will be required to adapt the device for widespread use in the scientific or industrial community. Key issues to be addressed will include among others:

- Integration on current sensor platforms (CTD/rosette, ROV, AUV…),
- Adaptation for long-term deployment within network of marine/environmental observatories (e.g. ESONET),
- Protection against biofouling and corrosion,
- Interface the sensor with networks and communication and data infrastructure mechanisms.

6.1.2 Detailed investigation of hydrothermal processes along the CIR

Using the new in situ technology being currently developed for deep sea exploration, further investigation of the segments 15 and 16 is required to 1) locate the sources and identify the vent-sources, based on the data collected during the KH-06-4 cruise, 2) sample the fluids to confirm the assumptions made in this Thesis, and 3) to determine whether there is a magmatic-hydrothermal interaction in these segments that responds specifically to the presence of the Reunion hot spot.

REFERENCES

Abraham, M.H. and Matteoli, E., 1988. The Temperature Variation of the Hydrophobic Effect. J. Chem. SOC., Faraday Trans 1, 85(6): 1985-2000.

Abril, G., Richard, S. and Guérin, F., 2006. In situ measurements of dissolved gases (CO_2 and CH_4) in a wide range of concentrations in a tropical reservoir using an equilibrator. Science of The Total Environment, 354(2-3): 246-251.

Aharon, P., Schwarcz, H.P. and Roberts, H.H., 1997. Radiometric dating of hydrocarbons seeps in the Gulf of Mexico. Geological Society American Bulletin, 109: 586–589.

Albert, K.J., Lewis, N.S., Schauer, C.L., Sotzing, G.A., Stitzel, S.E., Vaid, T.P. and Walt, D.R., 2000. Cross-Reactive Chemical Sensor Arrays. Chemical Review, 100(7): 2595-2626.

Artuso, F., Chamard, P., Piacentino, S., di Sarra, A., Meloni, D., Monteleone, F., Sferlazzo, D.M. and Thiery, F., 2007. Atmospheric methane in the Mediterranean: Analysis of measurements at the island of Lampedusa during 1995-2005. Atmospheric Environment, 41(18): 3877-3888.

Bach, W., Banerjee, N.R., Dick, H.J.B. and Baker, E.T., 2002. Discovery of ancient and active hydrothermal systems along the ultra-slow spreading Southwest Indian Ridge 10°-16°E. Geochemistry, Geophysics, Geosystems, 3(7): 15.

Baer, D.S., Paul, J.B., Gupta, M. and O'Keefe, A., 2002. Sensitive absorption measurements in the near-infrared region using off-axis integrated-cavity-output spectroscopy. Applied Physics B: Lasers and Optics, 75(2): 261-265.

Bake, K.D. and Walt, D.R., 2008. Multiplexed Spectroscopic Detections. Annu. Rev. Anal. Chem., 1(1): 17.1-17.33.

Baker, E.T., 1990. Hydrothermal plume prospecting: hydrographic and geochemical techniques. In: G.R. McMurray (Editor), Gorda Ridge: A Seafloor Spreading Center in the United States Exclusive Economic Zone. Springer-Verlag, New-York, pp. 155-167.

Baker, E.T., German, C.R. and Elderfield, H., 1995. Hydrothermal Plumes Over Spreading-Center Axes: Global Distributions and Geological Inferences. In: A.G. Union (Editor), Seafloor Hydrothermal Systems: Physical, Chemical, Biological, and Geological Interactions, pp. 47-71.

Baker, E.T., Edmonds, H.N., Michael, P.J., Bach, W., Dick, H.J.B., Snow, J.E., Walker, S.L., Banerjee, N.R. and Langmuir, C.H., 2004. Hydrothermal venting in magma deserts: The ultraslow-spreading Gakkel and Southwest Indian Ridges. Geochemistry Geophysics Geosystems, 5(8).

Baker, E.T. and German, C.R., 2004. On the global distribution of hydrothermal vent fields. In: C.R. German, J. Lin and L.M. Parson (Editors), Mid-Ocean Ridges: Hydrothermal Interactions Between the Lithosphere and Oceans. Geophysical Monograph Series, pp. 245-266.

Bange, H.W., Bartell, U.H., Rapsomanikis, S. and Andreae, M.O., 1994. Methane in the Baltic and North Seas and a reassessment of the marine emission of methane. Global Biogeochem. Cycles, 8: 465-480.

Bange, H.W., Ramesh, R., Rapsomanikis, S. and Andreae, M.O., 1998. Methane in surface waters of the Arabian Sea. Geophys. Res. Lett., 25(19): 3547-3550.

Banghar, A.R. and Sykes, L.R., 1969. Focal Mechanisms of Earthquakes in the Indian Ocean and Adjacent Regions. J. Geophys. Res., 74(2): 632-649.

Barsan, N., Schweizer-Berberich, M. and Göpel†, W., 1999. Fundamental and practical aspects in the design of nanoscaled SnO_2 gas sensors: a status report. Fresenius' Journal of Analytical Chemistry, 365(4): 287-304.

Bartik, K., Luhmer, M., Dutasta, J.P., Collet, A. and Reisse, J., 1998. ^{129}Xe and ^{1}H NMR Study of the Reversible Trapping of Xenon by Cryptophane-A in Organic Solution. J. Am. Chem. Soc., 120(4): 784-791.

Bell, R.J., Short, R.T., van Amerom, F.H.W. and Byrne, R.H., 2007. Calibration of an In Situ Membrane Inlet Mass Spectrometer for Measurements of Dissolved Gases and Volatile Organics in Seawater. Environ. Sci. Technol., 41(23): 8123-8128.

Benounis, M., Jaffrezic-Renault, N., Dutasta, J.P., Cherif, K. and Abdelghani, A., 2005. Study of a new evanescent wave optical fibre sensor for methane detection based on cryptophane molecules. Sensors and Actuators B, 107(1): 32-39.

Benounis, M., Aka-Ngnui, T., Jaffrezic, N. and Dutasta, J.P., 2008. NIR and optical fiber sensor for gases detection produced by transformation oil degradation. Sens. Actuators A, 141(1): 76-83.

Beranzoli, L., Braun, T., Calcara, M., Casale, P., De Santis, A., D'anna, G., Di Mauro, D., Etiope, G., Favali, F., Fuda, J.-L., Frugoni, F., Gamberi, F., Marani, M.P., Millot, C., Montuori, C. and Smriglio, G., 2003. Mission results from the first GEOSTAR observatory (Adriatic Sea, 1998). Earth Planets Space, 55: 361-3373.

Berner, U., Poggenburg, J., Faber, E., Quadfasel, D. and Frische, A., 2003. Methane in ocean waters of the Bay of Bengal: its sources and exchange with the atmosphere. Deep Sea Research II, 50: 925-950.

Bieri, R.H., 1974. Dissolved conservative gases in seawater. In: E.D. Goldberg (Editor), The Sea. Wiley, New York.

Bischoff, J.L. and Rosenbauer, R.J., 1989. Salinity variations in submarine hydrothermal systems by layered double-diffusive convection. Journal of Geology, 97: 613-623.

Bonatti, E., Honnorez, J. and Ferrara, G., 1971. Peridotite-Gabbro-Basalt Complex from the Equatorial Mid-Atlantic Ridge. Philosophical Transactions of the Royal Society of London. Series A, Mathematical and Physical Sciences, 268(1192): 385-402.

Bougault, H., Aballea, M., Radford-Knoery, J., Charlou, J.L., Baptiste, P.J., Appriou, P., Needham, H.D., German, C. and Miranda, M., 1998. FAMOUS and AMAR segments on the Mid-Atlantic Ridge: ubiquitous hydrothermal Mn, CH_4, [delta]^{3}He signals along the rift valley walls and rift offsets. Earth and Planetary Science Letters, 161(1-4): 1-17.

Brewer, P.G., Malb, G., Pasteris, J.D., White, S.N., Peltzer, T., Wopenka, B., Freeman, J. and Brown, M.O., 2004. Development of a laser Raman spectrometer for deep-ocean science. Deep Sea Res. I, 51: 739-753.

Briais, A.R., 1995. Structural analysis of the segmentation of the Central Indian Ridge between 20°30'S (Rodriguez Triple Junction). Marine Geophysical Researches, 17: 431-467.

Brockwell, P.J. and Davis, R.A., 1986. The Analysis of Time Series: Theory and Methods. Springer-Verlag, New York.

Bruhn, F.C., Carsey, F.D., Kohler, J., Mowlem, M., German, C.R. and Behar, A., 2005. MEMS Enablement and Analysis of the Miniature Autonomous Submersible Explorer. IEEE Journal of Ocean Engineering, 30(1): 165-178.

Bruneau, L., Jerlov, N.G. and Koczy, F.F., 1953. Physical and chemical methods (+ Appendix). Reports of the Swedish deep-sea expedition., 3(4): 99-112.

Buerck, J., Zimmermann, B., Mayer, J. and Ache, H.J., 1996. Integrated optical NIR-evanescent wave absorbance sensor for chemical analysis. Fresenius J. Anal. Chem., 354: 284-290.

Buerck, J., Mensch, M. and Kraemer, K., 1998. Field Experiments with a Portable Fiber-Optic Sensor System for Monitoring Hydrocarbons in Water. Field Analytical Chemistry and Technology, 2(4): 205-219.

Buerck, J., Roth, S., Kraemer, K., Scholz, M. and Klaas, N., 2001. Application of a fiber-optic NIR-EFA sensor system for in situ monitoring of aromatic hydrocarbons in contaminated groundwater. Journal of Hazardous Materials, 83(1-2): 11-28.

Buffett, B.A., 2000. Clathrate Hydrates. Annu. Rev. Earth Planet. Sci., 28(1): 477-507.

Burck, J. and Sensfelder, E., 1999. Optical fiber sensors for the distributed measurement of hydrocarbons. In: R.A. Lieberman (Editor), Chemical, Biochemical, and Environmental Fiber Sensors X. SPIE, Boston, MA, USA, pp. 98-109.

Bussell, J., Klinkhammer, G., Collier, R.W., Linke, P., Appel, F., Heeschen, K., Suess, E., De Angelis, M.A. and Masson, M., 1999. Applications of the METS methane sensor to the in situ determination of methane over a range of timescales and environments. , EOS Trans. Am. Geophys. Union.

Bussmann, I. and Schink, B., 2006. A modified diffusion-based methane sensor and its application in freshwater sediment. Limnology and Oceanography: Methods, 4: 275-283.

Camilli, R. and Hemond, H., 2004. NEREUS/Kemonaut, a mobile autonomous underwater mass spectrometer. Trends in analytical chemistry, 23(4): 307-313.

Campbell, A.C., Edmond, J.M., Colodner, D., Palmer, C.P. and Falkner, K.K., 1987. Chemistry of hydrothermal fluids from the Mariana Trough arc basin in comparison to mid-ocean ridge fluids. EOS Trans. Am. Geophys. Union, 68: 1531.

Canceill, J., Gottarelli, G. and Palmieri, P., 1987. Synthesis and Exciton Optical Activity of D3-Cryptophanes. J. Am. Chem. Soc., 109: 6454-6464.

Canceill, J. and Collet, A., 1988. Two-step Synthesis of D_3 and C_{3h} Cryptophanes. J.C.S. Chem. Comm., 9: 582-584.

Carbonaro, A., Walczak, R., Calderale, P.M. and Ferrari, M., 2004. Nano-pore silicon membrane characterization by diffusion and electrical resistance. Journal of Membrane Science, 241(2): 249-255.

Carotta, M.C., Guidi, V., Martinelli, G., Nagliati, M., Puzzovio, D. and Vecchi, D., 2008. Sensing of volatile alkanes by metal-oxide semiconductors. Sensors and Actuators B: Chemical, 130(1): 497-501.

Cave, R.R. and German, C.R., 1998. Box-coring around Rainbow? Have you lost your MARbles? BRIDGE Newsletters, 15: 12-15.

Charlou, J.-L. and Donval, J.-P., 1993. Hydrothermal methane venting between 12°N and 26°N along the Mid-Atlantic Ridge. J. Geophys. Res., 98: 9625-9642.

Charlou, J.L., Dimitriev, L., Bougault, H. and Needham, D., 1988. Hydrothermal CH_4 between 12° and 15° N over the Mid-Atlantic Ridge. Deep Sea Research, 35: 121-131.

Charlou, J.L., Bougault, H., Appriou, P., Jean-Baptiste, P., Etoubleau, J. and Birolleau, A., 1991a. Water column anomalies associated with hydrothermal activity between 11°40 and 13°N on the East Pacific Rise: Discrepancies between tracers,. Deep Sea Research, 38: 569-596.

Charlou, J.L., Bougault, H., Appriou, P., Nelsen, T. and Rona, P., 1991b. Different TDM/CH_4 hydrothermal plume signatures: TAG site at 26°N and serpentinized ultrabasic diapir at 15°05'N on the Mid-Atlantic Ridge. Geochimica et Cosmochimica Acta, 55(11): 3209-3222.

Charlou, J.L., Donval, J.P., Jean-Baptiste, P., Dapoigny, A. and Rona, P., 1996. Gases and helium isotopes in high temperature solutions sampled before and after ODP leg 158 drilling at TAG hydrothermal field (26°N, MAR). Geophysical Research Letters, 23(23): 3491-3494.

Charlou, J.L., Fouquet, Y., Bougault, H., Donval, J.P., Etoubleau, J., Jean-Baptiste, P., Dapoigny, A., Appriou, P. and Rona, P.A., 1998. Intense CH_4 plumes generated by serpentinization of ultramafic rocks at the intersection of the 15°20'N fracture zone and the Mid-Atlantic Ridge. Geochimica et Cosmochimica Acta, 62(13): 2323-2333.

Charlou, J.L., Donval, J.P., Douville, E., Jean-Baptiste, P., Radford-Knoery, J., Fouquet, Y., Dapoigny, A. and Stievenard, M., 2000. Compared geochemical signatures and the evolution of Menez Gwen (37°50'N) and Lucky Strike (37°17'N) hydrothermal fluids,

south of the Azores Triple Junction on the Mid-Atlantic Ridge. Chemical Geology, 171(1-2): 49-75.

Charlou, J.L., Donval, J.P., Fouquet, Y., Jean-Baptiste, P. and Holm, N., 2002. Geochemistry of high H_2 and CH_4 vent fluids issuing from ultramafic rocks at the Rainbow hydrothermal field (36°14'N, MAR). Chemical Geology, 191(4): 345-359.

Charlou, J.L., Donval, J.P., Zitter, T., Roy, N., Jean-Baptiste, P., Foucher, J.P. and Woodside, J., 2003. Evidence of methane venting and geochemistry of brines on mud volcanoes of the eastern Mediterranean Sea. Deep Sea Res. I, 50(8): 941-958.

Charlou, J.L., Donval, J.P., Fouquet, Y., Ondreas, H., Knoery, J., Cochonat, P., Levache, D., Poirier, Y., Jean-Baptiste, P. and Fourre, E., 2004. Physical and chemical characterization of gas hydrates and associated methane plumes in the Congo-Angola Basin. Chemical Geology, 205(3-4): 405-425.

Chinowsky, T.M., Quinn, J.G., Bartholomew, D.U., Kaiser, R. and Elkind, J.L., 2003. Performance of the Spreeta 2000 integrated surface plasmon resonance affinity sensor. Sens. Actuators B, 91(1-3): 266-274.

Christodoulou, D., Papatheodorou, G., Ferentinos, G. and Masson, M., 2003. Active seepage in two contrasting pockmark fields in the Patras and Corinth gulfs, Greece. Geo-Marine Letters, 23(3): 194-199.

Chung, H., Choi, H.J. and Ku, M.S., 1999. Rapid identification of petroleum products by near-infrared spectroscopy. Bulletin of the Korean Chemical Society, 20(9): 1021-1025.

Cicerone, R.J. and Oremland, R.S., 1988. Biogeochemical aspects of atmospheric methane. Global Biogeochemical Cycles, 2(4): 299-327.

Clark, J.F., Washburn, L., Hornafius, J.S. and Luyendyck, B., 2000. Dissolved hydrocarbon flux from natural marine seeps to the Southern California Bight. Journal of Geophysical Research, 105(C5): 11,509-11,522.

Collet, A., 1987. Cyclotriveratrylenes and cryptophanes. Tetrahedron, 43(24): 5725-5759.

Collet, A., Dutasta, J.-P., Lozach, B. and Canceill, J., 1993. Cyclotriveratrylenes and cryptophanes: Their synthesis and applications to host-guest chemistry and to the design of new materials, Supramolecular Chemistry I — Directed Synthesis and Molecular Recognition, pp. 103-129.

Collet, A., 1996. Cryptophanes. In: F. Vogtle (Editor), Comprehensive Supramolecular Chemistry. Pergamon, pp. 325-365.

Collier, R. and Klinkhammer, G., 2000. Applications of the METS Methane Sensor to the In-situ Detection of Methane Over a Range of Time Scales and Environments, RIDGE In situ Sensors Workshop.

Collier, R.W. and Lilley, M.D., 2005. Composition of shelf methane seeps on the Cascadia Continental Margin. Geophys. Res. Lett., 32: L06609, doi:10.1029/2004GL022050.

Connelly, D.P., German, C.R., Asada, M., Okino, K., Egorov, A., Naganuma, T., Pimenov, N.V., Cherkashev, G. and Tamaki, K., 2007. Hydrothermal activity on the ultra-slow spreading southern Knipovich Ridge. Geochemistry, Geophysics, Geosystems, 8(8).

Corliss, J.B., Dymond, J., Gordon, L.I., Edmond, J.M., Von Herzen, R.P., Ballard, R.d., Green, K., Williams, D., Bainbridge, A., Crane, K. and Van Andel, T.H., 1979. Submarine thermal springs on the Galapagos Rift. Science, 203: 1073-1083.

Costa, J.C.S., Sant'Ana, A.C., Corio, P. and Temperini, M.L.A., 2006. Chemical analysis of polycyclic aromatic hydrocarbons by surface-enhanced Raman spectroscopy. Colloquium Spectroscopicum Internationale XXXIV - CSI XXXIV, 70(5): 1011.

Cowen, J.P., Wen, X. and Popp, B.N., 2002. Methane in aging hydrothermal plumes. Geochim. Cosmoch. Acta, 66(20): 3563-3571.

Cram, D.J., Tanner, M.E. and Knobler, C.B., 1991. Guest Release and Capture by Hemicarcerands Introduces the Phenomenon of Constrictive Binding. J. Am. Chem. Soc., 113: 7717-7727.

Culshaw, B., Muhammad, F., Stewart, G., Murray, S., Pinchbeck, D., Norris, J., Cassidy, S., Wilkinson, M., Williams, D., Crisp, I., Van Ewyk, R. and McGhee, A., 1992. Evanescent wave methane detection using optical fibres. Electronics Letters, 28(24): 2232-2234.

Culshaw, B., Stewart, G., Dong, F., Tandy, C. and Moodie, D., 1998. Fibre optic techniques for remote spectroscopic methane detection--from concept to system realisation. Sensors and Actuators B: Chemical, 51(1-3): 25-37.

Currie, L.A., 1997. Detection: International update, and some emerging di-lemmas involving calibration, the blank and multiple detection decisions. Chemom. Intell. Lab. Systems, 37: 151-181.

Damgaard, L.R., Larsen, L.H. and Revsbech, N.P., 1995. Microscale biosensors for environmental monitoring. TrAC Trends in Analytical Chemistry, 14(7): 300.

Damgaard, L.R., Revsbech, N.P. and Reichardt, W., 1998. Use of an Oxygen-Insensitive Microscale Biosensor for Methane to Measure Methane Concentration Profiles in a Rice Paddy. Applied and Environmental Microbiology, 64(3): 864-870.

Damgaard, L.R., Nielsen, L.P. and Revsbech, N.P., 2001. Methane microprofiles in a sewage biofilm determined with a microscale biosensor. Water Research, 35(6): 1379.

Damm, E., Mackensen, A., Budeus, G., Faber, E. and Hanfland, C., 2005. Pathways of methane in seawater: Plume spreading in an Arctic shelf environment (SW-Spitsbergen). Continental Shelf Research, 25(12-13): 1453-1472.

Dass, C., 2007. Fundamentals of contemporary mass spectrometry. Wiley, New York, 585 pp.

de Angelis, M.A., Lilley, M.D. and Baross, J.A., 1993. Methane oxidation in deep-sea hydrothermal plumes of the endeavour segment of the Juan de Fuca Ridge. Deep Sea Research Part I: Oceanographic Research Papers, 40(6): 1169-1186.

De Gregorio, S., Gurrieri, S. and Valenza, M., 2005. A PTFE membrane for the in situ extraction of dissolved gases in natural waters: Theory and applications. Geochem. Geophys. Geosyst., 6(9): Q09005, doi:10.1029/2005GC000947.

de Wit, M.J., 2005. Valuing copper mined from ore deposits. Ecological Economics, 55(3): 437-443.

Debeda, H., Dulau, L., Dondon, P., Menil, F., Lucat, C. and Massok, P., 1997. Development of a reliable methane detector. Sensors and Actuators B: Chemical, 44(1-3): 248-256.

Demeestere, K., Dewulf, J., De Witte, B. and Van Langenhove, H., 2007. Sample preparation for the analysis of volatile organic compounds in air and water matrices. Journal of Chromatography A, 1153(1-2): 130-144.

DeMets, C., Gordon, R.G., Argus, D.F. and Stein, S., 1990. Current plate motions. Geophysical Journal International, 101(2): 425-478.

Deng, L., Han, L., Liang, W., Cao, Z., Xu, C., Zhang, W., Gong, Z. and Gao, X., 2007. A mid-infrared spectrometer based on difference frequency generation. Optics and Lasers in Engineering, 45(11): 1055-1058.

Detrick, R.S., Sinton, J.M., Ito, G., Canales, J.P., Behn, M., Blacic, T., Cushman, B., Dixon, J.E., Graham, D.W. and J.J., M., 2002. Correlated geophysical, geochemical, and volcanological manifestations of plume-ridge interaction along the Galápagos Spreading Center. Geochem. Geophys. Geosyst., 3(10): doi:10.1029/2002GC000350.

Douville, E., Charlou, J.L., Oelkers, E.H., Bienvenu, P., Jove Colon, C.F., Donval, J.P., Fouquet, Y., Prieur, D. and Appriou, P., 2002. The rainbow vent f luids (36°14'N, MAR): the influence of ultramafic rocks and phase separation on trace metal content in Mid-Atlantic Ridge hydrothermal fluids. Chemical geology, 184: 37-48.

Dunk, R.M., Peltzer, E.T., Walz, P. and Brewer, P.G., 2005. Seeing a Deep Ocean CO_2 Enrichment Experiment in a New Light: Laser Raman Detection of Dissolved CO_2 in Seawater. Environmental Science and Technology, 39(24): 9630-9636.

Edmond, J.M., Measures, C., McDuff, R.E., Chan, L.H., Collier, R., Grant, B., Gordon, L.I. and Corliss, J.B., 1979. Ridge crest hydrothermal activity and the balances of the major and minor elements in the ocean: The Galapagos data. Earth and Planetary Science Letters, 46(1): 1-18.

Elderfield, H. and Schultz, A., 1996. Mid-Ocean Ridge Hydrothermal Fluxes and the Chemical Composition of the Ocean. Annual Review of Earth and Planetary Sciences, 24(1): 191-224.

Ellis, J.W., 1927. New Infra-Red Absorption Bands of Methane. National Academy of Sciences, pp. 202-207.

Faber, E., Gerling, P., Berner, U. and Sohns, E., 1994. Methane in Ocean Waters: Concentration and Carbon Isotope Variability at East Pacific Rise and in the Arabian Sea. In: J. Van Ham, L.J.H.M. Janssen and R.J. Swart (Editors), International Symposium: Non-CO_2 greenhouses gases: why and how to control? Springer, Maastricht, The Netherlands.

Favali, P. and Beranzoli, L., 2005. Seafloor Observatory Science: a review. Annals of Geophysics, 48(5).

Fisher, R.L., Leonard Johnson, G. and C., H., 1967. Mascarene Plateau, western Indian Ocean. GSA Bulletin, 78(10): 1247-1266.

Fleischer, M. and Meixner, H., 1995. Sensitive, selective and stable CH_4 detection using semiconducting Ga_2O_3 thin films. Sensors and Actuators B: Chemical, 26(1-3): 81-84.

Fleischmann, M., Hendra, P.J. and McQuillan, A.J., 1974. Raman spectra of pyridine adsorbed at a silver electrode. Chem. Phys. Lett., 26: 163-166.

Fouquet, Y., 1997. Where are the large hydrothermal sulphide deposits in the ocean? Phil. Trans. R. Soc. London. A, 355: 427-441.

Frankignoulle, M., Borges, A. and Biondo, R., 2001. A new design of equilibrator to monitor carbon dioxide in highly dynamic and turbid environments. Water Research, 35(5): 1344-1347.

Fukasawa, T., Hozumi, S., Morita, M., Oketani, T. and Masson, M., 2006. Dissolved Methane Sensor for Methane Leakage Monitoring in Methane Hydrate Production. Oceans 2006, 19: 1-6.

Fusaro, A.J., Baco, A.R., Gerlach, G. and Shank, T.M., 2008. Development and characterization of 12 microsatellite markers from the deep-sea hydrothermal vent siboglinid Riftia pachyptila. Molecular Ecology Resources, 8(1): 132-134.

Gabard, J. and Collet, A., 1981. Synthesis of a (D_3)-Bis(cyclotriveratrylenyl) Macrocage by Stereospecific Replication of a (C_3)-Subunit. J.C.S. Chem. Comm., 21: 1137-1139.

Gamo, S., Chiba, H., Masuda, H., Edmonds, H.N., Fujioka, K., Kodama, Y., Nanba, H. and Sano, Y., 1996a. Chemical characteristics of hydrothermal fluids from the TAG mound of the mid-Atlantic ridge in August 1994: implications for spatial and temporal variability of hydrothermal activity. Geophysical Research Letters, 23(23): 3483-3486.

Gamo, T., Sakai, H., Nakayama, E., Ishida, K. and Kimoto, H., 1994. A submersible flow-through analyzer for in situ colorimetric measurement down to 2000 m depth in the ocean. Analytical Sciences, 10: 843-848.

Gamo, T., Nakayama, E., Shitashima, K., Isshiki, K., Obata, H., Okamura, K., Kanayama, S., Oomori, T., Koizumi, T., Matsumoto, S. and Hasumoto, H., 1996b. Hydrothermal plumes at the Rodriguez triple junction, Indian ridge. Earth and Planetary Science Letters, 142(1-2): 261-270.

Gamo, T., Chiba, H., Yamanaka, T., Okudaira, T., Hashimoto, J., Tsuchida, S., Ishibashi, J.-i., Kataoka, S., Tsunogai, U. and Okamura, K., 2001. Chemical characteristics of newly discovered black smoker fluids and associated hydrothermal plumes at the Rodriguez Triple Junction, Central Indian Ridge. Earth and Planetary Science Letters, 193(3-4): 371-379.

Garel , L., Dutasta, J.P. and Collet, A., 1993. Complexation of methane and chlorofluorocarbons by cryptophane-A in organic solution. Angew.Chem. Int. Ed. Engl., 32: 1169-1171.

German, C.R., Briem, J., Chin, C., Danielsen, M., Holland, S., James, R., Jónsdóttir, A., Ludford, E., Moser, C., Ólafsson, J., Palmer, M.R. and Rudnicki, M.D., 1994. Hydrothermal activity on the Reykjanes Ridge: the Steinahóll vent-field at 63°06'N. Earth and Planetary Science Letters, 121(3-4): 647-654.

German, C.R., Klinkhammer, G. and Rudnici, M.D., 1996. The Rainbow hydrothermal plume, 36°15'N, MAR. Geophysical Research Letters, 23(21): 2979-2982.

German, C.R., Baker, E.T., Mevel, C., Tamaki, K. and Team, t.F.S., 1998a. Hydrothermal activity along the southwest Indian Ridge. Nature, 395: 490-493.

German, C.R., Richards, K.J., Rudnicki, M.D., Lam, M.M. and Charlou, J.L., 1998b. Topographic control of a dispersing hydrothermal plume. Earth and Planetary Science Letters, 156(3-4): 267-273.

German, C.R., Livermore, R.A., Baker, E.T., Bruguier, N.I., Connelly, D.P., Cunningham, A.P., Morris, P., Rouse, I.P., Statham, P.J. and Tyler, P.A., 2000. Hydrothermal plumes above the East Scotia Ridge: an isolated high-latitude back-arc spreading centre. Earth and Planetary Science Letters, 184(1): 241-250.

German, C.R., Connelly, D.P., Evans, A.J., Murton, B.J., Curewitz, D., Okino, K., Statham, P.J. and Parson, L.M., 2001. Hydrothermal activity along the Central Indian Ridge: Ridges, hotspots, and philately. EOS Trans. Am. Geophys. Union, 82(47).

German, C.R. and Von Damm, K.L., 2003. Hydrothermal Processes. In: D.H. Heinrich and K.T. Karl (Editors), Treatise on Geochemistry. Pergamon, Oxford, pp. 181-222.

German, C.R., 2004. National and international programmes for the investigation of seafloor hydrothermal activity: the international state of the art, Kingston, Jamaica.

German, C.R. and Lin, J., 2004. The thermal structure of the oceanic crust, ridge-spreading and hydrothermal circulation: how well do we understand their inter-connections?, The Thermal Structure of the Oceanic Crust and the Dynamics of Seafloor Hydrothermal Circulation. American Geophysical Union, pp. 1-18.

German, C.R., Lin, J. and Parson, L.M., 2004. Mid Ocean Ridges: Hydrothermal interactions between the lithosphere and the oceans. Geophysical Monograph, 148. American Geophysical Union, 311 pp.

German, C.R., Baker, E.T., Connelly, D.P., Lupton, J.E., Resing, J., Prien, R., Walker, S.D., Edmonds, H.N. and Langmuir, C., 2006. Hydrothermal exploration of the Fonualei Rift and Spreading Center and the Northeast Lau Spreading Center. Geochemistry, Geophysics, Geosystems, 7(11).

German, C.R., Bennett, S.A., Connelly, D.P., Evans, A.J., Murton, B.J., Parson, L.M., Prien, R.D., Ramirez-Llodra, E., Jakuba, M., Shank, T.M., Yoerger, D.R., Baker, E.T., Walker, S.L. and Nakamura, K., 2008a. Hydrothermal activity on the southern Mid-Atlantic Ridge: Tectonically- and volcanically-controlled venting at 4-5°S. Earth and Planetary Science Letters, 273(3-4): 332-344.

German, C.R., Yoerger, D.R., Jakuba, M., Shank, T.M., Langmuir, C.H. and Nakamura, K.-i., 2008b. Hydrothermal exploration with the Autonomous Benthic Explorer. Deep Sea Research Part I: Oceanographic Research Papers, 55(2): 203-219.

Gharib, J.J., Sansone, F.J., Resing, J.A., Baker, E.T., Lupton, J.E. and Massoth, G.J., 2005. Methane dynamics in hydrothermal plumes over a superfast spreading center: East Pacific Rise, 27.5°-32.3°S. Journal of Geophysical Research, 110(B10101).

Glud, R.N., Tengberg, A., Kuhl, M., Hall, P.O.J., Klimant, I. and Holst, G., 2001. An in situ instrument for planar O_2 optode measurements at benthic interfaces. Limnology and Oceanography, 46(8): 2073-2081.

Goos, F. and Hanchen, H., 1947. Ein neuer und fundamentaler versuch zur totalreflektion. Ann. Phys., 1: 333-346.

Graedel, T.E. and Crutzen, P.J., 1993. Atmospheric Change. An Earth System Perspective. Freeman and Company, New York, 446 pp.

Gutiérrez, J., Getino, J., Horrillo, M.C., Arés, L., Robla, J.I., García, C. and Sayago, I., 1998. Electrical characterization of a thin film tin oxide sensor array for VOCs detection. Thin Solid Films, 317(1-2): 429-431.

Ha, N.B. and Kronfeldt, F.-D., 2004. Surface Enhanced Raman Spectroscopy (SERS) for In-Situ Analysis of Mixures of Polycyclic Aromatic Hydrocarbons (PAHs) in Seawater, The Ninth Asia Pacific Physics Conference, Hanoi, Vietnam.

Hakemian, A.S. and Rosenzweig, A.C., 2007. The Biochemistry of Methane Oxidation. Annual Review of Biochemistry, 76(1): 223-241.

Halász, I. and Schneider, W., 1961. Quantitative Gas Chromatographic Analysis of Hydrocarbons with Capillary Column and Flame Ionization Detector. Analytical Chemistry, 33(8): 978-982.

Hansen, J., Fung, I., Lacis, A., Rind, D., Lebedeff, S., Ruedy, R., Russell, G. and Stone, P., 1988. Global climate changes as forecast by Goddard Institute for Space Studies three-dimensional model. J. Geophys. Res., 93: 9341-9364.

Harrick, N.J., 1979. Internal reflection spectroscopy. Harrick Scientific Corporation, New York.

Hashimoto, S., Tanaka, T., Yamashita, N. and Maeda, T., 2001. An automated purge and trap gas chromatography-mass spectrometry system for the sensitive shipboard analysis of volatile organic compounds in seawater. J. Sep. Sci., 24: 97-103.

Heeschen, K.U., Collier, R., de Angelis, M.A., Suess, E., Rehder, G., Linke, P. and Klinkhammer, G., 2005. Methane sources, distributions, and fluxes from cold vent sites at Hydrate Ridge, Cascadia Margin. Global Biogeochemical Cycles, 19(GB2016).

Heise, H.M., Bittner, A., Kupper, L. and Butvina, L.N., 1997. Comparison of evanescent wave spectroscopy based on silver halide fibres with conventional ATR-IR spectroscopy. Journal of Molecular Structure, 410-411: 521-525.

Hemond, H. and Camilli, R., 2002. NEREUS: engineering concept for an underwater mass spectrometer. Trends in analytical chemistry, 21(8): 526-533.

Herzig, P.M. and Pluger, W.L., 1988. Exploration for hydrothermal activity near the Rodriguez Triple Junction, Indian Ocean. Can. Mineralog., 26: 721-736.

Holm, N.G. and Charlou, J.L., 2001. Initial indications of abiotic formation of hydrocarbons in the Rainbow ultramafic hydrothermal system, Mid-Atlantic Ridge. Earth and Planetary Science Letters, 191(1-2): 1-8.

Holman, K.T., 2004. Cryptophanes: Molecular Containers. In: J.A. Atwood and J.W. Steed (Editors), Encyclopedia of Supramolecular Chemistry. Marcel Dekker, New York, pp. 340-348.

Homola, J., 1997. On the sensitivity of surface plasmon resonance sensors with spectral interrogation. Sensors and Actuators B: Chemical, 41(1-3): 207-211.

Homola, J., Yee, S.S. and Gauglitz, G., 1999. Surface plasmon resonance sensors: review. Sensors and Actuators B: Chemical, 54(1-2): 3-15.

Homola, J., 2003. Present and future of surface plasmon resonance biosensors. Anal. Bioanal. Chem., 377: 528-539.

Horita, J. and Berndt, M.E., 1999. Abiogenic Methane Formation and Isotopic Fractionation Under Hydrothermal Conditions. Science, 285(5430): 1055-1057.

Houghton, J.T., Jenkins, G.J. and Ephraums, J.J., 1990. Climate Change. The IPCC assessment. Cambridge University Press, pp. 18-22.

Houweling, S., Kaminski, T., Dentener, F., Lelieveld, J. and Heimann, M., 1999. Inverse modeling of methane sources and sinks using the adjoint of a global transport model. J. Geophys. Res., 106(D21): 26137-26160.

Hylton, K. and Mitra, S., 2007. Automated, on-line membrane extraction. Journal of Chromatography A, 1152(1-2): 199-214.

Ince, R. and Narayanaswamy, R., 2006. Analysis of the performance of interferometry, surface plasmon resonance and luminescence as biosensors and chemosensors. 569(1-2): 1.

IPCC, 2007. IPCC Fourth Assessment Report, WMO-UNEP.

Ishibashi, J., Wakita, H., Okamura, K., Nakayama, E., Feely, R.A., Lebon, G.T., Baker, E.T. and Marumo, K., 1997. Hydrothermal methane and manganese variation in the plume over the superfast-spreading southern East Pacific Rise. Geochimica et Cosmochimica Acta, 61(3): 485-500.

Jalbert, J. and Gilbert, R., 1994. Comparison between headspace and vacuum gas extraction techniques for the gas chromatographic determination of dissolved gases from transformer insulating oils, IEEE International Symposium on Electrical Insulation, Pittsburg, USA, pp. 123-129.

James, A.T. and Martin, A.J., 1952. Gas-liquid partition chromatography; the separation and micro-estimation of volatile fatty acids from formic acid to dodecanoid acid. The Biochemical Journal, 50(5): 679-690.

Jean-Baptiste, P., Belviso, S., Alaux, G., Nguyen, B.C. and Mihalopoulos, N., 1990. ^{3}He and methane in the Gulf of Aden. Geochimica et Cosmochimica Acta, 54(1): 111-116.

Jean-Baptiste, P., Mantisi, F., Pauwells, H., Grimaud, D. and Patriat, P., 1992. Hydrothermal ^{3}He and manganese plumes at 19°29'S on the Central Indian Ridge. Geophysical Research Letters, 19(17): 1787-1790.

Johnson, J.E., 1999. Evaluation of a seawater equilibrator for shipboard analysis of dissolved oceanic trace gases. Analytica Chimica Acta, 395(1-2): 119-132.

Johnson, K.S., Beehler, C.L. and Sakamoto-Arnold, C.M., 1986. A submersible flow analysis system. Analytica Chimica Acta, 179: 245-257.

Johnson, R.C., Cooks, R.G., Allen, T.M., Cisper, M.E. and Hemberger, P.H., 2000. Membrane introduction Mass Spectrometry: Trends and applications. Mass Spectrometry Reviews, 19(1): 1-37.

Kadko, D., 1993. An assessment of the effect of chemical scavenging within submarine hydrothermal plumes upon ocean geochemistry. Earth and Planetary Science Letters, 120(3-4): 361-374.

Katayama, H., Karasudani, T., Ishii, K., Marubayashi, K. and Ueda, H., 1999. Development of a Gas-Liquid Equilibrator for Estimating CO_2 Flux at the Ocean Surface. J. Atmos. Oceanic Technol., 16(10): 1450-1455.

Keir, R.S., Greinert, J., Rhein, M., Petrick, G., Sultenfu, J. and Furhaupter, K., 2005. Methane and methane carbon isotope ratios in the Northeast Atlantic including the Mid-Atlantic Ridge (50°N). Deep Sea Research Part I: Oceanographic Research Papers, 52(6): 1043.

Keir, R.S., Schmale, O., Walter, M., Sültenfuß, J., Seifert, R. and Rhein, M., 2008. Flux and dispersion of gases from the "Drachenschlund" hydrothermal vent at 8°18' S, 13°30' W on the Mid-Atlantic Ridge. Earth and Planetary Science Letters, 270(3-4): 338-348.

Kelley, D.S., Karson, J.A., Fruh-Green, G.L., Yoerger, D.R., Shank, T.M., Butterfield, D.A., Hayes, J.M., Schrenk, M.O., Olson, E.J., Proskurowski, G., Jakuba, M., Bradley, A., Larson, B., Ludwig, K., Glickson, D., Buckman, K., Bradley, A.S., Brazelton, W.J., Roe, K., Elend, M.J., Delacour, A., Bernasconi, S.M., Lilley, M.D., Baross, J.A., Summons, R.E. and Sylva, S.P., 2005. A Serpentinite-Hosted Ecosystem: The Lost City Hydrothermal Field. Science, 307(5714): 1428-1434.

Keppler, F., Hamilton, J.T.G., Bras, M. and Röckmann, T., 2006. Methane emissions from terrestrial plants under aeroboc conditions. Nature, 439.

Kibelka, G.P.G., Timothy Short, R., Toler, S.K., Edkins, J.E. and Byrne, R.H., 2004. Field-deployed underwater mass spectrometers for investigations of transient chemical systems. Talanta, 64(4): 961.

Klinkhammer, G.P., 1994. Fiber optic spectrometers for in-situ measurements in the oceans: the ZAPS Probe. Marine Chemistry, 47(1): 13-20.

Klitgord, K.D. and Mugie, J.D., 1974. The Galapagos spreading centre: A near-bottom geophysical study. Geophys. J. R. Astron. Soc., 38: 563-586.

Klunder, G.L., Bürck, J., Ache, H.-J., Silva, R.J. and Russo, R.E., 1994. Temperature Effects on a Fiber-Optic Evanescent Wave Absorption Sensor. Appl. Spectrosc., 48: 387-393.

Kolb, B. and Ettre, L.S., 1997. Static Headspace - Gas Chromatography: Theory and Practice. Wiley, New York, 658 pp.

Kotelnikova, S., 2002. Microbial production and oxidation of methane in deep subsurface. Earth-Science Reviews, 58(3-4): 367-395.

Kraft, M., 2004. Vibrational spectrocopic sensors, SCOS.

Kretschmann, E. and Raether, H., 1963. Radiative decay of nonradiative surface plasmons by light. Naturforsch, A 23: 2135-2136.

Kroger, S., Piletsky, S. and Turner, A.P.F., 2002. Biosensors for marine pollution research, monitoring and control. Marine Pollution Bulletin, 45(1-12): 24-34.

Kroger, S. and Law, R.J., 2005a. Sensing the sea. Trends in Biotechnology, 23(5): 250-256.

Kroger, S. and Law, R.J., 2005b. Biosensors for marine applications. We all need the sea, but does the sea need biosensors? Biosensors and Bioelectronics, 20: 1903-1913.

Kukanskis, K., Elkind, J., Melendez, J., Murphy, T., Miller, G. and Garner, H., 1999. Detection of DNA Hybridization Using the TISPR-1 Surface Plasmon Resonance Biosensor. Analytical Biochemistry, 274(1): 7-17.

Kumar Suresh, P., Vallabhan, C.P.G., Nampoori, V.P.N., Sivasankara pillai, V.N. and Radhakrishnan, P., 2002. A fibre optic evanescent wave sensor used for the detection of trace nitrites in water. Journal of Optics A: Pure and Applied Optics, 4: 247-250.

Kvenvolden, K.A., 1988. Methane hydrate-a major reservoir of carbon in the shallow geosphere? . Chem. Geol., 71: 41-51.

Lacis, A., Hansen, J., Lee, P., Mitchell, T. and Lebedeff, S., 1981. Greenhouse effect of trace gases. Geophys. Res. Lett., 8: 1035-1038.

Lamontagne, R.A., Rose-Pehrsson, Grabowski, K.E. and Knies, D.L., 2001. Response of METS Sensor to Methane Concentrations Found on the Texas-Louisiana Shelf in the Gulf of Mexico, Naval Research Laboratory.

Langseth, M.G. and Taylor, P.I., 1967. Recent measurements in the Indian Ocean. J. Geophys. Res., 72: 6249.

Lawrence, N.S., 2006. Analytical detection methodologies for methane and related hydrocarbons. Talanta, 69(2): 385-392.

Le Bris, N., Sarradin, P.-M., Birot, D. and Alayse-Danet, A.-M., 2000. A new chemical analyzer for in situ measurement of nitrate and total sulfide over hydrothermal vent biological communities. Marine Chemistry, 72(1): 1-15.

Le Bris, N., Sarradin, P.M. and Pennec, S., 2001. A new deep-sea probe for in situ pH measurement in the environment of hydrothermal vent biological communities. Deep Sea Research Part I, 48: 1941-1951.

Le Person, J., Colas, F., Compère, C., Lehaitre, M., Anne, M.L., Boussard-Plédel, C., Bureau, B., Adam, J.L., Deputier, S. and Guilloux-Viry, M., 2008. Surface plasmon resonance in chalcogenide glass-based optical system. Sensors and Actuators B: Chemical, 130(2): 771-776.

Lein, A.Y., Grichuk, D.V., Gurvich, E.G. and Bogdanov, Y.A., 2000. A new type of hydrogen- and methane-rich hydrothermal solutions in the Rift zone of the Mid-Atlantic Ridge. . Dokl. Earth Sci., 375A(9): 1304-1391.

Long, D.A., 1977. Raman Spectroscopy. Mc-Graw-Hill, New York.

Lovley, D.R., Dwyer, D.F. and Klug, M.J., 1982. Kinetic analysis of competition between sulfate reducers and methanogens for hydrogen in sediments. Appl. Environ. Microbiol., 43: 1373-1379.

Lowell, R.P., Rona, P. and Von Herzen, R.P., 1995. Seafloor hydrothermal systems. Journal of Geophysical Research, 100(B1): 327-352.

Lupton, J.E., Baker, E.T. and Massoth, G.J., 1999. Helium, heat, and the generation of hydrothermal event plumes at mid-ocean ridges. Earth and Planetary Science Letters, 171(3): 343-350.

Lupton, J.E., Butterfield, D.A., Lilley, M.D., Evans, L., Nakamura, K., Chadwick, W., Resing, J., Embley, R.E., Olson, E., Proskurowski, G., Baker, E.T., de Ronde, C., Roe, K.K., Greene, R., Lebon, G. and Young, C., 2006. Submarine venting of liquid carbon dioxide on a Mariana Arc volcano. Geochem. Geophys. Geosyst., 7(8).

Luther III, G.W., Glazer, B.T., Ma, S., Trouwborst, R.E., Moore, T.S., Metzger, E., Kraiya, C., Waite, T.J., Druschel, G., Sundby, B., Taillefert, M., Nuzzio, D.B., Shank, T.M., Lewis, B.L. and Brendel, P.J., 2008. Use of voltammetric solid-state (micro)electrodes for studying biogeochemical processes: Laboratory measurements to real time measurements with an in situ electrochemical analyzer (ISEA). Marine Chemistry, 108(3-4): 221-235.

Maddaloni, P., Gagliardi, G., Malara, P. and De Natale, P., 2006. Off-axis integrated-cavity-output spectroscopy for trace-gas concentration measurements: modeling and performance. J. Opt. Soc. Am. B, 23(9): 1938-1945.

Mah, R.A., Ward, D.M., Baresi, L. and Glass, T.L., 1977. Biogenesis of Methane. Annu Rev Microbiol, 31(1): 309-341.

Malara, P., Maddaloni, P., Gagliardi, G. and De Natale, P., 2006. Combining a difference-frequency source with an off-axis high-finesse cavity for trace-gas monitoring around 3 μm. Opt. Express, 14(3): 1304-1313.

Mann, D.P., Paraskeva, T., Pratt, K.F.E., Parkin, I.P. and Williams, D.E., 2005. Metal oxide semiconductor gas sensors utilizing a Cr-zeolite catalytic layer for improved selectivity. Meas. Sci. Technol., 16(5): 1193-1200.

March, R.E., 1997. An introduction to quadrupole ion trap mass spectrometry. Journal of Mass Spectrometry, 32(4): 351-369.

Marinaro, G., Etiope, G., Gasparoni, F., Calore, D., Cenedese, S., Furlan, F., Masson, M., Favali, F. and Blandin, J., 2004. GMM - a gas monitoring module for long-term detection of methane leakage from the seafloor. Environmental Geology, 46(8): 1053-1058.

Masson, M., Marx, S. and Weitkamp, C., 1997. New sensor for underwater hydrocarbon monitoring., Enviro-Sense: 3rd European Symposium on Environmental Sensing, Munich, Germany.

Mastalerz, V., de Lange, G.J., Dahlmann, A. and Feseker, T., 2007. Active venting at the Isis mud volcano, offshore Egypt: Origin and migration of hydrocarbons. Chemical Geology, 246(1-2): 87-106.

Mau, S., Valentine, D.L., Clark, J.F., Reed, J., Camilli, R. and Washburn, L., 2007. Dissolved methane distributions and air-sea flux in the plume of a massive seep field, Coal Oil Point, California. Geophysical Research Letters, 34.

Mauriz, E., Calle, A., Abad, A., Montoya, A., Hildebrandt, A., Barcelo, D. and Lechuga, L.M., 2006. Determination of carbaryl in natural water samples by a surface plasmon resonance flow-through immunosensor. Biosens. Bioelectron., 21(11): 2129-2136.

McCollom, T.M., 2000. Geochemical constraints on primary productivity in submarine hydrothermal vent plumes. Deep Sea Research Part I: Oceanographic Research Papers, 47(1): 85-101.

McDonald, J.C., Duffy, D.C., Anderson, J.R., Chiu, D.T., Wu, H., Schueller, O.J.A. and Whitesides, G.M., 2000. Fabrication of microfluidic systems in poly(dimethylsiloxane). Electrophoresis, 21(1): 27-40.

McKenzie, D. and Sclater, J.G., 1971. The evolution of the Indian Ocean since the Late Cretaceous. Geophys. J. R. Astron. Soc., 24: 437-528.

Melson, W.G. and Thompson, G., 1971. Petrology of a Transform Fault Zone and Adjacent Ridge Segments. Philosophical Transactions of the Royal Society of London. Series A, Mathematical and Physical Sciences, 268(1192): 423-441.

Merewether, R., Olsson, M.S. and Lonsdale, P.F., 1985. Acoustically Detected Hydrocarbon Plumes Rising From 2-km Depths in Guaymas Basin, Gulf of California. J. Geophys. Res., 90(B4): 3075-3085.

Merkel, T., Graeber, M. and Pagel, L., 1999. A new technology for fluidic microsystems based on PCB technology. Sensors and Actuators A: Physical, 77(2): 98-105.

Messica, A., Greenstein, A., Katzir, A., Schiessl, U. and Tacke, M., 1994. Fiber-optic evanescent wave sensor for gas detection. Optics Letters, 19(15): 1167-1169.

Messica, A., Greenstein, A. and Katzir, A., 1996. Theory of fiber-optic, evanescent-wave spectroscopy and sensors. Applied Optics, 35(13): 2274-2284.

Middelburg, J.J., Klaver, G., Nieuwenhuize, J., Wielemaker, A., de Haas, W., Vlug, T. and van der Nat, J., 1996. Organic matter mineralization in intertidal sediments along an estuarine gradient. Marine Ecology Progress Series, 132: 157-168.

Middelburg, J.J., Nieuwenhuize, J., Iversen, N., Høgh, N., de Wilde, H., Helder, W., Seifert, R. and Christof, O., 2002. Methane distribution in European tidal estuaries. Biogeochemistry, 59(1): 95-119.

Miwa, S. and Arakawa, T., 1996. Selective gas detection by means of surface plasmon resonance sensors. Thin Solid Films, 281-282(1-2): 466-468.

Mizaikoff, B., 1999. Mid-Infrared evanescent wave sensors - a novel approach for subsea monitoring. Meas. Sci. Technol., 10: 1185-1194.

Moorhead, J.G., 1932. The Near Infrared Absorption Spectrum of Methane. Physical Review, 39(1): 83-88.

Mossier-Boss, P.A. and Lieber, S.H., 2003. Detection of volatile organic compouds using surface enhanced Raman spectroscopy substrates mounted on a thermoelectric cooler. Analtica Chimica Acta, 488: 15-23.

Mottl, M.J., Sansone, F.J., Geoffrey Wheat, C., Resing, J.A., Baker, E.T. and Lupton, J.E., 1995. Manganese and methane in hydrothermal plumes along the East Pacific Rise, 8°40' to 11°50'N. Geochimica et Cosmochimica Acta, 59(20): 4147-4165.

Mullen, K.I., L.G., C., D-X., W. and K.T., C., 1992. Trace Detection of Ionic Species with Surface Enhanced Raman Spectroscopy. Spectroscopy, 7: 25-33.

Mullineaux, L.S. and France, S.C., 1995. Dispersal of deep-sea hydrothermal vent fauna. In: S.E. Humphris, R.A. Zierenberg, L.S. Mullineaux and R.E. Thomson (Editors), Seafloor hydrothermal systems: physical, chemical, biological, and geochemical interactions. Geophysical Monograph. American Geophysical Union, pp. 408-424.

Munch, U., Blum, N. and Halbach, P., 1999. Mineralogical and geochemical features of sulfide chimneys from the MESO zone, Central Indian Ridge. Chemical Geology, 155(1-2): 29.

Murphy, T., Lucht, S., Schmidt, H. and Kronfeldt, H.-D., 2000. Surface-enhanced Raman scattering (SERS) system for continuous measurements of chemicals in sea-water. J. Raman. Spectrosc., 31: 943-948.

Murton, B.J., Tindle, A.G., Milton, J.A. and Sauter, D., 2005. Heterogeneity in southern Central Indian Ridge MORB: Implications for ridge-hotspot interaction. Geochemistry, Geophysics, Geosystems, 6(3).

Murton, B.J., Baker, E.T., Sands, C.M. and German, C.R., 2006. Detection of an unusually large hydrothermal event above the slow-spreading Carlsberg Ridge: NW Indian Ocean. Geophysical Research Letters, 33: doi:10.1029/2006GL026048.

Nadezhdinskii, A., Berezin, A., Chernin, S., Ershov, O. and Kutnyak, V., 1999. High sensitivity methane analyzer based on tuned near infrared diode laser. Spectrochimica Acta Part A: Molecular and Biomolecular Spectroscopy, 55(10): 2083-2089.

Nakagawa, K., T., K., Shelkovnikov, A.S., de Labachelerie, M. and Ohtsu, M., 1994. Highly sensitive detection of molecular absorption using a high finesse optical cavity. Opt. Commun., 107: 369-372.

Nauret, F., Abouchami, W., Galer, S.J.G., Hofmann, A.W., Hemond, C., Chauvel, C. and Dyment, J., 2006. Correlated trace element-Pb isotope enrichments in Indian MORB along 18-20°S, Central Indian Ridge. Earth and Planetary Science Letters, 245(1-2): 137-152.

Newman, K.R., Cormier, M.-H., Weissel, J.K., Driscoll, N.W., Kastner, M., Solomon, E.A., Robertson, G., Hill, J.C., Singh, H., Camilli, R. and Eustice, R., 2008. Active methane venting observed at giant pockmarks along the U.S. mid-Atlantic shelf break. Earth and Planetary Science Letters, 267(1-2): 341-352.

Nicollian, E.H. and Brews, J.R., 1982. MOS (metal Oxide Semiconductor): Physics and Technology. Wiley, 928 pp.

Nielsen, A.H. and Nielsen, H.H., 1935. The Infrared Absorption Bands of Methane. Physical Review, 48(11): 864.

Nitkin, P.I., Anokhin, P.M. and Beloglazov, A.A., 1997. Chemical Sensors Based on Surface Plasmon Resonance in Si Grating Structures, Transducers'97: International Conference on Solid-State Sensors and Actuators, Chicago.

Nuster, R., Paltauf, G. and Burgholzer, P., 2006. Sensitivity of surface plasmon resonance sensors for the measurement of acoustic transients in liquids. IEEE Ultrasonics Symposium: 768-771.

Nylander, C., Liedberg, B. and Lind, T., 1982. Gas detection by means of surface plasmon resonance. Sens. Actuators, 3: 79-88.

O'Keefe, A., 1998. Integrated cavity output analysis of ultra-weak absorption. Chemical Physics Letters, 293(5-6): 331-336.

Okajima, H., Kakuma, S., Uchida, K., Wakimoto, Y. and Noda, K., 2006. Measurement of methane gas concentration using an infrared LED, SICE-ICASE International Joint Conference, Bexco, Busan, Korea.

Okamura, K., Kimoto, H., Saeki, K., Ishibashi, J., Obata, H., Maruo, M., Gamo, T., Nakayama, E. and Nozaki, Y., 2001. Development of a deep-sea in situ Mn analyzer and its application for hydrothermal plume observation. Marine Chemistry, 76(1-2): 17-26.

Pandey, P. and Chauhan, R.S., 2001. Membranes for gas separation. Progress in Polymer Science, 26(6): 853-893.

Paul, J.B., Lapson, L. and Anderson, J.G., 2001. Ultrasensitive Absorption Spectroscopy with a High-Finesse Optical Cavity and Off-Axis Alignment. Appl. Opt., 40(27): 4904-4910.

Paull, C.K., Ussler III, W., Borowski, W.S. and Spiess, F.N., 1995. Methane-rich plumes on the Carolina continental rise: Associations with gas hydrates. Geology, 23(1): 89-92.

Peters, J.P. and Van Slyke, D.D., 1932. Quantitative Clinical Chemistry. Baillere, Tindall and Cox, London, 325 pp.

Pironon, J., Grimmer, J.O.W., Teinturier, S., Guillaume, D. and Dubesy, J., 2003. Dissolved methane in water: temperature effect on Raman quantification in fluid inclusions. Journal of Geochemical Exploration, 78-79: 111-115.

Pitarke, J.M., Silkin, V.M., Chulkov, E.V. and Echenique, P.M., 2007. Theory of surface plasmons and surface-plasmon polaritons. Reports on Progress in Physics, 70: 1-87.

Pluger, W.L., Herzig, P.M., Becker, K., Deissmann, G., Schops, D., Lange, L., Jenisch, A., Ladage, S., Richnow, H.H., Schulz, T. and Michaelis, W., 1990. Discovery of hydrothermal fields at the Central Indian Ridge. Mar. Min., 9: 73-86.

Prien, R., 2007. The future of chemical in situ sensors. Marine Chemistry, 107: 422-432.

Proskurowski, G., Lilley, M.D., Seewald, J.S., Fruh-Green, G.L., Olson, E.J., Lupton, J.E., Sylva, S.P. and Kelley, D.S., 2008. Abiogenic Hydrocarbon Production at Lost City Hydrothermal Field. Science, 319(5863): 604-607.

Raichlin, Y., Marx, S., Gerber, L. and Katzir, A., 2004. Infrared fiber optic evanescent wave spectroscopy and its applications for the detection of toxic materials in water, in situ and in real time. In: J.C. Carrano and A. Zukauskas (Editors), Optically Based Biological and Chemical Sensing for Defence. SPIE, pp. 145-153.

Ramanathan, V., 1988. The greenhouse theory of climate change: A test by an inadvertent global experiment. Science, 240(4850): 293-299.

Rathgeb, F., Reichl, D., Herold, M., Mader, O., Mutschler, T. and Gauglitz, G., 2000. Dyeless optical detection of ammonia in the gaseous phase using a pH-responsive polymer - characterization of the sorption process. Fresenius' Journal of Analytical Chemistry, 368(2): 192-195.

Reeburgh, W.S., 2003. Global Methane Biogeochemistry. Treatise on Geochemistry, 4: 1-25.

Reeburgh, W.S., 2007. Oceanic Methane Biogeochemistry. Chem. Rev., 107: 486-513.

Rego, R., Caetano, N. and Mendes, A., 2005. Hydrogen/methane and hydrogen/nitrogen sensor based on the permselectivity of polymeric membranes. Eurosensors XVIII 2004 - The 18th European Conference on Solid-State Transducers, 111-112: 150.

Rehder, G., Collier, R.W., Heeschen, K., Kosro, P.M., Barth, J. and Suess, E., 2002. Enhanced marine CH_4 emissions to the atmosphere off Oregon caused by coastal upwelling. Global Biogeochem. Cycles, 16(3): 10.1029/2000GB001391.

Robb, W.L., 1968. Thin Silicone Membranes. Their Permeation Properties and Some Applications. Ann. N.Y. Acad. Sciences, 146: 119-137.

Rogalski, A. and Chrzanowski, K., 2002. Infrared devices and techniques. Opto-electronics review, 10(2): 11-136.

Rona, P., McGregor, B.A., Betzer, P.R., Bolger, G.W. and Krause, D.C., 1975. Anomalous water temperatures over Mid-Atlantic Ridge crest at 26°N latitude. Deep Sea Research, 22: 611-618.

Sackmann, M. and Materny, A., 2006. Surface enhanced Raman scatterring (SERS) - a quantitative analytical tool? Journal of Raman Spectroscopy, 37: 305-310.

Schaetzel, P., Bendjama, Z., Vauclair, C. and Nguyen, Q.T., 2001. Ideal and non-ideal diffusion through polymers: Application to pervaporation. Journal of Membrane Science, 191(1-2): 95-102.

Scheirer, D.S., Baker, E.T. and Johnson, K.T.M., 1998. Detection of hydrothermal plumes along the Southeast Indian Ridge near the Amsterdam-St. Paul Plateau. Geophysical Research Letters, 25(1): 97-100.

Schierbaum, K.D., Weimar, U. and Göpel, W., 1992. Comparison of ceramic, thick-film and thin-film chemical sensors based upon SnO_2. Sensors and Actuators B: Chemical, 7(1-3): 709-716.

Schirrer, R., Thepin, P. and Torres, G., 1992. Water absorption, swelling, rupture and salt release in salt-silicone rubber compounds. J. Mat. Sci., 27(13): 3424-3434.

Schmidt, H., Murphy, T. and Kronfeldt, H.-D., 1998. Detection of chemicals in seawater with surface-enhanced Raman scattering, CLEO, pp. 402-403.

Schmidt, H., Bich Ha, N., Pfannkuche, J., Amann, H., Kronfeldt, H.-D. and Kowalewska, G., 2004. Detection of PAHs in seawater using surface-enhanced Raman scattering (SERS). Mar. Poll. Bull., 49: 229-234.

Schmitt, M., Faber, E., Botz, R. and Stoffers, P., 1991. Extraction of Methane from Seawater Using Ultrasonic Vacuum Degassing. Analytical Chemistry, 63(5): 529-532.

Scholander, P.F., 1947. Analyzer for accurate estimation of respiratory gases in one-half cubic centimeter samples. J. Biol. Chem, 167: 235-250.

Schramm, U., Roesky, C.E.O., Winter, S., Rechenbach, T., Boeker, P., Schulze Lammers, P., Weber, E. and Bargon, J., 1999. Temperature dependence of an ammonia sensor in humid air based on a cryptophane-coated quartz microbalance. 57(1-3): 233.

Schwotzer, G., Latka, I., Lehmann, H. and Willsch, R., 1997. Optical sensing of hydrocarbons in air or in water using UV absorption in the evanescent field of fibers. Sensors and Actuators B: Chemical, 38-39: 150-153.

SCOR, 2007. GEOTRACES - An international study of the global marine biogeochemical cycles of Trace Elements and their Isotopes. Chemie der Erde - Geochemistry, 67: 85-131.

Scranton, M.I., 1977. The Marine Geochemistry of Methane, Massachussets Institute of Technology/Woods Hole Oceanographic Institution.

Seyfried, W.E., Johnson, K.S. and Tivey, M.K., 2000. In-Situ Sensors: Their Development and Application for the Study of Chemical, Physical and Biological Systems at Mid-Ocean Ridges, NSF/Ridge 2000, Aptos and Moss Landing, California.

Shioda, T., Takamatsu, N., Suzuki, K. and Shichijyo, S., 2003. Influence of water sorption on refractive index of fluorinated polyimide. Polymer, 44: 137-142.

Short, R.T., Fries, D.P., Toler, S.K., Lembke, C.E. and Byrne, R.H., 1999. Development of an underwater mass-spectrometry system for in situ chemical analysis. Meas. Sci. Technol., 10: 1195-1201.

Short, R.T., Fries, D.P., Kerr, M.L., Lembke, C.E., Toler, S.K., Wenner, P.G. and Byrne, R.H., 2001. Underwater Mass Spectrometers for in situ Chemical Analysis if the Hydrosphere. Journal of American Society for Mass Spectrometry, 12: 676-682.

Silveira, J.P., Anguita, J., Briones, F., Grasdepot, F. and Bazin, A., 1998. Micromachined methane sensor based on low resolution spectral modulation of IR absorption radiation. Sensors and Actuators B: Chemical, 48(1-3): 305-307.

Skala, T., Veltruska, K., Moroseac, M., Matolinova, I., Cirera, A. and Matolin, V., 2004. Redox process of Pd-SnO_2 system. Surface Science, 566: 1217-1221.

Smith, E.A. and Corn, R.M., 2003. Surface Plasmon Resonance Imaging as a Tool to Monitor Biomolecular Interactions in an Array Based Format. Applied Spectroscopy, 57(11): 320A-332A.

Sohn, J.H., Atzeni, M., Zeller, L. and Pioggia, G., 2008. Characterisation of humidity dependence of a metal oxide semiconductor sensor array using partial least squares. Sensors and Actuators B: Chemical, 131(1): 230-235.

Sosna, M., Denuault, G., Pascal, R.W., Prien, R.D. and Mowlem, M., 2007. Development of a reliable microelectrode dissolved oxygen sensor. Sens. Actuators B, 123(1): 344-351.

Souteyrand, E., Nicolas, D., Martin, J.R., Chauvet, J.P. and Perez, H., 1996. Behaviour of cryptophane molecules in gas media. Sens. Actuators B, 33(1-3): 182-187.

Stewart, G., Jin, W. and Culshaw, B., 1997. Prospects for fibre-optic evanescent-field gas sensors using absorption in the near-infrared. Sensors and Actuators B: Chemical, 38(1-3): 42-47.

Stiles, P.L., Dieringer, J.A., Shah, N.C. and Van Duyne, R.P., 2008. Surface-Enhanced Raman Spectroscopy. Annu. Rev. Anal. Chem., 1: 601-262.

Swinnerton, J.W. and Linnenbom, V.J., 1967. Determination of the C1 to C4 hydrocarbons in sea water by gas chromatography. Journal of Gas Chromatography, 5: 570-573.

Syage, J.A., Nies, B.J., Evans, M.D. and Hanold, K.A., 2001. Field-portable, high-speed GC/TOFMS. Journal of the American Society for Mass Spectrometry, 12(6): 648-655.

Taga, K., Mizaikoff, B. and Kellner, R., 1994. Fiber optic evanescent field sensors for gaseous species using MIR transparent fibers. Fresenius' Journal of Analytical Chemistry, 348(8): 556-559.

Tai, H., Tanaka, H. and Yoshino, T., 1987. Fiber-optic evanescent-wave methane-gas sensor using optical aborption for the 3.392-μm line of a He-Ne laser. Optics Letters, 12(6): 437-439.

Tengberg, A., De Bovee, F., Hall, P., Berelson, W., Chadwick, D., Ciceri, G., Crassous, P., Devol, A., Emerson, S., Gage, J., Glud, R., Graziottini, F., Gundersen, J., Hammond, D., Helder, W., Hinga, K., Holby, O., Jahnke, R., Khripounoff, A., Lieberman, S., Nuppenau, V., Pfannkuche, O., Reimers, C., Rowe, G., Sahami, A., Sayles, F., Schurter, M., Smallman, D., Wehrli, B. and De Wilde, P., 1995. Benthic chamber and profiling landers in oceanography -- A review of design, technical solutions and functioning. Progress In Oceanography, 35(3): 253-294.

Tengberg, A., Almroth, E. and Hall, P., 2003. Resuspension and its effects on organic carbon recycling and nutrient exchange in coastal sediments: in situ measurements using new experimental technology. Journal of Experimental Marine Biology and Ecology, 285-286: 119-142.

Tengberg, A., 2004. Accurate oxygen monitoring made possible with optodes, OCEANS '04. MTTS/IEEE TECHNO-OCEAN '04, pp. 110-114 Vol.1.

Toepke, M.W. and Beebe, D.J., 2006. PDMS absorption of small molecules and consequences in microfluidic applications. Lab Chip, 6: 1484-1486.

Tortell, P., 2005. Dissolved gas measurements in oceanic waters made by membrane inlet mass spectrometry. Limnology and Oceanography: Methods, 3: 24-37.

Tosner, Z., Petrov, O., Dvinskikh, S.V., Kowalewski, J. and Sandstrom, D., 2004. A ^{13}C solid-state NMR study of cryptophane-E:chloromethane inclusion complexes. Chem. Phys. Lett., 388: 208-211.

Tsunogai, U., Kou, S., Kimoto, H. and Kimoto, T., 2007. Development of in-situ methane sensor in seawater, 51th Annual Meeting of the Geochemical Society of Japan.

Tyler, S., Bull, J.M., Parson, L.M. and Tuckwell, G.W., 2007. Numerical modelling of non-transform discontinuity geometry: Implications for ridge structure, volcano-tectonic fabric development and hydrothermal activity at segment ends. Earth and Planetary Science Letters, 257(1-2): 146-159.

Upstill-Goddard, R.C., Barnes, J., Frost, T., Punshon, S. and Owens, N.J.P., 2000. Methane in the Southern North Sea: Low-Salinity Inputs, Estuarine Removal, and Atmospheric Flux. Global Biogeochem. Cycles, 14(4): 1205-1217.

Urashi, T. and Arakawa, T., 2001. Detection of lower hydrocarbons by means of surface plasmon resonance. Sens. Actuators B, 76(1-3): 32-35.

Valentine, D.L., Kastner, M., Wardlaw, G.D., Wang, X., Purdy, A. and Bartlett, D.H., 2005. Biogeochemical interactions of marine methane seeps, Hydrate Ridge, Oregon. Journal of Geophysical Research, 110: doi:10.1029/2005JG000025.

Van Dover, C., 2000. The Ecology of Deep-Sea Hydrothermal Vents. Princeton University Press, Princeton, USA.

Van Dover, C.L., Humphris, S.E., Fornari, D., Cavanaugh, C.M., Collier, R., Goffredi, S.K., Hashimoto, J., Lilley, M.D., Reysenbach, A.L., Shank, T.M., Von Damm, K.L., Banta, A., Gallant, R.M., Gotz, D., Green, D., Hall, J., Harmer, T.L., Hurtado, L.A., Johnson, P., McKiness, Z.P., Meredith, C., Olson, E., Pan, I.L., Turnipseed, M., Won, Y., Young, C.R., III and Vrijenhoek, R.C., 2001. Biogeography and Ecological Setting of Indian Ocean Hydrothermal Vents. Science, 294(5543): 818-823.

Van Dover, C.L., Aharon, P., Bernhard, J.M., Caylor, E., Doerries, M., Flickinger, W., Gilhooly, W., Goffredi, S.K., Knick, K.E. and Macko, S.A., 2003. Blake Ridge methane seeps: characterization of a soft-sediment, chemosynthetically based ecosystem. Deep Sea Research Part I: Oceanographic Research Papers, 50(2): 281-300.

van Rij, L.N., van Landschoot, R.C. and Schoonman, J., 2001. Detection of methane in oxygen-poor atmospheres using a catalytic asymmetric sensor design. Sensors and Actuators B: Chemical, 75(1-2): 111-120.

Varney, M.S., 2000. Introduction to Chemical Sensors in Oceanography. In: M.S. Varney (Editor), Chemical Sensors in Oceanography. Gordon and Breach Publishers, Southampton, pp. 1-47.

Von Damm, K., Edmond, J.M., Measures, C. and Grant, B., 1985. Chemistry of submarine hydrothermal solutions at Guaymas Basin, Gulf of California. Geochimica et Cosmochimica Acta, 49: 2221-2237.

Von Damm, K.L., 1990. Seafloor Hydrothermal Activity: Black Smoker Chemistry and Chimneys. Annu. Rev. Earth Planet. Sci., 18(1): 173-204.

Von Damm, K.L., Buttermore, L.G., Oosting, S.E., Bray, A.M., Fornari, D.J., Lilley, M.D. and Shanks Iii, W.C., 1997. Direct observation of the evolution of a seafloor `black smoker' from vapor to brine. Earth and Planetary Science Letters, 149(1-4): 101-111.

Von Damm, K.L., Bray, A.M., Buttermore, L.G. and Oosting, S.E., 1998. The geochemical controls on vent fluids from the Lucky Strike vent field, Mid-Atlantic Ridge. Earth and Planetary Science Letters, 160(3-4): 521-536.

Wahlen, M., 1993. The global methane cycle. Ann. Rev. Earth Planet. Sci., 21: 407-426.

Walker, S.L., Baker, E.T., Massoth, G.J. and Hey, R.H., 2004. Short-term variations in the distribution of hydrothermal plumes along a superfast spreading center, East Pacific Rise, 27 30' - 32 20'S. Geochemistry Geophysics Geosystems, 5(12): 9.

Weissenbacher, N., Lendl, B., Frank, J., Wanzenbock, H.D., Mizaikoff, B. and Kellner, R., 1997. Continuous surface enhanced Raman spectroscopy for the detection of trace organic pollutants in aqueous systems. Journal of Molecular Structure, 410-411: 539-542.

Welhan, J.A. and Craig, H., 1979. Methane and hydrogen in East Pacific Rise hydrothermal fluids. Geophysical Research Letters, 6(11).

Welhan, J.A. and Craig, H., 1983. Methane, hydrogen and helium in hydrothermal fluids at 21°N on the East Pacific Rise. In: P. Rona, K. Boström, L. Laubier and K.L.J. Smith (Editors),

Hydrothermal processes at seafloor spreading centers. Plenum Press, New York, pp. 391-410.

Werle, P., Slemr, F., Maurer, K., Kormann, R., Mucke, R. and Janker, B., 2002. Near- and mid-infrared laser-optical sensors for gas analysis. Optics and Lasers in Engineering, 37(2-3): 101-114.

White, S.N., Dunk, R.M., Peltzer, E.T., Freeman, J.J. and Brewer, P.G., 2006. In situ Raman analyses of deep-sea hydrothermal seep systems (Gorda Ridge and Hydrate Ridge). Geochemistry, Geophysics, Geosystems, 7(5): 12.

Williams, G. and Coles, G.S.V., 1999. The semistor: a new concept in selective methane detection. Sensors and Actuators B: Chemical, 57(1-3): 108-114.

Wolery, T.J. and Sleep, N.H., 1976. Hydrothermal circulation and geochemical flux at mid-ocean ridges. J. Geol., 84: 249-275.

Xu, Y., Cottenden, A. and Barrie Jones, N., 2006. A theoretical evaluation of fibre-optic evanescent wave absorption in spectroscopy and sensors. Optics and Lasers in Engineering, 44: 93-101.

Yamazoe, N. and Miura, N., 1994. Environmental gas sensing. Sensors and Actuators B: Chemical, 20(2-3): 95-102.

Yea, K.-h., Lee, S., Kyong, J.B., Choo, J., Lee, E.K., Joo, S.-W. and Lee, S., 2005. Ultra-sensitive trace analysis of cyanide water pollutant in a PDMS microfluidic channel using surface-enhanced Raman spectroscopy. The Analyst, 130: 1009-1011.

Young, M.A., Stuart, D.A., Lyandres, O., Glucksberg, M.R. and Van Duyne, R.P., 2004. Surface-enhanced Raman spectrsocopy with a laser pointer light source and miniature spectrometer. Can. J. Chem., 82: 1435-1441.

Zellner, R., Georgii, H.W., Mentel, T.F., Sausen, R., Baumgartel, H., Grunbein, W. and Hensel, F., 1999. Global Aspects of Atmospheric Chemistry. Springer, 334 pp.

Zeninari, V., Parvitte, B., Courtois, D., Kapitanov, V.A. and Ponomarev, Y.N., 2003. Methane detection on the sub-ppm level with a near-infrared diode laser photoacoustic sensor. Infrared Physics & Technology, 44(4): 253-261.

Zhang, L.M. and Uttamchandani, D., 1988. Optical chemical sensing employing surface plasmon resonance. Electronics Letters, 24(23): 1469-1470.

Zhang, Z., Ouriadov, A.V., Willson, C. and Balcom, B.J., 2005. Membrane gas diffusion measurements with MRI. Journal of Magnetic Resonance, 176(2): 215-222.

APPENDICES

Appendix 1: Plume chemistry data from Central Indian Ridge (segments 15 and 16)

CTD #	Depth	CH_4 (nM)	TDMn (nM)	TDFe (nM)	CH_4/Mn	CH_4/Fe	Fe/Mn
CTD 2	2851	2.24	1.58	1.30	1.41	1.72	0.82
	2750	2.28	1.54	1.08	1.48	2.11	0.70
	2700	2.55	1.41	2.10	1.81	1.22	1.49
	2650	2.22	1.14	4.24	1.95	0.52	3.72
	2550	2.18	1.01	1.73	2.16	1.26	1.71
	2500	1.02	1.28	1.74	0.79	0.59	1.35
	2450	1.42	1.93	2.13	0.74	0.67	1.10
	2350	1.96	0.96	2.54	2.04	0.77	2.66
	2200	2.07	0.89	2.27	2.31	0.91	2.54
	2100	2.06	0.66	0.80	3.12	2.58	1.21
	2000	2.20	0.26	1.14	8.36	1.94	4.32
	1500	1.97	0.29	2.00	6.70	0.99	6.80
	1000	2.01	0.36	0.02	5.66	84.14	0.07
	800	2.74	0.35	1.99	7.86	1.38	5.70
CTD 20	2619	2.01	2.30	1.82	0.87	1.10	0.79
	2500	2.53	2.66	1.89	0.95	1.34	0.71
	2487	2.17	2.82	1.84	0.77	1.18	0.65
	2475	2.47	4.31	5.03	0.57	0.49	1.17
	2464	2.42	5.86	2.72	0.41	0.89	0.46
	2445	2.78	6.04	4.27	0.46	0.65	0.71
	2435	3.00	4.49	5.78	0.67	0.52	1.29
	2419	2.43	1.85	4.29	1.32	0.57	2.32
	2409	2.39	1.87	4.03	1.28	0.59	2.16
	2400	2.33	1.30	2.45	1.79	0.95	1.88
	2000	2.71	7.62	1.63	0.35	1.66	0.21
CTD 22	2539	5.34	3.47	3.72	1.54	1.44	1.07
	2500	2.32	5.91	1.75	0.39	1.33	0.30
	2420	1.41	9.08	4.32	0.16	0.33	0.48
CTD 23	2540	2.12	19.66	3.47	0.11	0.61	0.18
	2510	1.60	25.73	5.74	0.06	0.28	0.22
	2480	2.99	8.14	6.73	0.37	0.44	0.83
	2450	2.40	2.15	4.11	1.11	0.58	1.91
CTD 25	2700	10.60	49.24	47.57	0.22	0.22	0.97
(tow-yo)	2674	8.94	27.16	76.23	0.33	0.12	0.36
	2702	9.19	66.52	67.04	0.14	0.14	0.99
	2700	6.43	68.21	81.59	0.09	0.08	0.84
	2700	6.20	58.58	67.78	0.11	0.09	0.86
	2710	6.17	68.65	44.63	0.09	0.14	1.54
	2730	5.80	35.61	35.31	0.16	0.16	1.01
CTD 26	2756	9.21	167.64	53.34	0.05	0.17	0.32
(tow-yo)	2747	7.96	144.84	60.58	0.05	0.13	0.42
	2737	7.24	131.84	59.33	0.05	0.12	0.45
	2717	7.44	135.46	57.90	0.05	0.13	0.43
	2707	7.54	137.16	57.48	0.05	0.13	0.42
	2697	5.47	99.66	50.73	0.05	0.11	0.51
	2687	3.91	71.10	47.84	0.05	0.08	0.67
	2677	4.16	75.79	43.12	0.05	0.10	0.57
	2600	3.88	70.67	34.28	0.05	0.11	0.49

Appendix 2: Published paper

C. Boulart, M. C. Mowlem, D. P. Connelly, J. Dutasta, and C. R. German, "A novel, low-cost, high performance dissolved methane sensor for aqueous environments," Opt. Express 16, 12607-12617 (2008)

A novel, low-cost, high performance dissolved methane sensor for aqueous environments

Cédric Boulart [1,*], Matthew C. Mowlem [1], Douglas P. Connelly [1], Jean-Pierre Dutasta [2], Christopher R. German [3]

[1] *National Oceanography Centre, Southampton, Waterfront Campus, European Way, SO14 3ZH, Southampton, U.K*
[2] *Laboratoire de Chimie, Ecole Normale Supérieure de Lyon, 46 Allée d'Italie, 69364 Lyon 07, France*
[3] *Woods Hole Oceanographic Institution, Clark South 276, MS#24, Woods Hole, Ma. 02543, USA*
** Corresponding author: cbo@noc.soton.ac.uk*

Abstract: A new method for in-situ detection and measurement of dissolved methane in aqueous media/environments with a limit of detection of 0.2 nM (3σ, and t_{90}~110s) and range (1-300 nM) is presented. The detection method is based on refractive index (RI) modulation of a modified PolyDiMethylSiloxane (PDMS) layer incorporating molecules of cryptophane-A [1] which have a selective and reversible affinity for methane [2]. The refractive index is accurately determined using surface plasmon resonance (SPR) [3]. A prototype sensor has been repeatedly tested, using a dissolved gas calibration system under a range of temperature and salinity regimes. Laboratory-based results show that the technique is specific, sensitive, and reversible. The method is suitable for miniaturization and incorporation into in situ sensor technology.

OCIS codes: (010.4450) Oceanic optics; (010.0280) Remote sensing and sensors; (130.6010) Sensors; (280.4788) Optical sensing and sensors.

References and links

1. E. Souteyrand, D. Nicolas, J. R. Martin, J. P. Chauvet, and H. Perez, "Behaviour of cryptophane molecules in gas media," Sens. Actuators B **33**, 182-187 (1996).
2. L. Garel , J. P. Dutasta, and A. Collet, "Complexation of methane and chlorofluorocarbons by cryptophane-A in organic solution," Angew.Chem. Int. Ed. Engl. **32**, 1169-1171 (1993).
3. T. M. Chinowsky, J. G. Quinn, D. U. Bartholomew, R. Kaiser, and J. L. Elkind, "Performance of the Spreeta 2000 integrated surface plasmon resonance affinity sensor," Sens. Actuators B **91**, 266-274 (2003).
4. W. S. Reeburgh, "Global Methane Biogeochemistry," Treatise on Geochemistry **4**, 1-25 (2003).
5. D. Amouroux, G. Roberts, S. Rapsomanikis, and M. O. Andreae, "Biogenic gas (CH_4, N_2O, DMS) Emission to the Atmosphere from Near-Shore of the North-western Black Sea," Estuar. Coast. Shelf Sci. **54**, 575-587 (2002).
6. G. Rehder, R. W. Collier, K. Heeschen, P. M. Kosro, J. Barth, and E. Suess, "Enhanced marine CH_4 emissions to the atmosphere off Oregon caused by coastal upwelling," Global Biogeochem. Cycles **16**, 10.1029/2000GB001391 (2002).
7. E. J. Sauter, S. I. Muyakshin, J.-L. Charlou, M. Schlüter, A. Boetius, K. Jerosch, E. Damm, J.-P. Foucher, and M. Klages, "Methane discharge from a deep-sea submarine mud volcano into the upper water column by gas hydrate-coated methane bubbles," Earth Planet. Sci. Lett. **243**, 354-365 (2006).
8. H. W. Bange, U. H. Bartell, S. Rapsomanikis, and M. O. Andreae, "Methane in the Baltic and North Seas and a reassessment of the marine emission of methane," Global Biogeochem. Cycles **8**, 465-480 (1994).
9. S. Houweling, T. Kaminski, F. Dentener, J. Lelieveld, and M. Heimann, "Inverse modeling of methane sources and sinks using the adjoint of a global transport model," J. Geophys. Res. **106**, 26137-26160 (1999).
10. W. J. Mitsch, and J. G. Gosselink, *Wetlands* (Wiley, New York, 2000).
11. E. T. Baker, R. N. Hey, J. E. Lupton, J. A. Resing, R. A. Feely, J. J. Gharib, G. J. Massoth, F. J. Sansone, M. Kleinrock, F. Martinez, D. F. Naar, C. Rodrigo, D. Bohnenstiehl, and D. Pardee, "Hydrothermal venting along Earth's fastest spreading center: East Pacific Rise, 27.5°-32.3°S," J. Geophys. Res. **107**, 2130, doi:2110.1029/2001JB000651 (2002).
12. K. A. Kvenvolden, "Methane hydrate-a major reservoir of carbon in the shallow geosphere? ," Chem. Geol. **71**, 41-51 (1988).

#95576 - $15.00 USD Received 29 Apr 2008; revised 28 May 2008; accepted 28 May 2008; published 6 Aug 2008

13. R. W. Collier, and M. D. Lilley, "Composition of shelf methane seeps on the Cascadia Continental Margin," Geophys. Res. Lett. **32**, L06609, doi:06610.01029/02004GL022050 (2005).
14. S. Kroger, and R. J. Law, "Sensing the sea," Trends in Biotechnology **23**, 250-256 (2005).
15. J. Bussell, G. Klinkhammer, R. W. Collier, P. Linke, F. Appel, K. Heeschen, E. Suess, M. A. De Angelis, and M. Masson, "Applications of the METS methane sensor to the in situ determination of methane over a range of timescales and environments. ," in *EOS Trans. Am. Geophys. Union*(1999).
16. R. T. Short, D. P. Fries, S. K. Toler, C. E. Lembke, and R. H. Byrne, "Development of an underwater mass-spectrometry system for in situ chemical analysis," Meas. Sci. Technol. **10**, 1195-1201 (1999).
17. S. De Gregorio, S. Gurrieri, and M. Valenza, "A PTFE membrane for the in situ extraction of dissolved gases in natural waters: Theory and applications," Geochem. Geophys. Geosyst. **6**, Q09005, doi:09010.01029/02005GC000947 (2005).
18. R. Camilli, and H. Hemond, "NEREUS/Kemonaut, a mobile autonomous underwater mass spectrometer," Trends in analytical chemistry **23**, 307-313 (2004).
19. R. Collier, and G. Klinkhammer, "Applications of the METS Methane Sensor to the In-situ Detection of Methane Over a Range of Time Scales and Environments," in *RIDGE In situ Sensors Workshop*(2000).
20. H.-D. Kronfeldt, H. Schmidt, H. Amann, B. D. MacCraith, M. Lehaitre, M. Leclercq, E. Bernabeu, B. Mizaikoff, and D. Grant, "Technical elements and Potential Application of Spectroscopy for Ocean Monitoring," in *OCEANS'98*(1998), pp. 1780-1784.
21. B. Mizaikoff, "Mid-Infrared evanescent wave sensors - a novel approach for subsea monitoring," Meas. Sci. Technol. **10**, 1185-1194 (1999).
22. T. Murphy, S. Lucht, H. Schmidt, and H.-D. Kronfeldt, "Surface-enhanced Raman scattering (SERS) system for continuous measurements of chemicals in sea-water," J. Raman. Spectrosc. **31**, 943-948 (2000).
23. P. G. Brewer, G. Malb, J. D. Pasteris, S. N. White, T. Peltzer, B. Wopenka, J. Freeman, and M. O. Brown, "Development of a laser Raman spectrometer for deep-ocean science," Deep Sea Res. I **51**, 739-753 (2004).
24. H. Schmidt, N. Bich Ha, J. Pfannkuche, H. Amann, H.-D. Kronfeldt, and G. Kowalewska, "Detection of PAHs in seawater using surface-enhanced Raman scattering (SERS)," Mar. Poll. Bull. **49**, 229-234 (2004).
25. K. Ideta, and T. Arakawa, "Surface plasmon resonance study for the detection of some chemical species," Sens. Actuators B **13**, 384-386 (1993).
26. E. Mauriz, A. Calle, A. Abad, A. Montoya, A. Hildebrandt, D. Barcelo, and L. M. Lechuga, "Determination of carbaryl in natural water samples by a surface plasmon resonance flow-through immunosensor," Biosens. Bioelectron. **21**, 2129-2136 (2006).
27. B. C. Sih, M. O. Wolf, D. Jarvis, and J. F. Young, "Surface-plasmon resonance sensing of alcohol with electrodeposited polythiophene and gold nanoparticle-oligothiophene films," J. Appl. Phys. **98**, 10.1063/1061.2138373 (2005).
28. T. Urashi, and T. Arakawa, "Detection of lower hydrocarbons by means of surface plasmon resonance," Sens. Actuators B **76**, 32-35 (2001).
29. C. Nylander, B. Liedberg, and T. Lind, "Gas detection by means of surface plasmon resonance," Sens. Actuators **3**, 79-88 (1982).
30. A. Collet, J.-P. Dutasta, B. Lozach, and J. Canceill, "Cyclotriveratrylenes and cryptophanes: Their synthesis and applications to host-guest chemistry and to the design of new materials," in *Supramolecular Chemistry I — Directed Synthesis and Molecular Recognition*(1993), pp. 103-129.
31. K. Bartik, M. Luhmer, J. P. Dutasta, A. Collet, and J. Reisse, "^{129}Xe and ^{1}H NMR Study of the Reversible Trapping of Xenon by Cryptophane-A in Organic Solution," J. Am. Chem. Soc. **120**, 784-791 (1998).
32. Z. Tosner, O. Petrov, S. V. Dvinskikh, J. Kowalewski, and D. Sandstrom, "A ^{13}C solid-state NMR study of cryptophane-E:chloromethane inclusion complexes," Chem. Phys. Lett. **388**, 208-211 (2004).
33. M. Benounis, N. Jaffrezic-Renault, J. P. Dutasta, K. Cherif, and A. Abdelghani, "Study of a new evanescent wave optical fibre sensor for methane detection based on cryptophane molecules," Proceedings of the 7th European Conference on Optical Chemical Sensors and Biosensors - EUROPT(R)ODE VII **107**, 32 (2005).
34. M. Benounis, T. Aka-Ngnui, N. Jaffrezic, and J. P. Dutasta, "NIR and optical fiber sensor for gases detection produced by transformation oil degradation," Sens. Actuators A **141**, 76-83 (2008).
35. J. Gabard, and A. Collet, "Synthesis of a (D_3)-Bis(cyclotriveratrylenyl) Macrocage by Stereospecific Replication of a (C_3)-Subunit," J.C.S. Chem. Comm. **21**, 1137-1139 (1981).
36. J. Canceill, and A. Collet, "Two-step Synthesis of D_3 and C_{3h} Cryptophanes," J.C.S. Chem. Comm. **9**, 582-584 (1988).
37. T. Brotin, N. Roy, and J. P. Dutasta, "Improved Synthesis of Functional CTVs and Cryptophanes Using $Sc(OTf)_3$ as Catalyst," J. Org. Chem. **70**, 6187-6195 (2005).
38. E. Kretschmann, and H. Raether, "Radiative decay of nonradiative surface plasmons by light," Naturforsch **A 23**, 2135-2136 (1963).
39. P. J. Brockwell, and R. A. Davis, *The Analysis of Time Series: Theory and Methods* (Springer-Verlag, New York, 1986).
40. J. W. Swinnerton, and V. J. Linnenbom, "Determination of the C1 to C4 hydrocarbons in sea water by gas chromatography," Journal of Gas Chromatography **5**, 570-573 (1967).
41. M. Sosna, G. Denuault, R. W. Pascal, R. D. Prien, and M. Mowlem, "Development of a reliable microelectrode dissolved oxygen sensor," Sens. Actuators B **123**, 344-351 (2007).
42. R. Schirrer, P. Thepin, and G. Torres, "Water absorption, swelling, rupture and salt release in salt-silicone rubber compounds," J. Mat. Sci. **27**, 3424-3434 (1992).
43. T. Shioda, N. Takamatsu, K. Suzuki, and S. Shichijyo, "Influence of water sorption on refractive index of fluorinated polyimide," Polymer **44**, 137-142 (2003).

#95576 - $15.00 USD Received 29 Apr 2008; revised 28 May 2008; accepted 28 May 2008; published 6 Aug 2008

44. L. A. Currie, "Detection: International update, and some emerging dilemmas involving calibration, the blank and multiple detection decisions," Chemom. Intell. Lab. Systems **37**, 151-181 (1997).
45. W. S. Reeburgh, "Oceanic Methane Biogeochemistry," Chem. Rev. **107**, 486-513 (2007).
46. J.-L. Charlou, and J.-P. Donval, "Hydrothermal methane venting between 12°N and 26°N along the Mid-Atlantic Ridge," J. Geophys. Res. **98**, 9625-9642 (1993).
47. J. P. Cowen, X. Wen, and B. N. Popp, "Methane in aging hydrothermal plumes," Geochim. Cosmoch. Acta **66**, 3563-3571 (2002).
48. C. K. Paull, W. Ussler III, W. S. Borowski, and F. N. Spiess, "Methane-rich plumes on the Carolina continental rise: Associations with gas hydrates," Geology **23**, 89-92 (1995).
49. J. L. Charlou, J. P. Donval, T. Zitter, N. Roy, P. Jean-Baptiste, J. P. Foucher, and J. Woodside, "Evidence of methane venting and geochemistry of brines on mud volcanoes of the eastern Mediterranean Sea," Deep Sea Res. I **50**, 941-958 (2003).
50. J. J. Middelburg, J. Nieuwenhuize, N. Iversen, N. Høgh, H. de Wilde, W. Helder, R. Seifert, and O. Christof, "Methane distribution in European tidal estuaries," Biogeochemistry **59**, 95-119 (2002).
51. N. Shakova, I. Semiletov, and G. Panteleev, "The distribution of methane on the Siberian Arctic shelves: Implications for the marine methane cycle," Geophys. Res. Lett. **32** (2005).
52. V. Kitidis, L. H. Tizzard, G. Uher, A. G. Judd, R. C. Upstill-Goddard, I. M. Head, N. D. Gray, G. Taylor, R. Duran, J. Iglesias, and S. Garcia-Gil, "The biogeochemical Cycling of Methane in Ria de Vigo, NW Spain: sediment Processing and Sea-Air exchange," J. Mar. Syst. **66**, 258-271 (2006).
53. H. W. Bange, R. Ramesh, S. Rapsomanikis, and M. O. Andreae, "Methane in surface waters of the Arabian Sea," Geophys. Res. Lett. **25**, 3547-3550 (1998).
54. G. L. Klunder, J. Bürck, H.-J. Ache, R. J. Silva, and R. E. Russo, "Temperature Effects on a Fiber-Optic Evanescent Wave Absorption Sensor," Appl. Spectrosc. **48**, 387-393 (1994).

1. Introduction

Methane (CH_4) has been studied as an important atmospheric component for over 200 years [4], and is thought to be responsible for between 15% and 22% of the greenhouse effect [5] [6] [7]. Aqueous environments, including wetlands and oceans represent important natural components of the global whole [8] [9] [10] [11] and have the potential to become major sources of methane to the atmosphere in a warmer climate [12]. However, their contribution to the global methane budget is not precisely known, due to our poor understanding of the different sources and processes that generate methane [8] [7], the remote location of the sources [13], and the lack of accurate and reliable measurements [14]. Information on the concentration and distribution of dissolved methane, in real time, would be of great value, therefore, in understanding the global methane cycle.

Current in-situ dissolved methane sensors are based on gaseous equilibration across a membrane [15] [16] [17], with subsequent detection, by semi-conduction [15], infrared spectroscopy (Contros GmBH, *pers. comm.*) or mass spectrometry [16] [18]. However, the silicon membranes used are unable to decouple methane concentrations from variabilities in all of: temperature, pressure, and concentrations of longer-chain hydrocarbons [18] [19]. As a result, there is an increasing interest in developing an ability to both detect the presence of, and measure the concentration of dissolved gases in aquatic environments using optical methods [20] [21] [22] [23] [24].

The strategy we have adopted here is to use an indicating polymeric layer whose refractive index (RI) is modified during the absorption of methane. In our method, RI is measured by Surface Plasmon Resonance (SPR) [3]. SPR offers electrical passivity, light weight, high sensitivity [25] and reversibility, allowing continuous, high throughput operations [26]. SPR has been used for the detection of gaseous alcohol [27] and C1-C4 hydrocarbons [28], for the determination of pesticides in water [26] and more generally, environmental pollution monitoring [29] [28].

In our design, dissolved methane detection and measurements are achieved by depositing a sensitive and selective polymeric film on the SPR gold layer. The reactive film consists of cryptophane-A molecules distributed within an optically transparent polymer coating. Cryptophanes are synthetic organic compounds with a cage-like structure defining a lipophilic cavity, which can complex neutral molecular species [30]. The general structure of cryptophanes is given in Fig. 1(a): the cavity volume is determined by Z functionalities, the external properties are dependent on the X and Y groups. One of the smallest of the series,

#95576 - $15.00 USD Received 29 Apr 2008; revised 28 May 2008; accepted 28 May 2008; published 6 Aug 2008

cryptophane-A (Fig. 1(b)), has an internal cavity suitable for accommodating small volatile compounds such as for instance methane, chlorofluorocarbons [2] or xenon [31]. In solution, it exhibits a strong affinity towards methane characterized by an association constant *Ka* = 130 M^{-1} at 298 K in tetrachloroethane [2]. Once included in the cavity, methane behaves as an integral part of the cryptophane-A, being bond by weak van der Waals forces [32]. The process of inclusion is reversible and dependent of the concentration of guest molecules present in the environment [2] [33]. Previous laboratory studies have shown that the specific absorption of gaseous methane in cryptophane-A, incorporated in an organic transparent cladding, led to an increase of the refractive index of the polymer proportional to the amount of encapsulated methane [33]. This property was used to enhance the performance of evanescent wave optical fibre sensors for the detection of methane in air [33] and the detection of gases in oil-filled transformers [34] but has never been used to detect dissolved methane in water.

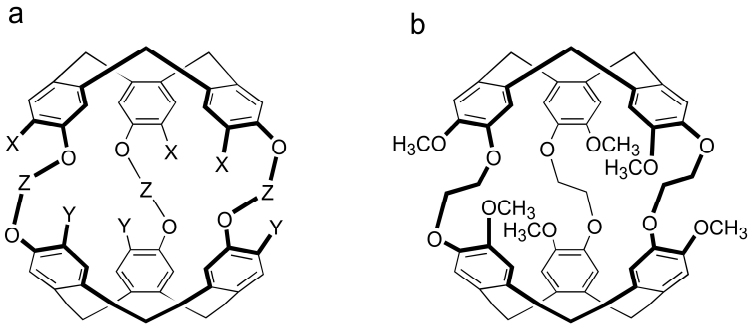

Fig. 1. General structure of cryptophane hosts; the cavity volume is determined by Z functionalities, the external properties are dependent on the X and Y groups (a) and molecular structure of cryptophane-A (b).

Here we present the first laboratory results of the detection and measurement of dissolved methane by monitoring the RI of a cryptophane-A loaded polymer-indicating layer, using SPR. These results are the first step towards a new low-cost and high performance in-situ methane sensor for application in freshwater and marine aqueous environments.

2. Experimental section

2.1 Methane sensor

The methane sensor was made of two parts: the reactive layer (sensing layer) and the SPR chip (Fig. 2). The reactive layer was modified PolyDiMethylSiloxane (PDMS – Siloprene K1000 + cross-linker K11 from SigmaAldrich® - refractive index 1.412) loaded with cryptophane-A [33] [34]. PDMS is a readily available and cheap polymer, and only 5mg or cryptophane-A is used per sensors. Though a commercial supply of cryptophane is not yet available, when mass produced this layer should be inexpensive. The synthesis of cryptophane-A was first reported by Gabard and Collet [35] following a multistep procedure. A two-step method was then developed starting from vanillyl alcohol and formic acid [36]. A recent procedure using scandium triflate under mild conditions was recently reported [37].

#95576 - $15.00 USD Received 29 Apr 2008; revised 28 May 2008; accepted 28 May 2008; published 6 Aug 2008

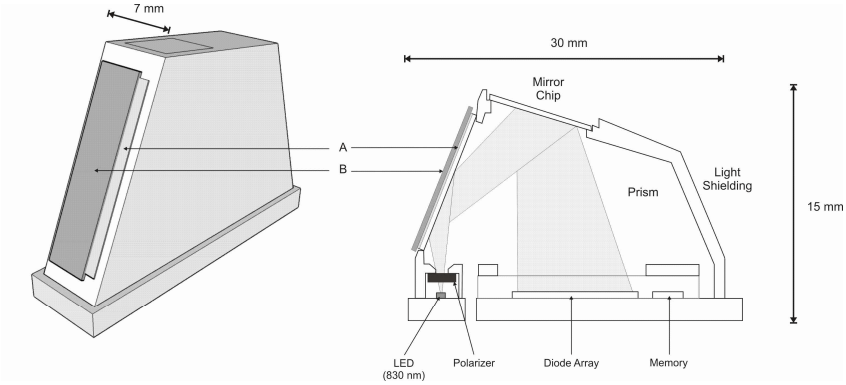

Fig. 2. Cross section of the methane sensor incorporating a Spreeta 2000 chip (adapted from Chinowsky et al., 2003) and the sensing film. A: gold layer (10 mm x 4 mm x 50 nm); B: reactive layer (PDMS+cryptophane A- 50-100 µm).

The SPR chip used was a Spreeta 2000 (Texas Instruments®) based on the Kretschmann configuration [38] and contained all of the optical components necessary for SPR measurements. This unit costs ~£250, enabling production of a low cost methane sensor. The sensor principle was described in Chinowsky *et al.* [3].

The polymer-cryptophane-A solution was drop-coated and spread over [28] four Spreeta gold surfaces. After the solvent was vaporized, a homogeneous and thin layer varying in thickness between 50-100 µm on each of the sensors was obtained. In order to validate the concept of the sensor, a polymeric layer was prepared without cryptophane and coated on a Spreeta chip in the same way as the methane sensor.

The system was adapted to be fully immersed in water. All experiments were performed in artificial seawater, prepared from Q-water (18.2MΩ cm) and sodium chloride (analytical grade).

Data were recorded by the appropriate software (provided with the Spreeta kit), which determines the RI from SPR curves (angle of resonance vs. light intensity). In our setup one data point (RI measurement) was given by one SPR curve. The frequency of measurements was set to be the same as the integration time, i.e. the time to operate the sensor and analyze the curve, automatically chosen by the software during the initialization phase. The frequency varied between 25 and 42.5 ms. The sensor output was treated as a time-series and decomposed by a 30s moving window average method [39].

2.2 Experimental set-up

Initial experiments (detection, reversibility, and calibration of the sensor) were performed at room temperature and atmospheric pressure by dissolving 20 ppm gas methane in artificial seawater (35 mg/L) prepared from degassed Q-water (18.2 MΩ cm) and NaCl (analytical grade). The highest concentration obtained with this set-up was 50 nM after 2h of bubbling. To test the reversibility of the response, the sensor was dipped in N_2-purged seawater maintained at equal temperature ($[CH_4]$ = 5 nM). Seawater samples were taken at regular timed intervals and analysed by headspace gas extraction followed by gas chromatography [40].

Accurate calibrations were carried out in a dissolved gas calibration system, adapted from [41] and described in Fig. 3. The principle consists of sequential replacement of initially low concentration solution (in closed vessel B) with volumes of concentrated solution from a reservoir (A), and homogenization (via stirring) after each addition for 2 to 3 minutes. After each addition and homogenization, the sensor output values were recorded and averaged for 2 minutes. The calculated concentration in the cell was dependent on the number of replacements (i), the concentration of methane in the reservoir (C_{sat}), the volume exchanged

#95576 - $15.00 USD Received 29 Apr 2008; revised 28 May 2008; accepted 28 May 2008; published 6 Aug 2008

(V_{ex}) and the volume of the measuring cell (V_{tot}), which remains constant. After the *i*th addition, the methane concentration is:

$$c_i = c_{i-1} + \frac{c_{sat}V_{ex}}{V_{tot}} - \frac{c_{i-1}V_{ex}}{V_{tot}} \quad (1)$$

Equation (1) was used to construct calibration plots allowing a very large number of points due to the small volume displaced by the pump (50 µl). The system was post-calibrated at the end of the experiment by analysing water samples using headspace gas extraction followed by gas chromatography. For all experiments, temperature was recorded independently by accurate temperature probes (0.01ºC).

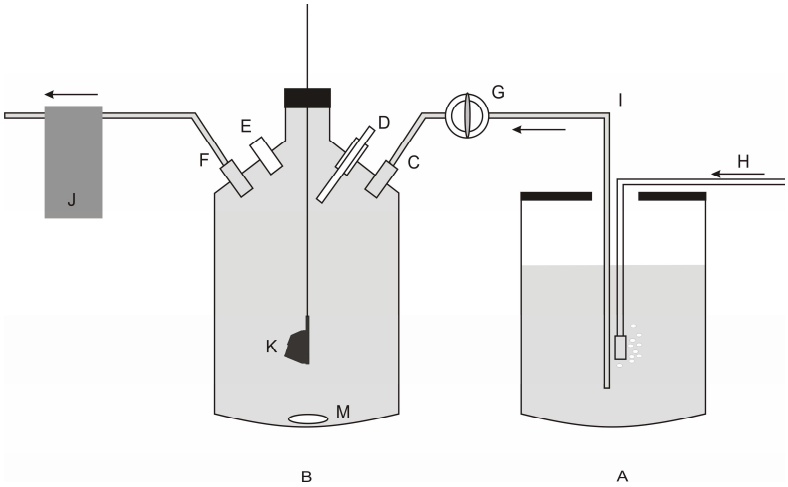

Fig. 3. Schematic representation of the gas calibration system. A: saturated solution reservoir, B: measurement cell, C: outlet connector, D: temperature probe, E: sampling port, F: outlet pump connector, G: valve, H: pure methane gas, I: glass tubing, J: pump, K: SPR sensor, M: magnetic stirrer.

3. Results and discussion

3.1 Sensor characterization

- Temporal response

The sensor was dipped alternately in a degassed (5 nM) and in a 50 nM dissolved CH_4 solution. The response to changes in dissolved methane concentration is presented in Fig. 4. Also shown, for comparison, are the equivalent responses of a Spreeta chip coated with a non-sensitive polymeric layer. A significant response can be observed for the methane sensor, whereas the RI of the non-sensitive polymeric layer did not change despite variations of dissolved methane concentration. The response time (t_{90}) between low concentration (5 nM) and high concentration (50 nM) was 1.8 minutes, i.e. 2.4 sec.nM^{-1}. However the response time to decreasing concentration is longer (~6.6 sec.nM^{-1}) but this hysteresis effect is reduced by stirring as shown by the step at the C:D boundary of Fig. 4. Stirring increases the concentration gradient between the sensing layer and the water which would explain the observed response.

#95576 - $15.00 USD Received 29 Apr 2008; revised 28 May 2008; accepted 28 May 2008; published 6 Aug 2008

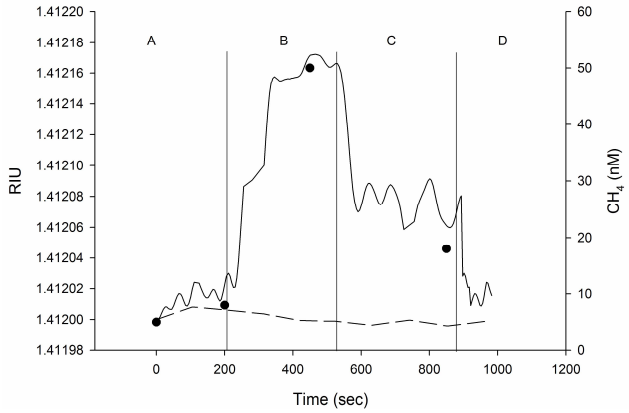

Fig. 4. Response of the sensor due to changes of dissolved methane concentration (solid line) compared with the response of non-sensing layer, i.e. without cryptophane (dashed line). Filled circles are the concentration of methane measured in control samples by gas chromatography. A: in degassed solution, B: in 50 nM CH4-solution, C: in degassed solution, D: in degassed solution with mixing.

- *Water absorption*

The sensing layer exhibits strong water absorption, as shown in Fig. 5, which is a common characteristic of PDMS-like polymers [42] [43]. The sensing layer required immersion for ~10 minutes to stabilize the signal before methane measurements could be made.

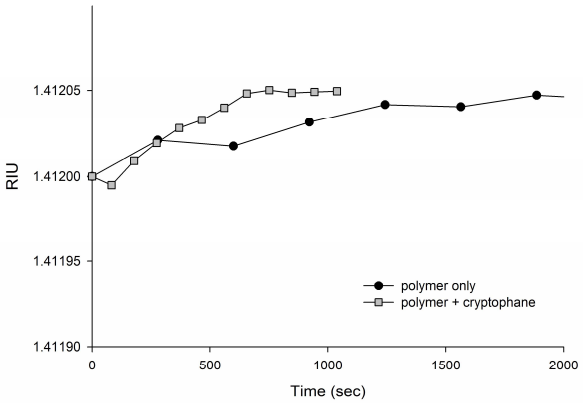

Fig. 5. Water absorption in the polymer (filled circles). 10 minutes are necessary to obtain a stable baseline at room temperature. The presence of cryptophane-A in the polymer (grey squares) does not influence the water absorption.

- *Sensitivity*

Figure 6(a) shows the results of sensor calibration using the gas calibration system. The system was soaked for 15 minutes in the water before the first measurement was performed to take the water absorption effect into account. A good relationship was observed between methane concentration and the RI of the sensing layer (R^2=0.9885). Previously Benounis *et al.* [33] reported that variations of the RI were dependent on the quantity of methane present in the media. The sensitivity calculated from our calibration curve is 5.5 10^{-6} RIU/nM. Several calibration curves (Fig. 6(b)) were obtained under varying experimental conditions (direct

#95576 - $15.00 USD Received 29 Apr 2008; revised 28 May 2008; accepted 28 May 2008; published 6 Aug 2008

bubbling or dissolved calibration systems), with an averaged R^2 of 0.95, highlighting the reproducibility of the sensor output. Table 1 gives a comparison of the sensitivities obtained for a number of different sensors of the same design but with subtly varying sensing layer properties (due to manufacturing tolerances). With the exception of "sensor 1" and "sensor 2 – 30days", calculated sensitivities were all in the same range (3.2 to 5.5 RIU/nM), emphasizing the reproducibility of the coating process. Reduced sensitivity could be the result of the lower quality of the sensing film due to, either the process of coating, or, the degradation of the layer over time. Contrary to Benounis *et al.* [33], where the sensing film was stable for several months, it was noted that the sensing film detaches from the Au surface overtime when used in seawater. To counter this effect, the sensing layer was replaced every two weeks.

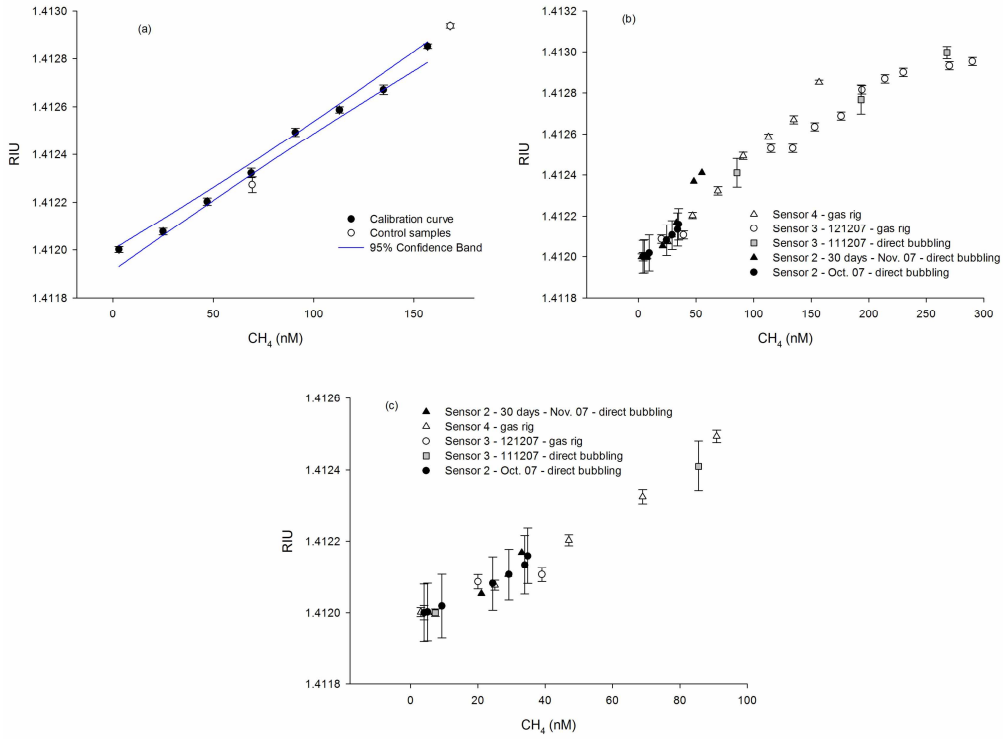

Fig. 6. Calibration curve obtained with "sensor 4" using the gas calibration rig (filled circles). Data were linearly fitted (R^2=0.9885). Errors bars are 2 times the standard deviation on RI measurement. Samples (opened circles) were taken for control (a). Calibration curves obtained in different experimental conditions (direct bubbling and gas calibration rig). Filled circles: sensor 2 (direct bubbling); filled triangles: sensor 2 – 30 days (direct bubbling); grey squares: sensor 3 (direct bubbling); opened circles: sensor 3 (gas rig); opened triangles: sensor 4 (gas rig) (b and c).

- *Noise, detection limits and operation range*

Sensor noise places a limit on the concentration of dissolved methane detectable by the sensor [3]. To correct for this the noise for each sensor was calculated from the standard deviation of the measurement (3σ) during stable conditions (lowest concentration of methane and temperature). Results are given in Table 1. Three factors contribute to the noise observed in the Spreeta: detector noise, shot noise and LED fluctuations [3]. Although the manufactured components have intrinsically low noise [3], it is necessary to optimize the noise performance by choosing an appropriate integration of signals as well as the RI measurement-time. In our experiments, the integration time of SPR measurements was automatically chosen by the software during the initialization of the sensor and the RI measurement frequency was adapted

#95576 - $15.00 USD Received 29 Apr 2008; revised 28 May 2008; accepted 28 May 2008; published 6 Aug 2008

to be the same as the integration time. The lowest noise level measured with our sensor was found to be 9 10^{-7} RIU (3σ – sensors 3 and 4). The noise level depends also on the experimental conditions as highlighted in the Table 1. The highest noise levels were obtained using the direct bubbling calibration system, which produced strong concentration gradients and agitation of the sensing layer and hence a high noise level.

Table 1. Sensitivity, noise and detection limits

	Calibration System	Sensitivity (10^{-6} RIU/nM)	Calibration curve R^2	Noise (10^{-6} RIU)	Detection limits (nM)
Sensor 1	Direct bubbling	7.8	0.906	10	1.28
Sensor 2	Direct bubbling	4.7	0.979	8	1.70
Sensor 2 – 30days	Direct bubbling	9.4	0.945	10	1.06
Sensor 3	Direct bubbling	3.7	0.985	7	1.89
Sensor 3 - 48h	Direct bubbling	4.5	0.921	7	1.56
Sensor 3 - 72h	Gas rig	3.2	0.949	0.9	0.28
Sensor 4	Gas rig	5.5	0.988	0.9	0.16
Manufacturer				0.1	

Although detection limits should be calculated from blank measurements (i.e. in presence of no methane) [44], they were obtained here from the noise levels measured in the sample with the lowest methane concentration, i.e. stable conditions. An estimate of the detection limits is given in Table 1 for each sensor. With the last set-up, which reduced the experimental noise level, the detection limit was 0.16 nM. To our knowledge, this is the first time that such low detection limits were measured for a dissolved methane sensor.

Calibrations show a good linear relationship up to 180 nM (Fig. 6(b)). The response of the sensor to concentrations between 180 and 300 nM is still reproducible despite a lower sensitivity. At methane concentrations greater than 300 nM, the calibration curve plateaus representing possible saturation of the sensor. The encapsulation of methane into cryptophane is a reversible process that depends on the equilibrium between the aqueous phase and the polymer. Saturation of the cryptophanes will therefore be related to the thermodynamic, e.g. the quantity of methane present in the aqueous solution and the association constant (K_a). The quality of the polymer may not have a role on the saturation of the sensing layer but on the diffusion of the gas through the polymer.

The current operation range of the sensor is in accordance with concentrations found in most of oceanic environments [45] and could be used for the investigation of key systems such deep sea hydrothermal plumes [46] [47], gas hydrate plumes [48] [49], continental shelf environments [50] [51] [52] or air-sea interface [8] [53].

3.2 Influence of environmental parameters

- *Temperature*

Figure 7 displays the effect of temperature on RI measurements for the polymeric layer (i.e. not loaded with Cryptophane-A) and the sensitive layer: the RI is inversely proportional to temperature. From these results it is evident that a high variation of temperature strongly influences the signal (2.35 10^{-5} RIU/°C) but it is unclear whether temperature influences the density of the polymer or the sensor performance itself. Changes in temperature modify the density of the polymer (i.e., number of C-H bonds per volume unit) and therefore the RI [54]. Spreeta chips are also dependent on temperature variations as they have no active temperature control and need to be calibrated for the temperature effect [3]. Future developments will require a detailed characterization of the temperature effect on the operating device. Once

#95576 - $15.00 USD Received 29 Apr 2008; revised 28 May 2008; accepted 28 May 2008; published 6 Aug 2008

these effects have been characterized measurement of water temperature, and the temperature of the SPR chip will enable compensation and hence improved sensor accuracy. For the majority of applications in the environment one could argue that temperature changes are not expected to be rapid, and/or widely varying. However, further experiments are required to study the sensor output when operated in different temperature range, as it might affect the Ka of the encapsulation.

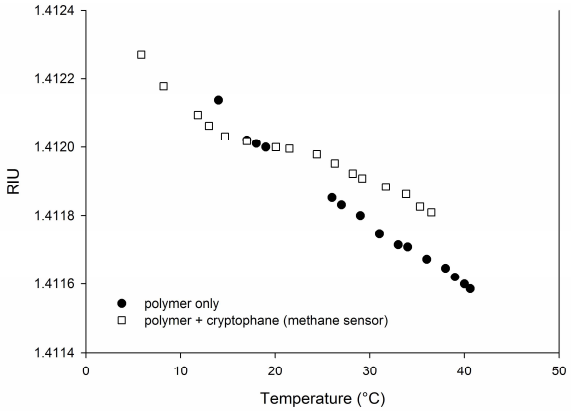

Fig. 7. Temperature effect on the sensor response (opened squares) compared with the response of a non-sensing layer (filled circles).

- *Salinity*

As the future sensor will operate in various conditions (from fresh water to marine environments) the effect of salinity on the sensor operability and response must also be tested. The salinity effect was tested by adding increasing concentrations of NaCl to the test apparatus to obtain varying salinities (0, 5, 10, 20, 25, 30, 35 and 40 PSU) whilst measuring the RI of the polymer. The salinity does not influence the RI of the coating (Fig. 8) as no significant RI changes were recorded.

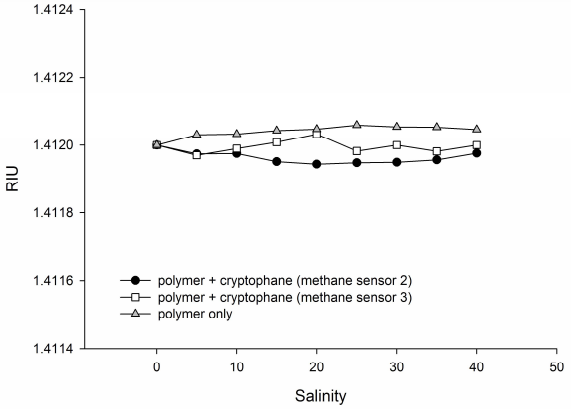

Fig. 8. Salinity effect on the sensor response (filled circles and opened squares) compared with the response of a non-sensing layer (grey triangles).

#95576 - $15.00 USD Received 29 Apr 2008; revised 28 May 2008; accepted 28 May 2008; published 6 Aug 2008

4. Conclusions and perspectives

A novel, low-cost method for the in-situ determination of dissolved methane concentrations is presented, based on refractive index modulation of a PDMS layer loaded with cryptophane-A molecules. The sensor described is low-cost as it utilizes a low-cost SPR sensor (SPREETA [3]), uses a cheap polymer substrate, and extremely small quantities of the cryptophane (~5mg per sensor). We have developed a laboratory system to test the principle of detection and to calibrate the response to methane concentration changes.

Results showed that the method was suitable for the detection of methane at low concentrations (1-300 nM), typical of open ocean environments, with detection limits lower than 0.2 nM. Cryptophane-A promises specificity to methane and is insensitive to larger hydrocarbons [33]. Our results show that the sensor is insensitive to the concentration of dissolved salts. Further investigation is required to evaluate cross-sensitivity effects from molecules of the same size as methane and an affinity constant suitable for encapsulation (ammonia, halomethanes).

Preliminary results obtained with a 50-100 μm thick membrane showed a quick response to increasing concentration (2.4 seconds per nM) but a hysteresis effect was observed when concentration was decreased. The hysteresis was reduced by maintaining a permanent concentration gradient between the sensing layer and the aqueous environment. Further development will include the optimization of the sensing layer: by reducing the thickness of the layer we expect a quicker diffusion of methane through the polymer and an optimization of the surface plasmon resonance measurement, as it is measured only within a few hundreds nanometers above the gold layer.

Laboratory experiments showed a degradation of the polymeric sensing film over time when the sensor was left in the water for more than two weeks. The degradation was both physical and chemical. It is possible to modify the chemical composition of the current polymer and to provide surface treatments of the gold to aid bonding. This will be undertaken in future research.

The calibration of the sensor was performed in the laboratory at room temperature (20°C). However, temperature influences dramatically the RI measurement. Further work will calibrate the sensor for different combinations of temperature and methane concentration.

Acknowledgments

This work has been supported and funded by EU-FP6-MoMAR network (MRTN-CT-2004-505026), NERC Technology Innovation Funds (NOCS), and NERC Core Strategic/Oceans 2025.

#95576 - $15.00 USD Received 29 Apr 2008; revised 28 May 2008; accepted 28 May 2008; published 6 Aug 2008